

**THREE-DIMENSIONAL SEISMIC
VELOCITY STRUCTURE OF THE
EARTH'S OUTERMOST
CORE AND MANTLE**

Thesis by
Monica Diane Kohler

In Partial Fulfillment of the Requirements
for the Degree of
Doctor of Philosophy

California Institute of Technology
Pasadena, California
1995

(Submitted November 29, 1994)

Acknowledgements

I have had the unusual opportunity to work with a relatively large number of faculty members during my graduate school tenure. Each shaped me as a scientist in a different way and caused me to look at my research with refreshingly different points of view. My first adviser, Prof. Toshiro Tanimoto, provided the opportunity to examine interior Earth structure with inversion techniques not often used for global outer core analysis. I am grateful to Prof. Don L. Anderson for agreeing to support me after Toshiro left for U. C. Santa Barbara. I enjoyed numerous conversations with Don concerning the geophysical implications for deep Earth structure suggested by three-dimensional Earth models of velocity structure, as well as the future of seismological research. Prof. Rob Clayton answered many questions about computational, numerical and statistical details in my work. Finally, I owe my initial interest in outer core structure to Prof. David Stevenson with whom I worked on a magnetohydrodynamic study of outermost core fluid motions during my first year at Caltech.

My sincere appreciation goes to all the Caltech graduate students, Seismo Lab staff, and U.S.G.S. scientists with whom I interacted both academically and socially. The wide variety of research projects carried out by students in the Seismological Lab was a source of further education and stimulation. The staff were always efficient and eager to help, especially Cheryl Contopulus and Dee Page. I will have special memories of the wonderful Caltech musicians with whom I performed in chamber music concerts, including a solo cello and piano recital at Dabney Hall during my third year. Likewise, I enjoyed the friendship of all those people who joined in on a long-lasting hobby that made life much

more enjoyable - floor and step aerobics. We made up a group of Caltech aerobics regulars who rarely missed Suzanna Webster's class at the gym during the noon hour.

I wish to say thank you to my family for their care and support. They have followed my studies from the beginning and allowed me to obtain the best education possible. My most heartfelt thanks goes to my husband, Pedro J. Pizarro, for his continuous love, encouragement, and support. In addition to being my best friend and pal, Pedro influenced my philosophical views of scientific research. We spent several wonderful years together at Caltech as graduate students and Resident Associates in an undergraduate residence hall. Those were the days when we could take off together for a day of skiing, mountain biking, or hiking in the San Gabriel Mountains.

Abstract

Obtaining an accurate, detailed picture of deep-Earth structure is of fundamental importance in a wide range of geophysical applications such as fluid dynamic, magnetohydrodynamic, and mineral physics models of the Earth which incorporate properties determined from seismology. Because it is such a drastic chemical and thermal boundary layer, the nature of the core-mantle boundary has important implications for deep-Earth processes, particularly those which have their origin in the lower mantle or outer core. Seismic data provide the most direct method of sampling the Earth's interior and are, therefore, useful for determining deep-Earth material properties.

The goal of this work has been to present models of three-dimensional, shear and compressional velocity structure which are self-consistent with the data and which can be used in other geophysical applications. The numerical inversions consisted of determining the three-dimensional structure of the outermost core and mantle of the Earth from long-period seismic waveforms. This approach is distinct from other global models of deep-Earth heterogeneity because it accounts for possible lateral heterogeneity in an outermost core layer whose properties are constrained by seismic phases which travel through the core-mantle boundary region.

This method is different from previous core studies in several important ways: synthetic seismograms are constructed using short-period normal modes for the entire set of body-wave phases which travel through the interior of the Earth (e.g., P, PP, S, SS, SKS). Over 5000 seismograms from global digital seismic networks were collected and processed. First-order perturbations in P-wave velocities in one outermost core layer and S-wave velocities within 11 mantle layers of varying thicknesses comprised the least-

squares solutions to the inverse problem. Spheroidal modes with periods between 33 and 100 sec were selected to model the body-wave portion of seismograms recorded from earthquakes which occurred globally.

The preferred model is a 12-layered model incorporating data weighted by inverse data variance. This model produces velocity anomalies in the mantle and outermost core which are acceptable for first-order perturbation methods. The results of one-layer inversions also point to the possible existence of lateral variations in the outermost core, most likely between $\pm 0.5\%$ but not as large as $\pm 5\%$. This model suggests that outermost core P-wave velocity perturbations accompany S-wave velocity perturbations in the lowermost mantle to produce observed variations in SKS-S and SKKS-SKS travel times. In addition, the patterns of structure vary smoothly and exhibit both large and small scale features. The spectral amplitudes fall off more rapidly for the lower mantle layers than for the upper mantle. The depth resolution displayed by the c_0^0 spherical harmonic term is 200-300 km for upper mantle layer midpoints and increases to 500-600 km for lower mantle layer midpoints.

The data variance reduction of entire body-wave portions as well as SnKS portions of seismograms are slightly better for the 12-layered model than for the 11-layered model; however, the total variance reductions were never very large. The results of the F ratio suggest that lateral velocity variations in the outermost core layer are not zero and that the deepest layer is statistically significant. This test does not require that the extra layer lie in the outermost core (as opposed to the lowermost mantle).

The results of pattern retrieval resolution tests support the conclusion that structure of the outermost core has been obtained independently from the mantle. Multiplicative factors have been calculated from the resolution tests using synthetic Earth models to place constraints on the amount of power leakage suspected from one region to another due to incomplete data coverage. An upper bound of 84% and a lower bound of 68% of the power of outermost core structure is, in fact, due to heterogeneity in the

outermost core. By the same analysis, less than 100% of the power of structure initially placed in the lowermost mantle was retrieved in that layer after the resolution inversion. An upper bound of 60% and a lower bound of 53% of the power of lowermost mantle structure is, in fact, due to D'' heterogeneity. Almost no leakage occurred from structure initially placed in the uppermost mantle layer.

Several possible sources of lateral velocity anomalies for the lowest layers are explored. Invoking thermal coupling between the mantle and core, one explanation is that the fluid surfaces are deformed due to cold downwellings of lower mantle, and as a result, outermost core fluid. This will give the appearance of lateral velocity anomalies. If lateral velocity anomalies indeed exist, they are likely to be due to a combination of lateral temperature variations and chemical inhomogeneity, suggested by mineral physics relationships.

Table of Contents

Acknowledgements	ii
Abstract.....	iv
Table of Contents	vii
List of Figures	x
List of Tables.....	xii
Chapter 1: Introduction	1
1.1 Core-mantle boundary region	1
1.1.a Core-mantle coupling.....	2
1.1.b SnKS phases.....	3
1.2 Background	6
1.2.a Outermost core.....	6
1.2.b Mantle	12
Chapter 2: Theory and Pattern Retrieval Resolution Constraints	15
2.1 Waveform construction by normal mode summation.....	15
2.2 First-order perturbation theory	21
2.3 Rayleigh wave constraints	28
2.4 Pattern retrieval resolution tests	29
2.4.a Outermost core layer.....	30
2.4.b Lowermost mantle layer.....	35
2.4.c Uppermost mantle layer	40
Chapter 3: Data Selection Methods.....	47
3.1 General description	47

3.2 Analysis and selection.....	52
3.2.a Cross-correlation technique.....	52
3.2.b Travel-time and epicentral distance windows.....	55
3.3 Normal mode data.....	57
3.4 Rayleigh wave phase perturbation data.....	61
Chapter 4: One-layer Inversions of SnKS Phases for Outermost Core Structure.....	62
4.1 Data set.....	63
4.1.a Analysis and description.....	63
4.1.b Travel time and epicentral distance range	63
4.2 SnKS waveform construction by normal mode summation.....	64
4.3 Ray parameter test	68
4.4 Results and discussion.....	70
4.4.a Lateral variation.....	70
4.4.b Raypath information	81
4.5 Conclusions.....	85
Chapter 5: Three-dimensional Inversions for Mantle and Outermost Core	
Velocities	87
5.1 Data set.....	88
5.2 Least-squares method.....	89
5.2.a Data weighting.....	91
5.2.b Damping schemes	92
5.3 Numerical solutions.....	93
5.3.a LINPACK routines	93
5.3.b Vectorization	97
5.4 Variance.....	98
5.5 Three-dimensional models	104
5.5.a 12-layered model with $1/v_b$ data weighting.....	105

5.5.b 11-layered model with $1/v_b$ data weighting	114
5.5.c 12-layered model with $1/M_0$ data weighting	121
5.5.d 11-layered model with $1/M_0$ data weighting.....	130
5.6 Resolution.....	136
5.7 F test.....	146
5.8 Conclusions.....	148
5.8.a Preferred model	148
5.8.b Source of outermost core heterogeneity	150
References.....	158
Appendix A1: A Theoretical, Magnetohydrodynamic Discussion	169
Appendix A2: An Adjustment to the Correction for Epicentral Distance due to Ellipticity.....	180

List of Figures

1.1 SKS and SKKS raypaths.....	5
2.1 Preliminary Reference Earth Model.....	20
2.2 Layer 12 initial synthetic Earth model	31
2.3 Resolution inversion results for layer 12 initial synthetic Earth model	34
2.4 Resolution inversion results for layer 11 initial synthetic Earth model	39
2.5 Resolution inversion results for layer 1 initial synthetic Earth model	43
3.1 Distance-number seismogram distribution	48
3.2 Locations of earthquakes and stations	49
3.3 Instrument response curves.....	51
3.4 Data-synthetic waveform fits with cross-correlation coefficient < 0.4	54
3.5 Body-wave phase amplitudes	56
3.6 Outermost core raypath coverage for one-layer inversions	58
3.7 Outermost core raypath coverage for three-dimensional inversions.....	59
3.8 Frechet depth kernels for $_{26}S_{21}$ and $_{22}S_{98}$	60
4.1 ISC travel-time curves	65
4.2 Ray parameter tests for SKS and SKKS waveform fits by normal modes.....	69
4.3 Before and after waveform fits for station CHTO.....	71
4.4 Before and after waveform fits for station RSNY	72
4.5 Distribution of number of data-synthetic SnKS waveform fit improvements	74
4.6 P-wave velocity perturbation map for model MDLSH.....	75
4.7 P-wave velocity perturbation map for modified model MDLSH	77
4.8 SKKS-SKS residual map from Souriau and Poupinet [1991].....	78
4.9 Geographical variation in P-wave velocity perturbations using MDLSH.....	79
4.10 Geographical variation in P-wave velocity perturbations using modified MDLSH	80
4.11 SKS and SKKS raypaths for distance of 112°	83

4.12 SKS and SKKS raypaths for distance of 129°	84
5.1 Data variance as a function of iteration number	94
5.2 Variance-damping parameter tradeoff curve	100
5.3 Data-synthetic seismogram fits before and after the inversion	102
5.4 Data-synthetic seismogram fits before and after the inversion	103
5.5 Results of 12-layer inversion using the I^1 data weighting scheme	108
5.6 Spectral amplitudes for model 11aSV_1P	110
5.7 PREM and modified PREM from model 11aSV_1P, and 11bSV	115
5.8 Results of 11-layer inversion using the I^1 data weighting scheme	118
5.9 Spectral amplitudes for model 11aSV	120
5.10 Results of 12-layer inversion using the I^2 data weighting scheme	125
5.11 Spectral amplitudes for model 11bSV_1P	127
5.12 Results of 11-layer inversion using the I^2 data weighting scheme	133
5.13 Spectral amplitudes for model 11bSV	135
5.14 Depth resolution for 12 target depths of model 11aSV_1P	138
5.15 Depth resolution for 11 target depths of model 11aSV	141
5.16 Depth resolution for 12 target depths of model 11bSV_1P	143
5.17 Depth resolution for 11 target depths of model 11bSV	145
A1.1 Temperature profiles near CMB	171
A1.2 CMB topography [Morelli and Dziewonski, 1987] and resulting core fluid flow	175
A1.3 CMB topography [Gudmundssen, 1989] and resulting core fluid flow	176
A1.4 Core fluid velocity from magnetic field data inversion [Bloxham, 1989a]	177
A2.1 Distance correction vs. angular order and group velocity for station TAU	182
A2.2 Distance correction vs. angular order and group velocity for station CHTO	183

List of Tables

2.1	Depths and thicknesses of layers	27
2.2	Percent total power in layers 1-12 after resolution inversions	36
2.3	Upper and lower bound multiplicative factors	45
3.1	Names and locations of GDSN stations.....	50
5.1	F test results of 11- and 12-layer inversions.....	147

Chapter 1: Introduction

1.1 Core-mantle boundary region

The core-mantle boundary (hereafter referred to as 'CMB') is the largest internal, seismic discontinuity in the Earth and separates two remarkably different compositional and thermodynamic regimes. Because it is such a drastic chemical and thermal boundary layer, its nature has important implications for deep Earth processes, particularly those which have their origin in the lower mantle (e.g., plumes) or outer core (e.g., magnetic field). Although the topography of the CMB and its effect on flow patterns of outer core and mantle fluid are not yet well determined, constraints on structure as well as the degree and type of coupling between core and mantle need to be understood in order to determine the three-dimensional nature of the CMB region. Since outer core flow patterns are responsible for the geomagnetic secular variation and the source of the geodynamo, it is desirable to know how CMB topography plays a role in fluid characteristics in the outermost part of the outer core and how it in turn is affected by lower mantle structure. The lower mantle is probably involved in large-scale dynamics in which hotter material rises in convection patterns as cooler material sinks, reflected in three-dimensional seismic structure. The present configuration of seismic anomalies in the lower mantle represents thermal and compositional heterogeneity, and may be related to CMB topography and outer core heterogeneity. This is the region of the Earth that provides the motivation for the work presented in this thesis.

1.1.a Core-mantle coupling

It is becoming more important, as geophysical models become more refined, to understand the extent to which flow in the core is controlled by the mantle. An increasing number of studies no longer treat the mantle and core as regions with independent characteristics. Studies in seismology, geodynamics, geomagnetism, mineral physics, and geodesy (among others) consider coupling between the mantle and core, and how one regime can influence the other. Regions in which the rate of secular variation and velocity anomalies are strongly correlated provide constraints on the thermal and mechanical coupling between the mantle and core. Specific types of interaction include thermal coupling in which the thermal variations in the lower mantle affect outer core fluid motions [e.g., Kohler and Stevenson, 1990; Jones, 1977; Ruff and Anderson, 1980; Bloxham and Gubbins, 1987, Bloxham and Jackson, 1990]. There is evidence for a relationship between strong circulatory core fluid flow and a hot region associated with CMB topography elevation beneath the southern Indian Ocean [Bloxham and Jackson, 1990; Kohler and Stevenson, 1990]. A discussion of one such model is presented in Appendix A1. Mineral physics observations point to the possibility of chemical interactions between core and mantle minerals at the CMB [Knittle and Jeanloz, 1986]. Coupling produced by effects of angular momentum through electromagnetic torques [Bullard *et al.*, 1950], pressure torques [Hide, 1969], or gravitational torques [Jault and LeMou el, 1989] have also been investigated.

The relationship between the Earth's mantle and core is the focus of numerous studies which consider the thermal and morphological nature of the CMB and its influence on core fluid motions. Various types of core-mantle boundary interactions have been proposed by which the morphology of the CMB, and the dynamics and temperature variations in the lower mantle affect motions of outer core fluid. Hide [1969] proposed a coupling mechanism which involved a hydrodynamical interaction between core fluid

motions and undulations in CMB topography. Jones [1977] proposed that thermal interaction influenced field geometry and caused some geomagnetic properties (e.g., reversal frequency) to vary on a mantle convection timescale. Ruff and Anderson [1980] proposed a model for the formation and evolution of the Earth's core by accretion and melting due to radioactive decay. They argued that fluid motions in the core are driven by differential heating in the lower mantle and that resulting motions could produce the geodynamo. In their secular variation study, Bloxham & Gubbins [1985] suggested thermal, electromagnetic, and topographic core-mantle interactions to explain the existence of static features in the Earth's magnetic field. The relationship was explored further by Bloxham & Gubbins [1987] who proposed thermal interaction between the core and lower mantle, where large lateral temperature variations just above the CMB influenced convection in the core. Core-mantle interaction has also been invoked to explain certain features of secular variation in the Earth's magnetic field such as westward drift. Such nondipole features are believed by some to be the result of differential rotation of outer core fluid relative to the deep outer core. In addition to using core-mantle interaction to explain stationary features of secular variation [Gubbins & Richards, 1986], Olson [1989] maintained that azimuthal drift of core fluid could be partially accounted for by thermal wind flow and that lateral temperature differences as small as 10^{-3} K/km could significantly excite thermal winds. Although most of the outer core is probably rotating rigidly in a cylindrical pattern [Zhang and Busse, 1990], it is very likely that the outermost 200 km or less of core fluid is behaving independently [Jault, 1988] and that the Earth's rotation causes differential flow with respect to the rest of the outer core.

1.1.b SnKS phases

Seismology provides the only direct method of sampling the outermost core. The problems of seismic velocity structure of the core, and core fluid motions based on the magnetic field have always been treated separately. Ultimately, models of the dynamo,

and nature and strength of the magnetic field in the core will be constrained by seismic structure results.

The seismic S_nKS phases (where n is an integer) are emitted from an earthquake source and travel through the mantle as S waves. Upon entering the core at the CMB, they are converted to P waves and reflect $(n-1)$ times on the underside of the CMB. They convert back to S waves on the upward leg of the raypath towards the Earth's surface. An illustration of raypaths for SKS and $SKKS$ can be seen in Fig. 1.1. Unlike for P_nKP phases, the core is not a low-velocity zone for S_nKS ; thus, they are more sensitive to structure at the top of the outer core because they have shallower turning points. SKS first emerges at epicentral distance, Δ , $\approx 62^\circ$ but is not easily observable until $\Delta \approx 85^\circ$ when it begins to arrive before the direct or diffracted S wave and large amplitude PS phases, all observed on radial component seismograms. SKS dives deeper into the outer core as the angle of incidence increases but its amplitude dies away by $\Delta \approx 140^\circ$. $SKKS$ separates from SKS at $\Delta \approx 94^\circ$, arriving up to three minutes later, and spends even more travel time in the outermost 200 km of the core since it turns closer to the CMB than SKS . Arrival times of S_nKS phases can be determined in data with periods less than one second, but data with considerably longer periods (> 100 sec) are most useful for determining global Earth structure via waveform inversions using normal mode and first-order perturbation methods. Thus, although the $SKKS$ phase is sometimes contained in the coda of long-period SKS and its arrival times cannot be observed, its waveform is used in the inversions.

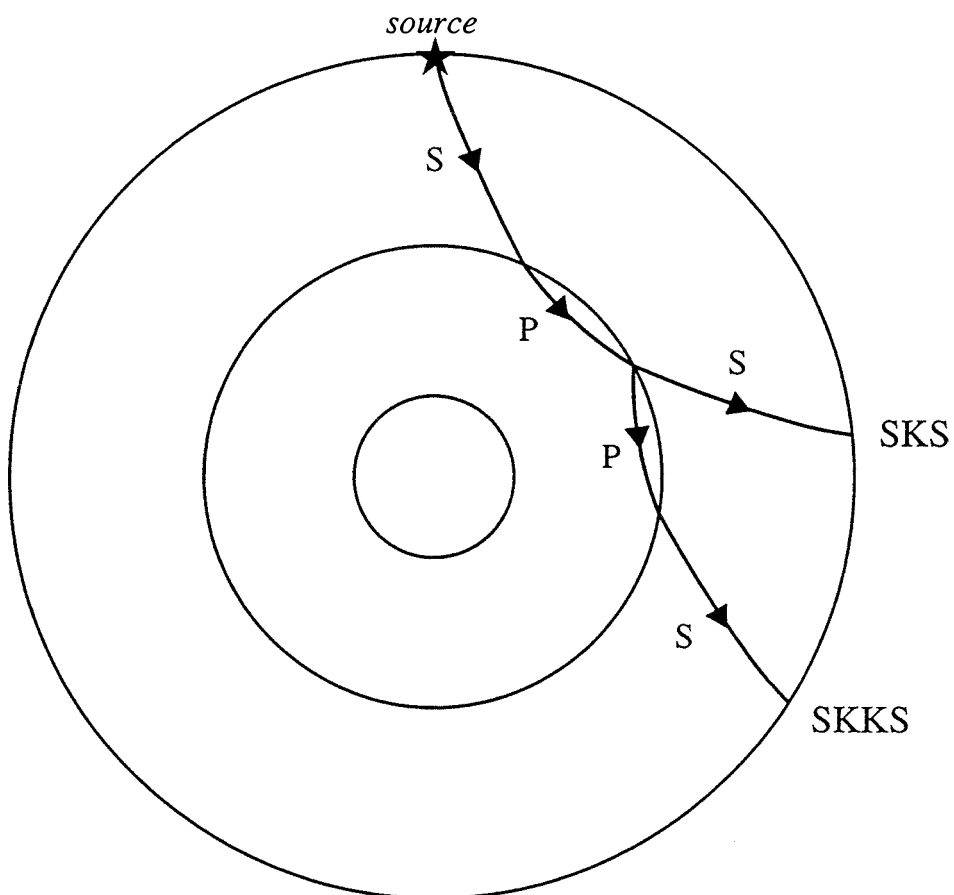


Fig. 1.1 Cross-section of the Earth illustrating SKS and SKKS raypaths.

1.2 Background

1.2.a Outermost core

A number of researchers have investigated the nature of the outermost core by examining seismic phases which travel through the region (also known as E') just below the CMB. However, few have searched for lateral variations in P-wave velocity because it is usually assumed that outer core fluid is homogeneous as a result of vigorous mixing and the inability to sustain lateral density variations [Stevenson, 1987] unless laterally varying material has been trapped in pools underneath CMB topographic highs [Lay and Young, 1990]. In addition, uncertainties in whole-mantle and D'' structure make it hard to attribute tomographic effects to the core. At the same time, the outer core is expected to be somewhat stratified due to the release of light elements from inner core growth [Fearn and Loper, 1981] and possible chemical interaction with the mantle. Seismological studies of the outer core are often limited for one or more reasons. Analyses are limited by small data sets or by constraints inherent in the techniques. One recurring feature of studies has been that they focus only on one dimension where outermost core velocity is defined in the radial direction, and no attempts have been made to determine if lateral variations exist. Another limitation is that the studies are regional. While seismologists have suggested the existence of heterogeneity, their analyses are often based on a limited number of data precluding the possibility of global interpretations directly from the results.

The first detailed studies of outermost core structure attempted to refine the radial variations in P-wave velocity with respect to whole Earth models. Gutenberg [1938] was one of the first to characterize the raypaths of the SKS phase and to refine outer core structure based on SnKS phases. He concluded that the travel-time curves of SKS were sensitive to velocities in the outer part of the core which ranged between 7.4 and 8.0

km/sec depending on distance; similar conclusions were drawn for SKKS. Gutenberg and Richter [1939] performed a detailed analysis of the travel times of SKS waves based on seismograms recorded in Pasadena, California and they tabulated their results for a distance range of 80°-150°, corrected and smoothed for zero focal depth.

Hales and Roberts [1970] also looked at radial variations in core velocity and took previous studies one step further by defining an empirical travel-time curve for SKS based on observed travel times. They examined travel times of SKS up to 126° from events recorded at the Long Range Seismic Measurements (LRSM) stations in North America and World-Wide Standardized Seismograph Network (WWSSN) stations in North America, specifically chosen for reasonably uniform azimuthal coverage. The travel times (in seconds) were tabulated and fit by the quadratic curve

$$T_{\text{SKS}} = (1493.96 \pm 0.27) + (4.61 \pm 0.01)(\Delta - 105.0) - (0.0440 \pm 0.0012)(\Delta - 105.0)^2$$

where Δ is the distance in degrees between the source and station. The all-positive deviations from the Jeffreys-Bullen SKS travel times [Jeffreys and Bullen, 1958] ranged from about 0.5 to 6.0 sec, while the S_{diff} -SKS travel times were consistently lower than the average calculated from a mean curve. From these observations and measurements, Hales and Roberts [1970] concluded that, although they considered it unlikely, one possible source of deviations was regionally varying outermost core velocities. (The other possibilities, which they also found unsatisfactory, were differences in CMB radius and upper mantle structure.) A year later, Hales and Roberts [1971] reported SKKS-SKS travel times for distances between 110° and 130°. Correcting for ellipticity and focal depth, the observed differences (in seconds) were added to the SKS travel-time polynomial given in Hales and Roberts [1970] to get

$$T_{\text{SKKS}} = 1539.18 + 7.02(\Delta - 105.0) - 0.0161(\Delta - 105.0)^2$$

and the differences were derived as

$$T_{\text{SKKS}} - T_{\text{SKS}} = 45.22 + 2.41(\Delta - 105.0) + 0.0279(\Delta - 105.0)^2.$$

Plots of this curve and individual measurements indicated that the outermost 250 km of core velocity was significantly lower than values (based only on extrapolation of SKS travel times) given by Jeffreys-Bullen [Jeffreys and Bullen, 1958] and Randall [1970] near the CMB. Hales and Roberts obtained P-wave velocities equal to 7.909, 7.907, 7.893, and 7.893 km/sec respectively for SKKS core arc distances of 85°, 90°, 95°, and 100°. These results, along with observed S3KS-SKKS travel times for three good records with $\Delta=152^\circ$ - 161° , lent support to the earlier conclusions for reduced outermost core velocities with respect to a radially-varying Earth model. The results were also in agreement with Nelson [1954] who constructed travel-time curves of SKS, SKKS, and S3KS from 1200 shallow, intermediate, and deep focus earthquakes recorded in Pasadena, California and Huancayo, Peru for epicentral distances between 75° and 175°. He found that the observations required lower velocities just inside the core relative to the published results of Gutenberg [1951] and Jeffreys [1939]. Both these studies, however, contradicted the results of Randall [1970] who obtained a revised velocity distribution table for SKS by combining information on the AB branch of PKP with International Seismological Centre Bulletin data grouped in one-degree distance ranges for earthquakes described in Herrin [1968] for $\Delta=97.5^\circ$ - 118.5° , combined with data from Hales and Roberts [1970] with $\Delta=83^\circ$ - 126° . His results indicated that velocity at the top of the core was 8.26 km/sec, somewhat greater than Jeffreys' value of 8.10 km/sec.

While the debate continued over radial velocity values for the outer core, the problem became more complex when studies began probing possible lateral variations in outermost core structure. Upon examining Earth velocity models, Bullen [1969] derived compressibility-pressure gradient curves and found evidence pointing to slight inhomogeneity in the outer 700 km of the core. He attributed this to phase changes rather

than changes in chemical composition. Further analysis [Bullen, 1970] resulted in the same conclusions along with the observation that the core seemed normal and uniform below the outermost 700 km.

Around this time, seismologists began to use full waveforms to obtain details in structure by attempting to fit waveform characteristics of SnKS phases. In particular, Choy [1977] found that SnKS waveforms were sensitive to velocity gradients in the upper 200 km of the outer core and the results suggested that velocities in the outer 200-300 km of the core were higher, but that the gradient was lower than that predicted by Hales and Roberts [1971], model 1066B [Gilbert and Dziewonski, 1975], and closer to Jeffreys-Bullen. Their analysis consisted of frequency-dependent, full wave theory (WKBJ is not useful near the turning point of the rays) to synthesize long-period seismograms of the SnKS phases for distances between 100° - 125° . Choy concluded that it was likely that the regeneration of the Earth's magnetic field was accompanied by stable stratification in the outer core. In addition, Kind and Müller [1975] used the reflectivity method to show that they could calculate theoretical seismograms that were a complete response that included S, SKS, and ScS (assuming a layered half-space whole Earth model with the Earth flattening approximation). Comparing the synthetic seismograms constructed for existing core models to long-period observations of SKS/SKKS amplitude ratios and travel-time differences for five deep-focus Tonga-Fiji earthquakes, they found that discrepancies could be removed with a new Earth model in which the outer core had increased velocities at a depth of about 3750 km [Kind and Müller, 1977]. They further stated that no other significantly different model could explain the observations and that the model implied pronounced chemical inhomogeneity in the core, compatible with the results of Choy [1977]. In a study by Schweitzer and Müller [1986] countering the results of Kind and Müller [1977], travel-time residuals of SKKS and SKS for 12 Tonga-Fiji events for $\Delta = 96^{\circ}$ - 117° recorded at North and South American stations were examined. Schweitzer and Müller found that the residuals were larger by 2-3 sec than those predicted by PREM, and

that the SKS/SKKS amplitude ratios were lower than PREM (Preliminary Reference Earth Model) [Dziewonski and Anderson, 1981] predictions at the same stations. However, this was not observed for Tonga-Fiji events to Eurasian and African stations, or from Sea of Japan events to North American and African stations. Their preferred explanation was lateral variations in the lower mantle since, they argued, the S3KS phase would be delayed such that it would be observed as a separate phase after SKKS even in long-period data if the outermost core were a high-velocity zone. They pointed out that this is almost never observed and, thus, lateral variations (due to temperature variations) could not be used to explain the data.

Schweitzer and Müller's conclusions point to an ambiguity in outer core analyses: because the SnKS phases also travel through the mantle, their signatures in seismograms reflect mantle heterogeneity as well as outer core structure. This has become all the more complicated by recent D" studies which suggest that the lowermost mantle may be quite heterogeneous. For example, Garnero and Helmberger [1988] found up to 8 sec SKS-S travel-time residuals (relative to Jeffreys-Bullen) and 2-3 sec SKKS-SKS residuals for the mid-Pacific CMB region. They concluded that the observations could be explained by several possibilities: up to 5% velocity increase in the top 300 km of the outer core, a 2% increase in S-wave velocity in the lower mantle northeast of Tonga, or lateral variations in D" shear wave velocities of up to 3%. However, they noted in this and in a later study [Garnero and Helmberger, 1993] in which they looked at S-SKS travel-time anomalies measured from short- and long-period data from deep-focus Fiji-Tonga events recorded in North America, that although outermost core lateral variations were not needed to explain the observations, the issue could not be resolved.

Accepting the possibility of both lowermost mantle and outermost core lateral variations, Lay and Young [1990] carried out a similar study in which long-period recordings of 21 intermediate and deep focus events in the western Pacific made at North American WWSSN and Canadian Seismic Network (CSN) stations. Nine SKS-SKKS

differential travel times and 21 SKS-S, SKS-S_{diff} or SKS-ScS differential travel times were compared to synthetics computed by the reflectivity method. They found that the SKS-SKKS anomalies were systematically negative by about 2 sec and that the travel times were insensitive to radially symmetric mantle-side structure because different models, one of which contained a fast D" layer, changed the anomalies by very little. They preferred the Hales and Roberts core models and concluded that the SKS-SKKS differential travel times could be explained by a core model which is 1-2% slower in the outer 50-100 km, possibly due to a stably-stratified chemical boundary layer combined with 3% lateral variations in S-wave velocity in the lowermost mantle.

At the other extreme was a pair of studies carried out by Souriau and Poupinet [1990, 1991] in which they were seeking not only the degree of outermost core lateral heterogeneity, but also geographical dependencies of heterogeneity. In the first study, they examined SKS and SKKS differential travel times for intermediate period Global Digital Seismograph Network (GDSN) and broad-band GEOSCOPE and Network of Autonomously Recording Seismographs (NARS) recordings of events ($\Delta = 83^\circ$ - 130°) relative to PREM. From these results they claimed to see clear latitudinal dependence of outermost core heterogeneity, with averaged residuals up to ± 1 sec at the higher latitudes due to slight velocity variations in the outermost core. They discarded D" heterogeneity as a source of residuals because the raypaths were far from the SKKS reflection points whose latitudes gave the observed pattern. However, in the second study which involved many more SKS, SKKS, and S3KS travel-time measurements from broad-band records, geographical dependency was not obvious. They reported strong but small regional variations in outermost core heterogeneity and concluded that their observations could be explained by a 2-5% S-wave velocity increase in D" and a small decrease in P-wave velocity in the upper 800 km of the core. They described a core model comprising a thin, low-velocity layer at the top resulting from the accumulation of light elements.

Recently, a triplet of studies by Tanaka and Hamaguchi [1993abc] focussed both on radial and lateral variations in P-wave velocity in the outermost core. They used travel times from long-period SKS, SKKS, and S3KS recordings from GDSN and WWSSN stations. Their observations came from about 300 seismograms recorded for 71 deep-focus earthquakes and they corrected for upper and lower mantle heterogeneity by incorporating the models SH425.2 [Su and Dziewonski, 1991] and LO2.56 [Dziewonski, 1984]. They concluded that the quadratic polynomial

$$T_{\text{SKS}} = 1427.52 + 3.771(\Delta - 115.0) - 0.0404(\Delta - 115.0)^2$$

fit the SKS travel-time (in seconds) data better than previous models and proposed an outermost core P-wave velocity of 8.016 km/sec, with higher velocities in the outer 200 km of the core than those of Hales and Roberts [1970, 1971] and velocities almost identical to those of Hales and Roberts in the region 200-400 km below the CMB. Further analysis of their data led them to suggest the existence of $\pm 0.3\%$ lateral velocity variations in the outermost 200 km from average residuals of 0.6 sec in a hemisphere bounded by the 120° E line of longitude including the Pacific, and -0.6 sec in the opposite hemisphere [Tanaka and Hamaguchi, 1993c]. A spherical harmonic analysis of their travel-time residuals indicated a strong $\ell = 1$ component, one and one-half times stronger than the $\ell = 2$ component.

1.2.b Mantle

The research presented in this thesis began with one-layer inversions for outermost core P-wave velocity perturbations and progressed onto 11- and 12-layer inversions for mantle S-wave and outermost core P-wave velocity perturbations. Therefore, it is useful to describe a few other recent mantle heterogeneity models for ease of comparison with the models presented here. Models for mantle heterogeneity have been based on travel-

time tomography [e.g., Masters *et al.*, 1992; Inoue *et al.*, 1990], or inversion of waveform data alone [e.g., Tanimoto, 1990a] while a few have combined travel times with waveform data [e.g., Su *et al.*, 1994]. This study is most similar to the inversion model MDLSH of Tanimoto [1990a] who used long-period tangential seismograms and toroidal mode data to invert for S-wave velocity anomalies in 11 mantle shells, expanding laterally in spherical harmonics up to degree and order six. Other methods of inversion include S phase travel-time residual and waveform inversion for S-wave velocity perturbations by normal mode summation, expanding radially in Chebyshev polynomials and laterally in spherical harmonics [Su *et al.*, 1994; Su and Dziewonski, 1992; Su *et al.*, 1992; Su and Dziewonski, 1991], S phase travel-time residual inversion for S-wave velocity in shells expanding laterally in spherical harmonics [Masters *et al.*, 1992; Woodward and Masters, 1991a; Woodward and Masters, 1991b; Woodward and Masters, 1991c], P phase travel-time inversions for P-wave velocity [Dziewonski *et al.*, 1977; Dziewonski, 1984; Hager and Clayton, 1989; Inoue *et al.*, 1990; Gudmundsson and Clayton, 1991; Gudmundsson *et al.*, 1990], and normal mode splitting caused by aspherical structure [e.g., Dahlen, 1968, 1969; Woodhouse and Dahlen, 1978; Woodhouse, 1980; Lognonné and Romanowicz, 1990; Widmer *et al.*, 1992].

These background studies provided the motivation for the work presented in this thesis. In Chapter 2, normal mode and first-order perturbation theory used in the inversions is outlined. Also, four structure resolution test results are presented as a method of placing constraints on the power in real Earth structure of the mantle and outermost core. Chapter 3 contains a description of the data sets and the cross-correlation condition used in the automated method of discarding unsuitable data. Chapter 4 describes the results of an initial, one-layer inversion for P-wave velocity perturbations in the outermost core. These were obtained by individual seismogram inversions of the SnKS waveform portion of seismograms with source-receiver distances between 110° and 130° . Chapter 5 describes the results of the three-dimensional waveform inversions using

entire body-wave portions of seismograms. Velocity anomalies are plotted as spherical harmonic expansions up to degree and order 12 with respect to PREM using 11 mantle shells and one outermost core shell. Results from 11-layer inversions are compared to 12-layer inversions using the F ratio to test the statistical significance of the outermost core layer. A discussion of possible sources of heterogeneity given by the preferred model is made in the conclusions of Chapter 5.

Chapter 2: Theory and Pattern Retrieval Resolution Constraints

2.1 Waveform construction by normal mode summation

If the Earth were laterally homogeneous and could be described by a radially-varying velocity model alone, rays would travel along great circle paths from source to receiver. As seismic rays travel from the earthquake source to receiver in the real Earth, they accumulate small deviations in travel times along the raypath due to laterally varying structure. To describe global, three-dimensional velocity anomalies, the data must include numerous raypaths with many different azimuths in order to better constrain the location of the anomaly which can lie anywhere on the raypath. The problem can alternately be described in terms of eigenfunction perturbations for the normal modes which are used to model surface displacement. Fermat's principle makes it possible to express the travel-time (or eigenfrequency) perturbations caused by perturbations in structural parameters as a linear problem. A form of Rayleigh's principle leads to the calculation of structural parameter perturbations by inversion of eigenfrequency perturbations and the structural parameter differential kernels. A summary of the theory used in the inversions presented in this thesis will be given in the first part of this chapter.

There remains the choice of how to parameterize the tomography problem. One widely used method is to divide the region of interest into discrete cells and assume that velocity perturbation is constant within each cell. The other method, used here, is the "global" approach in which the perturbations are expanded in terms of a linear

combination of continuous basis functions. The natural choice for this is a spherical harmonic expansion with associated Legendre polynomials. The advantages are that the spectral content and resolution of the solution are easily examined. This method also allows smoothing in areas for which there is little or no data due to lack of earthquake or station coverage.

The observed displacement in a seismogram can be expressed as the sum of normal modes and their associated excitation coefficients

$$\mathbf{u}(\mathbf{r}, t) = \sum_n \sum_\ell \sum_m {}_n a_\ell^m \cdot {}_n s_\ell^m(\mathbf{r}, \theta, \varphi) e^{i_n \omega_\ell t} \quad [2.1]$$

where ${}_n s_\ell^m(\mathbf{r}, \theta, \varphi)$ are the homogeneous solutions (eigenfunctions subject to some boundary conditions) with associated eigenfrequencies ${}_n \omega_\ell$. The excitation coefficients are given by ${}_n a_\ell^m$. As is standard in normal mode theory, n denotes the radial order (fundamental: $n = 0$ or overtone: $n > 0$), ℓ denotes angular order (also referred to as 'degree'), and m denotes azimuthal order (also referred to as 'order'). Spatial coordinates are referenced with respect to the three-dimensional, spherical coordinate system, $(\mathbf{r}, \theta, \varphi)$.

Accounting for an earthquake to provide the excitation source in the Earth, the external force is applied as a Heaviside step function in time, $\mathbf{f}(\mathbf{r}, t) = \mathbf{f}(\mathbf{r})H(t)$. After Laplace transforming the equations of motion, substituting in the expression for excitation coefficients as functions of the eigenfunctions and body force, and inverse Laplace transforming, the expression for displacement in a continuum becomes

$$\mathbf{u}(\mathbf{r}, t) = \sum_n \sum_\ell \sum_m \left({}_n \Psi_\ell^m \right) {}_n s_\ell^m(\mathbf{r}, \theta, \varphi) \frac{(1 - \cos {}_n \omega_\ell t)}{{}_n \omega_\ell^2} \quad [2.2]$$

where t is time [Gilbert, 1970]. If the external force is applied as a spatial delta function $\mathbf{f}(\mathbf{r}) = \mathbf{F}\delta(\mathbf{r} - \mathbf{r}_s)$ acting at the source location, \mathbf{r}_s , then,

$${}_n \Psi_\ell^m = \int_V \mathbf{F}(\mathbf{r}, t) {}_n s_\ell^{m*} \delta(\mathbf{r} - \mathbf{r}_s) dV \quad [2.3]$$

$$= \mathbf{F} \cdot {}_n \mathbf{s}_\ell^{m*}(\mathbf{r}_s) \quad [2.4]$$

[Phinney and Burridge, 1973]. The double couple or point dislocation is used to describe the mechanism of the earthquakes used in these inversion and the effects of source complexity are not included.

If a stress τ_0 is applied at the source location \mathbf{r}_s at time $t = 0$,

$$\tau_0(\mathbf{r}, t) = \mathbf{M} \delta(\mathbf{r} - \mathbf{r}_s) H(t) \quad [2.5]$$

giving the relationship between stress and the moment tensor, \mathbf{M} , which specifies the source completely [Phinney and Burridge, 1973]. Recalling that $\mathbf{f} = \nabla \cdot \tau_0$, it follows that the external force can be written

$$\mathbf{f} = \nabla \cdot [\mathbf{M} \delta(\mathbf{r} - \mathbf{r}_s) H(t)]. \quad [2.6]$$

Since τ_0 is taken at the point source,

$${}_n \Psi_\ell^m = - \int_V (\nabla \cdot {}_n \mathbf{s}_\ell^{m*} : \mathbf{M}) \delta(\mathbf{r} - \mathbf{r}_s) dV \quad [2.7]$$

$$= - \int_V (\mathbf{M} : {}_n \boldsymbol{\varepsilon}_\ell^{m*}) \delta(\mathbf{r} - \mathbf{r}_s) dV, \quad [2.8]$$

thus,

$$\mathbf{M} : {}_n \boldsymbol{\varepsilon}_\ell^{m*}(\mathbf{r}_s) = \sum_{i=1}^3 \sum_{j=1}^3 M_{ij} \varepsilon_{ij}(\mathbf{r}_s) \quad [2.9]$$

where $\varepsilon_{ij}(\mathbf{r}_s)$ are the elements of the strain tensor associated with normal mode ${}_n \mathbf{s}_\ell^m(\mathbf{r})$ and the sign change arises from use of the chain rule. The displacement is then

$$\mathbf{u}(\mathbf{r}, t) = \sum_n \sum_\ell \sum_m (\mathbf{M} : {}_n \boldsymbol{\varepsilon}_\ell^{m*}(\mathbf{r}_s)) {}_n \mathbf{s}_\ell^m(\mathbf{r}, \theta, \varphi) \frac{(1 - \cos_n \omega_\ell t)}{n \omega_\ell^2} \exp\left(\frac{-n \omega_\ell t}{2_n Q_\ell}\right) \quad [2.10]$$

including the effects of attenuation, ${}_n Q_\ell$, for a particular mode.

In the previous equation, the static response of the Earth (i.e., static field of earthquakes) is ω^{-2} . This is the limit of displacement for $t \rightarrow \infty$ or $\omega \rightarrow 0$. However, the instrument response of the static field is zero. Therefore, the static field expression is subtracted from the displacement in order to construct the correct synthetic seismogram corresponding to the Global Digital Seismograph Network instrument responses.

Recall that vector field $\mathbf{u}(\mathbf{r}, t)$ can be written

$$\begin{aligned} {}_n\mathbf{u}_\ell^m(\mathbf{r}, t) &= {}_nU_\ell^m(\mathbf{r})Y_\ell^m(\theta, \varphi)\hat{\mathbf{r}} + {}_nV_\ell^m(\mathbf{r})\nabla Y_\ell^m(\theta, \varphi)\hat{\boldsymbol{\theta}} + {}_nW_\ell^m(\mathbf{r})(-\hat{\mathbf{r}} \times \nabla Y_\ell^m(\theta, \varphi))\hat{\boldsymbol{\phi}} \\ &= {}_nU_\ell^m(\mathbf{r})\mathbf{R}_\ell^m(\theta, \varphi) + {}_nV_\ell^m(\mathbf{r})\mathbf{S}_\ell^m(\theta, \varphi) + {}_nW_\ell^m(\mathbf{r})\mathbf{T}_\ell^m(\theta, \varphi) \end{aligned} \quad [2.11]$$

with associated Legendre functions $Y_\ell^m(\theta, \varphi)$ [Takeuchi and Saito, 1972]. ${}_nU_\ell^m(\mathbf{r})$, ${}_nV_\ell^m(\mathbf{r})$, ${}_nW_\ell^m(\mathbf{r})$ are the radial eigenfunctions associated with spheroidal (U, V) and toroidal (W) motions; $\mathbf{R}_\ell^m(\theta, \varphi)$, $\mathbf{S}_\ell^m(\theta, \varphi)$, and $\mathbf{T}_\ell^m(\theta, \varphi)$ are the corresponding surface vector harmonics.

Evaluated at the surface of the Earth (radius = a), radial component seismogram displacement becomes

$$u_\theta(a, \theta, \varphi, t) = \sum_n \sum_\ell \frac{-\cos_n \omega_\ell t}{n\omega_\ell^2} \exp\left(\frac{-n\omega_\ell t}{2_n Q_\ell}\right) \cdot {}_nV_\ell(a) \cdot \sum_m (\mathbf{M} : {}_n\boldsymbol{\varepsilon}_\ell^m(\mathbf{r}_s)) \nabla Y_\ell^m(\theta, \varphi) \quad [2.12]$$

since only the average multiplet eigenfrequency, ${}_n\omega_\ell$, is known for each mode. The insignificant toroidal contribution has not been included in this expression. Substituting spheroidal mode eigenfunctions and spherical components of strain into the expression for excitation coefficients, and using "epicentral" coordinates in which the source is located at the pole ($\theta = 0$), instead of geographical coordinates (i.e., the limit of $\boldsymbol{\varepsilon}_\ell^m(\mathbf{r}_s)$ as the source approaches $\theta = 0$ along the meridian $\varphi = 0$) [Dziewonski and Woodhouse, 1983b]

$$u_\theta(a, \theta, \varphi, t) = \sum_n \sum_\ell R_n \cdot \frac{-\cos_n \omega_\ell t}{n\omega_\ell^2} \exp\left(\frac{-n\omega_\ell t}{2_n Q_\ell}\right) \quad [2.13]$$

where

$$R = {}_n V_\ell(r) \cdot \left\{ -k_0 \left[\partial_r U(r_s) M_{rr} + \frac{F(r_s)}{2} (M_{\theta\theta} + M_{\varphi\varphi}) \right] \partial_\theta P_\ell^0(\theta) + 2k_1 E_s(r_s) [M_{r\theta} \cos\varphi + M_{r\varphi} \sin\varphi] \partial_\theta P_\ell^1(\theta) - 2 \frac{k_2 V(r_s)}{r} [(M_{\theta\theta} - M_{\varphi\varphi}) \cos 2\varphi + 2M_{\theta\varphi} \sin 2\varphi] \partial_\theta P_\ell^2(\theta) \right\} [2.14]$$

with

$$F \equiv r^{-1} [2U - \ell(\ell+1)V],$$

$$E_s \equiv \partial_r V - r^{-1}(V - U),$$

and

$$k_m \equiv \frac{1}{2^m} \sqrt{\frac{(2\ell+1)(\ell+m)!}{4\pi(\ell-m)!}}$$

which arise from the integration of the excitation coefficients over the volume of the Earth. Source parameters for each earthquake were obtained from Harvard centroid moment tensor solutions (referred to as 'CMT solutions') [e.g., Dziewonski and Woodhouse, 1983a]. Note that the coordinate transformation limits the range of m to $-2 \leq m \leq 2$. The CMT solutions are obtained by nonlinear, least-squares inversions of long-period waveforms; 50-60 sec body-wave data extending from the P wave to the arrival of the fundamental mode surface waves, as well as < 135 sec surface wave data, are inverted for the best point source (epicentral coordinates, depth and origin time) in addition to the six independent elements of the seismic moment tensor.

The velocity inversion approach involved the construction of synthetic seismograms and their displacement derivatives with respect to velocity by summation of 5262 normal modes. The mode eigenfunctions and eigenfrequencies had already been computed for the initial, laterally homogeneous Earth model, Preliminary Reference Earth Model (hereafter referred to as PREM) shown in Fig. 2.1 [Dziewonski and Anderson, 1981]. The eigenfunctions were not recomputed after each iteration and earthquake

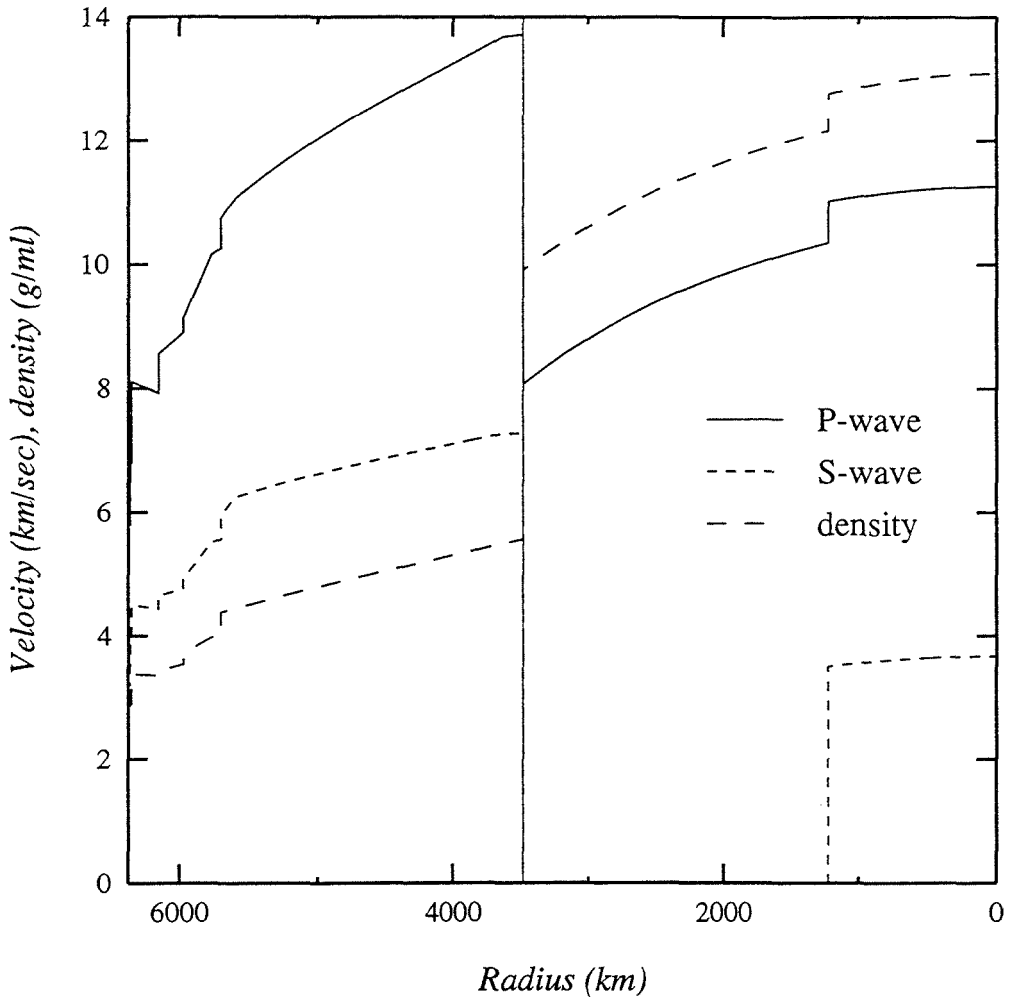


Fig. 2.1 Preliminary Reference Earth Model [Dziewonski and Anderson, 1981].

sources were not relocated. Ideally, however, a more accurate approach would be to recompute the eigenfunctions and source parameters after each iteration using the newly-determined three-dimensional Earth model. The drawback to this, of course, is that it requires a large amount of extra computer time. Solutions for velocity perturbations are computed using perturbation theory and the least-squares method [e.g., Tanimoto, 1987]. Epicentral distance corrections due to ellipticity were made following the method outlined in Woodhouse and Dziewonski [1984]. However, their approximations were not appropriate for some modes used in our body-wave analysis; in particular, the correction was not accurate for $\ell < 5$. As a result, a modified version of the distance correction was applied to the spheroidal normal mode set. Details are contained in Appendix A2.

2.2 First-order perturbation theory

It is assumed that real Earth structure is not very different from a theoretical, initial Earth model. If global, average perturbations to the initial Earth model are less than 10% (assumed by many normal mode studies), first-order perturbation theory serves as a convenient approach to solving for lateral variations in seismic velocities.

According to perturbation theory, if $s = f(t)$, then $s + \Delta s = f(t + \Delta t)$, so that $\Delta s = f(t + \Delta t) - f(t)$. A form of Rayleigh's Principle says that the square of the eigenfrequency is stationary for small variations in displacements from the exact solution; i.e., calculation of the ratio of potential energy to kinetic energy using an approximate trial solution with first-order deviations from the exact eigenfunction gives the eigenfrequency accurate to first order. From variational theory, small perturbations in Earth structure (i.e., seismic velocities) produce perturbations in eigenfrequencies. Thus, perturbations to displacement can be expressed as

$$u_\theta + \delta u_\theta = \sum_k \frac{R}{\omega_k^2} \cdot [-\cos(\omega_k + \delta\omega_k)t] \exp\left[\frac{-(\omega_k + \delta\omega_k)t}{2Q_k}\right] \quad [2.15]$$

$$= \sum_k \frac{R}{\omega_k^2} \cdot [-\cos\omega_k t \cos\delta\omega_k t + \sin\omega_k t \sin\delta\omega_k t] \exp\left[\frac{-(\omega_k + \delta\omega_k)t}{2Q_k}\right] \quad [2.16]$$

where $\delta\omega_k \ll \omega_k$ and R has already been defined in Eq. [2.14]. Note that the subscripts n , ℓ , and m have been replaced with k to denote a specific normal mode multiplet. Also, the spherical coordinate notation has been dropped for simplicity. Displacement is now given as the summation over a finite number of modes. Since $\delta\omega_k \ll 1$, $\cos\delta\omega_k t \approx 1$ and $\sin\delta\omega_k t \approx \delta\omega_k t$. Also, since mode attenuation $Q_k \gg 1$, it is assumed that $\delta\omega_k Q_k^{-1} \approx 0$. As a result, the simplified expression for displacement and its perturbation is given as

$$u_\theta + \delta u_\theta = \sum_k \frac{R}{\omega_k^2} \cdot (-\cos\omega_k t + \delta\omega_k t \sin\omega_k t) \exp\left(\frac{-\omega_k t}{2Q_k}\right). \quad [2.17]$$

The left-hand side of this is computed as

$$\delta u_\theta = u^d(t) - u^s(t) \quad [2.18]$$

where $u^d(t)$ is the observed seismogram, and $u^s(t)$ is the synthetic seismogram computed with PREM. In terms of partial differentials,

$$\begin{aligned} u^d(t) - u^s(t) &= \sum_k \frac{R}{\omega_k^2} \cdot (\delta\omega_k t \sin\omega_k t) \exp\left(\frac{-\omega_k t}{2Q_k}\right) \quad [2.19] \\ &= \sum_k \frac{\partial u}{\partial \omega} \delta\omega_k \\ &= \sum_k \left(\frac{\partial u}{\partial \omega} \frac{\partial \omega}{\partial \rho} \right) \delta\rho + \sum_k \left(\frac{\partial u}{\partial \omega} \frac{\partial \omega}{\partial \alpha} \right) \delta\alpha + \sum_k \left(\frac{\partial u}{\partial \omega} \frac{\partial \omega}{\partial \beta} \right) \delta\beta \end{aligned}$$

using the chain rule. In reality, eigenfrequency perturbations, $\delta\omega_k$, are not directly calculated, and the velocity perturbations are. Perturbations due to slight variations in the location of internal discontinuities with respect to the reference model have been

neglected; however, there is an important tradeoff between boundary and velocity perturbations. If the discontinuity contributions had been included, they would have been subtracted from the expression for eigenfrequency perturbations for specific modes. Similar perturbation methods have been used by Lerner-Lam and Jordan [1983] and Woodhouse and Dziewonski [1984].

This expression can also be derived by differentiation. Upon differentiating displacement with respect to ω ,

$$\left. \frac{\partial u}{\partial \omega} \right|_{\omega=\omega_k} = \frac{R}{\omega_k^2} \cdot \left[(t \sin \omega_k t) + \left(\frac{t}{2Q_k} \cdot \cos \omega_k t \right) \right] \exp\left(\frac{-\omega_k t}{2Q_k}\right) \quad [2.20]$$

where k denotes the k^{th} normal mode. Multiplying both sides by perturbation in eigenfrequency, $\delta\omega_k$,

$$\frac{\partial u}{\partial \omega} \delta\omega_k = \frac{R}{\omega_k^2} \cdot \left[(\delta\omega_k t \sin \omega_k t) + \left(\frac{\delta\omega_k t}{2Q_k} \cdot \cos \omega_k t \right) \right] \exp\left(\frac{-\omega_k t}{2Q_k}\right). \quad [2.21]$$

But $\delta\omega_k \ll 1$ and $Q_k \gg 1$, yielding $\frac{\delta\omega_k}{Q_k} \approx 0$. Thus,

$$\frac{\partial u}{\partial \omega} \delta\omega_k = \frac{R}{\omega_k^2} \cdot (\delta\omega_k t \sin \omega_k t) \exp\left(\frac{-\omega_k t}{2Q_k}\right). \quad [2.22]$$

The wavelength of average, global Earth structure given by the solutions is much greater than the wavelengths of the normal modes used in the inversion. For this case, Jordan [1978] approximated the k^{th} mode eigenfrequency perturbation as a local average along the raypath from the earthquake source to the receiver; i.e.,

$$\delta\omega_k = \frac{1}{\Delta_{SR}} \int_S^R \delta\omega_{\text{local}}(\theta, \phi) ds \quad [2.23]$$

where Δ_{SR} is the epicentral distance from the source (S) to the receiver (R). This approximation is known to degrade the results laterally [Li and Tanimoto, 1993], but still remains a good, initial attempt to constrain the structure.

The local eigenfrequency perturbation can, in turn, be expressed in terms of perturbations in density and seismic velocities:

$$\delta\omega_{\text{local},k} = \omega_k \int_0^a \left(K_{\rho,k}(r) \frac{\delta\rho}{\rho} + K_{\alpha,k}(r) \frac{\delta\alpha}{\alpha} + K_{\beta,k}(r) \frac{\delta\beta}{\beta} \right) dr \quad [2.24]$$

where $K_{\alpha,k}(r)$ is the Frechet kernel for P-wave velocity as a function of depth for the k^{th} mode, $K_{\beta,k}(r)$ is the kernel for S-wave velocity, $K_{\rho,k}(r)$ is the Frechet kernel for density, and 'a' denotes the radius of the Earth. For the frequency range considered here, however, $K_{\rho,k}(r)$ is much smaller than the kernels for P- and S-wave velocities; therefore, the density perturbation term can be neglected, yielding

$$\delta\omega_{\text{local},k} = \omega_k \int_0^a \left(K_{\alpha,k}(r) \frac{\delta\alpha}{\alpha} + K_{\beta,k}(r) \frac{\delta\beta}{\beta} \right) dr. \quad [2.25]$$

In this development, the kernels have been normalized by ω^2 and kinetic energy, which arises from their derivation from Rayleigh's principle and first-order perturbation theory. Tomographic [Dziewonski and Woodhouse, 1987; Davies, 1990; Li *et al.*, 1991b; Pulver and Masters, 1990] and laboratory [Sumino and Anderson, 1984; Simmons and Wang, 1971; Duffy and Ahrens, 1992a; Duffy and Ahrens, 1992b] experiments provide evidence for a linear relationship between P-wave and S-wave perturbations which changes with depth within the mantle. This is a useful tool, both because it simplifies the inverse problem and because teleseismic S-wave amplitudes are much larger than P-wave amplitudes and dominate the least-squares inversions for velocity. This relationship is defined as

$$\chi \frac{\delta\beta}{\beta} = \frac{\delta\alpha}{\alpha} \quad [2.26]$$

where χ is a scalar. By incorporating this linear relationship, the number of unknown parameters is reduced by one half, making the inversion more reasonable in size. The inversions incorporated $\chi = 0.6$ for the upper mantle (layers 1-3), and $\chi = 0.5$ for the lower mantle (layers 4-11), both values lying between experimentally determined maxima and minima [see above references]; χ was held constant within each depth layer.

Expanding P-wave and S-wave velocities in spherical harmonic expansions,

$$\frac{\delta\alpha}{\alpha} = \sum_{\ell=0}^{\ell_{\max}} \sum_{m=-\ell}^{\ell} a_{\ell}^m Y_{\ell}^m(\theta, \varphi) \quad [2.27]$$

and

$$\frac{\delta\beta}{\beta} = \sum_{\ell=0}^{\ell_{\max}} \sum_{m=-\ell}^{\ell} b_{\ell}^m Y_{\ell}^m(\theta, \varphi), \quad [2.28]$$

where ℓ_{\max} is the maximum angular order (= 12), the full expression for eigenfrequency perturbation can now be given as

$$\delta\omega_k = \omega_k \left\{ \sum_{\ell} \sum_m \left[\frac{1}{\Delta_{SR}} \int_S Y_{\ell}^m(\theta) ds \right] \cdot \left[\sum_{i=1}^{11} (b_{\ell}^m)_i \int_{r_i}^{r_{i+1}} (\chi K_{\alpha}(r) + K_{\beta}(r)) dr \right] + \left[\sum_{j=12}^{12} (a_{\ell}^m)_j \int_{r_j}^{r_{j+1}} K_{\alpha}(r) dr \right] \right\} \quad [2.29]$$

where a_{ℓ}^m and b_{ℓ}^m are the coefficients of expansion, r denotes the radius of the top of each layer, and $P_{\ell}^m(\theta)$ ($Y_{\ell}^m(\theta, \varphi) = P_{\ell}^m(\theta)e^{im\varphi}$) are the associated Legendre functions fully normalized as

$$P_{\ell}^m(\theta) \equiv \sqrt{(2 - \delta_{0m})(2\ell + 1)} \frac{(\ell - m)!}{(\ell + m)!} P_{\ell m}(\theta).$$

$P_{\ell m}(\theta)$ are the unnormalized Legendre functions [e.g., Aki and Richards, 1980]. The mantle was divided into 11 layers, denoted by i , and j denotes the outermost core layer. Table 2.1 gives the radii and thicknesses defining the 12 layers used in the inversions [after Tanimoto, 1990a]. Velocity perturbations (given by percentages) $\delta\alpha/\alpha$ and $\delta\beta/\beta$ were held constant within each layer. Finally,

$$\delta u_{\theta} = \sum_k \frac{R}{\omega_k^2} \cdot (t \sin \omega_k t) \exp\left(\frac{-\omega_k t}{2Q_k}\right) \cdot \left\{ \sum_{\ell} \sum_m \left[\frac{1}{\Delta_{SR}} \int_S^R Y_{\ell}^m(\theta, \varphi) ds \right] \cdot \left[\sum_{i=1}^{11} (b_{\ell}^m)_i \cdot \int_{r_i}^{r_{i+1}} (\chi K_{\alpha,k}(r) + K_{\beta,k}(r)) dr + \sum_{j=12}^{12} (a_{\ell}^m)_j \int_{r_j}^{r_{j+1}} K_{\alpha,k}(r) dr \right] \right\}. \quad [2.30]$$

Eq. [2.30] gives an explicit representation for displacement at the Earth's surface in terms of the model parameters (PREM), the source via the elements of the moment tensor, and the variations in model parameters with respect to PREM. The inversion for the model parameter perturbations by an iterative, least-squares approach forms the basis for the problem of obtaining three-dimensional maps of Earth structure through phase shifts which are reflected as linear increases of phase perturbation in the seismogram.

This is an approximation of the first-order Born approximation in which it is assumed that heterogeneity is localized and that perturbations in Earth structure can be represented by phase shifts alone in the waveform data. When the wavelength is small compared to the scale length of inhomogeneity, the amplitude perturbation is smaller than the phase perturbation, close to what is expected from geometric ray theory; i.e., the inhomogeneous region is smooth and can be considered a piecewise homogeneous region [Aki and Richards, 1980]. Thus, the Born approximation is only valid when the loss of energy due to scattering is small compared to the total energy. No coupling effects have been included in the above expressions. When the equation of motion is modified to account for perturbations in density and velocity, and forward and inverse Laplace

Table 2.1 Radii, depths, and thicknesses of layers used in three-dimensional velocity inversions.

Layer	Top radius (km)	Bottom radius (km)	Top depth (km)	Bottom depth (km)	Thickness (km)
1	6371	6151	0	220	220
2	6151	5971	220	400	180
3	5971	5701	400	670	270
4	5701	5349	670	1022	352
5	5349	5087	1022	1284	262
6	5087	4816	1284	1555	271
7	4816	4555	1555	1816	261
8	4555	4283	1816	2088	272
9	4283	4012	2088	2359	271
10	4012	3741	2359	2630	271
11	3741	3480	2630	2891	261
12	3480	3280	2891	3091	200

transformed assuming a step function type source, the resulting expression for displacement can be related to the derivation given above which includes Jordan's [1978] 'multiplet location parameter' [Tanimoto, 1984]. Note, however, that the effects of mode coupling have not been included in the inversion results presented here.

2.3 Rayleigh wave constraints

The data provide relatively uneven coverage of the upper mantle, so the surface wave eigenfrequency perturbation results of Zhang [1992] have been included in the inversions to constrain upper mantle structure. Zhang [1992] used Rayleigh wave data to invert for upper mantle velocity and solved for eigenfrequency perturbations in terms of spherical harmonic expansions for fundamental spheroidal modes ${}_0S_{33}$ to ${}_0S_{131}$. The eigenfrequency perturbations are functions of surface wave group velocities and perturbations in phase velocities, which in turn are expanded in spherical harmonics via

$$\left(\frac{\delta\omega}{\omega}\right)_{\text{standing wave,k}} = \frac{U_k}{C_k} \left(\frac{\delta C}{C}\right)_T = \sum_{\ell=0}^{\ell_{\max}} \sum_{m=-\ell}^{\ell} R_{\ell,k}^m Y_{\ell}^m(\theta, \varphi) \quad [2.31]$$

where R_{ℓ}^m are the phase perturbation expansion coefficients for a specific eigenfrequency.

Hence,

$$\left(\frac{\delta\omega}{\omega}\right)_{\text{standing wave,k}} = \left(\frac{\delta\omega}{\omega}\right)_{\text{local,k}} = \int_0^a \left(K_{\alpha,k}(r) \frac{\delta\alpha}{\alpha} + K_{\beta,k}(r) \frac{\delta\beta}{\beta} \right) dr \quad [2.32]$$

$$= \sum_{\ell} \sum_m Y_{\ell}^m(\theta, \varphi) \left[\sum_{i=1}^{11} \left(b_{\ell}^m \right)_i \cdot \int_{r_i}^{r_{i+1}} (\chi K_{\alpha,k}(r) + K_{\beta,k}(r)) dr \right]. \quad [2.33]$$

Equating terms of the same angular and azimuthal order

$$R_{\ell,k}^m = \sum_{i=1}^{11} \left(b_{\ell}^m \right)_i \cdot \int_{r_i}^{r_{i+1}} \left(\chi K_{\alpha,k}(r) + K_{\beta,k}(r) \right) dr \quad [2.34]$$

where, as before, $\left(b_{\ell}^m \right)_i$ are the coefficients of expansion for which we have solved. The value of the right hand side of Eq. [2.34] is usually non-zero only for the top four layers of the 11- and 12-layer models.

2.4 Pattern retrieval resolution tests

It is a well-known problem in inverse theory that even though many parameters are obtained independently, there exists some dependence of one set of parameters on another. For example, in inversions for multi-layered structure, the power of one set of structure coefficients will often leak into the structure coefficients for adjacent layers. This is because raypath coverage in the Earth is not complete due to the limited number of station and event locations. Regions which deviate from the one-dimensional Earth model may not be sampled by the data set; as a result, there is uncertainty about where the regions actually exist in the models. For example, if a region of positive velocity anomaly in the lower mantle is not sampled by many raypaths, the results of the inversion may place part of it in the layer above and part in the layer below its actual location. Constraints can be placed on the power contained in specific layers relative to the others by examining the parameter amplitudes for a particular layer of interest. To find such constraints, a theoretical inversion for Earth structure is carried out for which an initial, synthetic model of Earth structure is known exactly. Synthetic data constructed from this initial Earth model are inverted for model parameters and the parameters for one region are compared to those of another in which some power leakage is suspected.

2.4.a Outermost core layer

Four pattern retrieval resolution tests were performed with the data set used in the 11- and 12-layer model inversions. The tests involved the construction of synthetic data based on a known Earth model. For the first synthetic Earth model, layers 1-11 were kept one-dimensional using PREM, and layer 12 was additionally assigned the pattern associated with unnormalized spherical harmonic term $c_1^1 = -0.01$, illustrated in Fig. 2.2. This corresponds to minimum and maximum velocities of -1.73% and 1.73%. The choice of this coefficient was based on the fact that it closely describes real-Earth velocity structure in layer 11 and because c_1^1 is the largest term in the 11th layer of the preferred Earth model discussed in Chapter 5. Thus, it was used so that the pattern of structure in layer 11 would have the best chance of showing up in layer 12 if power leakage due to poor resolution occurred. A complete set of 6375 synthetic, radial seismograms was constructed using this Earth model and inverted for Earth structure in all 12 layers using inverse techniques and damping parameters described in Chapter 5. Seismograms were weighted by $1/M_0$ to damp large amplitude waveforms from large earthquakes more heavily. A matrix eigenvalue damping scheme was also incorporated into the inversion, although it served to control the amplitude of the coefficients, but not the ratios of amplitudes between layers or the power distribution. The results were analyzed after the first iteration only, since it is known from previous experience that further iterations do not change the structure patterns or coefficient ratios; only the coefficient amplitudes varied from one iteration to the next. The results for the 12-layered model of the first inversion are given in Fig. 2.3. Contours are given every 0.1% in this figure. Contour lines represent spherical harmonic expansions of structure with $\ell_{\max} = 12$. Solid contours indicate positive velocity variations and dashed contours indicate negative velocity variations. Each layer for which structure is given is indicated at the top by its depth range. It is clear from this figure that the original pattern of synthetic Earth

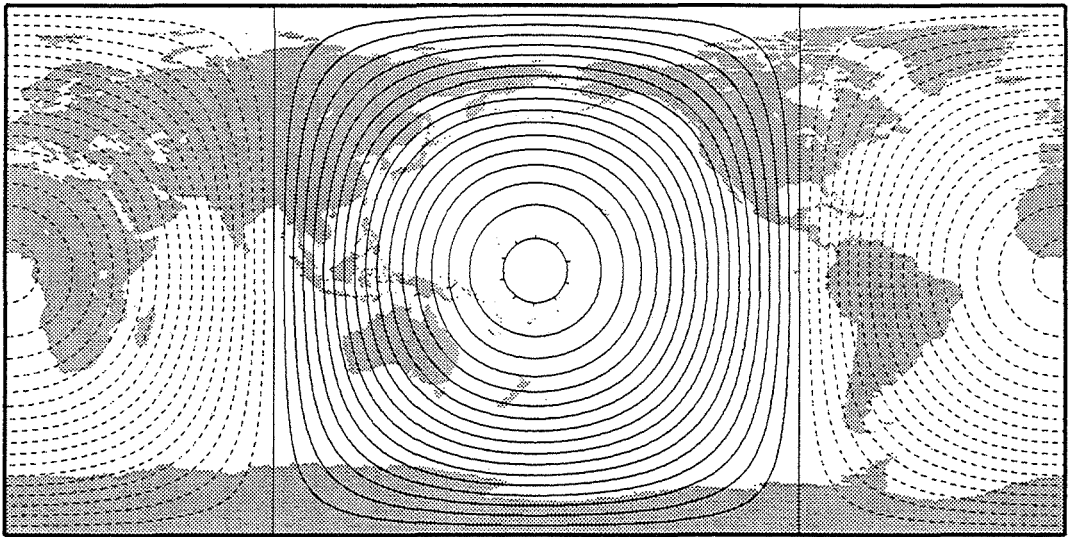
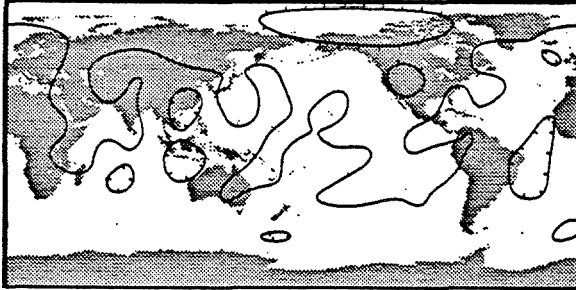
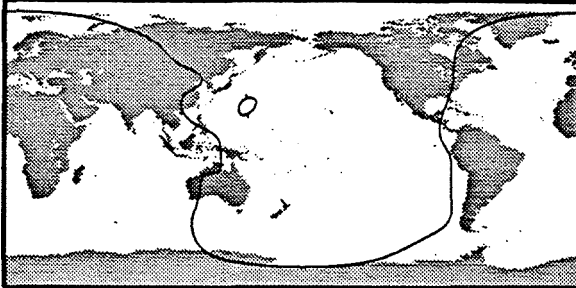


Fig. 2.2 Initial synthetic Earth model pattern defined by spherical harmonic term $c_1^1 = -0.01$ in the outermost core (layer 12).

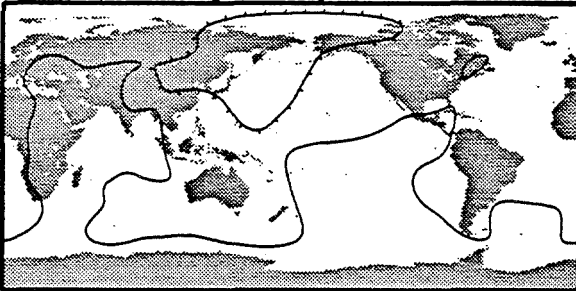
Layer 1-depth range 0-220 km



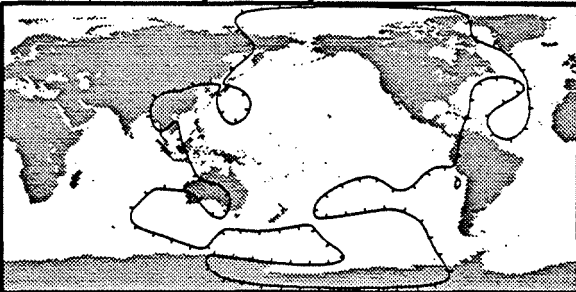
Layer 2-depth range 220-400 km



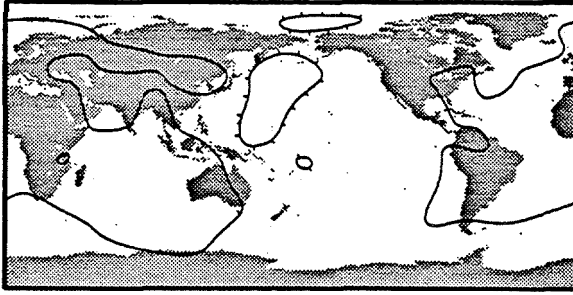
Layer 3-depth range 400-670 km



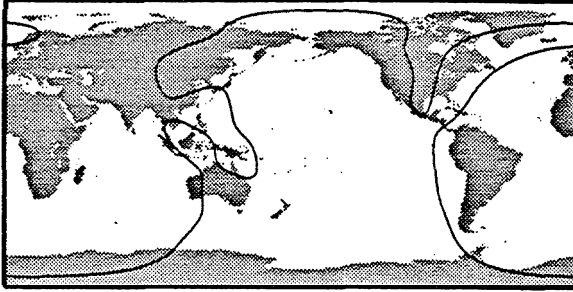
Layer 4-depth range 670-1022 km



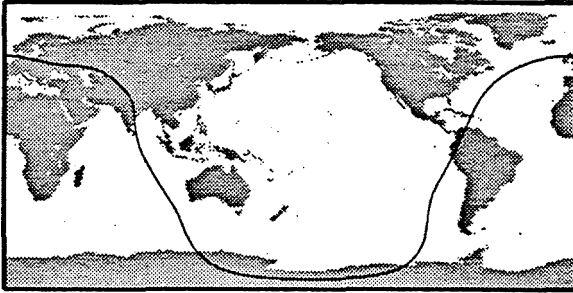
Layer 5-depth range 1022-1284 km



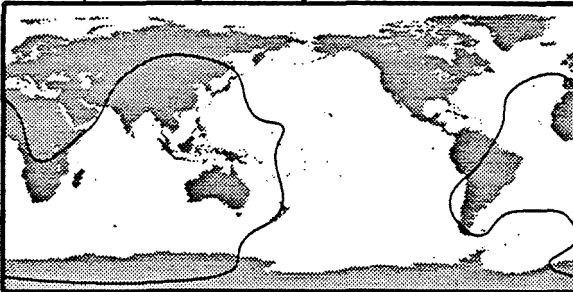
Layer 6-depth range 1284-1555 km



Layer 7-depth range 1555-1816 km



Layer 8-depth range 1816-2088 km



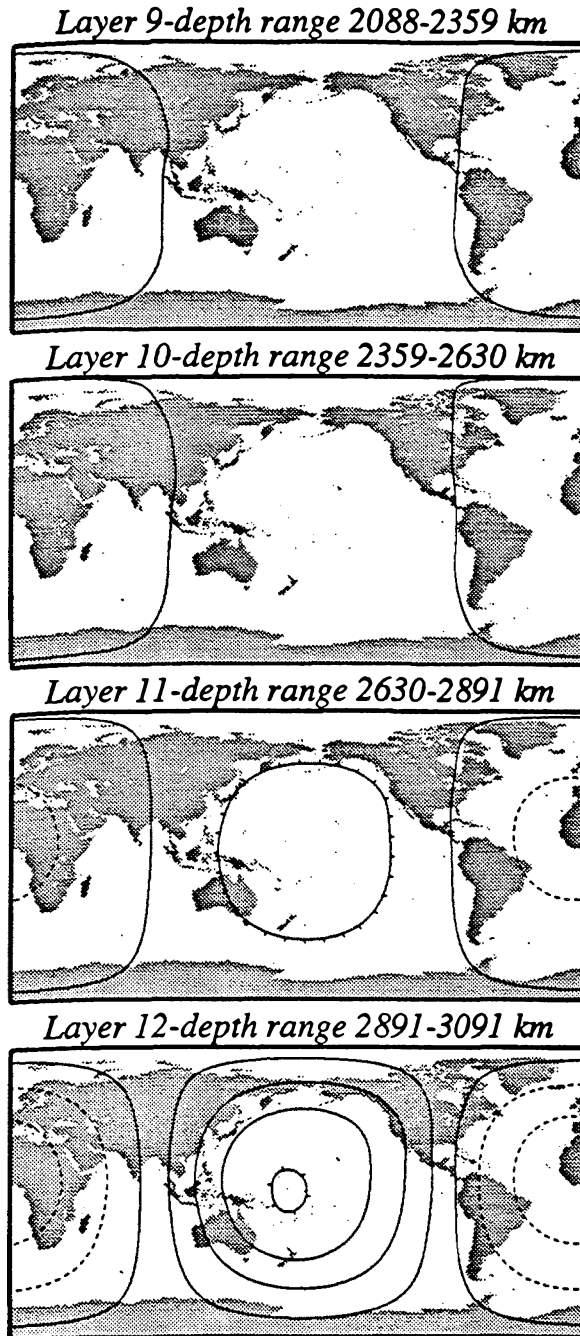


Fig. 2.3 Results for layers 1-12 from inversion for synthetic Earth model given in Fig. 2.2. Velocity (layers 1-11: S-wave; layer 12: P-wave) contours are given every 0.1%. Solid lines indicate positive velocity perturbations while dashed lines indicate negative velocity perturbations. The first solid contour indicates zero velocity anomaly.

structure has been retained in layer 12, but that there is some leakage of this pattern into layer 11. These plots resolve two important issues: the core phases in the data waveforms have supplied information specifically about the outermost core, separate from D" in the lower mantle. Also, calculations of power exhibited by layer 12 compared to layer 11 indicate that layer 12 contains much of the original pattern and total power after the inversion. The first column in Table 2.2 shows the percentage of total power contained in each layer after the inversion, where the top of the column indicates (in parentheses) which layer originally contained the synthetic Earth model given by $c_1^1 = -0.01$. From the values given in Table 2.2 it can be concluded that an upper bound of 84% of the total power obtained for layer 12 in real-data inversions actually resides in the outermost core. It is not surprising that the input patterns have leaked into surrounding layers regardless of the location of the initial heterogeneity. After all, many of the phases used to determine core structure also record the signature of mantle heterogeneity and no seismic tomography inverse problem is so well formulated that all eigenvalues are independent.

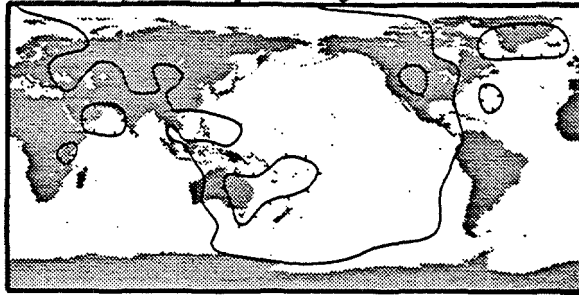
2.4.b Lowermost mantle layer

The second pattern retrieval resolution test was conducted to determine what degree of leakage occurred into surrounding layers if the same pattern was put in layer 11 in order to place additional constraints on final Earth structure models. For the second synthetic Earth model, layers 1-10 and 12 were kept one-dimensional using PREM, and layer 11 was additionally assigned the pattern associated with spherical harmonic term $c_1^1 = -0.01$. The pattern is the same as that given in Fig. 2.2. Again, a complete set of 6375 synthetic, radial seismograms was constructed using this Earth model and inverted for Earth structure in all 12 layers. The results for the 12-layered model of the second resolution inversion are given in Fig. 2.4. Contours are given every 0.1% in this figure. As before, solid contours indicate positive velocity variations and dashed contours indicate negative velocity variations. Contour lines represent spherical harmonic expansions of

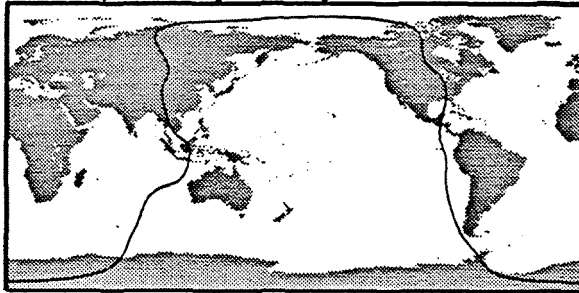
Table 2.2 Percent power contained in layers 1-12 after resolution inversions described in text. The top of each column indicates the layer (in bold) which contained the original synthetic Earth model described by spherical harmonic $c_1^1 = -0.01$. The rows indicate the % total power contained in layers 1-12 after the inversions.

Layer	Percent power after 1st synthetic test (12)	Percent power after 2nd synthetic test (11)	Percent power after 3rd synthetic test (1)
1	0.00057	0.00383	99.42763
2	0.01320	0.01628	0.23180
3	0.00135	0.00306	0.06923
4	0.00524	0.02046	0.25640
5	0.00332	0.00368	0.00060
6	0.03852	0.06604	0.00917
7	0.17266	0.10423	0.00008
8	0.02470	0.35463	0.00287
9	0.92019	1.98101	0.00107
10	1.67041	29.43006	0.00072
11	13.45450	60.09549	0.00041
12	83.69535	7.92123	0.00002

Layer 1-depth range 0-220 km



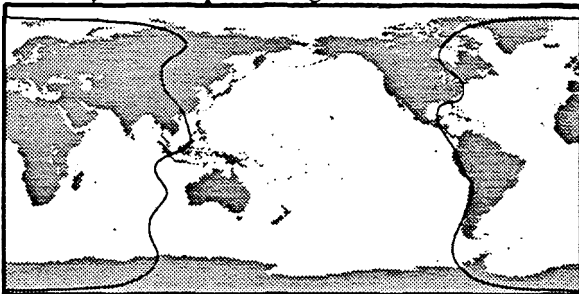
Layer 2-depth range 220-400 km



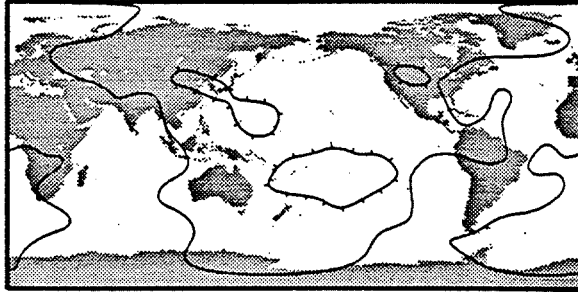
Layer 3-depth range 400-670 km



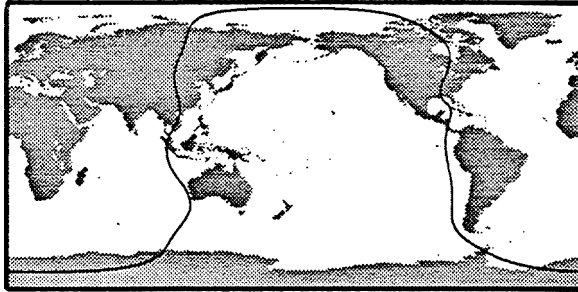
Layer 4-depth range 670-1022 km



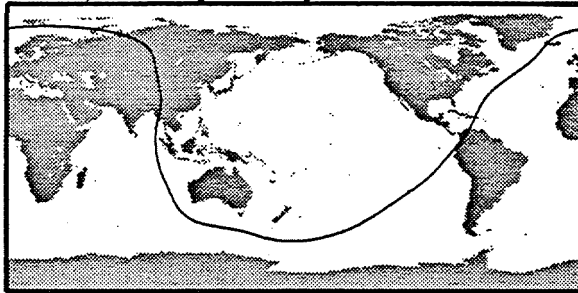
Layer 5-depth range 1022-1284 km



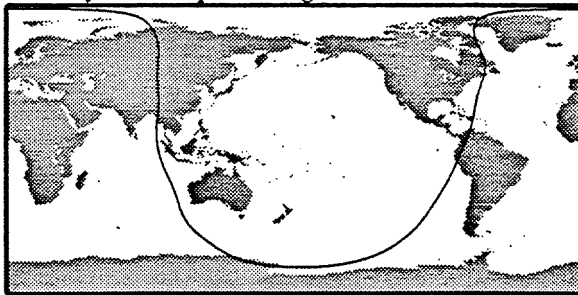
Layer 6-depth range 1284-1555 km



Layer 7-depth range 1555-1816 km



Layer 8-depth range 1816-2088 km



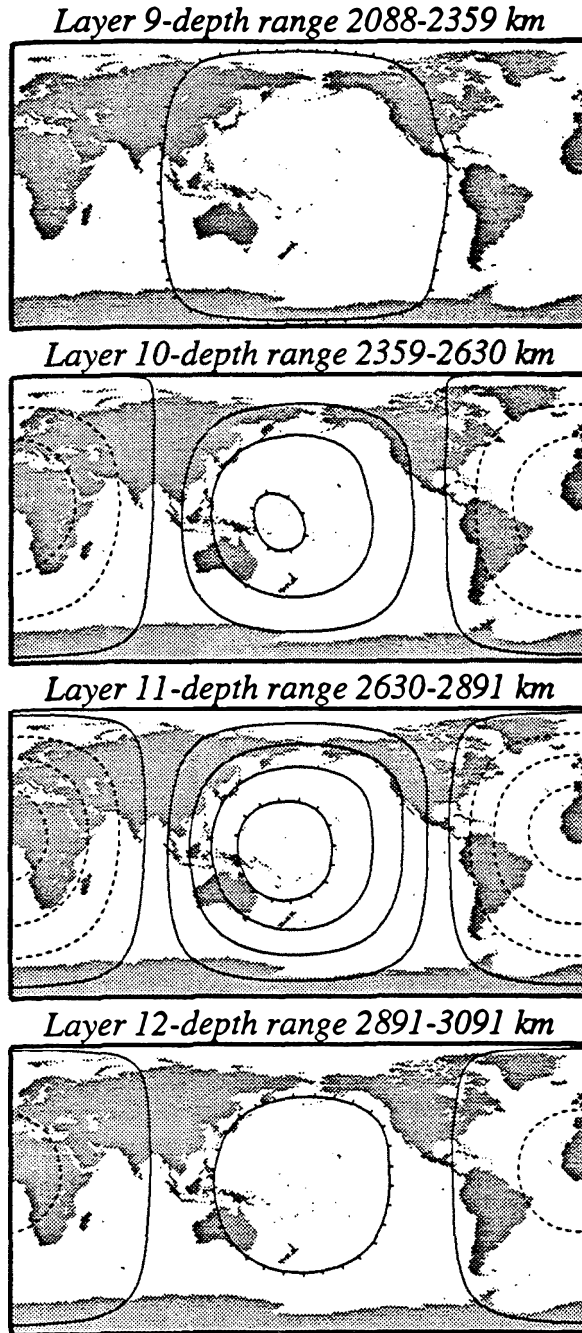


Fig. 2.4 Results for layers 1-12 from inversion for synthetic Earth model described in text. Velocity (layers 1-11: S-wave; layer 12: P-wave) contours are given every 0.1%. Solid lines indicate positive velocity perturbations while dashed lines indicate negative velocity perturbations. The first solid contour indicates zero velocity anomaly.

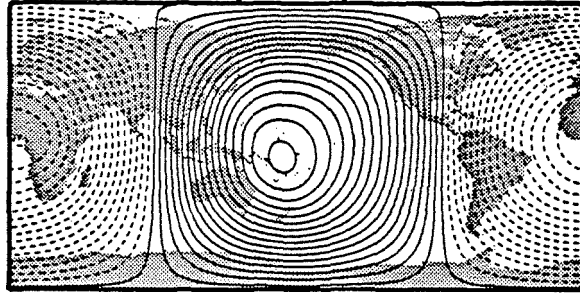
structure with $\ell_{\max} = 12$. The figure shows that the original pattern of synthetic Earth structure has been retained in layer 11, but that there is a little more leakage of this pattern into layers 10 and 12 than in the previous case. These plots once again indicate that specific phases in the waveforms are providing information about the lowermost mantle separately from the outermost core. From the values in Table 2.2 it can be concluded that an upper bound of 60% of the total power obtained for layer 11 in real-data inversions actually resides in D".

2.4.c Uppermost mantle layer

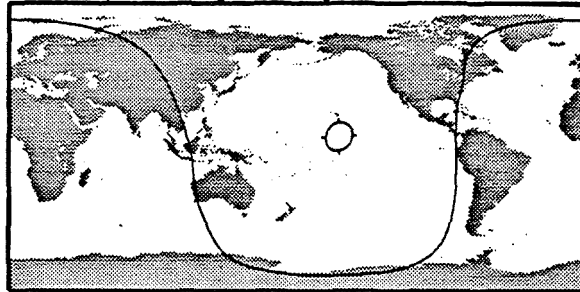
The third test was conducted to determine what degree of leakage occurred if the same pattern was placed in layer 1. This was to test if structure placed in the uppermost mantle would leak into lowermost mantle layers. For the third synthetic Earth model, layers 2-12 were kept one-dimensional using PREM, and layer 1 was additionally assigned the pattern associated with spherical harmonic term $c_1^1 = -0.01$, the same as that shown in Fig. 2.2. Again, a complete set of 6375 synthetic, radial seismograms was constructed using this Earth model and inverted for Earth structure in all 12 layers. The results for the 12-layered model of the third resolution inversion are given in Fig. 2.5. Contours are given every 0.1% in this figure. As before, solid contours indicate positive velocity variations and dashed contours indicate negative velocity variations. Contour lines represent spherical harmonic expansions of structure with $\ell_{\max} = 12$. This figure shows that almost all of the original pattern of synthetic Earth structure pattern and power has been retained in layer 1. These plots demonstrate that not only are waveforms providing independent information about the uppermost mantle layer, but that almost no power is leaking into the lowermost mantle layers. As the third column of Table 2.2 shows, over 99% of the total power of these inversions results is contained in layer 1.

A fourth test was performed to determine if synthetic structure placed in the middle of the mantle affected lower mantle or outermost core structure. For this synthetic

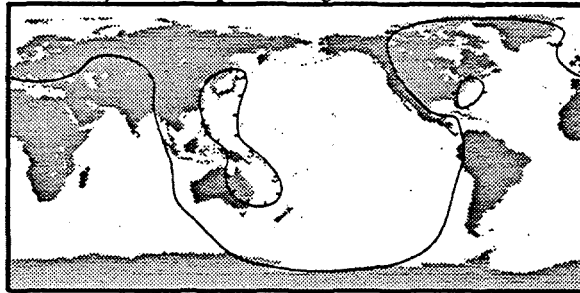
Layer 1-depth range 0-220 km



Layer 2-depth range 220-400 km



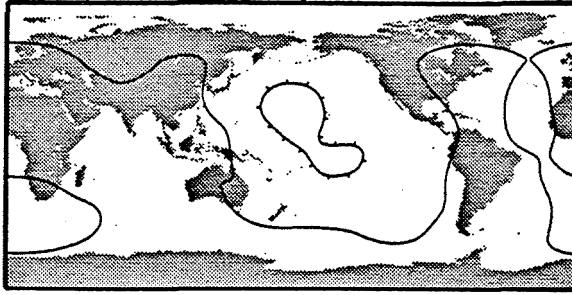
Layer 3-depth range 400-670 km



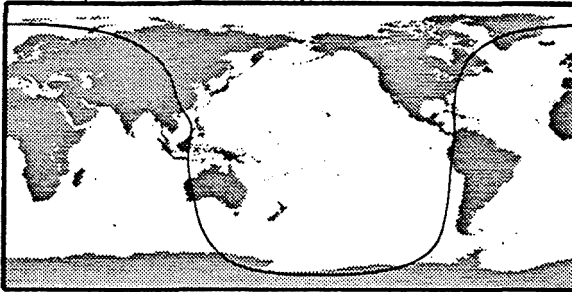
Layer 4-depth range 670-1022 km



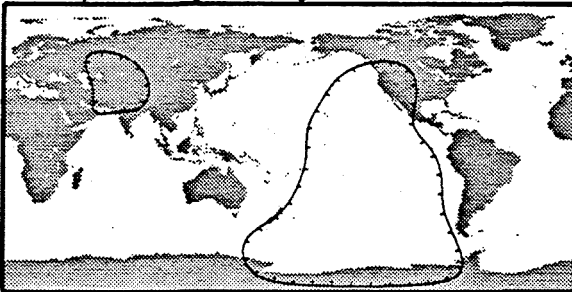
Layer 5-depth range 1022-1284 km



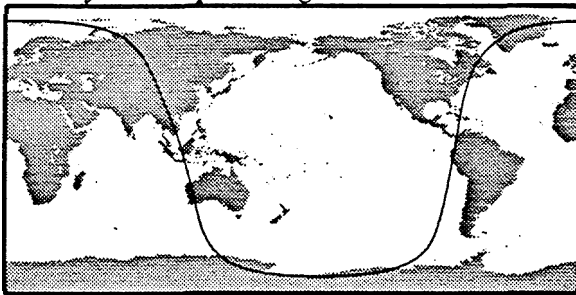
Layer 6-depth range 1284-1555 km



Layer 7-depth range 1555-1816 km



Layer 8-depth range 1816-2088 km



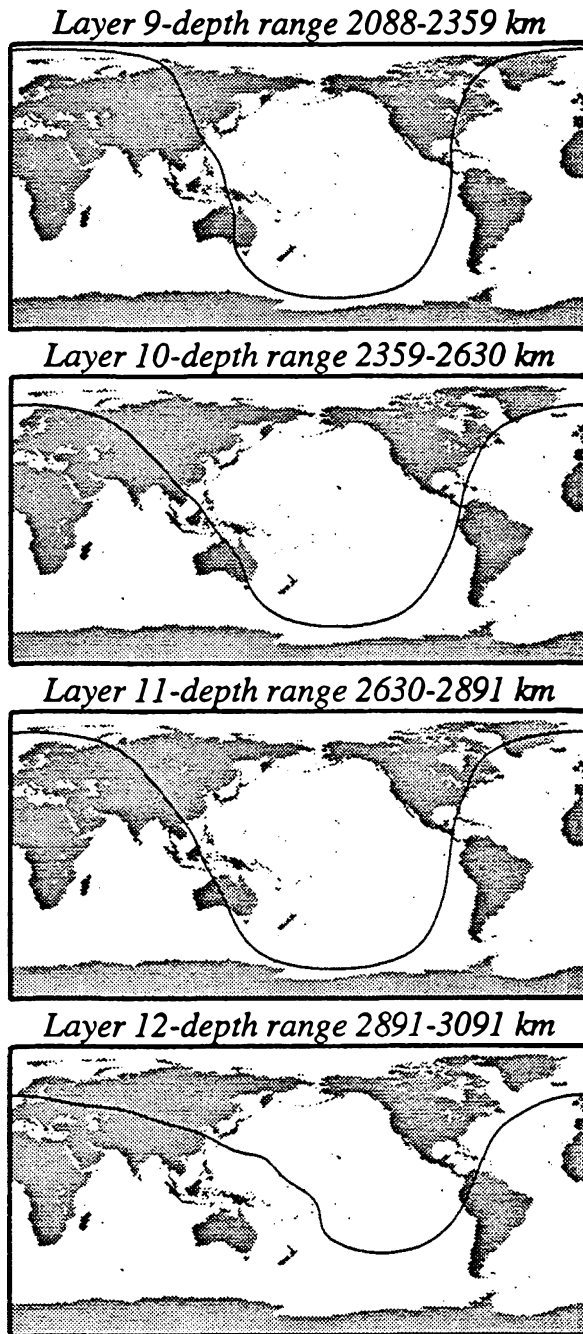


Fig. 2.5 Results for layers 1-12 from inversion for synthetic Earth model described in text. Velocity (layers 1-11: S-wave; layer 12: P-wave) contours are given every 0.1%. Solid lines indicate positive velocity perturbations while dashed lines indicate negative velocity perturbations. The first solid contour indicates zero velocity anomaly.

Earth model, layer 6 was assigned the pattern associated with spherical harmonic term $c_1^1 = -0.01$ and the inversion was carried out using the same approach as above. The results of this test indicate that very little power leakage occurred outside of layer 6. This is good evidence for the assertion that there is very little power leakage into layers 11 and 12 from the mid and upper mantle.

Because the relative values of structure power vary in the upper, mid, and lower mantle, the pattern retrieval resolution results must be interpreted with appropriate weights when applying them together to different parts of the mantle from that which contained the original synthetic Earth model. Using the results of the first two pattern retrieval resolution tests, upper and lower bounds can be placed on the amount of power that actually originates from outermost core and lowermost mantle velocity structure. To this end, we have computed multiplicative scalar factors by which to multiply the total power in layers 11 and 12 from real-Earth structure inversions to determine upper and lower bounds on the total power of each layer. These bounds affect the unnormalized power and spectral amplitudes but not the patterns of velocity structure. Because power is related to the square of the velocity amplitude, the upper and lower bound velocity amplitudes are found by multiplying by the square root of the multiplicative factors.

The percentages of power retrieved presented in Table 2.2 were used to estimate the factors which are given in Table 2.3. The method by which the factors were determined is as follows: the upper bound multiplicative factor for layer 12 was determined as the amount of power remaining in layer 12 after the resolution inversion for structure in that layer (first resolution test). The lower bound was found by subtracting the weighted percentage of power which had leaked into layer 12 from the resolution inversion for structure in layer 11. The weight was determined as the ratio of absolute power from real-Earth structure for layer 12 to layer 11. The factor for layer 11 was determined similarly.

Table 2.3 Upper and lower bound multiplicative factors for structure power in layers 11 and 12. This factor is multiplied by the total power in the corresponding layers to find the upper and lower bounds on the total power of real-Earth inversions. The velocity field amplitudes of the real-Earth inversions, whose results are given in Chapter 5, are multiplied by the square root of the multiplicative factors.

Multiplicative factor	Layer 12	Layer 11
\aleph_{\max}	0.84	0.60
\aleph_{\min}	0.68	0.53

To find the actual value of the multiplicative factors, \aleph_{\min} , for layers 11 and 12, let the total power (absolute, unnormalized) in layer 12 be A and in layer 11, B. Then the minimum amount of power residing in layer 12 from the real-Earth structure inversion is

$$\aleph_{\min} A = (0.837)A - (0.0792)B \quad [2.35]$$

and the multiplicative factor is

$$\aleph_{\min} = 0.837 - (0.0792) \frac{B}{A} \quad [2.36]$$

where 0.837 and 0.0792 are from Table 2.2. The value of $\frac{B}{A}$ was determined from real-Earth inversions to be 2.0. Similarly, the minimum amount of power residing in layer 11 is

$$\aleph_{\min} B = (0.601)B - (0.1345)A \quad [2.37]$$

and the multiplicative factor is

$$\aleph_{\min} = 0.601 - (0.1345) \frac{A}{B} \quad [2.38]$$

where 0.601 and 0.1345 are from Table 2.2. The values of \aleph_{\min} for layers 11 and 12 are given in Table 2.3. Of course, this assumes that all other spherical harmonic coefficients behave like c_1^1 and that no other layers leak into 11 or 12. With unlimited computer resources and time, the ideal test would involve pattern retrieval resolution inversions for patterns in all layers with coefficients other than c_1^1 , in addition to coefficient combinations.

Chapter 3: Data Selection Methods

3.1 General description

The data consist of filtered Global Digital Seismograph Network (GDSN) long-period, radial-component seismograms provided by the National Earthquake Information Center (NEIC). The seismograms came from event tapes which were generated by extracting day tape data with event magnitudes greater than 5.5 recorded between 1980 and 1987. The data set includes seismograms from the Seismic Research Observatories (SRO), Abbreviated Seismic Research Observatories (ASRO), Regional Seismic Test Network (RSTN), Digital World-Wide Standardized Seismograph Network (DWWSSN), and the China Digital Seismograph Network (CDSN). The sources are characterized by depths between 10 and 663 km (the distance-quantity distribution is shown in Fig. 3.1), and moments between 10^{24} and 10^{27} dyne-cm. Fig. 3.2a shows the locations of the earthquakes and 3.2b shows the locations of the stations which recorded the seismograms used in the inversions. The names and locations of the stations are given in Table 3.1. As Fig. 3.2a illustrates, the earthquakes are globally well-distributed along major plate boundaries. Although the stations are not quite as evenly distributed, their locations allow reasonably good raypath coverage considering the years during which data were collected. Coverage is best under the Pacific Ocean from the large number of paths between Pacific events and North American stations. It is most sparse for the lowest latitudes due to the lack of stations in the Southern Hemisphere. The instrument responses for instruments in the networks listed above are shown in Fig. 3.3. Each waveform record included

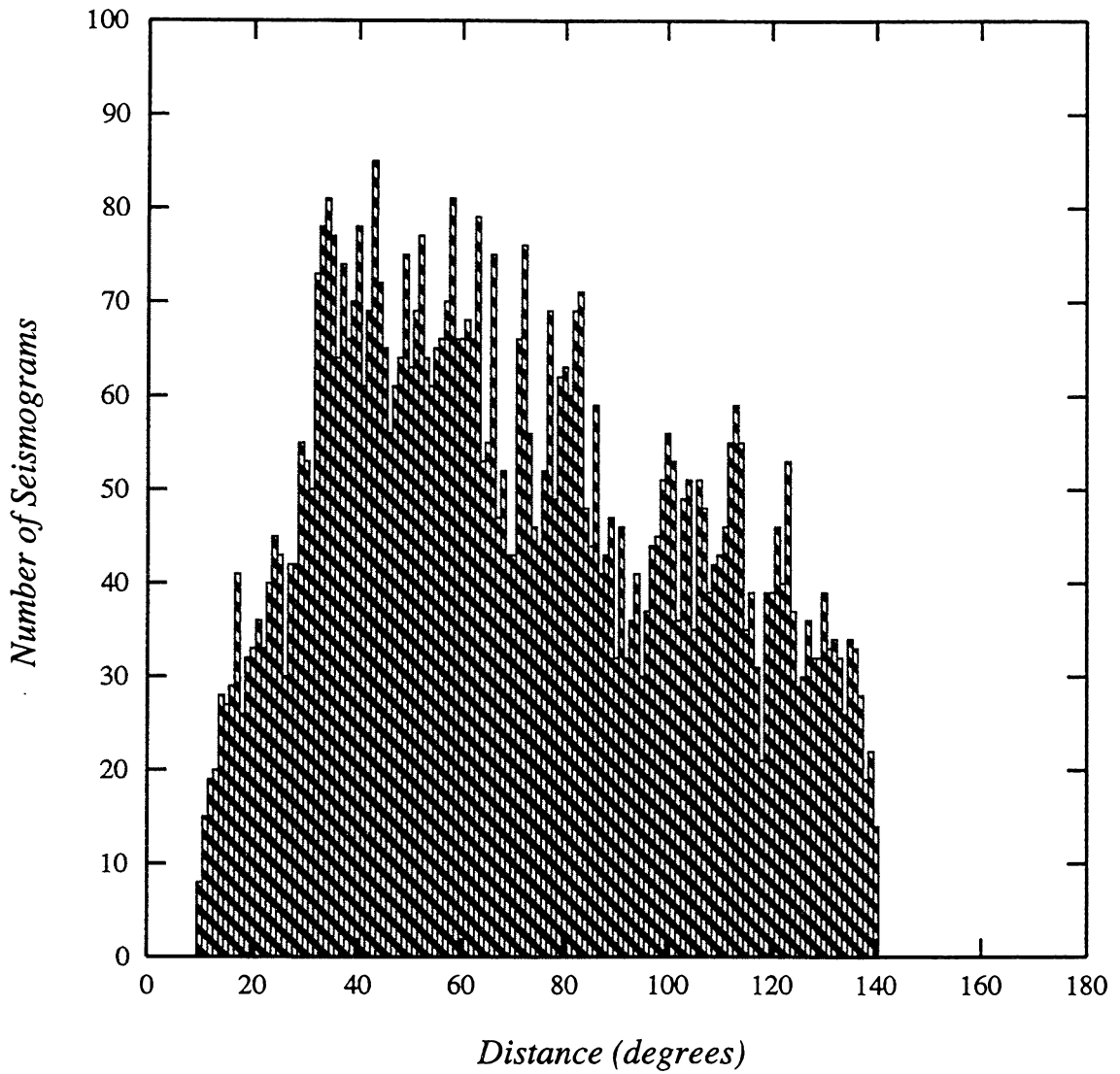
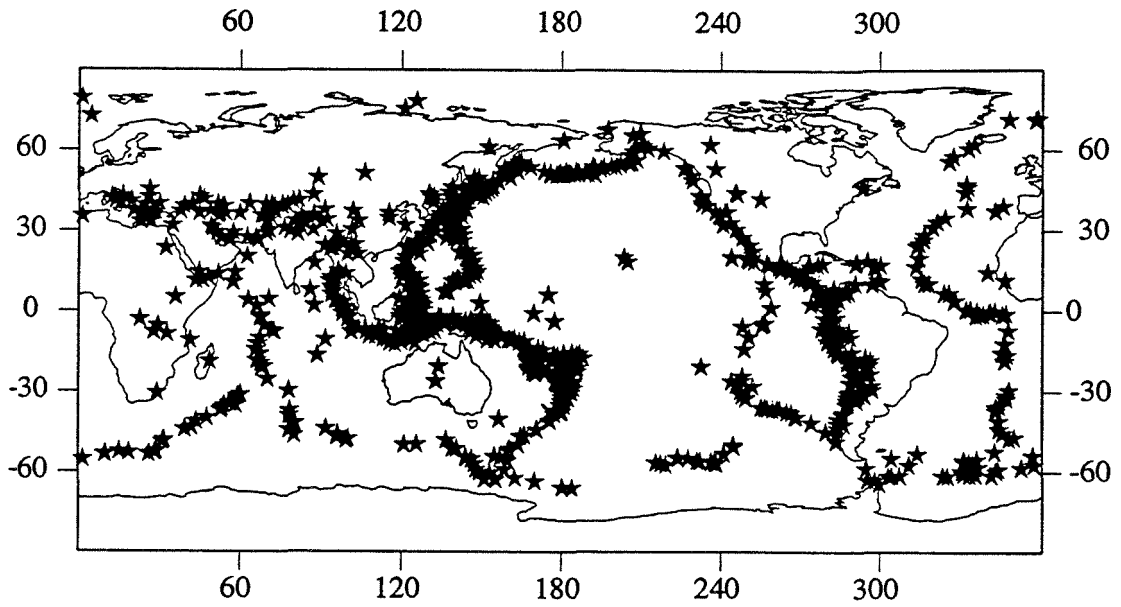


Fig. 3.1 Distribution of number of seismograms within 1° distance bins.

(a)



(b)

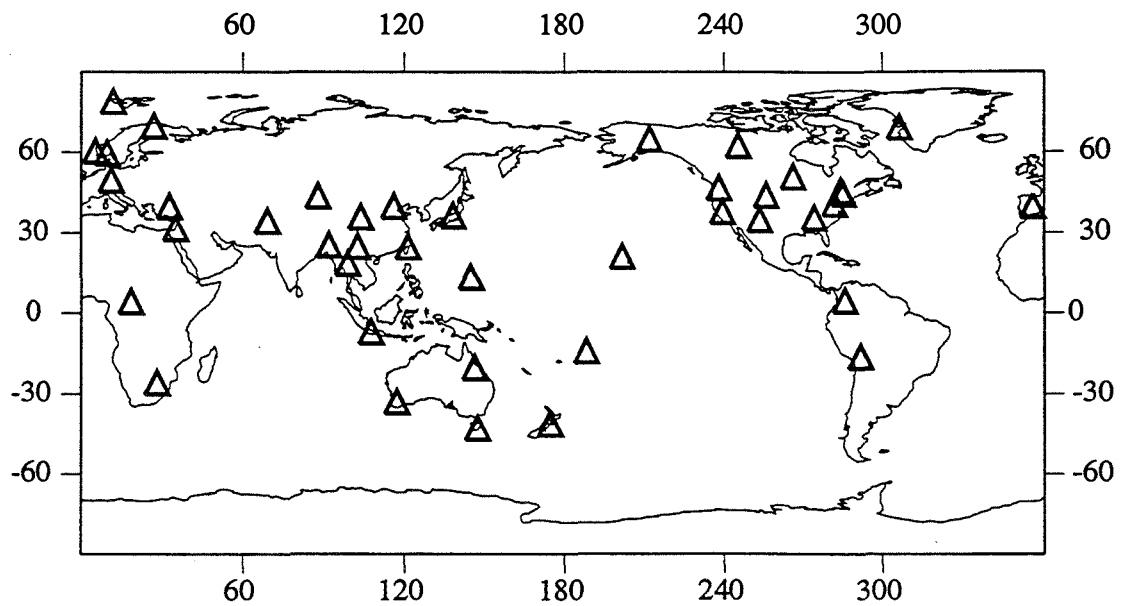


Fig. 3.2 Locations of the (a) 971 earthquakes and (b) stations which contributed data to the one-layer and three-dimensional inversions.

Table 3.1 Names and locations of GDSN stations which recorded waveforms used in the one-layer and three-dimensional inversions.

Station name	Network	Location
ANMO	SRO	Albuquerque, New Mexico
ANTO	SRO	Ankara, Turkey
BCAO	SRO	Bangui, Central African Republic
BGIO	SRO	Bar Giyyora, Israel
BOCO	SRO	Bogota, Colombia
CHTO	SRO	Chiang Mai, Thailand
GAC	SRO	Glen Almond, Quebec, Canada
GRFO	SRO	Grafenberg, Germany
GUMO	SRO	Guam, Mariana Islands
NWAO	SRO	Narrogin, Australia
SHIO	SRO	Shillong, India
SNZO	SRO	South Karori, Wellington, New Zealand
TATO	SRO	Taipei, Taiwan
CTAO	ASRO	Charters Towers, Australia
KA AO	ASRO	Kabul, Afghanistan
KONO	ASRO	Kongsberg, Norway
MAJO	ASRO	Matsushiro, Japan
ZOBO	ASRO	Zongo Valley, Bolivia
AFI	DWWSSN	Afiamalu, Western Samoa
ALQ	DWWSSN	Albuquerque, New Mexico
BER	DWWSSN	Bergen, Norway
COL	DWWSSN	College, Alaska
GDH	DWWSSN	Godhaven, Greenland
HON	DWWSSN	Honolulu, Hawaii
JAS	DWWSSN	Jamestown, California
JAS1	DWWSSN	Jamestown, California
KBS	DWWSSN	Kings Bay, Spitzbergen, Norway
KEv	DWWSSN	Kevo, Finland
LEM	DWWSSN	Lemban, Indonesia
LON	DWWSSN	Longmire, Washington
SCP	DWWSSN	State College, Pennsylvania
SLR	DWWSSN	Silverton, South Africa
TAU	DWWSSN	Tasmania, Australia
TOL	DWWSSN	Toledo, Spain
RSCP	RSTN	Cumberland Plateau, Tennessee
RSNT	RSTN	Yellowknife, NWT, Canada
RSNY	RSTN	Adirondack, New York
RSON	RSTN	Red Lake, Ontario, Canada
RSSD	RSTN	Black Hills, South Dakota
BJI	CDSN	Beijing, China
LZH	CDSN	Lhasa, China
WMQ	CDSN	Urumqi, China
KMI	CDSN	Kunming, China

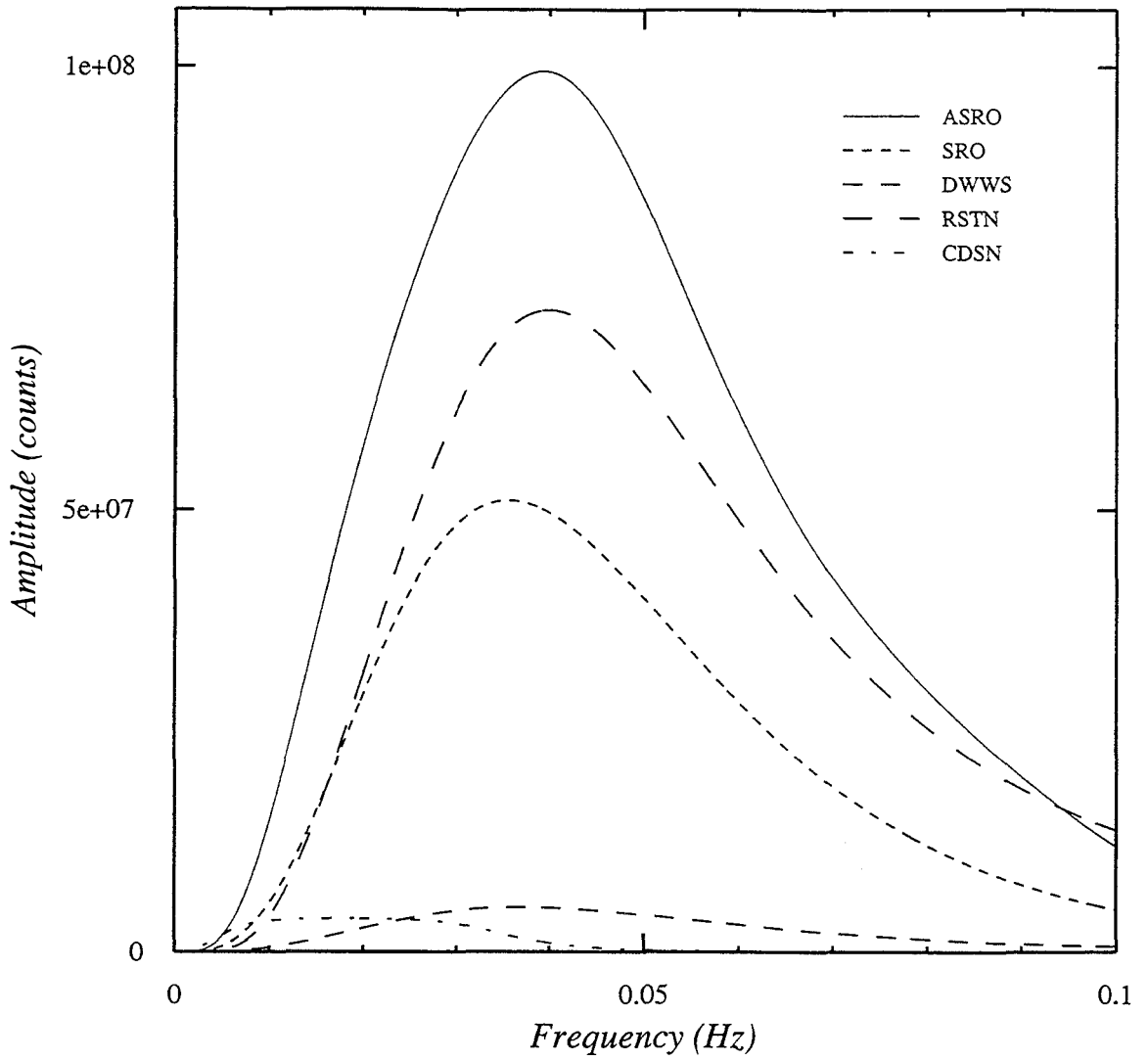


Fig 3.3 Instrument response curves for SRO, ASRO, DWSSN, RSTN, and CDSN networks.

information about the complex response function of the instrument which recorded it (with peak instrument response amplitudes occurring at periods from 25-28 sec), and header information including year, time (to milliseconds), epicentral distance, azimuth, back azimuth (both measured clockwise from north), number of data points, and sampling interval of the seismogram. Source parameters including location, depth, time, and six independent elements of the seismic moment tensor were obtained from Harvard centroid moment tensor solutions (also referred to as 'CMT solutions') [e.g., Dziewonski and Woodhouse, 1983a]. The instrument response was convolved with the synthetic seismograms in order to perform a direct comparison of synthetic seismograms with observed waveforms at each station.

3.2 Analysis and selection

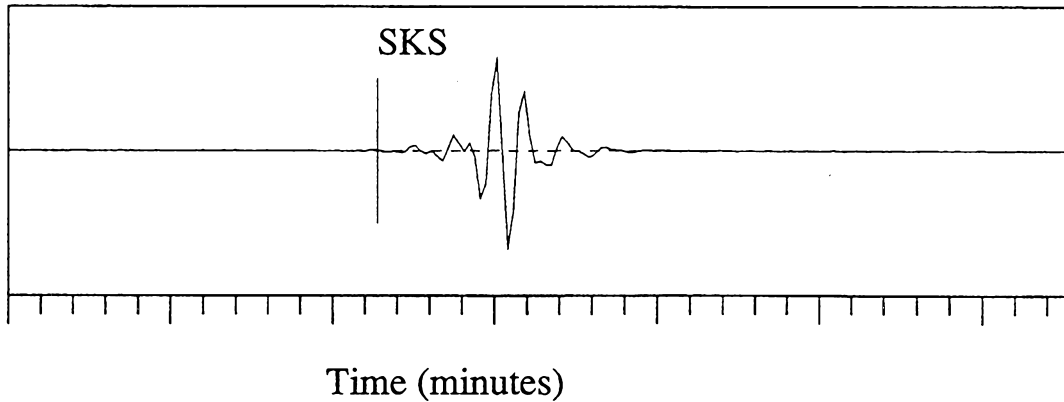
The initial list included 22,987 radial seismograms which were obtained by resampling the raw data at a 10 sec time interval and cosine filtering for periods between 20 and 666.67 sec (0.0015-0.050 Hz). Seismograms were limited to epicentral distances between 10° and 140°, and refiltered for periods between 33 and 100 seconds (0.01-0.03 Hz). Specifically, the filter was designed as a cosine function between frequencies 0.01-0.015, and 0.025-0.03, and unity between 0.015-0.025 Hz. Earthquakes which had produced half-duration times (given by the CMT solution as the shift in origin or centroid time in the absence of source complexity) larger than 17 sec were discarded with the justification that the point source approximation was no longer valid for this frequency range.

3.2.a Cross-correlation technique

The advantage to using GDSN data is that the numerous waveform recordings provide fairly good global raypath coverage, a requirement for three-dimensional, global

velocity inversions. However, one disadvantage is that a large portion of the data is noisy. The low signal-to-noise ratios are due to a variety of sources including random spikes from power surges and fluctuations (e.g., lightning, wind), non-seismic signals, and signal processing errors (e.g., windowing the time series such that part or none of the seismogram is included, incorrect polarity). An automated cross-correlation measurement technique was used as an objective method for discarding noisy or non-existent signals in the data set. An initial synthetic seismogram was computed for the body-wave portion of each record and the cross-correlation coefficient was computed for each synthetic-data pair before the inversions were performed. All synthetic-data pairs with coefficients less than 0.4 were discarded. The choice of a threshold coefficient of 0.4 was based on the desire to have a data set with good to moderately poor initial synthetic-data fits, but not to include fits that were very poor due to noisy, or non-existent data. This value corresponds to a phase shift of about 66 degrees in two identical sine functions. Thus, the cross-correlation coefficient condition allowed us to retain relatively poor data-synthetic fits for the inversion. Several hundred synthetic-data pairs with coefficients < 0.4 were examined to visually confirm that good data were not being thrown out by this technique. In all cases, the correlation could not be improved by a stationary time shift between the data and synthetic. Examples of two synthetic-data pairs that were removed from the data set because their corresponding cross-correlation coefficients were too low are shown in Fig. 3.4. This figure shows initial fits that are extremely poor due to large-amplitude signals that are probably non-seismic. To even out the distribution of seismic events so that regions with heavy coverage would not bias the results, the surface of the Earth was divided into 5° by 5° cells and the total number of seismograms produced by all earthquakes which had occurred within each cell was limited.

860712(RSCP.r) distance=103.1 degrees cross correlation= 0.36



820306(BER.r) distance=109.5 degrees cross correlation= -0.19

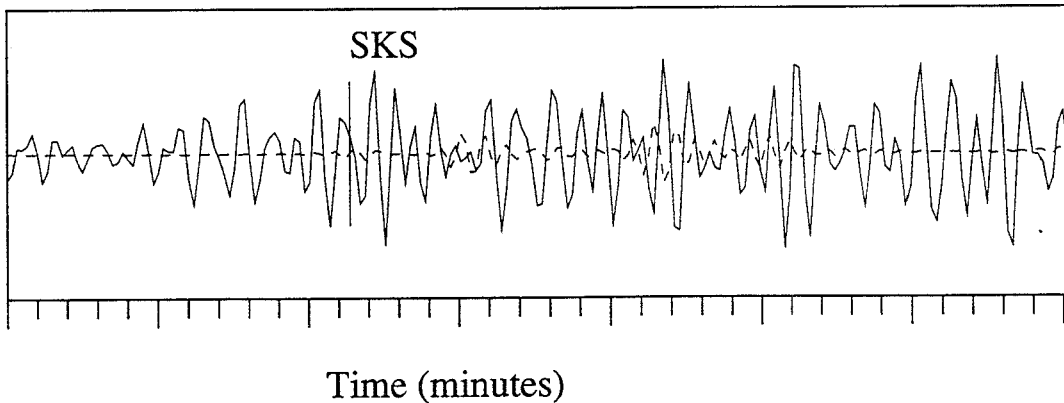


Fig. 3.4 Examples of data (solid lines)-synthetic (dashed lines) waveform fits using PREM as the initial Earth model which were discarded because their corresponding cross-correlation coefficients (given at the top right of each waveform) were < 0.4 .

3.2.b Travel-time and epicentral distance windows

Each seismogram was windowed for the time series segment containing only body-wave phases, beginning 30 sec before the direct or diffracted P-wave arrival and ending 30 sec (for $\Delta \leq 60^\circ$), 120 sec (for $60^\circ < \Delta < 100^\circ$), or 360 sec (for $\Delta \geq 100^\circ$) before the fundamental Rayleigh wave arrival (for the inversion results given in Chapter 5). The P-wave and diffracted P arrivals were obtained from the IASP91 Earth model travel-time tables [Kennett and Engdahl, 1991] and the Rayleigh wave arrival was estimated by calculating the travel time of the surface waves for a group velocity of 3.84 km/sec. This value is slightly higher than the maximum group velocity (3.8392 km/sec) given by the spheroidal modes used in the inversions. However, the higher value was used to ensure that the Rayleigh waves were not included in the inversion since their large amplitudes would have dominated the solution. Including a large number of body-wave phases in the waveform inversion was desirable for several reasons: the different phases carry information about various parts of the Earth's deep interior so that the resulting Earth model is not biased by a very small number of phases, errors from travel-time determinations do not enter the problem, and structure information is provided by amplitudes in addition to phase shifts. The disadvantage, however, is that the S phases dominate with their larger amplitudes. In particular, the phases which contributed most heavily to the inversion were direct and diffracted S, PS, SS and SSS. P waves were included, but probably did not contribute much due to their small amplitudes (see Fig. 3.5 for comparison).

The time window was modified for the one-layer inversions with corresponding results given in Chapter 4. For these inversions, the waveform was windowed for the time series beginning 30 sec before the SKS arrival time and ending 20 sec before either the estimated diffracted S or the PKKP arrival time (depending on distance) in order to obtain structure information solely from outer core phases. The SKS travel times were obtained

850804(CTAO.r) distance=104.2 degrees

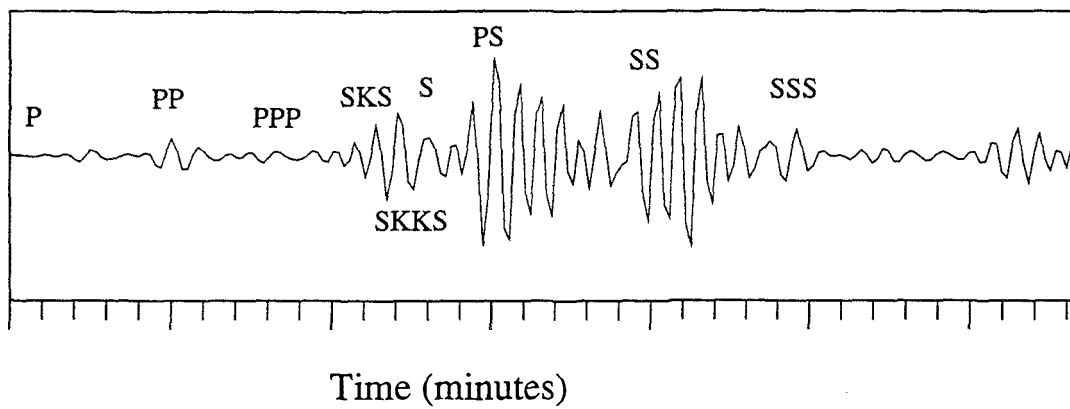


Fig. 3.5 Radial seismogram recorded at CTAO for earthquake which occurred in Central California, showing relative body-wave phase amplitudes.

using the Jeffreys-Bullen travel-time table [Jeffreys and Bullen, 1958]. To illustrate the different raypath characteristics, raypath calculations for the turning point depths of SKKS indicate that it turns just below CMB (e.g., ~ 100 km below the CMB for 112° and ~ 200 km for 121°). Thus, it samples the structure of a large portion of the outermost core. SKS has deeper turning points (e.g., ~ 1200 km below the CMB for 112° and ~ 1500 km for 121°).

The final, smaller data set for the individual SnKS waveform inversions (Chapter 4) included 2335 seismograms (i.e., source-receiver pairs) from 741 earthquakes with $110^\circ \leq \Delta \leq 130^\circ$, all of which occurred in the Southern Hemisphere. Fig. 3.6 illustrates the outermost core raypath coverage provided by this data set. The final, complete data set for the mantle-core velocity inversions (Chapter 5) comprised 6375 seismograms from 916 earthquakes with $10^\circ \leq \Delta \leq 140^\circ$, which had occurred globally. Outermost core raypath coverage provided by this complete data set is illustrated in Fig. 3.7; it is clear from this figure that adding more long-distance data improved outermost core raypath sampling, especially in the Southern Hemisphere.

3.3 Normal mode data

Raypath coverage plots give a clear picture of exactly how Earth structure is sampled by phases in the data, but normal mode sampling is not quite as straightforward. A good picture of spheroidal normal mode energy distribution can be obtained by depth plots of the Frechet (sensitivity) kernels. These are the same kernels used to calculate the displacement derivatives for the first-order perturbation problem summarized in Chapter 2. The kernels illustrate the radial sensitivity of the spheroidal modes to Earth structure. For example, Fig. 3.8a shows that spheroidal mode ${}_{26}S_{21}$ has most of its P-wave energy in the outer core and is contributing to SnKS waveforms; all the SV energy is in the mantle. By contrast ${}_{22}S_{98}$ (Fig. 3.8b) has all of its P-wave and most of its SV energy in the upper

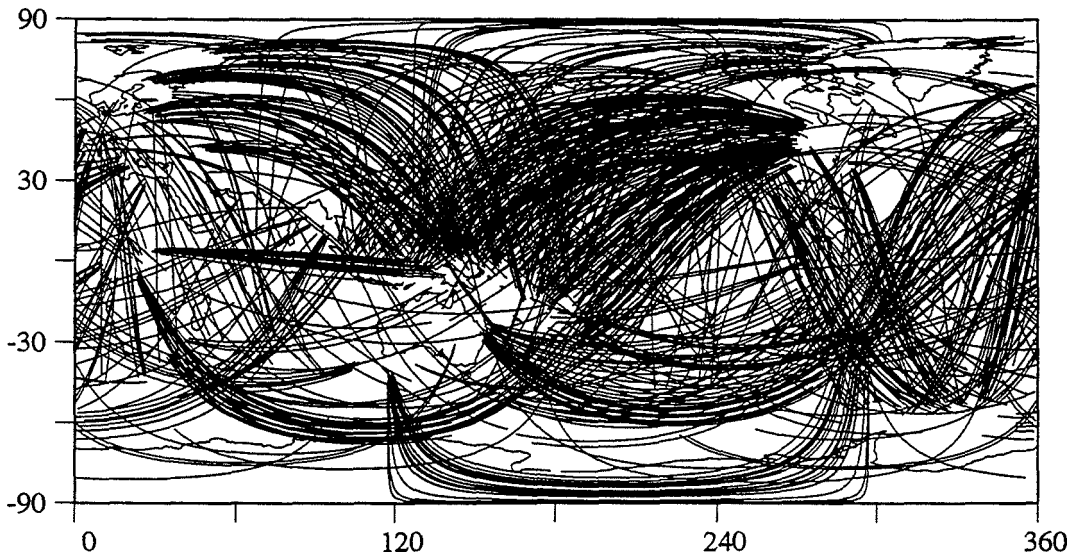


Fig. 3.6 Outermost core raypath coverage for data used in one-layer inversions; the results of these inversions are presented in Chapter 4.

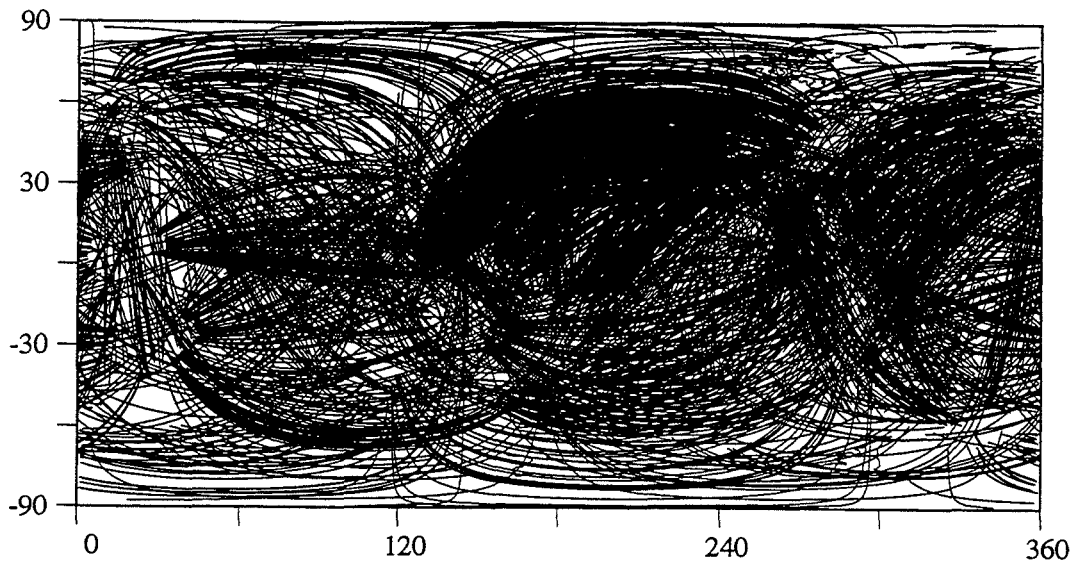


Fig. 3.7 Outer core raypath coverage from data used in the three-dimensional inversions; the results of these inversions are presented in Chapter 5.

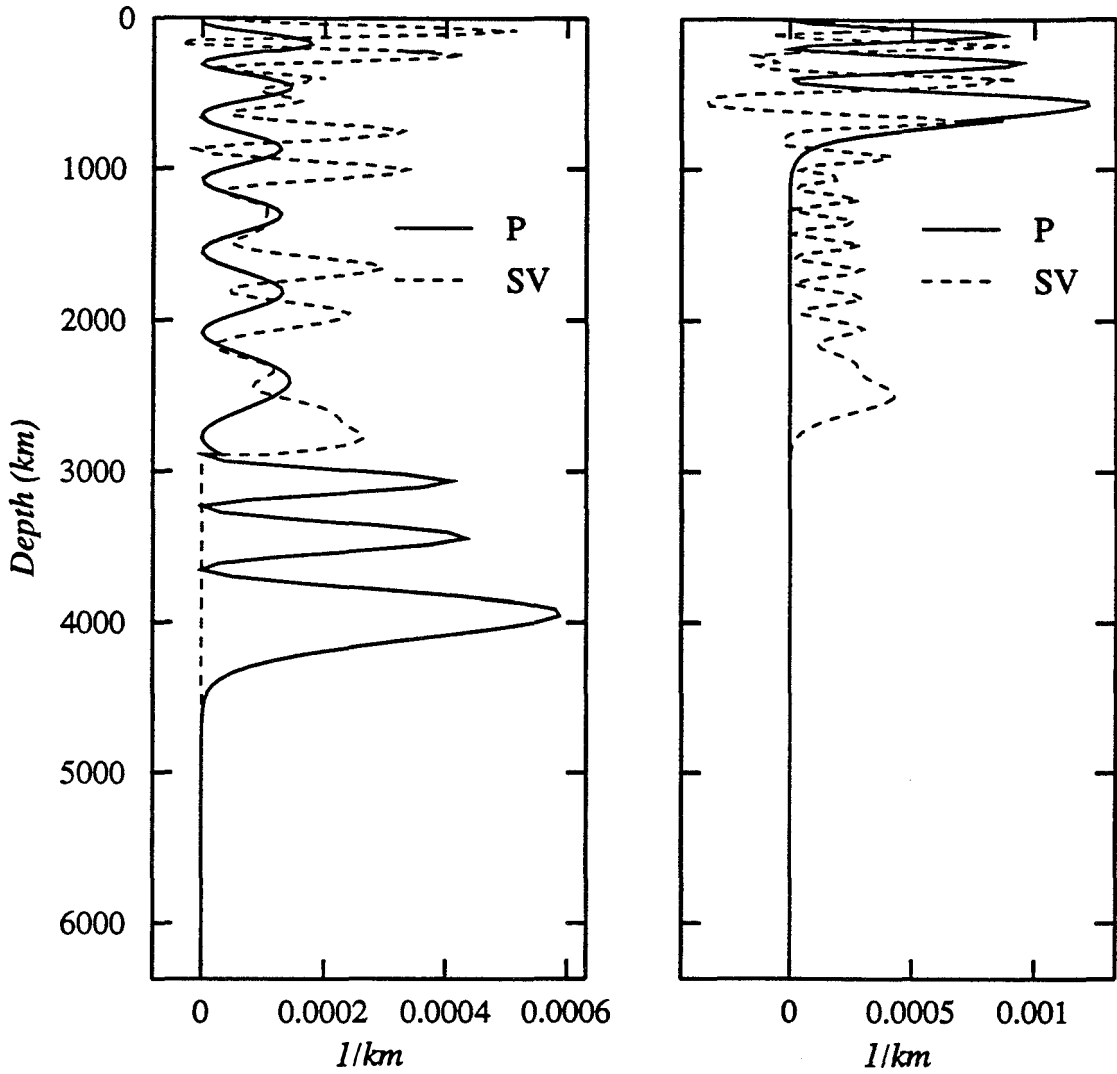


Fig. 3.8 Frechet kernels for spheroidal modes ${}_{26}S_{21}$ and ${}_{22}S_{98}$ plotted as functions of depth.

mantle and is not contributing to lower mantle phases in the waveforms. This can be viewed another way, described in more detail in Chapter 4: in order to determine how normal modes were being summed to form the core phases, the number of modes was limited first to those with ray parameters close to that of SKS and, second, of SKKS. The resulting waveforms match the SKS and SKKS phases independently, as expected.

3.4 Rayleigh wave phase perturbation data

The data provide relatively uneven coverage of the upper mantle, so the Rayleigh wave eigenfrequency perturbation results of Zhang [1992] have been included in the inversions to constrain upper mantle structure. Zhang [1992] used Rayleigh wave data to invert for upper mantle velocity, and solved for eigenfrequency perturbations in terms of spherical harmonic expansions for fundamental spheroidal modes ${}_0S_{33}$ to ${}_0S_{131}$. The eigenfrequency perturbations are functions of surface wave group velocities and perturbations in phase velocities, which in turn are expanded in spherical harmonics.

Chapter 4: One-layer Inversions of SnKS Phases for Outermost Core Structure

An initial, one-layered model of outermost core structure via the inversion of SnKS phases is presented in this chapter. The most readily observable of the SnKS suite of body-wave phases is the SKS phase which originates at $\Delta \approx 62^\circ$, emerges as a first arrival after its travel-time crossover with S at $\Delta \approx 85^\circ$, and dies out after $\Delta \approx 140^\circ$. SKKS arrives just after SKS and usually overlaps with the SKS trace in a long-period seismogram. These phases provide a wealth of information about outermost core structure, especially long-distance SKKS. In this study (also published in Kohler and Tanimoto [1992]), the SnKS phases were inverted for P-wave velocity perturbations in a single, 200 km thick layer at the top of the outer core. The scalar velocity anomalies were obtained relative to the starting Earth model, PREM, and plotted at the midpoint of each source-receiver raypath. P-wave velocity perturbations for each source-receiver pair were independently obtained from the SnKS portion of the waveform and two mantle S-wave heterogeneity models were incorporated in an attempt to remove the mantle heterogeneity signature from the waveforms. The inversion results indicate that lateral variations in P-wave velocity in the outermost core produce better waveform fits of SnKS phases after the inversions and that the patterns of variation do not appear to be geographically dependent. However, the large amplitudes and small-scale oscillations in pattern indicate that mantle heterogeneity is not entirely removed by this method.

4.1 Data set

4.1.a Analysis and description

The data comprise a subset of the total set described in Chapter 3. The original Global Digital Seismograph Network (GDSN) long-period, radial-component seismograms came from event tapes which were generated by extracting day tape data recorded between 1980 and 1987 from the SRO, ASRO, RSTN, and DWWSSN networks; the seismograms were filtered for periods between 33 and 100 seconds and limited by the cross-correlation coefficient of the synthetic seismograms and data. Each waveform record included information about the complex response function of the instrument which recorded it (with peak instrument response amplitudes occurring at periods from 25-28 sec) and header information including year, time (to milliseconds), epicentral distance, azimuth, back azimuth (measured clockwise from north), number of data points, and sampling interval of the seismogram. Source parameters including location were obtained from Harvard centroid moment tensor solutions [e.g., Dziewonski and Woodhouse, 1983a]. The instrument response was convolved with the synthetic seismogram in order to perform a direct comparison of synthetic seismogram with observed waveform at each station. After limiting the distance range, the data set included 2335 seismograms (i.e., source-receiver pairs) from 741 earthquakes, all of which occurred in the Southern Hemisphere. Each of these seismograms was then individually inverted for P-wave velocity perturbations along the raypath. Fig. 3.6 illustrates the outermost core raypath coverage provided by this data set.

4.1.b Travel time and epicentral distance range

Source-receiver distances for the scalar velocity inversions were limited to 110° - 130° in which SKS and SKKS are best isolated in the waveform from nearby phases which

are not sensitive to outer core structure. Although the two phases overlap with SKS arriving first, this was not a problem since the construction of synthetic seismograms by normal modes also produced the overlap and knowledge of the exact arrival times was not necessary. As Fig. 4.1 illustrates, it was important to avoid preceding travel-time body wave phases (such as PPP which samples the crust and mantle) and succeeding phases (such as diffracted S which samples only the mantle, and PKKP which samples the deeper outer core) in order to prevent the mapping of mantle heterogeneity into core structure. Within this distance window, the travel-time window was limited to that which contained SKS and SKKS, beginning 30 sec before the SKS arrival time and ending ~ 20 seconds before the arrival time of the diffracted S phase; this was estimated by calculating the travel-time arrivals from the slope of the travel-time curves for 12 depth intervals. Although it was impossible to put a formal error on diffracted S arrival times, the choice of the earliest probable diffracted S arrival times reflected the conservative nature of the window selection. Because so many seismograms were being analyzed, an automated procedure was devised by which only the desired time portion of the seismogram was isolated and searched for SnKS traces.

4.2 SnKS waveform construction by normal mode summation

Seismograms were individually inverted for P-wave velocity perturbations along the raypaths using perturbation theory and a simple least-squares method [e.g., Tanimoto, 1987]. Velocity inversion for the outermost core was computed assuming a laterally homogeneous initial Earth model in the core. The full theory behind the global, three-dimensional inversions has already been discussed in Chapter 2. For clarity and convenience, the modifications to the theory used in the one-layer inversions presented in this chapter is summarized as follows: the synthetic radial displacement and perturbation to displacement of seismograms were constructed as

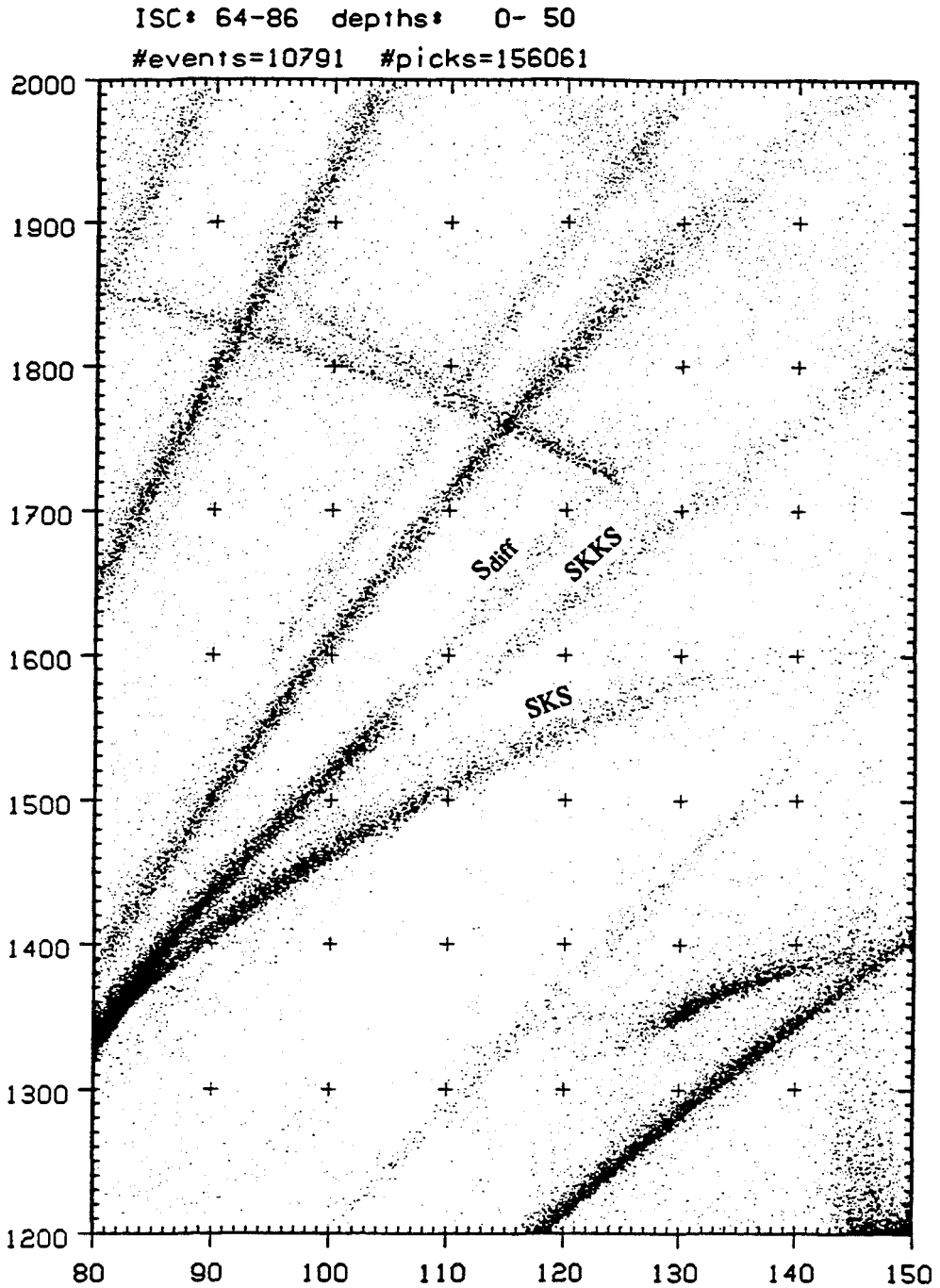


Fig. 4.1 International Seismological Center travel-time curves derived from 15,6061 picks corresponding to 10,791 events occurring between 1964 and 1986, with depths of 0-50 km. This window shows picks for distances between 80° and 150° and arrival times between 120 and 2000 sec; the SnKS phases are readily distinguishable.

$$u_{\theta} + \delta u_{\theta} = \sum_k \frac{R}{\omega_k^2} \cdot (-\cos \omega_k t + \delta \omega_k t \sin \omega_k t) \exp\left(\frac{-\omega_k t}{2Q_k}\right) \quad [4.1]$$

where $\delta \omega_k$ is the perturbation to the eigenfrequency ω_k of the k^{th} multiplet ($\delta \omega_k \ll \omega_k$), t is time, and R is given by Eq. [2.14]. In this formulation, $\delta \omega_k$ contains information about the differences between the theoretical Earth model and the true Earth which are reflected in differences between data and synthetic seismogram, δu_{θ} . The local eigenfrequency approach [Jordan, 1978] (Eq. [2.23]) was incorporated where the local eigenfrequency shift is integrated along the great circle path from the source to the receiver. For the portion of the ray traveling through the core,

$$\delta \omega_{\text{local},k} = \omega_k \int_{r_1}^{r_2} K_{\alpha,k}(r) \frac{\delta \alpha}{\alpha} dr \quad [4.2]$$

where $\delta \alpha / \alpha$ is the fractional deviation of P-wave velocity, $K_{\alpha,k}$ is the Frechet kernel for the k^{th} spheroidal mode, and r_1 and r_2 denote the bottom and top radii (3280 and 3480 km, respectively) of the outermost core layer.

There exists a question of uniqueness regarding the use of SnKS phases to model outermost core properties since they also travel through and sample the upper and lower mantle. This problem is partially circumvented by incorporating two mantle heterogeneity models to remove its signature from the SnKS waveforms. The first is MDLSH, an S-wave mantle velocity model [Tanimoto, 1990a] which was computed using long-period (40-100 sec) SH body waves and 1000 long-period (100-500 sec) Love waves. S-wave velocity in MDLSH is expanded up to degree and order 6. Although the maximum angular order is only six, it has been argued that mantle heterogeneity is dominated by low order harmonics [Tanimoto, 1990a,b; Su and Dziewonski, 1991]. Thus, most of the mantle signal should be removed by the first few harmonics. It should be noted that this model, in addition to all other global models, is a long-wavelength model of average

velocity structure. A spherical harmonic expansion was used to smooth structure laterally and no smoothing was used radially. Velocity was held constant within 11 shells of varying thicknesses. The second mantle heterogeneity model used in the one-layer inversions is a modification of MDLSH. In a test of whether the amplitudes of the velocity patterns given in MDLSH were large enough to describe mantle heterogeneity, the lower mantle values (layers 4-11) were doubled. In effect, this produced a different synthetic velocity model with the same patterns as MDLSH but with larger S-wave velocity perturbations in the lower mantle.

Including the mantle S-wave velocity model in the problem, perturbation to displacement can now be expressed as perturbations to P- and S-wave velocities in the mantle and P-wave velocities in the core. Accounting for mantle heterogeneity, the partial derivative of displacement, therefore, becomes

$$\delta u_{\theta} = \sum_k \frac{R}{\omega_k^2} \cdot (t \sin \omega_k t) \exp\left(\frac{-\omega_k t}{2Q_k}\right) \cdot \left\{ \sum_{\ell} \sum_m \left[\frac{1}{\Delta_{SR}} \int_S^R Y_{\ell}^m(\theta, \varphi) ds \right] \cdot \left[\sum_{i=1}^{11} (b_{\ell}^m)_i \int_{r_i}^{r_{i+1}} (\chi K_{\alpha,k}(r) + K_{\beta,k}(r)) dr + \sum_{j=12}^{12} (a_{\ell}^m)_j \int_{r_j}^{r_{j+1}} K_{\alpha,k}(r) dr \right] \right\} \quad [4.3]$$

where $(b_{\ell}^m)_i$ are coefficients of a spherical harmonic expansion of S-wave velocity structure solutions for the 11 mantle layers. The assumption that

$$\frac{\delta\alpha}{\alpha} = 0.5 \frac{\delta\beta}{\beta} \quad [4.4]$$

has been used to simplify the problem. The resulting vector equation becomes

$$\mathbf{Ax} = \mathbf{b} \quad [4.5]$$

where the elements of \mathbf{A} are computed from the right-hand side of Eq. [4.3], \mathbf{b} consists of the difference between data and synthetics, δu_{θ} , and x is the scalar value $\delta\alpha/\alpha$ for an individual seismogram; Eq. [4.5] was solved by a simple least-squares method. In the

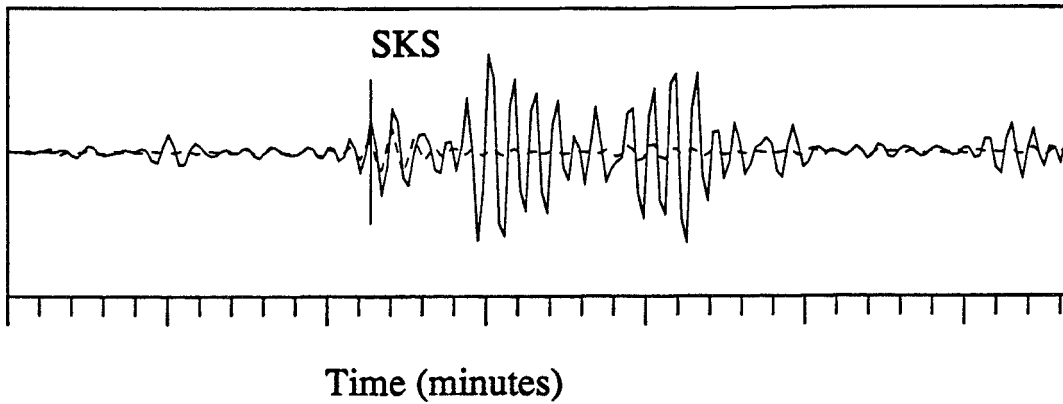
following sections it will be shown that incorporation of mantle velocity models of this kind is probably not sufficient for subtracting the effects of mantle heterogeneity on SnKS waveform inversion.

4.3 Ray parameter test

Waveforms of SKS and SKKS overlap in long-period data, but this is not a problem because it is not necessary to identify the arrival of the phases being modeled. Of the over 5000 modes used in the summation, however, not all contributed specifically to SnKS waveforms. Furthermore, just by looking at the total synthetic waveform it was not clear that some modes were contributing mainly to the SKS phase while different modes were contributing mainly to the SKKS waveform. Hence, a test was carried out to see if normal mode waveforms could give waveform information about SKS and SKKS separately. This is important because while SKS turns at depths of 1200-1800 km below the CMB in the limited distance range, SKKS travels through the outermost core to depths of only 150-500 km. Since it can be shown that SKKS is being fit separately, this provides evidence for independent, more complete information from the outermost layer of the core. In the first test, synthetics were constructed by summing normal modes within a limited ray parameter $p = \left(\ell + \frac{1}{2}\right) / \omega_k$ window around that of SKS. For SKS, the ray parameter was obtained by calculating $p = \left(\frac{\partial T}{\partial \Delta}\right)_{\text{SKS}}$ numerically from the Jeffreys-Bullen travel-time table [Jeffreys and Bullen, 1958]. A window of $p_{\text{SKS}} \pm 30$ sec/rad was applied to the normal mode set, resulting in the summation of fewer than 500 modes. It was observed that only SKS, and not SKKS, was being fit in this ray parameter window, illustrated in Fig. 4.2a. The second test consisted of summing modes with ray parameters within a window around that of SKKS. For SKKS, the ray parameter was obtained by calculating

(a)

850804(CTAO.r) distance=104.2 degrees



(b)

850804(CTAO.r) distance=104.2 degrees

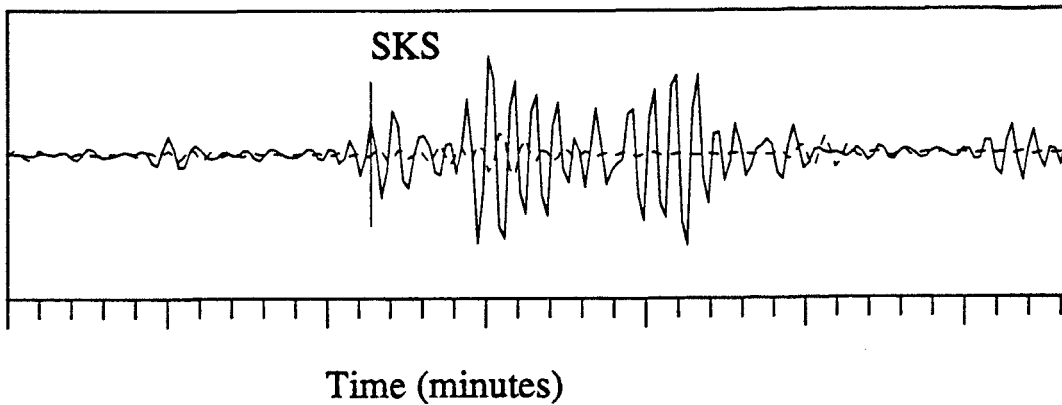


Fig. 4.2 Ray parameter tests for SKS and SKKS waveform fitting by normal modes. (a) For the SKS test, a window of $p_{SKS} \pm 30 \text{ sec/rad}$ was applied to the normal mode set, resulting in the summation of fewer than 500 modes; notice that only SKS, and not SKKS, was fit with modes in this ray parameter window. (b) For the SKKS test, a window of $p_{SKKS} \pm 30 \text{ sec/rad}$ was applied to the normal mode set; the SKKS waveform was fit with this window.

$$p = \left(\frac{\partial T}{\partial \Delta} \right)_{\text{SKKS}} = 10.401 - 0.0322\Delta \quad [4.6]$$

from the polynomial fit to SKKS arrival times

$$T_{\text{SKKS}} = 1539.18 + 7.02(\Delta - 105.0) - 0.016(\Delta - 105.0)^2 \quad [4.7]$$

given in Hales and Roberts [1971] where Δ is epicentral distance. In this case, a window of $p_{\text{SKKS}} \pm 30$ sec/rad was applied to the normal mode set and it was observed that the SKKS waveform was being fit, illustrated in Fig. 4.2b. However, even though these tests were performed with a limited number of modes, the final inversion was performed with all 5000+ modes.

4.4 Results and discussion

4.4.a Lateral variation

Although the procedure has been automated, a number of individual seismograms and their corresponding synthetic seismograms were analyzed before and after the inversions to make sure that the results could be explained by the improvement in corresponding waveform fits. Fig. 4.3 shows the results of the inversion of a Nov. 22, 1984 mid-Atlantic earthquake recorded in Chiang Mai, Thailand (CHTO), 118.2° away. This figure shows about 7 minutes of data (solid line), beginning just before the arrival of SKS, and the synthetic seismograms (dashed line) computed before (top box) and after (bottom box) the inversion. The brackets indicate the limited time window used in the inversion and the phases being fit are SKS and the portion of SKKS which arrives before diffracted S. About 2.3% lower velocity was required to minimize the misfit between the data and PREM synthetics. Fig. 4.4 shows the results of an Oct. 12, 1984 southeast

841122(CHTO.r) distance=118.2 degrees

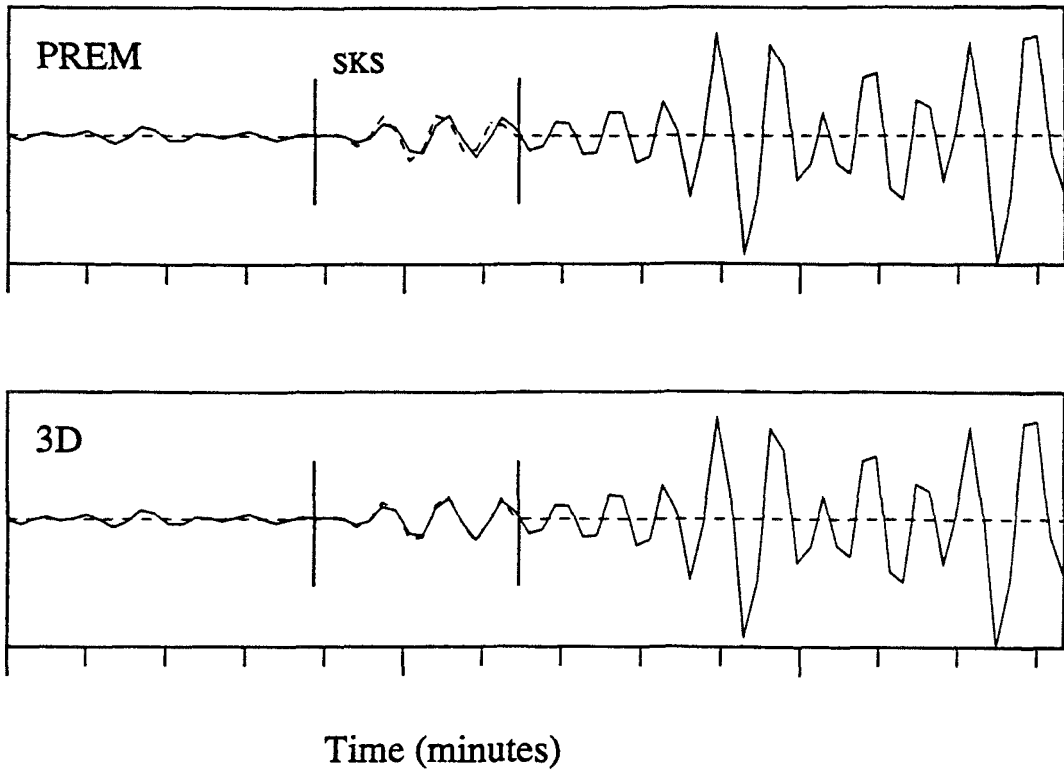


Fig. 4.3 Results before and after the individual inversion of a seismogram recorded at station CHTO (Chiang Mai, Thailand) on November 22, 1984. The vertical line segments indicate the limited time window used in the inversion. About 2.3% lower velocity was required to minimize the misfit between data (solid lines) and PREM synthetics (top dashed line).

841012(RSNY.r) distance=118.2 degrees

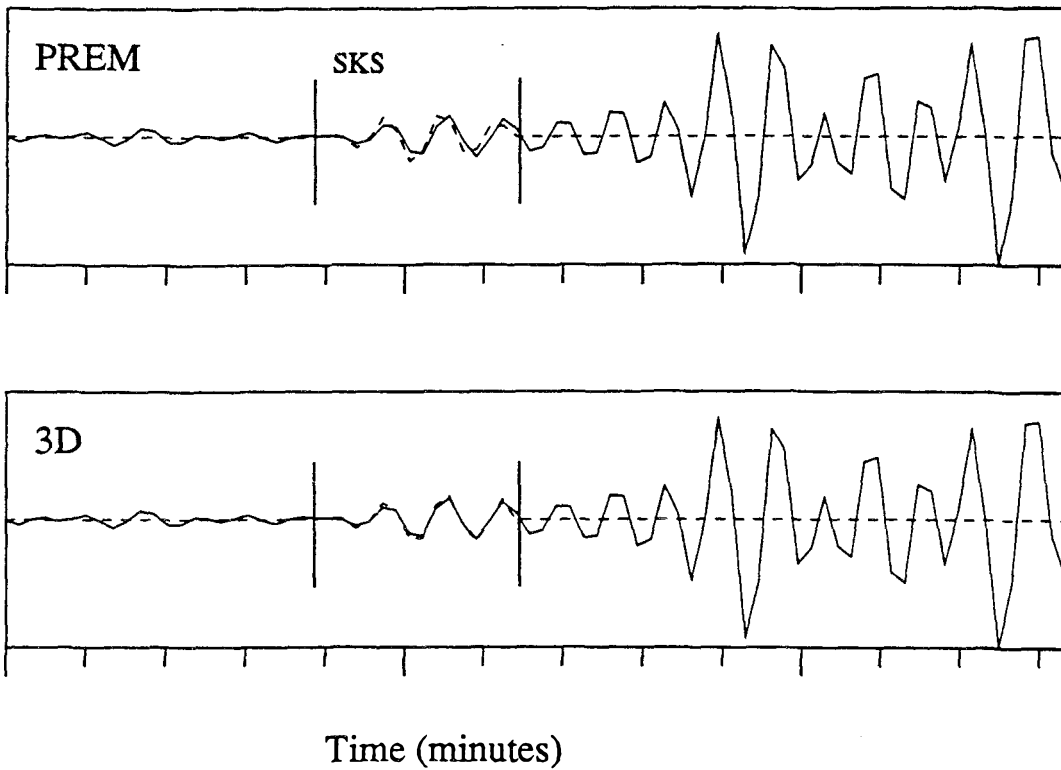


Fig. 4.4 Results before and after individual inversion of a seismogram recorded at station RSNY (Adirondack, New York) on October 12, 1984. The vertical line segments indicate the limited time window used in the inversion. About 2.6% velocity increase was required to minimize the misfit between data (solid lines) and PREM synthetics (top dashed line).

Pacific earthquake recorded at Adirondack, NY (RSNY), 114.7° away. A velocity increase of 2.6% was required to minimize the misfit. These figures illustrate how $\delta\alpha/\alpha$ is reflected in the time shift between data and synthetics. Results from 838 seismograms had produced $\delta\alpha/\alpha \leq 5\%$ for the outermost core using MDLSH to account for mantle heterogeneity. The distribution of data-synthetic SnKS waveform fit improvements (data variance reduction) using the results of this inversion is shown in Fig. 4.5. As this figure shows, the improvement in fit is good for a large number of data-synthetic pairs.

Fig. 4.6 shows the map of P-wave velocity perturbation results with respect to PREM for the 838 seismograms. Open circles represent negative velocity variation with respect to the initial model, closed circles represent positive velocity variation, and the diameters of the circles are scaled down from the maximum absolute threshold value, shown at the top right of the figure. The circles are plotted at the location of the midpoint between the source and the station, i.e., the bounce point of SKKS. Velocity perturbations vary between $\pm 5\%$ and the pattern of variation is not clearly confined to any one latitudinal or longitudinal region, although there appears to be a higher concentration of points of positive variation near the equator. This may result from the lack of more complete raypath coverage. From this map, there is no obvious zone of low P-wave velocity throughout the entire layer, as Lay and Young [1990] have proposed. Rather, there exist regional patterns of high and low velocity variation.

There is a clear pattern of high velocity in the outermost core under the mid-Pacific Ocean, along the western boundary of South America, and under the southwest and central portions of the Indian Ocean. Note that continents are given on the map only to help identify regions of variation that occur in the outermost core. There appears to be a ring of low velocity variation circling the north Pacific Ocean into Asia, and under the mid-Atlantic Ocean, although these regions contain inconsistencies which can not be easily explained. There are also regions of small-scale as well as large-scale velocity patterns.

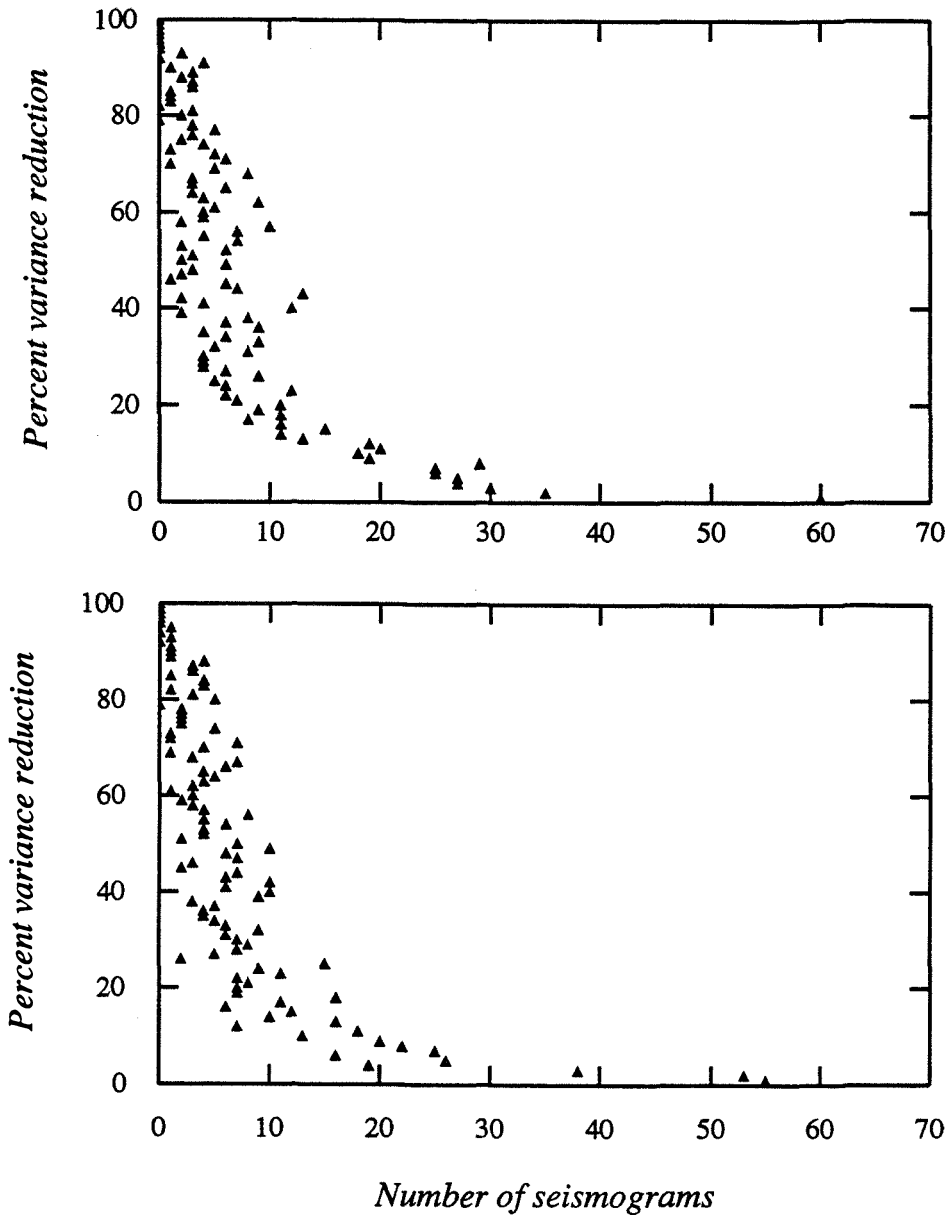


Fig. 4.5 Distribution of number of data-synthetic SnKS waveform fit improvements (percent data variance reductions) within 1% bins, using the results of the first inversion. This figure shows that the improvement in fit is good for a large number of data-synthetic pairs.

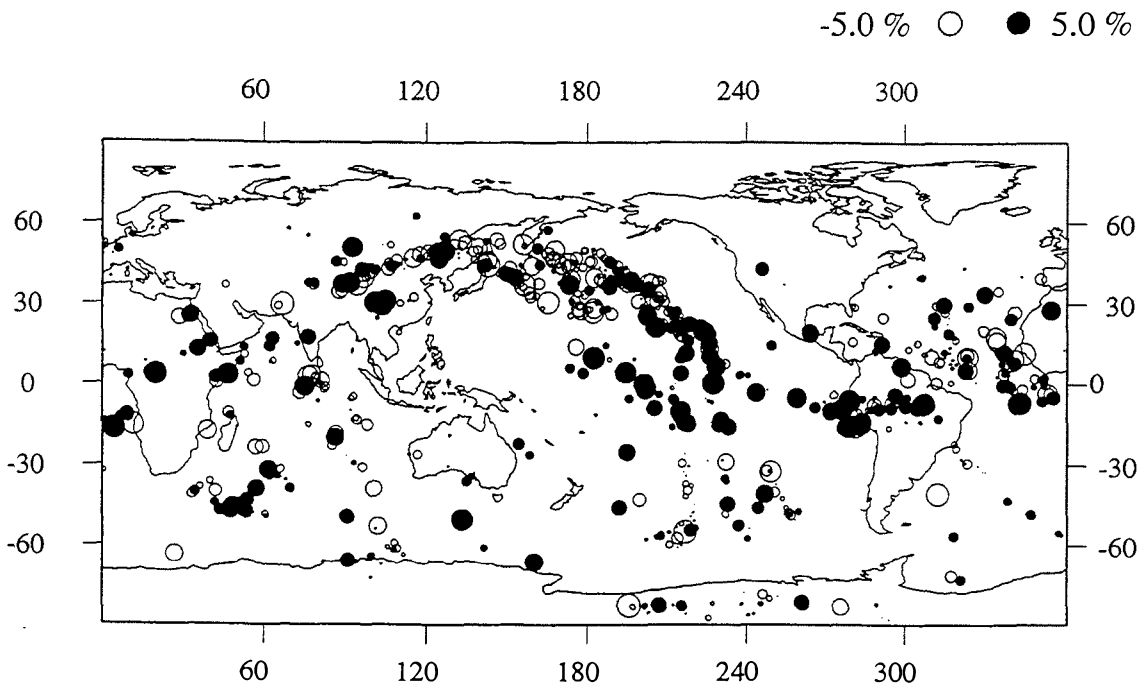


Fig. 4.6 P-wave velocity variation results for 838 seismograms, plotted at the midpoint between source and station, using the mantle heterogeneity model MDLSH [Tanimoto, 1990a]. Closed circles represent positive velocity variation and open circles represent negative velocity variation.

In a test of the sensitivity of these results to different mantle models, the magnitude of lower mantle heterogeneity was changed by doubling the velocity perturbation values of MDLSH in layers 4-11. As Fig. 4.7 shows, the pattern of P-wave velocity perturbations in the outermost core resulting from the modified mantle heterogeneity model is almost unchanged from Fig. 4.6. This suggests that either the outermost core is the source of all velocity variation, or that the results depend on mantle models with smaller wavelength resolution than current global mantle heterogeneity models provide (the more likely of the two possibilities). It is unlikely that incorporation of different mantle models derived by various inversion techniques [e.g., Su *et al.*, 1994; Zhang and Tanimoto, 1991; Woodward and Masters, 1991a; Woodward and Masters, 1991b] will change the solution very much. As Su and Dziewonski [1991] point out, the models referenced above agree quite well, especially for angular order numbers less than 6, i.e., long-wavelength features. However, the cutoff periods of these analyses limits the resolution length scales of mantle structure and it is not yet possible to confidently determine lateral structure for wavelengths less than about 1000 km.

Fig. 4.8 shows the results of SKKS-SKS residuals given in Souriau and Poupinet [1991]. Their dataset, consisting of filtered seismograms from broad-band digital seismograms, has almost no overlap with the data used in this study. However, Fig. 4.8 indicates inconsistencies similar to those observed in this study, for example regions of both positive and negative residuals exist under the Pacific Ocean, in the mid-Atlantic Ocean, and in central Asia. There are areas of consistently positive and negative velocity anomalies but there exists no clear dependence of residuals on latitude. Fig. 4.9a shows P-wave velocity perturbation values for this study (same as the results shown in Fig. 4.6) plotted against latitude. Fig. 4.9b shows the same values plotted against longitude. These figures show more clearly that there is a fairly random scatter of positive and negative velocity anomalies for all latitudes and longitudes. Plotting perturbation values from Fig. 4.7 against latitude and longitude produces similar patterns (Fig. 4.10).

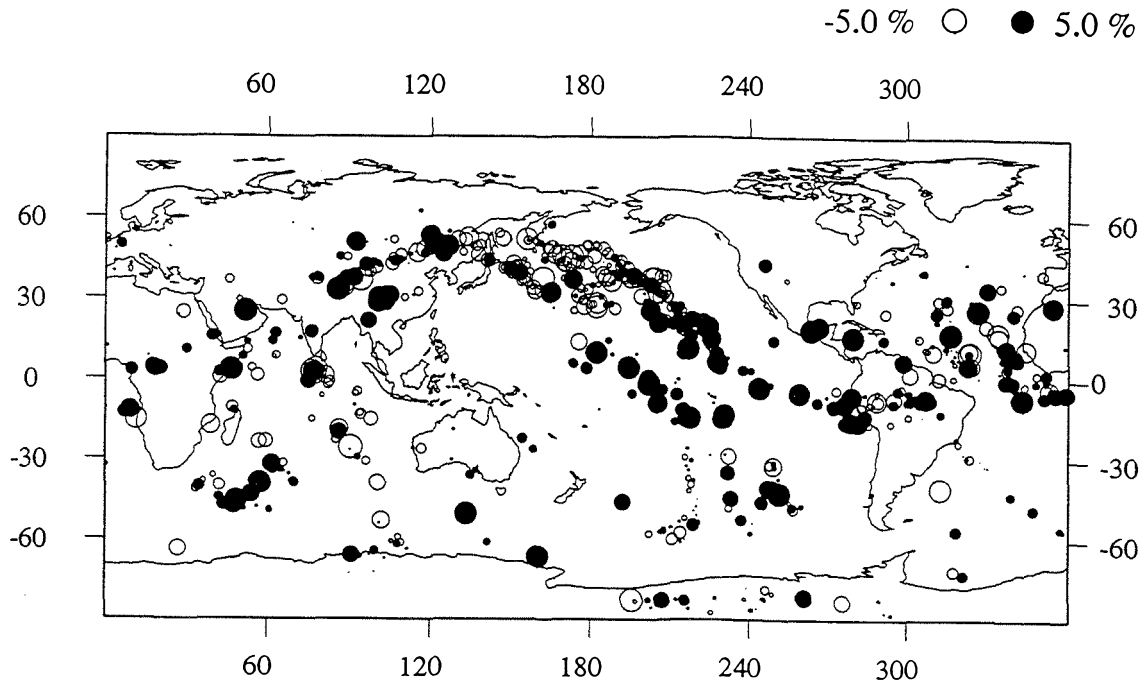


Fig. 4.7 P-wave velocity variation results for 812 seismograms, plotted at the midpoint between source and station, using the modified (described in text) mantle heterogeneity model of Tanimoto [1990a]. Closed circles represent positive velocity variation and open circles represent negative velocity variation.

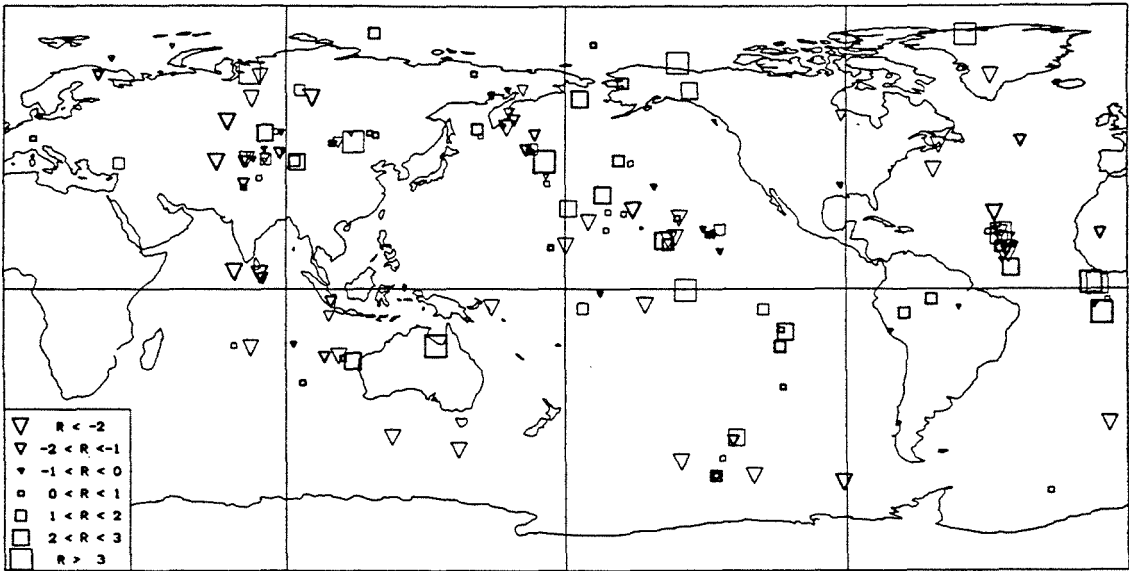


Fig. 4.8 Map of SKKS-SKS residuals from Souriau and Poupinet [1991] (their Fig. 9). Residuals are given in units of seconds.

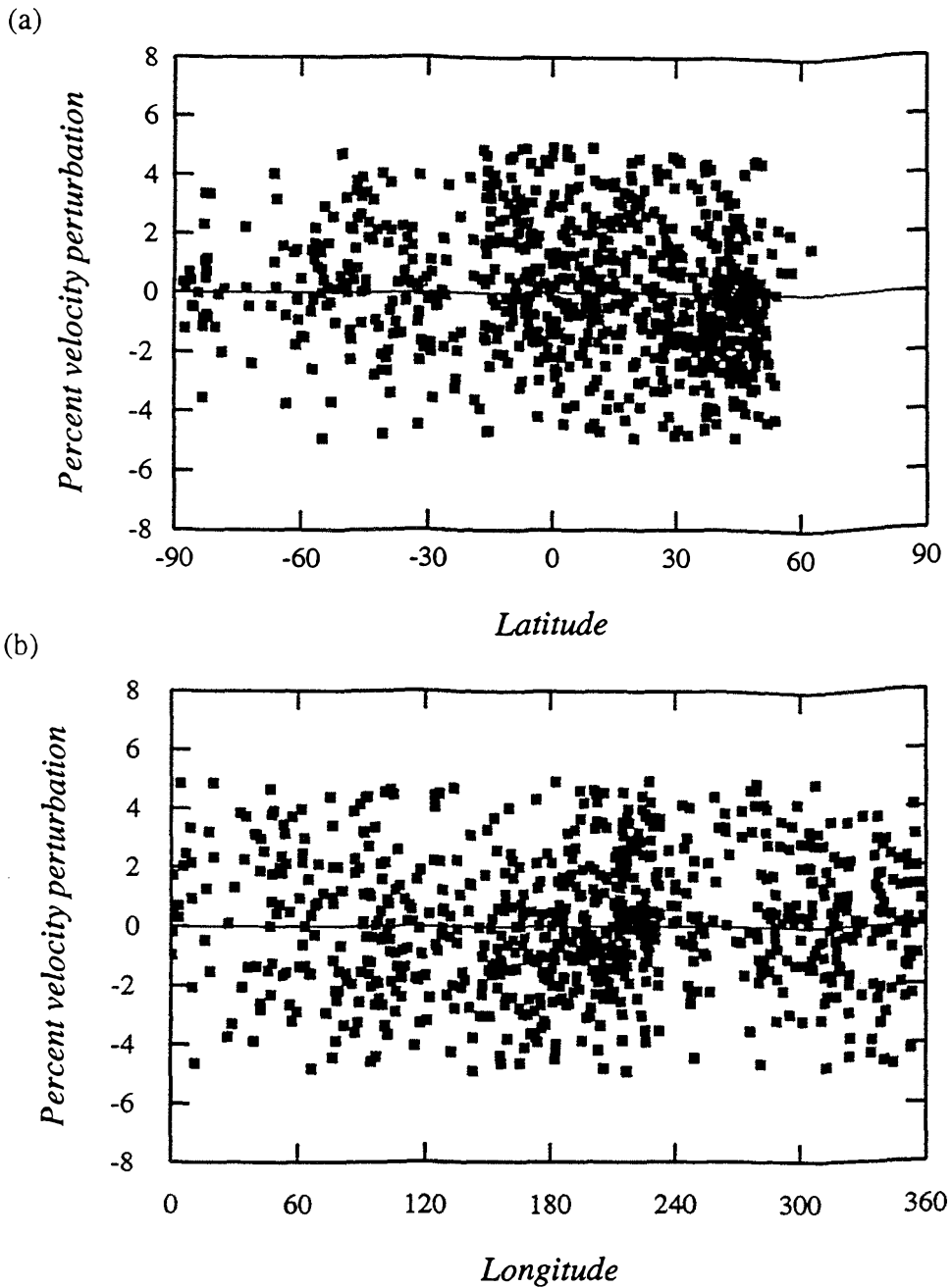


Fig. 4.9 P-wave velocity variation associated with Fig. 4.6 plotted against (a) latitude and (b) longitude. The scarcity of data for high latitudes is a result of using only Southern Hemisphere earthquakes.

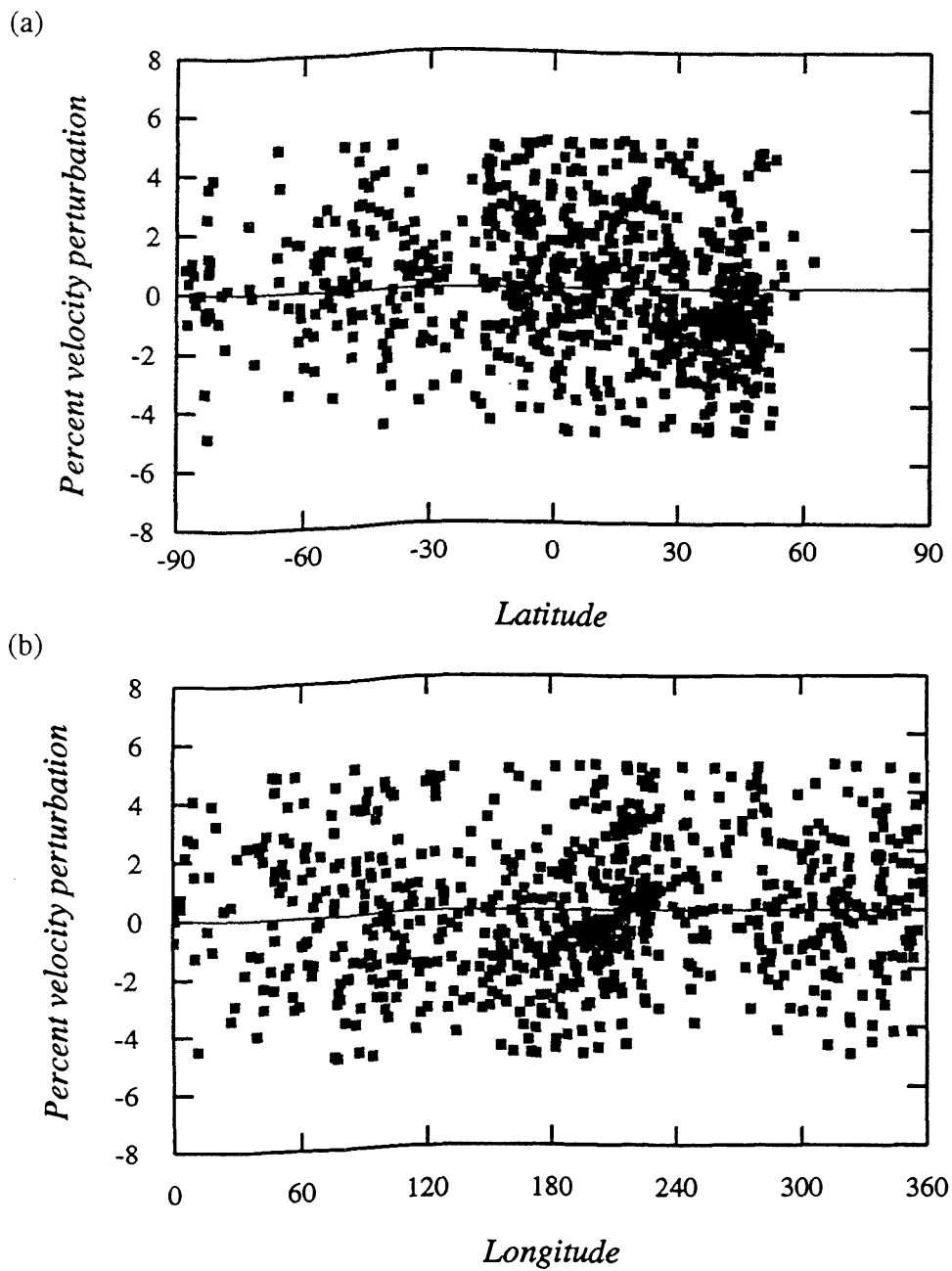


Fig. 4.10 P-wave velocity variation associated with Fig. 4.7 plotted against (a) latitude and (b) longitude. The scarcity of data for high latitudes is a result of using only Southern Hemisphere earthquakes.

The question then is: are the observed velocity perturbations (or SKKS-SKS residuals) due only to outermost core properties or is there contamination from the lower mantle or CMB topography, and how can it be shown that this might be the case? One indication that these results may be influenced by lower mantle heterogeneity is the unexpectedly high and low values of velocity perturbations. Based on physical arguments for the fluid nature of the outermost core, velocity variation is expected to be much less than $\pm 5\%$. The more obvious evidence for contamination, however, are regions of inconsistencies in velocity variation. Although there may be areas where velocity variation changes rapidly from negative to positive and vice versa, the changes are probably not so abrupt on such small wavelengths for a relatively homogeneous outermost core, as observed in our results. The locations of adjacent positive and negative velocity variations are not a result of crisscrossing raypaths; in most locations, the raypaths are roughly parallel.

If CMB topography is invoked to explain residuals in SKKS-SKS travel times, ~ 10 km of raised or depressed topography is needed to produce a change in SKKS-SKS of 2 sec, corresponding to a velocity variation of $< 1\%$. It is unlikely that CMB topography amplitude is much larger than that [Gwinn *et al.*, 1986]; thus, CMB topography is not sufficient to explain the larger variations in P-wave velocity. The following numerical raypath modeling results for SKS and SKKS indicate that contamination by lower mantle heterogeneity is a reasonable explanation for the pattern inconsistencies in the one-layer inversion velocity maps.

4.4.b Raypath information

Using PREM (~ 200 homogeneous layers) as an Earth model for P- and S-wave velocities, the raypaths of SKS and SKKS were analyzed for two sample surface source-receiver distances. Regardless of takeoff angle from the earthquake source, SKS and SKKS have the most similar raypaths in the top few layers of the Earth model. The

deeper the rays travel, the more they have diverged from the source and become separated from each other. Thus, when SKS and SKKS raypaths are traveling more than a wavelength apart, they no longer sample the same region of the Earth, and their seismogram signatures reflect properties of laterally different regions in the Earth. For this frequency range, a wavelength offset translates into lateral offsets of greater than about 200 km. If raypaths are separated in the lower mantle by greater than the wavelength corresponding to the shortest observed period, it becomes questionable whether waveform modeling or travel-time residual analysis provides information solely about the outermost core. SnKS waveform fitting and SKKS-SKS travel-time residuals may reflect significant lower mantle heterogeneity not removed by long-wavelength mantle structure models in addition to outermost core heterogeneity. Another reason to consider lower mantle effects more carefully is that the results of Tanimoto [1990a] indicate that heterogeneity power has a secondary peak at the bottom of the mantle (D'').

Results are presented here which may help constrain the significance of lower mantle heterogeneity in SKS vs. SKKS raypaths for two cases. For an epicentral distance of about 112° and source depth of 33 km, SKS and SKKS raypaths are about 850 km apart upon entering the core, as shown in Fig. 4.11. Also for this case, raypaths become separated more than about 200 km at Earth radius of about 5200 km, or 1700 km above the CMB, indicated in Fig. 4.11 by the dashed circle. In the second case, for an epicentral distance of about 129° , the raypaths are about 700 km apart when they enter the core, shown in Fig. 4.12. For this case, the raypaths become separated more than 200 km at Earth radius equal to about 5100 km, or 1600 km above the CMB, also shown in Fig. 4.12 by the dashed circle. SKS and SKKS are clearly being influenced by totally different mantle structure as much as 1500 km above the CMB, the wavelength of which is smaller than the resolution length scales afforded by long-period normal mode mantle structure of Tanimoto [1990a] and others.

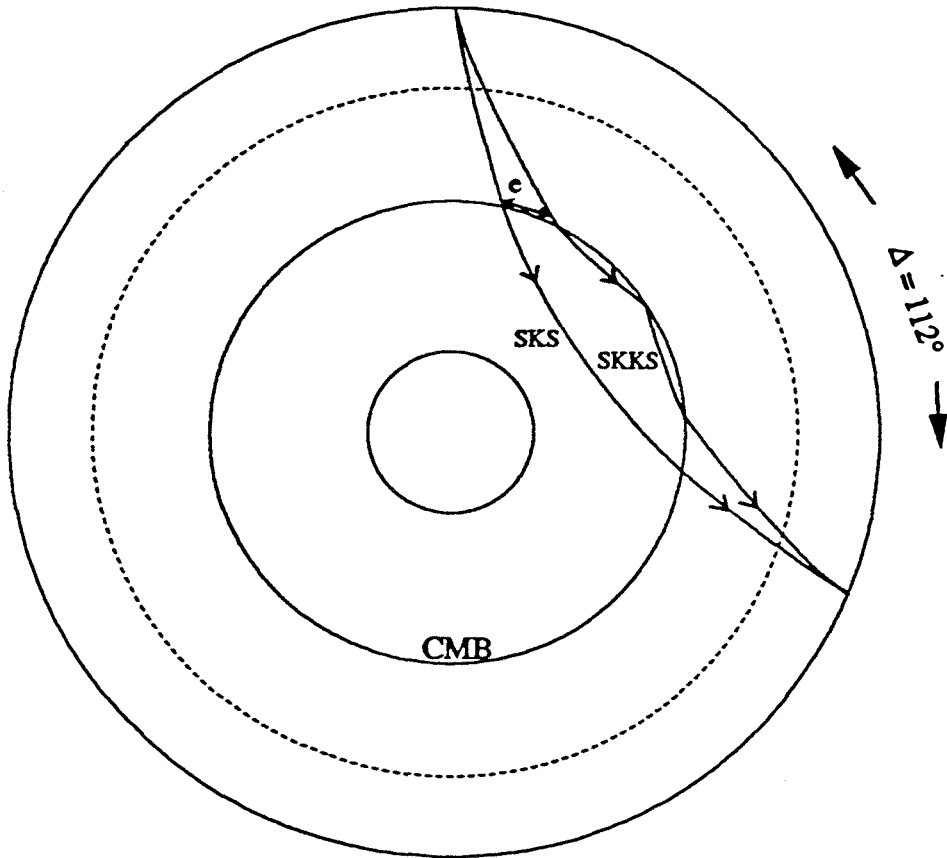


Fig. 4.11 SKS and SKKS raypaths for source-receiver distance of 112° . The two raypaths are separated by a distance of about 850 km upon entering the core, denoted by the letter e . They become separated by more than one wavelength (about 200 km for this frequency range) at a radius of about 5200 km, denoted by the dashed circle.

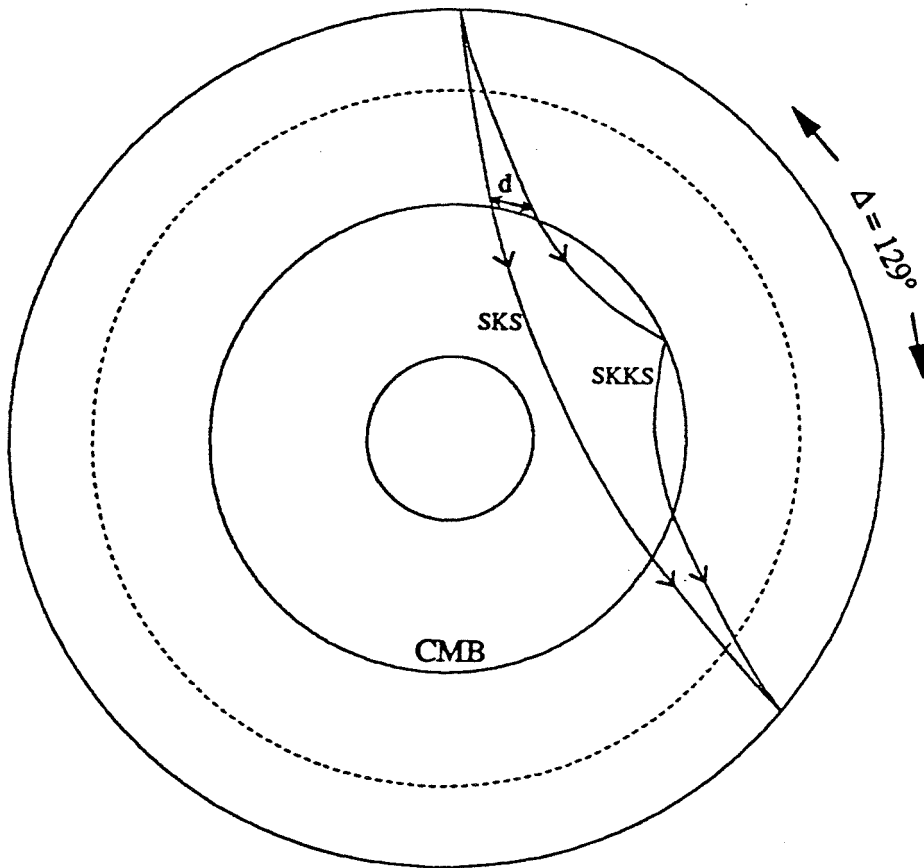


Fig. 4.12 SKS and SKKS raypaths for source-receiver distance of 129° . The two raypaths are separated by a distance of about 700 km upon entering the core, denoted by the letter d. They become separated by more than one wavelength (about 200 km for this frequency range) at a radius of about 5100 km, denoted by the dashed circle.

4.5 Conclusions

Inversion of portions of individual, radial-component seismograms has yielded a global plot of hypothetical P-wave velocity structure in the outer 200 km of the core. Analysis of numerous data and synthetic seismogram pairs before and after the inversion indicates that outermost core phases SKS and SKKS are being fit, but it is not clear how much lower mantle heterogeneity, in addition to outermost core structure, is affecting their waveforms. An attempt was made to remove the effects of mantle heterogeneity by incorporating the mantle velocity model MDLSH of Tanimoto [1990a] and a modified version of MDLSH. Figures of P-wave velocity results, plotted at the midpoint between source and receiver show large-scale patterns of positive and negative lateral velocity variations; there are also regions of inconsistencies not simply explained by CMB topography or crisscrossing raypaths.

From these plots, the following conclusions can be made. There is no obvious dependence of outermost core anomalies on latitude or longitude, and the pattern of anomalies suggests large and small scale structure in the outermost core layer. A ray parameter test indicates that SKS and SKKS phases (and, therefore, information about the outermost core) are being individually modeled by normal modes. The results of the inversions produce much improved data-synthetic SnKS waveform fits. However, there still remains uncertainty about the degree of mantle heterogeneity contamination in the solution. The large amplitudes of P-wave velocity perturbations are best explained by the mapping of some lower mantle structure into the outermost core. This explanation is supported by raypath modeling results which indicate that SKS and SKKS are sampling laterally different structure relative to normal mode wavelengths, starting well above the CMB. Thus, their travel-time residuals are not reliable for obtaining outermost core

velocity alone. Incorporation of a modified version of MDLSH does not significantly change these solutions, suggesting that the resolution length scales of global mantle models are too large to remove important smaller wavelength (< 1000 km) mantle heterogeneity effects. These results suggest that simultaneous waveform inversion for P- and S-wave velocities is a more reliable way of constructing a model of outermost core structure, the subject of Chapter 5.

Chapter 5: Three-dimensional Inversions for Mantle and Outermost Core Velocities

The results of three-dimensional inversions for global velocity structure in the mantle and outermost core are presented in this chapter. This approach is distinct from other global models of deep Earth heterogeneity because it accounts for possible lateral heterogeneity in the outermost core. Up to now, global models of lateral velocity structure focussed on the mantle alone: for example, the velocity model of Su *et al.* [1994] contains lateral variations in S-wave velocity throughout the mantle using radial Chebyshev polynomials for radial smoothing. Woodward and Masters [1991c], and Tanimoto [1990a] solve for S-wave velocity variations in 11 mantle layers from the surface of the Earth to the CMB. Velocity anomalies of the models presented in this chapter are expressed as spherical harmonic expansions up to degree and order 12 using the same shell assignments as in Tanimoto [1990a]. Maximum angular order 12 may be too high considering the raypath coverage provided by the data set and increasing evidence for large-scale heterogeneity, especially in the lower mantle [Tanimoto, 1990ab; Su and Dziewonski, 1991]. However, it was important to try to avoid the effects that aliasing may cause for cutoff angular orders that are too low.

Most models of mantle heterogeneity are derived from surface wave and normal mode analysis [e.g., Backus, 1964; Toksöz and Anderson, 1966; Backus and Gilbert, 1967,1968,1970; Gilbert and Dziewonski, 1975; Nolet, 1975; Gilbert, 1976; Cara, 1976; Jordan, 1978; Masters *et al.*, 1982; Nakanishi and Anderson, 1983,1984; Woodhouse and Dziewonski, 1984; Nataf *et al.*, 1984,1986; Montagner, 1985; Romanowicz and Roullet, 1986; Giardini *et al.*, 1987; Romanowicz, 1987; Romanowicz and Snieder, 1988;

Tanimoto, 1987,1988; Li *et al.*, 1991ab]. Others invert travel-time observations for seismic velocity perturbations [e.g., Woodward and Masters, 1991abc; Su *et al.*, 1994; Inoue *et al.*, 1990; Clayton and Comer, 1983; Masters *et al.*, 1992]. The drawbacks with relying upon travel-time observations such as ScS-S and SS-S are that resulting models are biased by coverage provided by those raypaths alone and contain errors arising from the determination of the phase arrival times. The models presented here are determined by waveform inversion and do not rely on absolute phase travel times. By including several thousand seismograms within a large distance range (10° - 140°), all body-wave phases are included in the inversion; thus, information about the entire mantle is contained in the seismograms. Normal modes are summed to construct synthetic waveforms. To summarize the approach, the radial displacement is given by Eq. [2.13] and perturbations to displacement are given by Eq. [2.30].

5.1 Data set.

The analysis and selection of the data set are described in detail in Chapter 3 and will be summarized for convenience here. The original Global Digital Seismograph Network (GDSN) long-period, radial-component seismograms came from event tapes which were generated by extracting day tape data recorded between 1980 and 1987 from the SRO, ASRO, RSTN, and DWWSSN networks; the seismograms were filtered for periods between 33 and 100 seconds and limited by the cross-correlation coefficient of the synthetic seismograms and data. Each waveform record included information about the complex response function of the instrument which recorded it (with peak instrument response amplitudes occurring at periods from 25-28 sec) and header information including year, time (to milliseconds), epicentral distance, azimuth, back azimuth (measured clockwise from north), number of data points, and sampling interval of the seismogram. Source parameters including location were obtained from Harvard centroid

moment tensor solutions [e.g., Dziewonski and Woodhouse, 1983a]. The instrument response was convolved with the synthetic seismogram in order to perform a direct comparison of synthetic seismogram with observed waveform at each station. After limiting the distance range to $10^\circ \leq \Delta \leq 140^\circ$, the data set included 6375 seismograms (i.e., source-receiver pairs) from 916 earthquakes which had occurred globally. The seismograms were simultaneously inverted for S-wave velocity perturbations in the mantle and P-wave velocity perturbations in the outermost core. Fig. 3.7 illustrates the outermost core raypath coverage provided by this data set.

Each seismogram was windowed for the time series segment containing only body-wave phases, beginning 30 sec before the direct or diffracted P-wave arrival and ending 30 sec (for $\Delta \leq 60^\circ$), 120 sec (for $60^\circ < \Delta < 100^\circ$), or 360 sec (for $\Delta \geq 100^\circ$) before the fundamental Rayleigh wave arrival. The P-wave and diffracted P arrivals were obtained from the IASP91 Earth model travel-time tables [Kennett and Engdahl, 1991] and the Rayleigh wave arrival was estimated by calculating the travel time of the surface waves for a group velocity of 3.84 km/sec.

5.2 Least-squares method

A solution \mathbf{m} ($\mathbf{m} = (\alpha, \beta)$) is sought such that the following is minimized:

$$\Phi = [\mathbf{D} - \mathbf{f}(\mathbf{m})]^2 \quad [5.1]$$

where \mathbf{D} is the data vector and \mathbf{m} is the model parameter vector. In this case, the following is minimized

$$\Phi = \sum_{i=1}^N \sum_t^{T_i} \left[u_t^d - u_t^s(\mathbf{m}) \right]_i^2 \quad [5.2]$$

where u_t^d is the t^{th} digitized time point of the i^{th} observed seismogram; u_t^s is the t^{th} time point of the i^{th} synthetic seismogram which is a function of the model parameters. The squared difference is summed over T_i time points in the data and synthetic seismogram (different for each seismogram), and over N total seismograms.

Using PREM [Dziewonski and Anderson, 1981] as the initial model, \mathbf{m}_0 , the relationship between data and the "nearest to perfect" model is linearized as

$$\mathbf{u}^s(\mathbf{m}, t) \approx \mathbf{u}^s(\mathbf{m}_0, t) + \mathbf{A}(t)\mathbf{x} \quad [5.3]$$

where

$$A_{tj} = \left(\frac{\partial u_t^s}{\partial x_j} \right), \quad [5.4]$$

and

$$\mathbf{x} = \mathbf{m} - \mathbf{m}_0 = \left(\frac{\delta\alpha}{\alpha}(r), \frac{\delta\beta}{\beta}(r) \right). \quad [5.5]$$

Since the difference between the data and the synthetic seismograms using PREM can be calculated, let

$$\mathbf{b} = \mathbf{u}^d - \mathbf{u}^s(\mathbf{m}_0) \quad [5.6]$$

i.e.,

$$b_t = \delta u_t = u_t^d - u_t^s. \quad [5.7]$$

Then,

$$\Phi = \sum_{i=1}^N \sum_{t=1}^{T_i} \sum_j^J [b_t - A_{tj}x_j]_i^2 \quad [5.8]$$

where J is the total number of parameters. Note that t depends on i . Therefore, for this problem,

$$\mathbf{Ax} = \mathbf{b}. \quad [5.9]$$

In order to solve for \mathbf{x} , form

$$\mathbf{E} = (\mathbf{b} - \mathbf{Ax})^2 = (\mathbf{b} - \mathbf{Ax})^T \mathbf{W}(\mathbf{b} - \mathbf{Ax}) \quad [5.10]$$

introducing a data weighting matrix, \mathbf{W} , and set $\partial E / \partial x_j = 0$. Thus, for the simultaneous body-wave inversion, the actual matrix equation used in the numerical procedures is

$$\mathbf{A}^T \mathbf{W} \mathbf{A} \mathbf{x} = \mathbf{A}^T \mathbf{W} \mathbf{b} \quad [5.11]$$

where the elements of \mathbf{A} are from the right hand side of Eq. [2.30]. The Rayleigh wave phase perturbation results have been included by adding the right-hand side of Eq. [2.34] to the elements of \mathbf{A} . \mathbf{W} is the data weighting matrix which will be discussed in the next section. Recall that the Rayleigh wave phase perturbation results contributed non-zero values only to the top four layers of structure.

5.2.a Data weighting

Care must be exercised when using seismograms from earthquakes of various sizes. Without data weighting, seismograms with large amplitudes would dominate the least-squares solutions since the amplitudes vary by orders of magnitude. A diagonal data weighting matrix, \mathbf{W} , is introduced which has been designed to counter the effects of differently-sized earthquakes. Two data weighting schemes have been used in the inversions and the diagonal elements of \mathbf{W} are given by the following definitions:

$$I^1 = \sum_{i=1}^N \frac{1}{(\sigma_b^2)_i} \sum_t^{T_i} \left[u_t^d - u_t^s(\mathbf{m}) \right]_i^2 \quad [5.12]$$

where σ_b^2 is the squared misfit between the i^{th} observed and synthetic seismogram and

$$I^2 = \sum_{i=1}^N \frac{1}{(M_0^2)_i} \sum_t^{T_i} \left[u_t^d - u_t^s(\mathbf{m}) \right]_i^2 \quad [5.13]$$

where M_0 is the seismic moment of the i^{th} earthquake. Although seismograms produced by large earthquakes are damped more heavily, these schemes do not take into account differences in amplitudes of phases contained in the same seismogram.

5.2.b Damping schemes

This is a nonlinear problem because the displacement perturbations are not linearly related to Earth structure and because of the presence of noise from unquantifiable sources. It can be solved by a succession of local linear iterations since it is assumed that the initial choice of Earth model (PREM) is close to the true Earth. Because noise is present in the signal, solutions are nonunique. However, the rate of convergence of the solutions can be influenced to different degrees by using a damping parameter scheme determined subjectively. Upon examination of previous inversions using similar methods, the damping scheme chosen was one in which the damping parameters form a matrix, \mathbf{L} , whose diagonal elements are equal to the squared inverse of the angular order, ℓ , of the corresponding expansion coefficient. The off-diagonal elements are equal to zero and \mathbf{L} is multiplied by a constant, λ^2 . This had the effect of damping higher ℓ terms more heavily and producing spectral amplitudes which followed ℓ^{-2} curves. The final form of the solution vector is then

$$\mathbf{x} = (\mathbf{A}^T \mathbf{W} \mathbf{A} + \lambda^2 \mathbf{L})^{-1} (\mathbf{A}^T \mathbf{W} \mathbf{b}). \quad [5.14]$$

This choice of damping scheme has been used before [Su *et al.*, 1994] and is supported by evidence for large-scale heterogeneity, especially in the lower mantle [Tanimoto, 1990ab; Su and Dziewonski, 1991] and physical arguments presented by Gubbins and Bloxham [1985].

The solution model vector for the $(m+1)^{\text{th}}$ iteration is given by

$$\mathbf{x}_{m+1} = \mathbf{x}_m + (\mathbf{A}^T \mathbf{W} \mathbf{A} + \lambda^2 \mathbf{L})^{-1} (\mathbf{A}^T \mathbf{W} \mathbf{b}_m) \quad [5.15]$$

where \mathbf{b}_m is the displacement residual after the contributions from PREM and the previous iteration model (\mathbf{x}_m) have been removed. The choice of cutoff iteration number was based on the value of the data variance after the iteration, σ_a^2 , given by Eq. [5.17]. As Fig. 5.1 illustrates for a sample inversion involving 12 layers and weighting scheme I¹, the variance decreases most after the first iteration. It falls off more gradually for succeeding iterations, approaching a constant. The inversion was stopped when the variance reduction was less than 1% the value of the previous iteration. The elements of the derivative matrix remain constant throughout the inversion.

5.3 Numerical solutions

5.3.a LINPACK routines

LINPACK [Dongarra *et al.*, 1989] is a mathematical software package of Fortran library subroutines to analyze and solve linear systems of simultaneous algebraic equations and related problems. It was designed to be efficient, machine independent, and fully portable (thus, the ability to run all subroutines on any machine at the Seismological Lab). The subroutines used to obtain the solutions to Eq. [5.11] were intended to deal with square coefficient matrices which are stored in computer memory as the solution is obtained. The solution process always involves two steps: first, the coefficient matrix is processed and various quantities associated with it are computed; second, the data array is processed resulting in the solution array.

The method used to factor the symmetric matrix is called 'diagonal pivoting factorization' and corresponds to block symmetric Gaussian elimination. The algorithm performs the elimination by beginning with the last column and moving to the first, and choosing multipliers such that zeroes are introduced into the last components of those

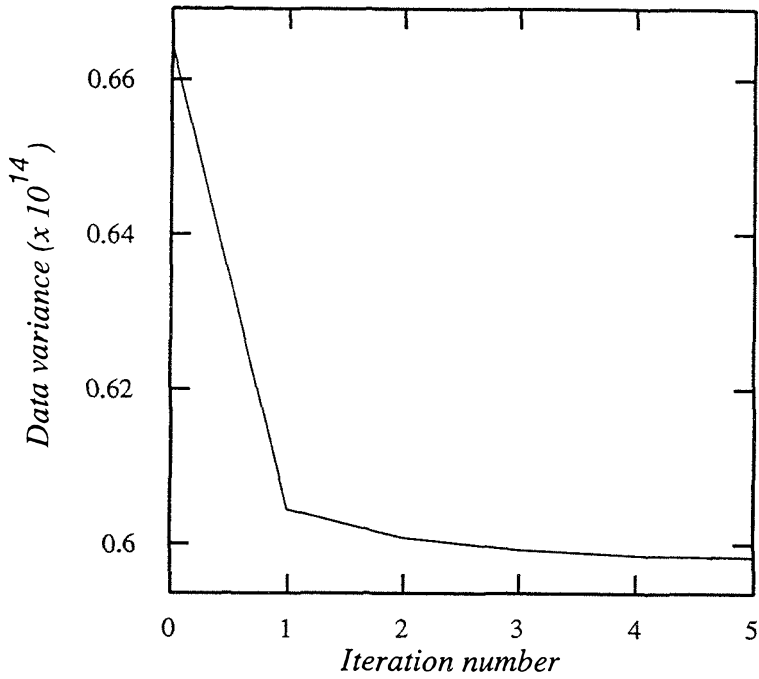


Fig. 5.1 Data variance as a function of iteration number. Note that the variance decreases the most after the first iteration and falls off more gradually for successive iterations. This curve was used to determine the cutoff iteration.

columns, corresponding to the off-diagonal elements. The permutation matrices (obtained by interchanging at most 2 rows or columns) are chosen so that the resulting pivots provide numerical stability. Both the multipliers and pivots are then used to solve the systems of linear equations.

LINPACK design makes use of TAMPR, a software development system which manipulates and formats Fortran programs to clarify their structure [Boyle and Dritz, 1974] and BLAS (Basic Linear Algebra Subprograms) [Lawson *et al.*, 1979] subroutines which contribute to speed, modularity, and clarity. The subroutines are conveniently labeled so that versions may be applied according to the form of the matrix (e.g., positive definite, symmetric indefinite packed), single or double precision math, and type of arithmetic (complex or real). The codes involve sequential access memory in which matrices are read and stored down columns instead of across rows, resulting in significant performance improvement.

Unlike singular value decomposition which checks for the presence of very small numbers as a measure of singularity, LINPACK's test for singularity is made by estimating the condition of a matrix by comparing the Gaussian elimination pivots to exact zero. The condition number associated with a matrix gives a measure of how near the matrix is to singularity and, thus, how much an error matrix will cause the solution to change; i.e., the condition number indicates how big a coefficient matrix is compared to the errors. This ratio is obtained by comparing the largest and smallest diagonal elements of the coefficient matrix, $(\mathbf{A}^T \mathbf{W} \mathbf{A} + \lambda^2 \mathbf{L})$. If the ratio is large, then $(\mathbf{A}^T \mathbf{W} \mathbf{A} + \lambda^2 \mathbf{L})$ is ill-conditioned due to such error sources as machine number truncation and round-off. The following general rule is applied: if the solution of a linear system of equations is computed in t -digit (decimal) arithmetic for which the condition number is 10^k , the solution will have no more than $t-k$ accurate figures [Dongarra *et al.*, 1989]. This is contingent upon scaling the elements of $(\mathbf{A}^T \mathbf{W} \mathbf{A} + \lambda^2 \mathbf{L})$ properly; the estimate of the absolute size of error in $(\mathbf{A}^T \mathbf{W} \mathbf{A} + \lambda^2 \mathbf{L})$ must be made roughly equal by scaling. Inspection of the condition

numbers of the solutions to Eq [5.11] using both weighting schemes indicates that they are $\sim 10^3$. From the general rule, this means that the solutions will have 11 accurate figures in double precision arithmetic on the 64-bit computers.

The subroutines used to obtain the solutions to the inversions are those designed to operate on full, real, symmetric (i.e., Hermitian) matrices stored in singly subscripted arrays (i.e., "packed form"). Furthermore, the matrices are indefinite (i.e., positive and negative eigenvalues) and operations are performed in double precision. Storing the symmetric matrices $(A^T W A + \lambda^2 L)$ in a singly subscripted array with $n(n+1)/2$ elements (where n = the number of rows) will save almost half the storage space required for a full symmetric matrix. The numerical results are identical and the computing time is about half that of full storage. Specifically, the subroutines compute the triangular factorization of matrices, estimate the matrix condition number, and obtain the solution of simultaneous linear equations (with varying damping parameters and schemes), and the inverse (for the depth resolution kernels). Their names and descriptions are given as follows:

dppco: performs double precision, symmetric, indefinite factorization of matrix **A** in packed form and estimates its condition number,

dppsl: uses the factorization of **A** to solve the symmetric, indefinite systems of linear equations in double precision,

dppdi: uses the factorization of **A** to compute its inverse.

Note that *dppsl* and *dppdi* are not called if the condition number is too large (which never occurred here). The inverse is actually calculated in terms of the solutions of linear equations, and not A^{-1} explicitly; this reformulation usually takes less time and produces more accurate results.

For an $n \times n$ matrix, the diagonal pivoting factorization requires at most $\frac{1}{6}n^3 + \frac{3}{4}n^2 + \frac{7}{3}n$ multiplications and divisions, $\frac{1}{6}n^3 + \frac{1}{4}n^2 + \frac{7}{6}n$ additions, and $\frac{1}{2}n^2 + \frac{3}{2}n$ storage. Obtaining the solution requires on the order of n^2 multiplications and n^2 additions. This is less time-intensive than SVD which can lead to misleading results if

the problem is not scaled right before the smallest eigenvalues are examined. Least-squares solutions will be stabilized by suppressing singular values below the error level [Dongarra *et al.*, 1989].

5.3.b Vectorization

The advantage with normal mode theory is that by using modes with frequencies within a specific bandwidth, all existing phases for a given source-receiver distance and source depth within the same frequency band will be modeled. The drawback is that the computation of the complete waveform requires a large amount of computer memory and time. The synthetic seismograms are composed of several hundred time points (the number depends on the source-receiver distance) and each time point consists of the summation of 5262 normal mode eigenfunctions. Hence, the calculations are time-consuming. Determining the solutions of unknown parameters by this approach involves mathematical operations on arrays, the largest of which contains over two million elements. Thus, the time it takes to obtain details of global Earth structure from inversions such as this is greatly reduced by the speed provided by a Cray Y-MP C90.

The computer code which performed the inversions contained numerous repetitive operations independently performed on each time point in every seismogram, making it conducive to vectorization. The code was modified so that various vectorization tools were incorporated to make it run more efficiently, ultimately reducing the total run time. For example, nested loops were structured so that innermost vectorizable loops were the longest. Also, subroutines were expanded within the main program when their vectorization proved to be more efficient than making individual subroutine calls. Various Cray Y-MP utilities (e.g., 'flowtrace', 'flowview', and 'prof') were used to identify the most CPU time-intensive subroutines and portions of the code in order to focus efforts on optimizing them. In addition, the results of the dependency analysis pre-processor phase of the compiler were invoked to automatically and manually insert autotasking directives

to identify candidate code sections for optimization. The hardware performance monitor ('hpm') provided a measure of machine performance while the code was tested with one sample seismogram. The most time-consuming portion of the code involved the calculation of the elements of $\mathbf{A}^T \mathbf{W} \mathbf{A}$ for each time point in the 6375 seismograms. A typical run which calculated the $\mathbf{A}^T \mathbf{W} \mathbf{b}$ and $\mathbf{A}^T \mathbf{W} \mathbf{A}$ arrays took about 9 hours on the Cray Y-MP C90 in batch mode, and about a week on a Sun SPARCstation 10. It was possible to take advantage of half priority queues on the Cray in which users are charged half the CPU time they use, but wallclock time increased from hours to days as a result of the decreased priority and heavy queue use.

5.4 Variance

The degree of misfit before and after the inversions was given by two measures: data variance and v-space variance. In each case, improvement of fit accounting for inversion results was measured by variance reduction; i.e., for an individual seismogram, the data variances (data-model misfits) before, σ_b^2 , and after, σ_a^2 , were calculated as

$$\sigma_b^2 = \mathbf{b}^T \mathbf{b} = (\mathbf{u}^d - \mathbf{u}^s)^T (\mathbf{u}^d - \mathbf{u}^s) \quad [5.16]$$

and

$$\sigma_a^2 = (\mathbf{b} - \mathbf{A} \mathbf{x})^T (\mathbf{b} - \mathbf{A} \mathbf{x}) \quad [5.17]$$

where \mathbf{u}^d is the observed seismogram and \mathbf{u}^s is the synthetic seismogram based on PREM. σ_a^2 is also referred to as 'data variance'. The percent variance reduction was obtained by computing

$$\frac{\sigma_b^2 - \sigma_a^2}{\sigma_b^2} \times 100 \quad [5.18]$$

and comparing with successive iterations. This measure was used as one way to determine the optimum damping parameter.

The v-space variances before, $\sigma_b'^2$, and after, $\sigma_a'^2$, were calculated as

$$\sigma_b'^2 = (\mathbf{A}^T \mathbf{W} \mathbf{b})^T (\mathbf{A}^T \mathbf{W} \mathbf{b}) = (\mathbf{A}^T \mathbf{W} (\mathbf{u}^d - \mathbf{u}^s))^T (\mathbf{A}^T \mathbf{W} (\mathbf{u}^d - \mathbf{u}^s)) \quad [5.19]$$

and

$$\sigma_a'^2 = (\mathbf{A}^T \mathbf{W} \mathbf{b} - (\mathbf{A}^T \mathbf{W} \mathbf{A} + \lambda^2 \mathbf{L}) \mathbf{x})^T (\mathbf{A}^T \mathbf{W} \mathbf{b} - (\mathbf{A}^T \mathbf{W} \mathbf{A} + \lambda^2 \mathbf{L}) \mathbf{x}) \quad [5.20]$$

with the percent v-space variance reduction computed, like before, as

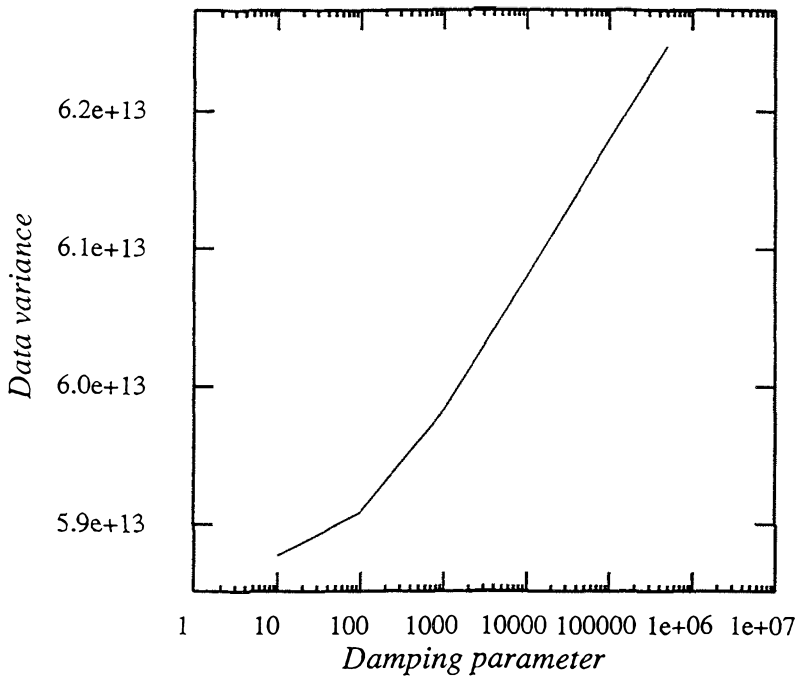
$$\frac{\sigma_b'^2 - \sigma_a'^2}{\sigma_b'^2} \times 100. \quad [5.21]$$

The advantage to using v-space variance is that it gives a larger variance reduction due to the fact that Eq. [5.11] is being solved instead of [5.9].

The v-space variance curve was also used to obtain the optimum damping parameter by choosing the point on the curve before which the variance reduction rose rapidly with increasing damping parameter. There exists the usual inverse problem of tradeoff between damping and variance. Increasing the damping parameter maps the null space into the solution by increasing the number of non-zero eigenvalues, thereby increasing the model variance. The variance reduction curve is used to choose an optimum damping parameter which represents a tradeoff between resolution and model variance. If the damping parameter is very small, then the depth resolution will be good with small half-widths at target depths, but the model variance will be large. At the other extreme, if the damping parameter is very large, then the model variance will be small but the resolution will be poor. The model variances were not calculated for these inversions, but the data variances, which exhibit just the opposite behavior, were calculated.

A typical tradeoff curve is shown in Fig. 5.2. This curve is associated with the 12-

(a)



(b)

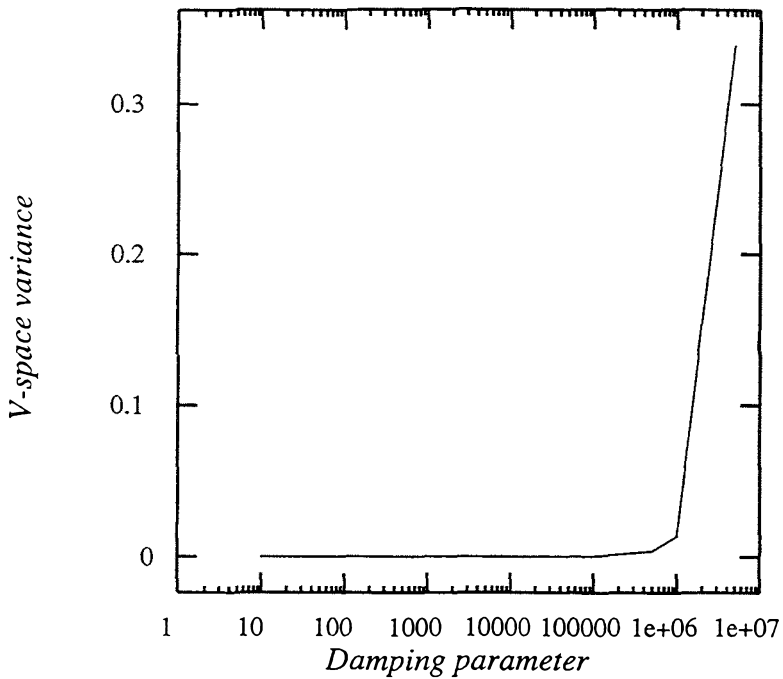


Fig. 5.2 Tradeoff curve for 12-layer, $1/v_b$ data weighting model demonstrating tradeoff between (a) data variance and damping parameter, and (b) v-space variance and damping parameter. The v-space variance curve, in particular, exhibits a sharp change in slope.

layer, I^1 data-weighting inversion (described in more detail in the next section) for which the data variance and v-space variance were calculated for a variety of damping parameters. The changes in variance are more important than the individual absolute values. Note the sharp increase in slope in the v-space variance curve. These curves were used to determine an optimum inversion damping parameter.

The total data variation reductions, defined by Eq. [5.18], were not large for the final models. This is to be expected, however, when large-scale, average velocity variations are determined on a global scale. While the misfit of individual data-synthetic pairs is determined, the resulting model represents average structure for that region of the Earth's interior. It is not possible to produce very large variance reductions by this method. If the inversions had involved determining structure along individual raypaths, as we observed in several single-raypath inversions, the variance reductions would have been larger. But the resulting Earth model would have displayed unrealistically large and small perturbations on short length scales and the resulting global models would have to be derived from the average of the individual raypath structures. Fig. 5.3 shows data-synthetic misfits using PREM (before the inversion) and three-dimensional model 11aSV_1P (after the inversion). This example represents the typical average data reduction after the inversion. The data was recorded at station RSSD in South Dakota from an earthquake which occurred on January 5, 1983 in the Philippine Islands. This figure shows the data as solid lines and the synthetic seismograms as dashed lines. Accounting for three-dimensional structure, the fit after the inversion resulted in a data variance reduction of 16.5%. Fig. 5.4 shows the data-synthetic misfits using the same Earth models for data recorded at station SNZO in New Zealand from an earthquake which occurred on August 4, 1987 off the coast of Nicaragua. This pair produced a data variance reduction of 15.8%.

830105(RSSD.r) distance=112.0 degrees depth= 17.0 km

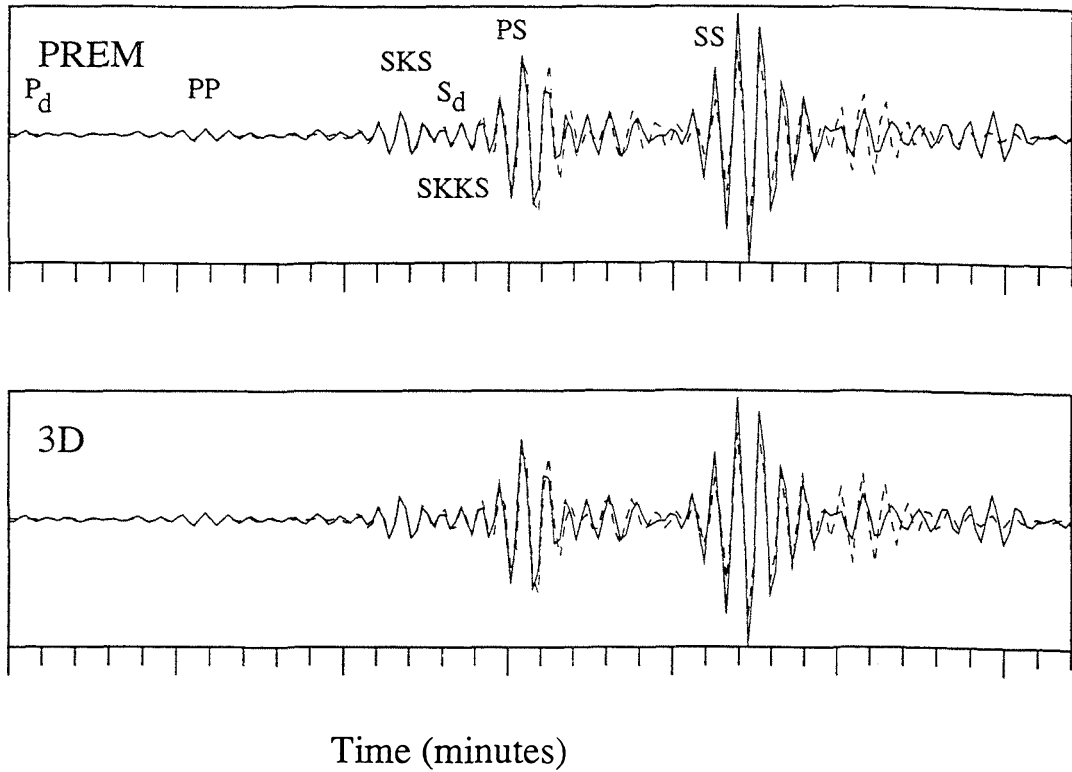


Fig 5.3 Data-synthetic seismogram fits before (PREM) and after (3D) the inversion. Data are given by solid lines and synthetics by dashed lines. This pair shows a data variance reduction of 16.5%.

870408(SNZO.r) distance=103.9 degrees depth= 20.0 km

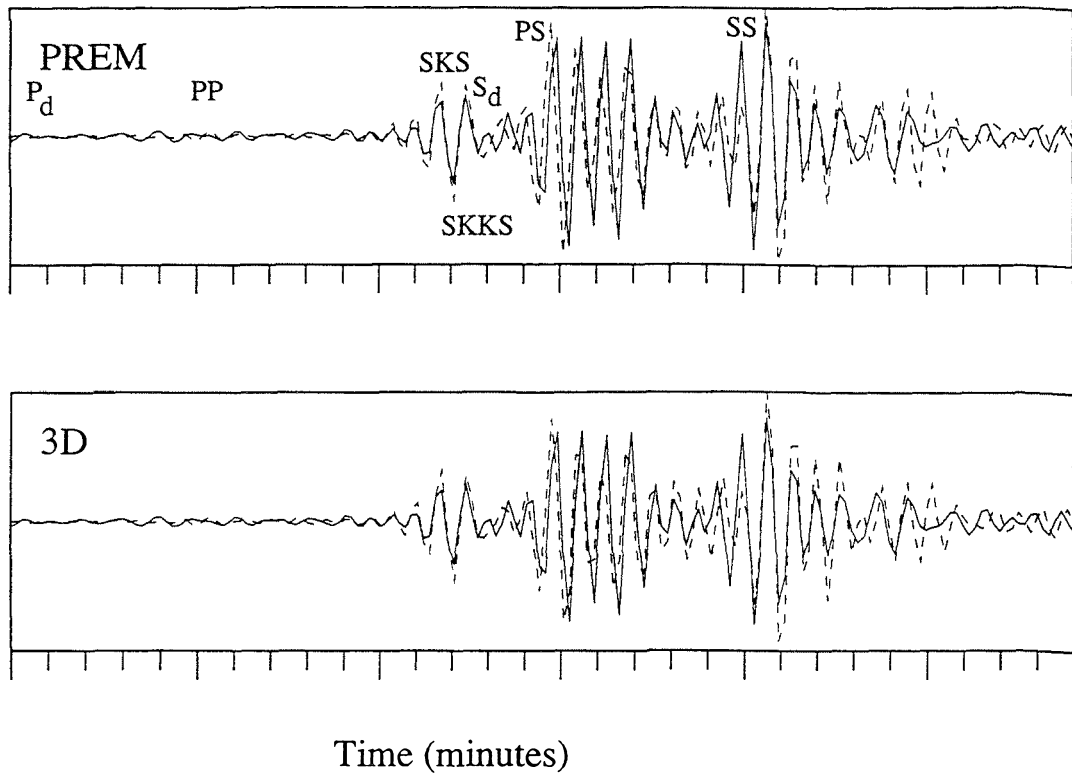


Fig. 5.4 Data-synthetic seismogram fits before (PREM) and after (3D) the inversion. Data are given by solid lines and synthetics by dashed lines. This pair shows a data variance reduction of 15.8%.

5.5 Three-dimensional models

This section contains descriptions and analyses of the four multi-layered Earth models using the inversion methods outlined above. Two inversions were performed for Earth models comprised of 12 shells of constant velocity and two are models with 11 shells (see Table 2.1 for layer depth ranges and thicknesses). The goal of the different parameterizations was to determine if the extra layer was statistically significant in describing Earth structure. A comparison of 11 vs. 12 layers will be made later in the chapter; the F ratio and variance reduction calculations of that part of the seismogram containing the SnKS phases are used as measures of the necessity of the extra parameters provided by the 12th layer. Of these pairs of inversions, one involved the inversion of data weighted by the scheme defined as I^1 in Eq. [5.12] and the other involved data weighted by the scheme defined as I^2 in Eq. [5.13]. The models will be presented in the following order and referred to by the name following in parentheses:

- *12 layers; $1/v_b$ data weighting (11aSV_IP)*
- *11 layers; $1/v_b$ data weighting (11aSV)*
- *12 layers; $1/M_0$ data weighting (11bSV_IP)*
- *11 layers; $1/M_0$ data weighting (11bSV)*

For each of the models, a series of plots containing contours of velocity perturbations associated with each layer will be shown. The contours represent the spherical harmonic expansion of velocity where maximum $\ell = 12$. The layer depth range is given at the top of the corresponding contour plot of that layer. Positive velocity perturbations are shown as solid contour lines and negative velocity perturbations are shown as dashed contour lines. The first solid line indicates the zero-value contour and the contour interval is indicated next to the corresponding layer. Perpendicular tic marks

on the contours indicate the direction of decreasing velocity. The continent outlines are given for reference on each layer plot. The c_0^0 term has been subtracted from each plot and velocity perturbations are relative to PREM. The spectral amplitudes of the inversion results are given by

$$S_\ell = \left\{ \frac{1}{2\ell+1} \sum_{m=0}^{\ell} \left[(a_\ell^m)^2 + (b_\ell^m)^2 \right] \right\}^{\frac{1}{2}} \quad [5.22]$$

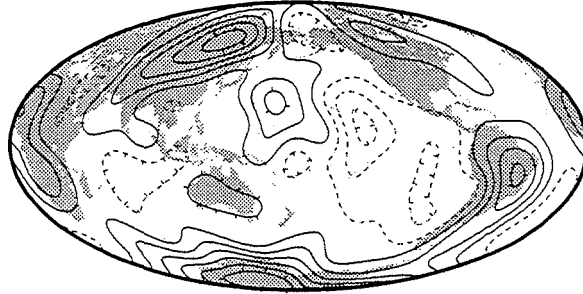
where a_ℓ^m and b_ℓ^m are the spherical harmonic expansion coefficients of velocity for each layer. For reasons outlined in the next few sections, our preferred three-dimensional Earth model is 11aSV_1P and the seismogram fits which appear in later sections use this model.

5.5.a 12-layered model with $1/v_b$ data weighting

The first set of inversions for Earth structure involved determining S-wave velocity anomalies in 11 mantle layers and P-wave velocity in one outermost core layer. The results of the inversion are given in Fig. 5.5. This analysis will begin with the upper mantle and move to the lower mantle since this is the order in which the plots are given. However, it should be noted that the lowermost mantle (layer 11) and outermost core (layer 12) are of most interest to this study. Fig. 5.6 shows spectral amplitudes for model 11aSV_1P; the amplitudes are plotted as functions of ℓ for individual layers.

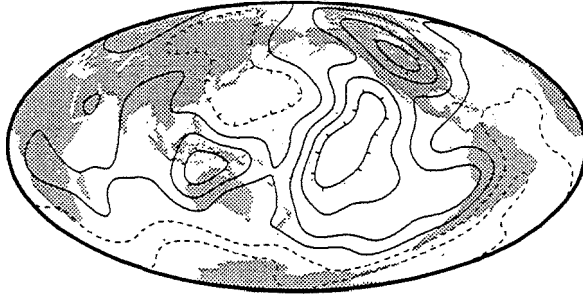
As with other whole-Earth models [Tanimoto, 1990a; Su *et al.*, 1994; Woodward and Masters, 1991c], the upper mantle is more heterogeneous than the rest of the mantle defined by rougher, small-wavelength patterns and larger lateral velocity anomaly amplitudes. As this plot shows, lateral velocity perturbations range from -3.4% to 5.9% in the top 220 km (layer 1) with a smaller range in layers 2-4, indicated by the contours. Anomalies at depths 0-220 km are most similar to global models of velocity where high velocity tends to occur under continents, especially large-scale tectonic features such as

Layer 1-depth range 0-220 km



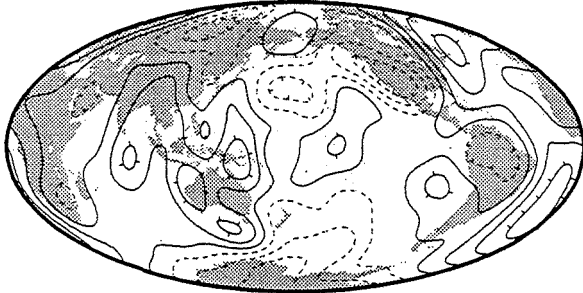
1.0%

Layer 2-depth range 220-400 km



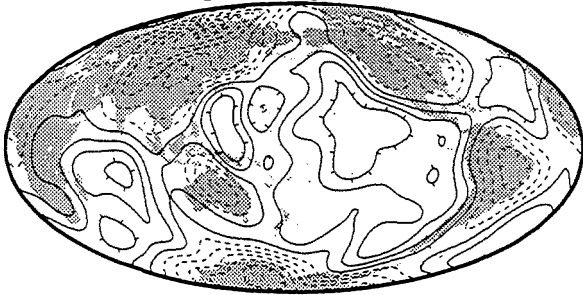
0.5%

Layer 3-depth range 400-670 km



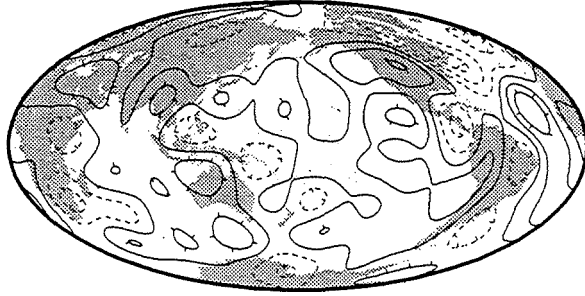
0.5%

Layer 4-depth range 670-1022 km



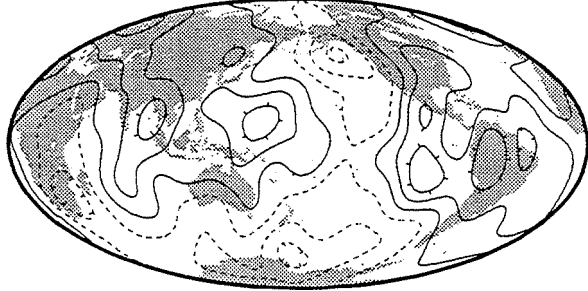
0.5%

Layer 5-depth range 1022-1284 km



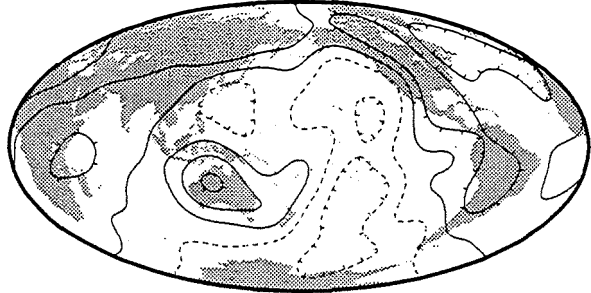
0.5%

Layer 6-depth range 1284-1555 km



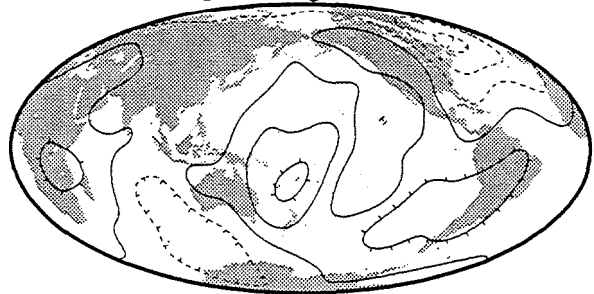
0.5%

Layer 7-depth range 1555-1816 km



0.5%

Layer 8-depth range 1816-2088 km



0.5%

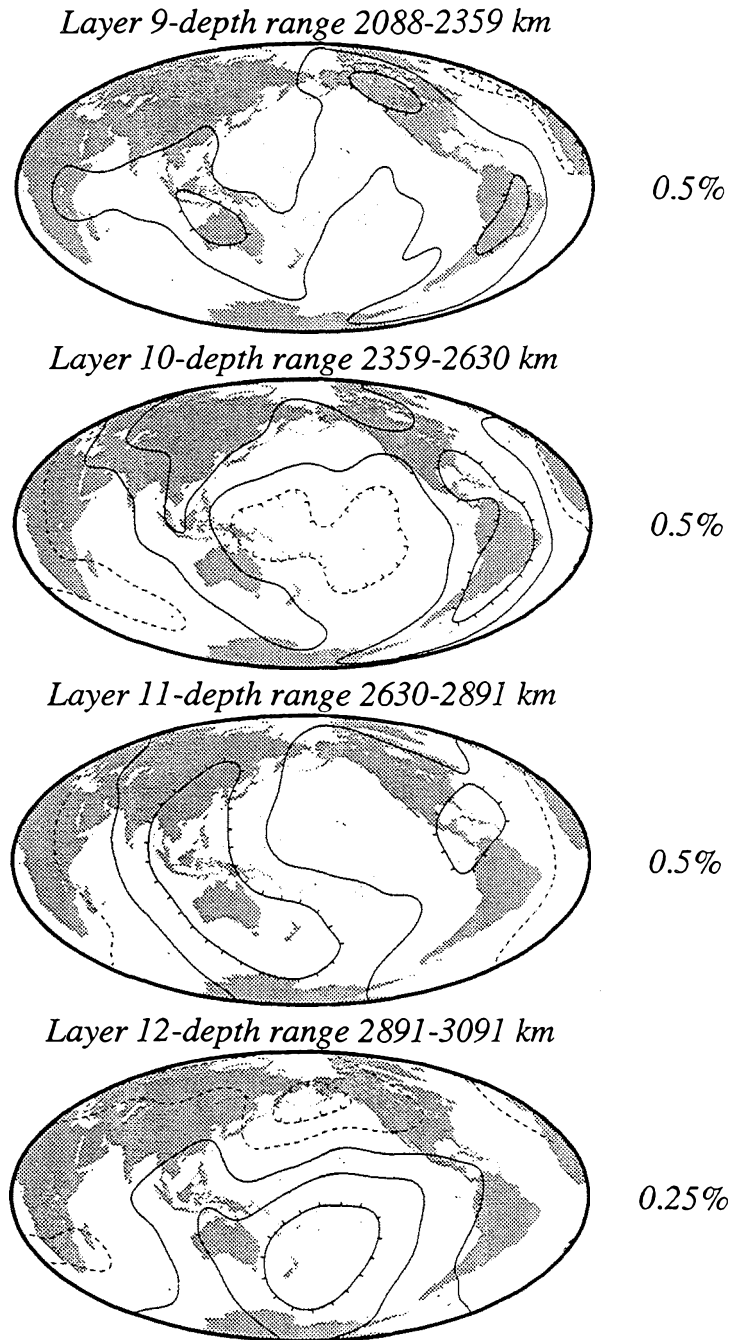
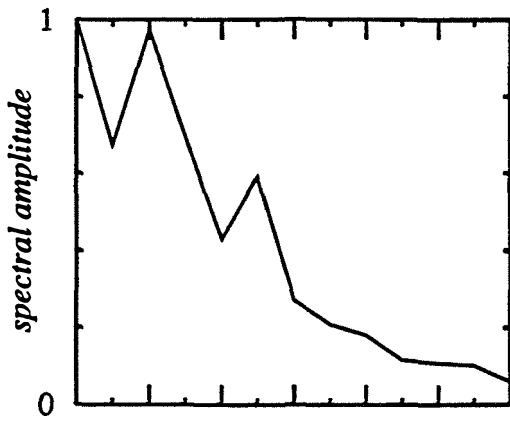
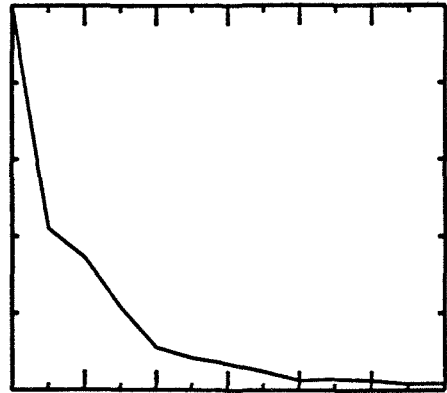
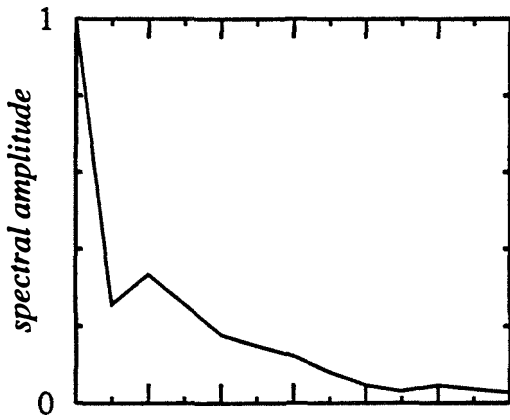
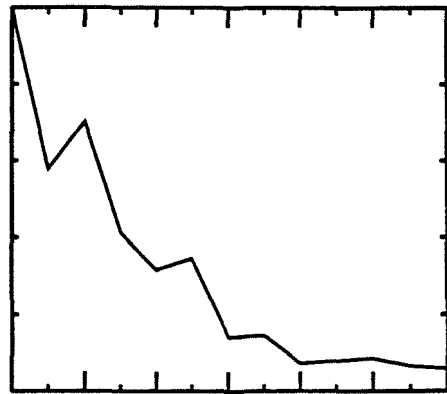
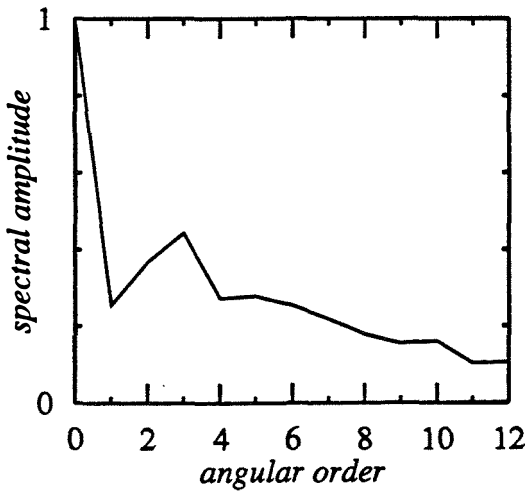
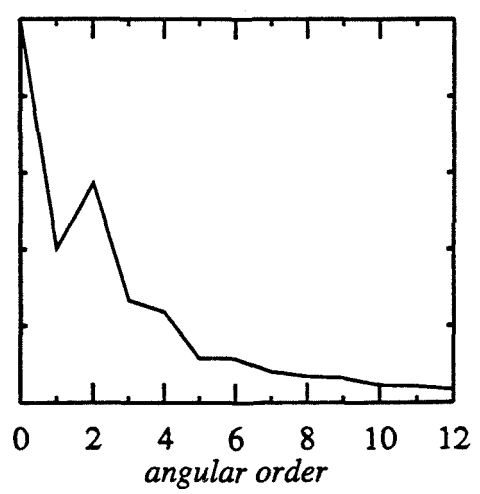


Fig. 5.5 Results of 12-layer inversion using the data weighting scheme defined by I^1 (model 11aSV_1P). Velocity (layers 1-11: S-wave; layer 12: P-wave) contours are given to the right of the corresponding layer. Solid lines represent positive velocity perturbations and dashed lines represent negative velocity perturbations. The first solid contour indicates the zero percent velocity anomaly.

Layer 1*Layer 2**Layer 3**Layer 4**Layer 5**Layer 6*

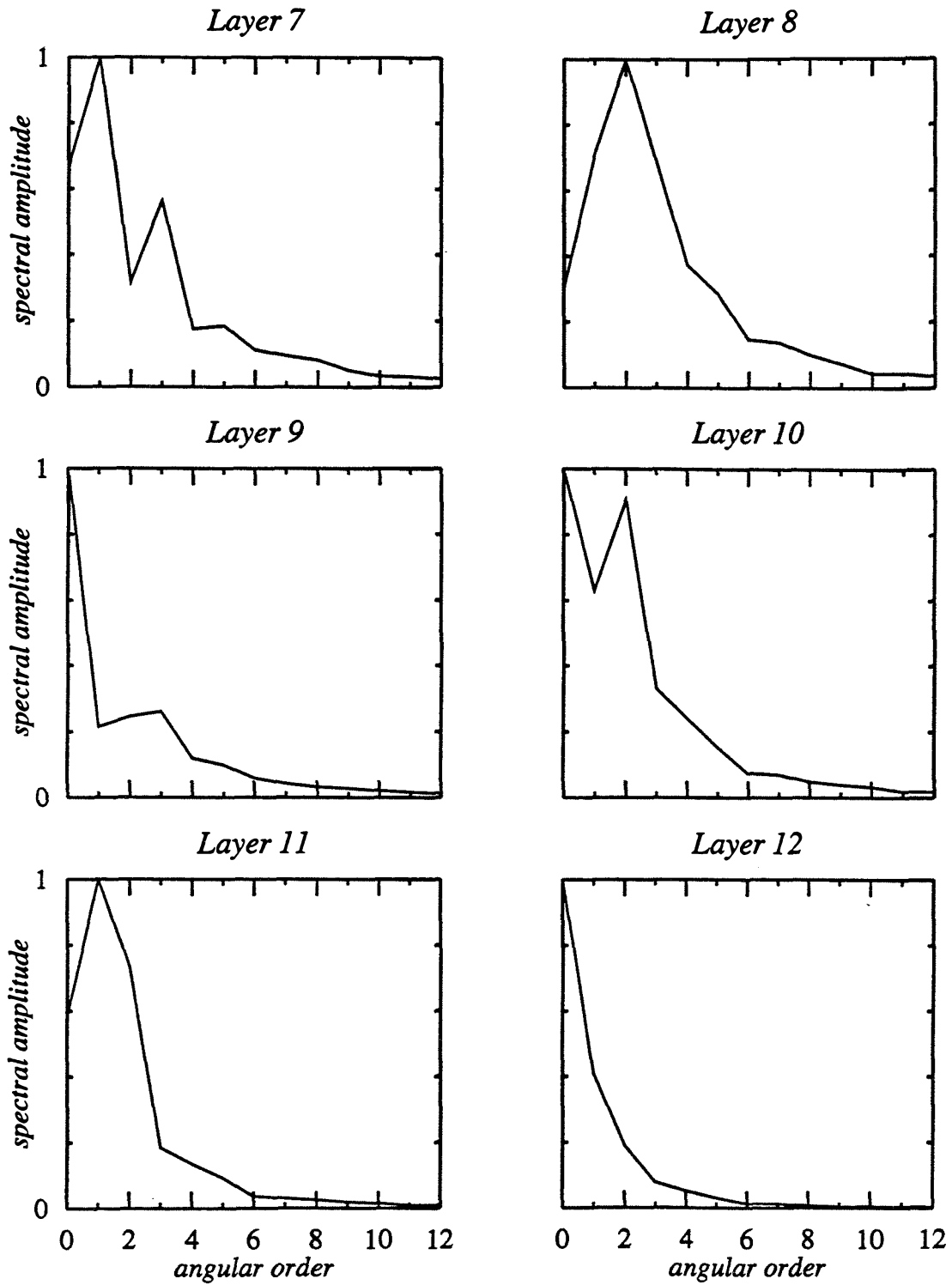


Fig. 5.6 Spectral amplitudes for model 11aSV_1P plotted as functions of ℓ for individual layers indicated at the top of each plot.

much of North and South America, Australia, Asia, and Africa. There is a large ring of low velocity under the Pacific Ocean, most likely related to the active tectonic features of the Pacific plate. At 220-400 km, the patterns have changed somewhat and correlations of high velocity with continents are not so high. There still exists a region of high velocity under North America and Australia; however, low velocity has moved under the Pacific Ocean and parts of Asia and South America. Layers 1 and 2 both have strong degree 2 components, but layer 1 also exhibits a relatively large degree 5 component (shown in Fig. 5.6). By 400-670 km in depth, the patterns are not related to the uppermost mantle, but there still exists a large degree of heterogeneity, again characterized by higher frequency, large amplitude anomalies. Regions of low velocity exist under most continents and the high velocity under the Pacific has grown smaller. The uppermost mantle features do not extend smoothly into the second and third layers, as observed in the other Earth models [Su *et al.*, 1994; Woodward and Masters, 1991c; Tanimoto, 1990a]. Some features remain throughout the upper mantle such as the high velocity under Australia and parts of the Pacific, but others are different, i.e., the low velocity that moves in under North and South America, and Asia. Large variations in velocity extend as deep as 1555 km, and for some layers (1, 4, 5, and 7, in particular), the spectral amplitudes do not fall off so quickly, indicating more numerous, small-scale features.

The addition of the Rayleigh wave eigenfrequency perturbation results of Zhang [1992] affected the first four layers only; there was no effect on structure for depths greater than 1022 km. The degree of scalar weighting given to the Rayleigh wave results affected the location and magnitude of the velocity patterns. The weighting was varied in the same manner as the inversion damping parameter and the results presented here represent solutions using both an optimum damping parameter and Rayleigh wave weighting parameter. Large weighting of the phase perturbations produced large upper mantle anomaly magnitudes and shifted the patterns around by several hundred km, close to the lateral resolution; in this case, the Rayleigh wave results were dominating the

inverse problem for the upper mantle. Regardless of weight, lower mantle patterns and magnitudes remained unchanged. Below a minimum weight, the Rayleigh wave results had no effect; in this case, upper mantle phases from the data set were determining the results of the inverse problem for the upper mantle layers. The final choice of weight represented a balance between the influence of the data and Rayleigh wave eigenfrequency perturbation information. A detailed analysis of upper mantle structure will not be made based on these results since surface waves were not included in the inversion.

The mid mantle starts out relatively heterogeneous with velocity anomalies ranging from -1.7% to 1.5% in the 1022-2088 km depth range. Large-scale (i.e., long-wavelength) features begin to appear at 1555 km depth and extend down to the CMB. The scale of the features is apparent in the spectral amplitudes shown in Fig. 5.6. Whereas layers 5 and 6 contain secondary amplitude peaks at $\ell = 2$ and $\ell = 3$, and do not fall off quite as rapidly, layers 8-12 show more rapid spectral amplitude declines for $\ell > 1$. By 1555 km, large regions of low velocity have appeared under the Pacific and north Atlantic, and regions of high velocity have appeared under North and South America, Asia, and Australia. These features all appear to some extent in other mantle heterogeneity models, although the strength of higher degree components varying from model to model.

Because of the motivation for the multi-layer inversions, most attention will be paid to the lowermost mantle and outermost core layers. The most notable feature of structure in these layers is that it is relatively long-wavelength for all inversion results (see Fig. 5.5). This is partly due to the decrease in radius for which the lateral variations are plotted; thus, part of the apparent wavelength change is not real. Lateral velocity perturbations vary between -1% and 1% in layers 10 and 11. There is a large ring of low velocity under much of Africa, possibly the same "African plume" referred to by Su *et al.* [1994]. The high velocity anomalies lie under continents (e.g., Asia, North and South America, and Australia). Note that references are made to surface features for convenience but associations with surface tectonics are not necessarily implied. Layer 10

exhibits the same low velocity under Africa, but the Pacific is underlain by low velocity which has disappeared by a depth of 2630 km.

Crossing the CMB into the outermost core, Fig. 5.5 shows that the anomalies are different for the outermost core. Layer 12 also exhibits relatively long-wavelength velocity structure with lateral velocity perturbations varying between -0.6% and 0.7% but the patterns are different from the lowermost mantle. The ring of high velocity anomaly remains in the south Pacific Ocean, and it is almost completely surrounded by low velocity regions. A small amount of low velocity remains under the southern part of Africa.

In the pattern retrieval resolution results of Chapter 2, synthetic Earth structure that was initially placed in the lowermost mantle layer leaked into the layer above and below, and structure initially placed in the outermost core leaked into the lowermost mantle. Referring to the results of the first two tests (see Table 2.3), less than 100% of the power of structure initially placed in layer 12 was retrieved in that layer after the inversion. Table 2.3 provides upper and lower bounds on the power of the structure in model 11aSV_1P in the form of multiplicative factors. Note that the velocity field amplitudes of the real-Earth inversions are multiplied by the square root of the multiplicative factors; i.e., based on these tests, an upper bound of 84% and a lower bound of 68% of the power of outermost core structure is, in fact, due to heterogeneity in the outermost core. By the same analysis, less than 100% of the power of structure initially placed in layer 11 was retrieved in that layer after the resolution inversion. An upper bound of 60% and a lower bound of 53% of the power of lowermost mantle structure is, in fact, due to D" heterogeneity. These uncertainties are due to the incomplete data coverage and errors which almost always arise in global inversions such as these.

The c_0^0 term has been removed from the three-dimensional analysis since it represents a baseline shift with respect to PREM. However, the values of the c_0^0 terms are important since they indicate how well PREM serves as an initial Earth model for different parts of the Earth. The velocity perturbations will be distributed about the

radially-varying values for each layer and average perturbation will be about zero, unless there is a systematic bias in certain regions (e.g., tectonic features, mantle convection characteristics, internal discontinuities). Fig. 5.7 comprises a plot in which the c_0^0 terms of the velocity expansion for model 11aSV_1P have been added to the velocity values given by PREM. As this plot shows, the c_0^0 values are small enough that the main features of PREM (e.g., velocity jumps at discontinuities) are still visible. Thus, PREM is serving as a good, average, one-dimensional initial Earth model. Looking at it another way, the inversions are stable enough that the c_0^0 terms in the matrices $(\mathbf{A}^T \mathbf{W} \mathbf{A} + \lambda^2 \mathbf{L})$ are not becoming unrealistically large. The same conclusions can be made from the c_0^0 values for models 11aSV, 11bSV_1P, and 11bSV.

5.5.b 11-layered model with $1/v_b$ data weighting

Model 11aSV comprises 11 mantle layers of S-wave velocity perturbations by inverting data using the weighting scheme defined by I^1 . 11aSV was obtained to compare the structural patterns and variance reductions with 11aSV_1P in order to assess the need for the 12th layer to describe lateral variations in velocity to explain the data. The input parameters for the two inversions were exactly the same except for a decrease in the number of layers by one. The results of the 11-layer inversion are given in Fig. 5.8 with plotting details the same as those for Fig. 5.5. Fig. 5.9 shows spectral amplitudes for model 11aSV; the amplitudes are plotted as functions of ℓ for individual layers.

As with model 11aSV_1P, the upper mantle layers are more heterogeneous than the rest of the mantle characterized, as before, by short-wavelength, large amplitude anomalies. As this plot shows, lateral velocity perturbations range from -3.4% to 5.9% in the top 220 km (layer 1) with a smaller range in layers 2-4. Not surprisingly, model 11aSV looks almost exactly like model 11aSV_1P for layers 1-10. The amplitudes and patterns of anomalies in these layers are almost exactly the same, as the contour lines in

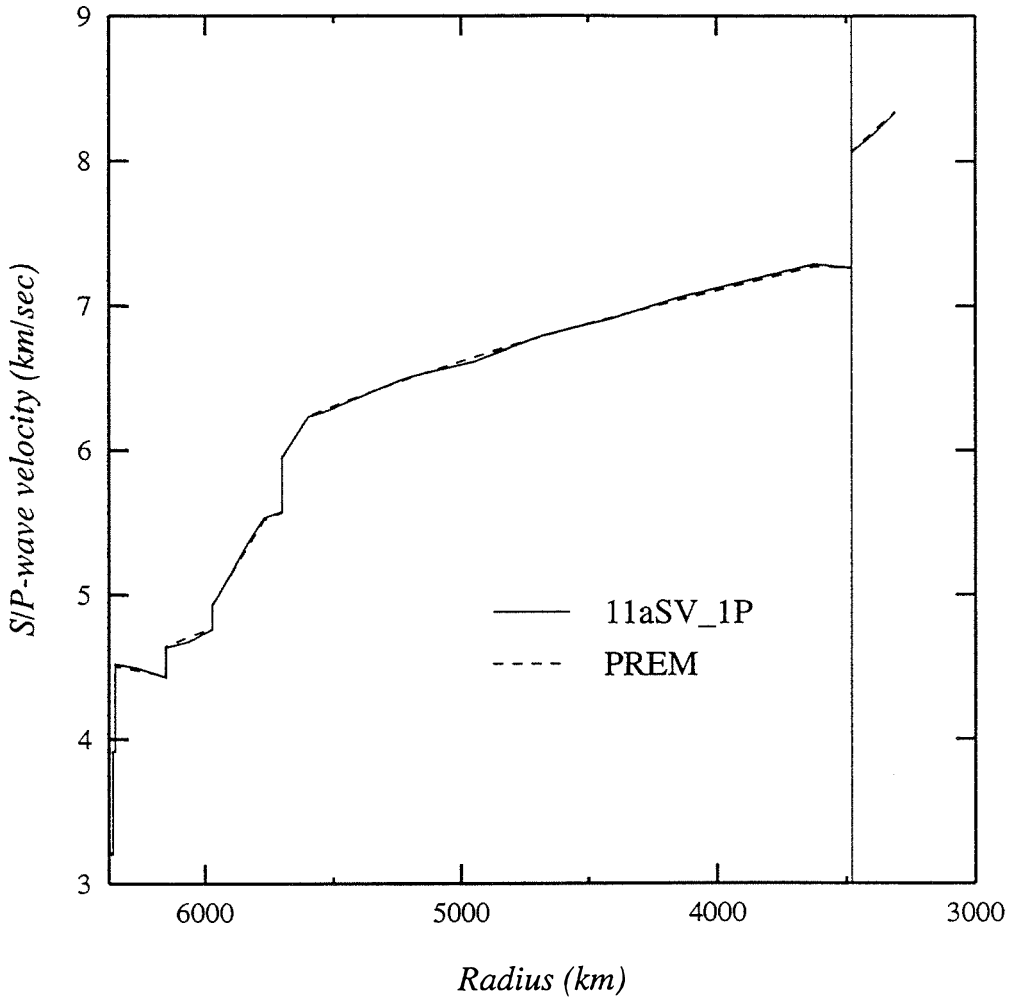
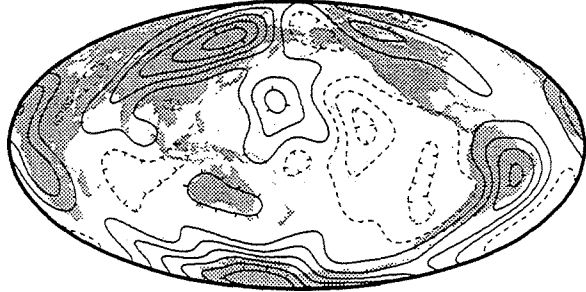


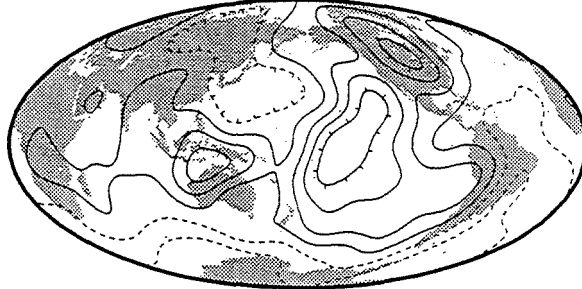
Fig. 5.7 Radially-varying Earth models PREM (solid lines) and PREM modified by adding the c_0^0 terms (dashed lines) from model 11aSV_1P. The plots for models 11aSV, 11bSV_1P, and 11bSV look very similar.

Layer 1-depth range 0-220 km



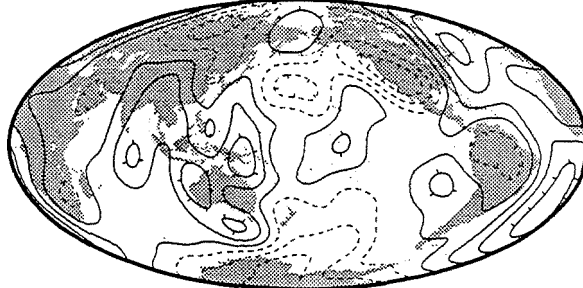
1.0%

Layer 2-depth range 220-400 km



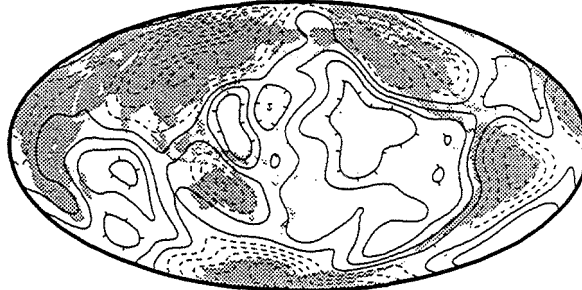
0.5%

Layer 3-depth range 400-670 km



0.5%

Layer 4-depth range 670-1022 km



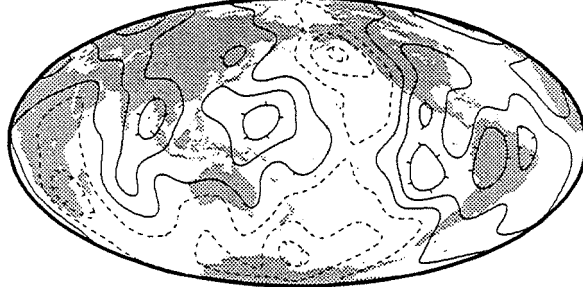
0.5%

Layer 5-depth range 1022-1284 km



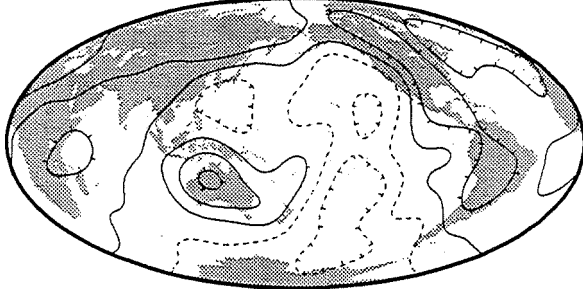
0.5%

Layer 6-depth range 1284-1555 km



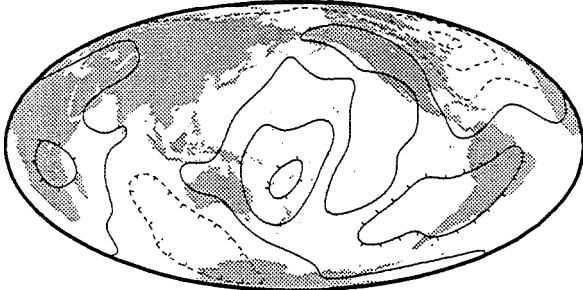
0.5%

Layer 7-depth range 1555-1816 km



0.5%

Layer 8-depth range 1816-2088 km



0.5%

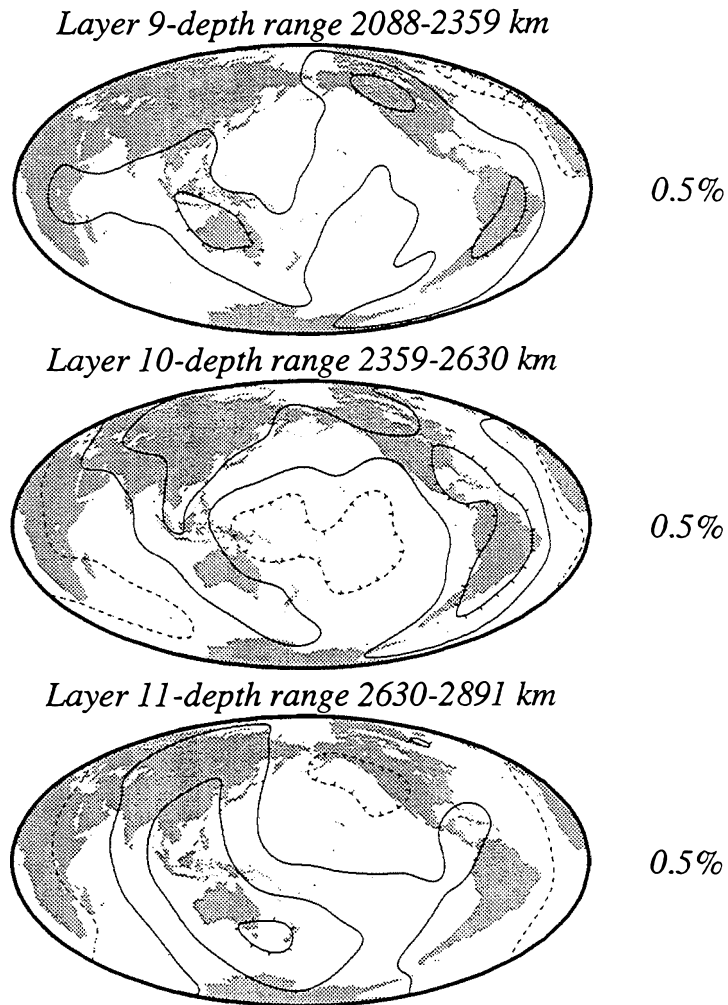
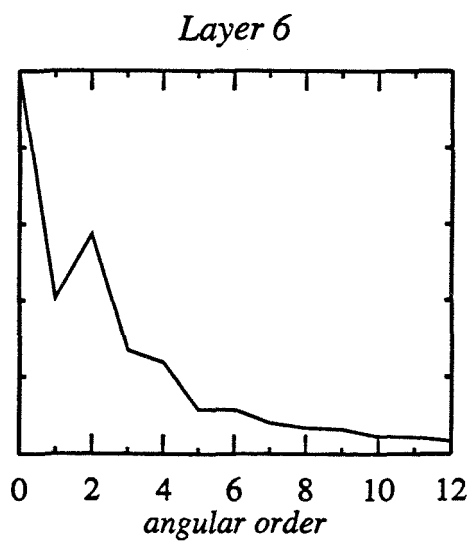
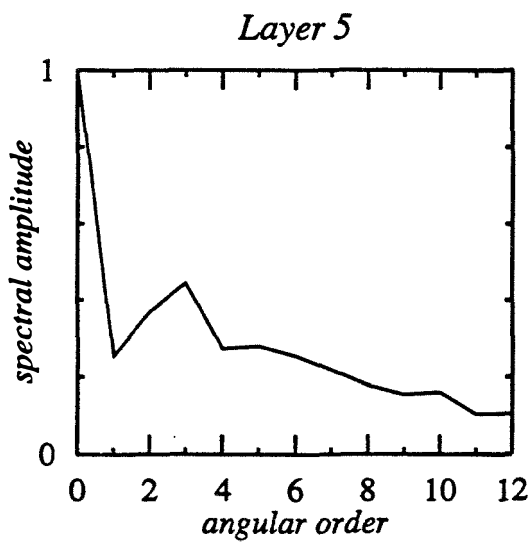
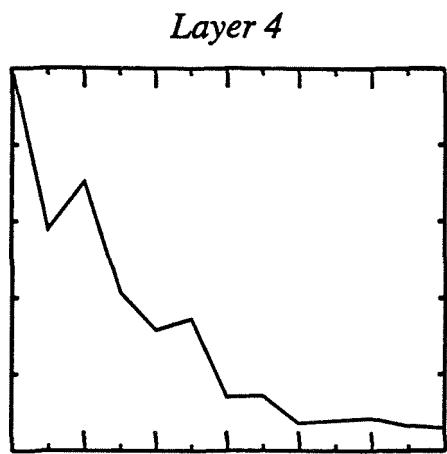
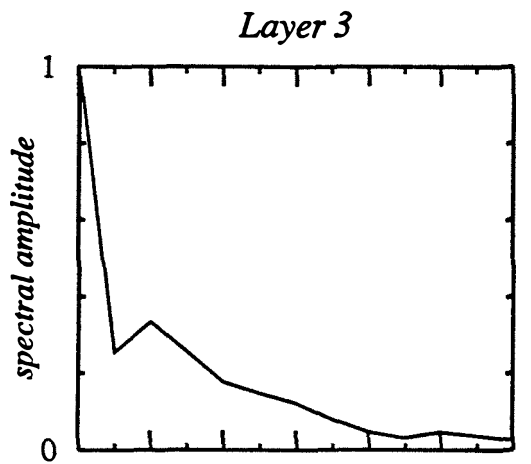
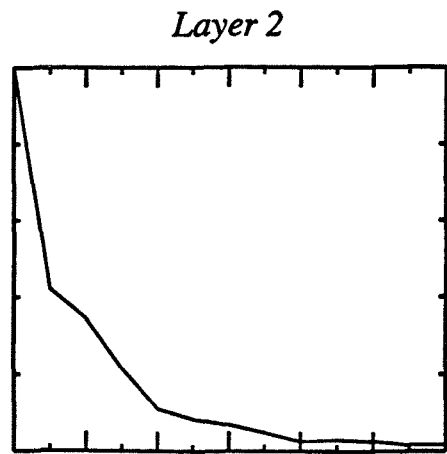
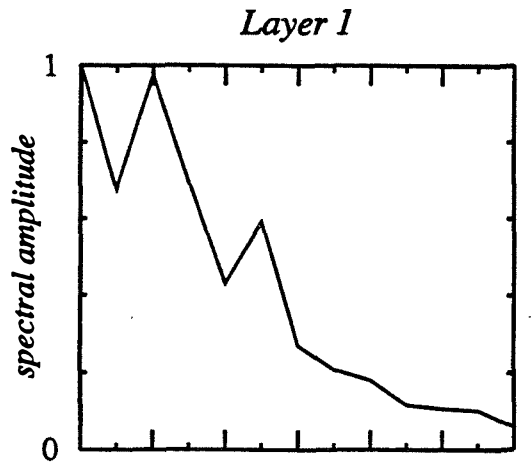


Fig. 5.8 Results of 11-layer inversion using the data weighting scheme defined by I^1 (model 11aSV). Velocity (layers 1-11: S-wave) contours are given to the right of the corresponding layer. Solid lines represent positive velocity perturbations and dashed lines represent negative velocity perturbations. The first solid contour indicates the zero percent velocity anomaly.



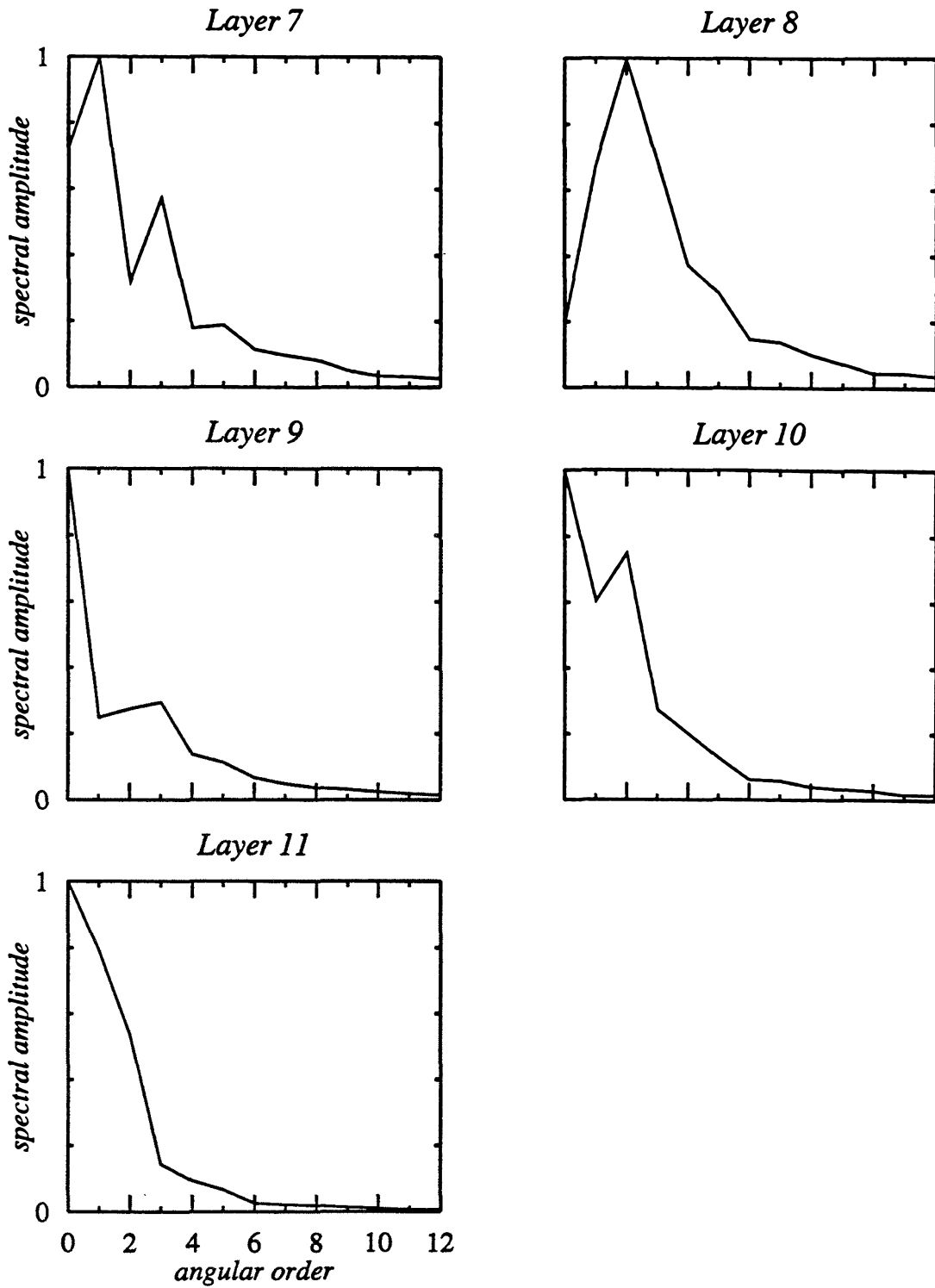


Fig. 5.9 Spectral amplitudes for model 11aSV plotted as functions of ℓ for individual layers indicated at the top of each plot.

Fig. 5.8 show. It follows from the similarity in models, especially for layers 1-10, that the spectral amplitudes are almost exactly the same, shown in Fig. 5.9.

The lowermost mantle, illustrated in layer 11 of Fig. 5.8 is slightly different from layer 11 in model 11aSV_1P. As before, there is a large ring of low velocity under much of Africa and high velocity anomalies lie under continents (e.g., Asia, North and South America, and Australia) for depths 2630-2891 km. However, the patterns given by the contour lines are slightly shifted (but most shifts are below lateral resolution levels); the range of lateral velocity perturbations in the lowermost mantle for 11aSV is -1% to 1% (same as model 11aSV_1P). A small region of weak, low velocity has cropped up in layer 11 of 11aSV under the western edge of North America. This figure suggests that some of the anomaly that was placed in the outermost core layer of 11aSV_1P was moved to the lowermost mantle in 11aSV. This result is also suggested by the pattern retrieval resolution tests presented at the end of Chapter 2. From the first of these resolution tests, it is clear that part of the structure in layer 12 leaks into layer 11 and upper bounds can be placed the degree of leakage. As we shall see in a later section, the F ratio will demonstrate that the extra parameters provided by the 12th layer in model 11aSV_1P are statistically significant. Lateral velocity variations in the 12th layer are different from zero at the 99% confidence level.

5.5.c 12-layered model with $1/M_0$ data weighting

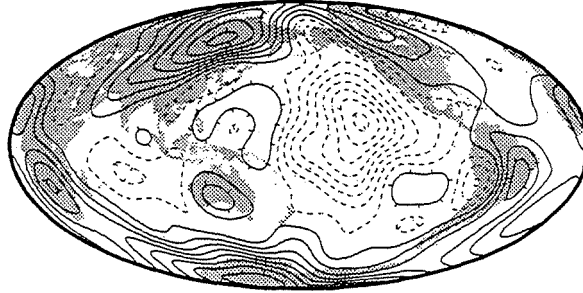
The second data weighting scheme is defined by Eq. [5.13] and the next pair of inversions was carried out to examine the differences in resulting Earth structure due to this weighting scheme. Model 11bSV_1P comprises 11 mantle layers in which S-wave velocity anomalies were solved for in addition to P-wave velocity perturbations in an outermost core layer. One result of the different weighting was that the values of the elements of $A^T W A$ and $A^T W b$ were changed by several orders of magnitude. Thus,

while the damping scheme remained the same, the value of the scalar damping parameter, λ , was changed.

The results of the 12-layer inversion are given in Fig. 5.10. The plotting details are the same as for Fig. 5.5. This analysis will again move from the upper mantle to the lower mantle since this is the order in which the plots are given. Fig. 5.11 shows spectral amplitudes for the model 11bSV_1P; the amplitudes are plotted as functions of ℓ for individual layers.

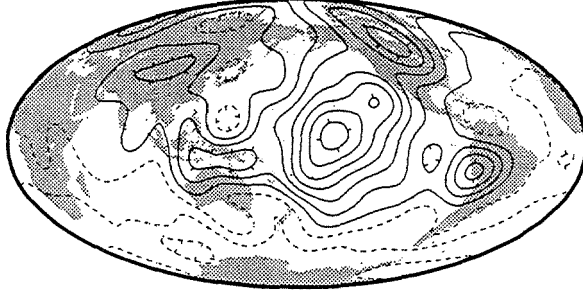
The upper mantle patterns of model 11bSV_1P are similar to those given by models 11aSV_1P and 11aSV. As before, the upper layers are more heterogeneous than the rest of the mantle, except that now large perturbations extend as deep as 1555 km. As this plot shows, lateral velocity perturbations range from a large -8% to 8% in the top 220 km (layer 1) with a smaller range in layers 2-4. Also as before (demonstrated by model 11aSV_1P), the first layer is most similar to crustal models of velocity where high velocity tends to lie under continents, especially large-scale tectonic features such as much of North America, Australia, Asia, and parts of Africa and South America. For depths 0-220 km in 11bSV_1P, there is a large ring of low velocity under the Pacific Ocean. Degrees 1 and 2 are the strongest, and the spectral amplitudes fall off more rapidly than those of 11aSV_1P, shown in Fig. 5.9. This is also apparent in layer 1 of Fig. 5.8. By 400-670 km depths, the patterns are not related to the uppermost mantle, but there still exists a large degree of heterogeneity. Regions of low velocity exist under most continents and the high velocity patch under the Pacific has grown smaller. The uppermost mantle features do not extend smoothly into the second and third layers. Some features remain throughout the upper mantle such as the high velocity under Australia and parts of the Pacific, but others are different such as the low velocity that moves in under North and South America, and Asia. Large variations in velocity extend as deep as 1555 km, but for most layers, the spectral amplitudes fall off more quickly than the rate exhibited by 11aSV_1P. The addition of the Rayleigh wave eigenfrequency perturbation results of Zhang [1992]

Layer 1-depth range 0-220 km



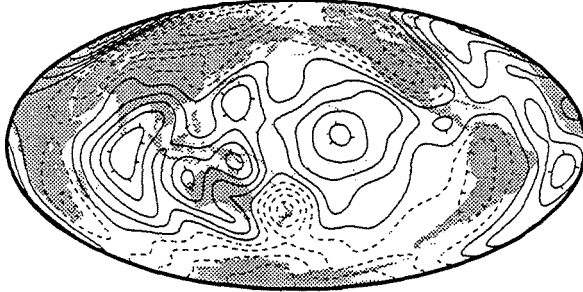
1.0%

Layer 2-depth range 220-400 km



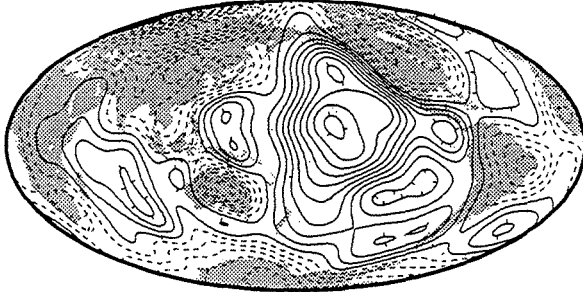
0.5%

Layer 3-depth range 400-670 km



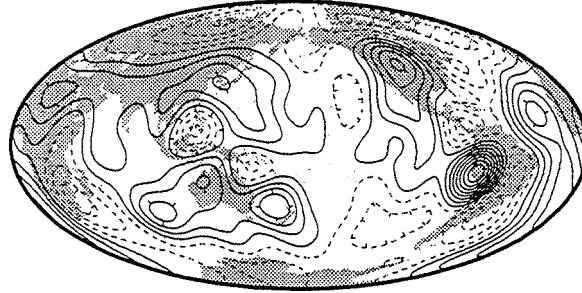
0.5%

Layer 4-depth range 670-1022 km



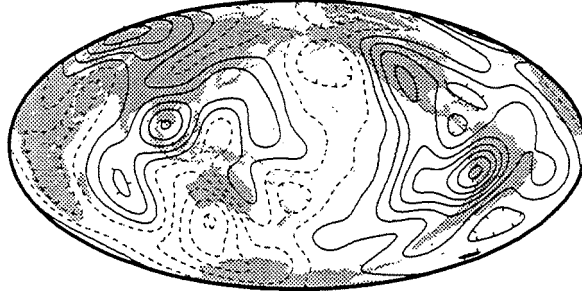
0.5%

Layer 5-depth range 1022-1284 km



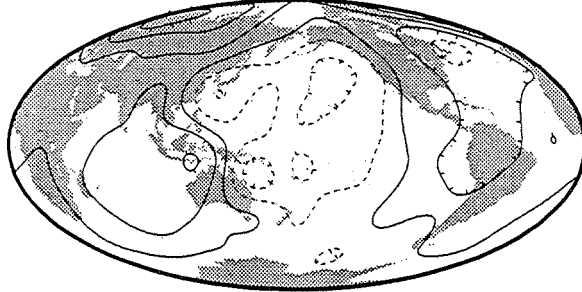
0.5%

Layer 6-depth range 1284-1555 km



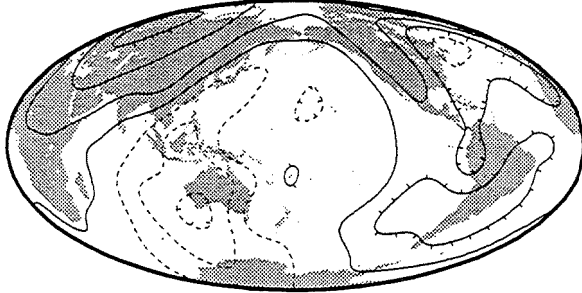
0.5%

Layer 7-depth range 1555-1816 km



0.5%

Layer 8-depth range 1816-2088 km



0.5%

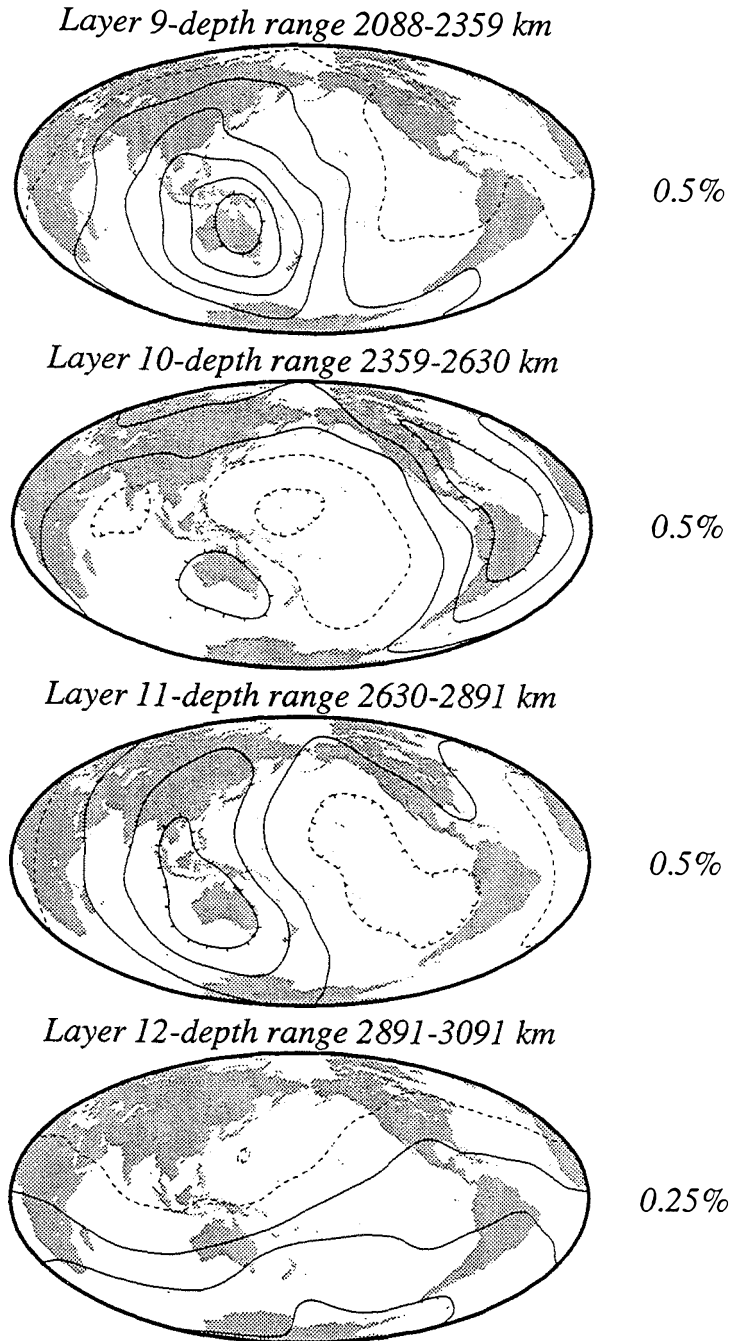
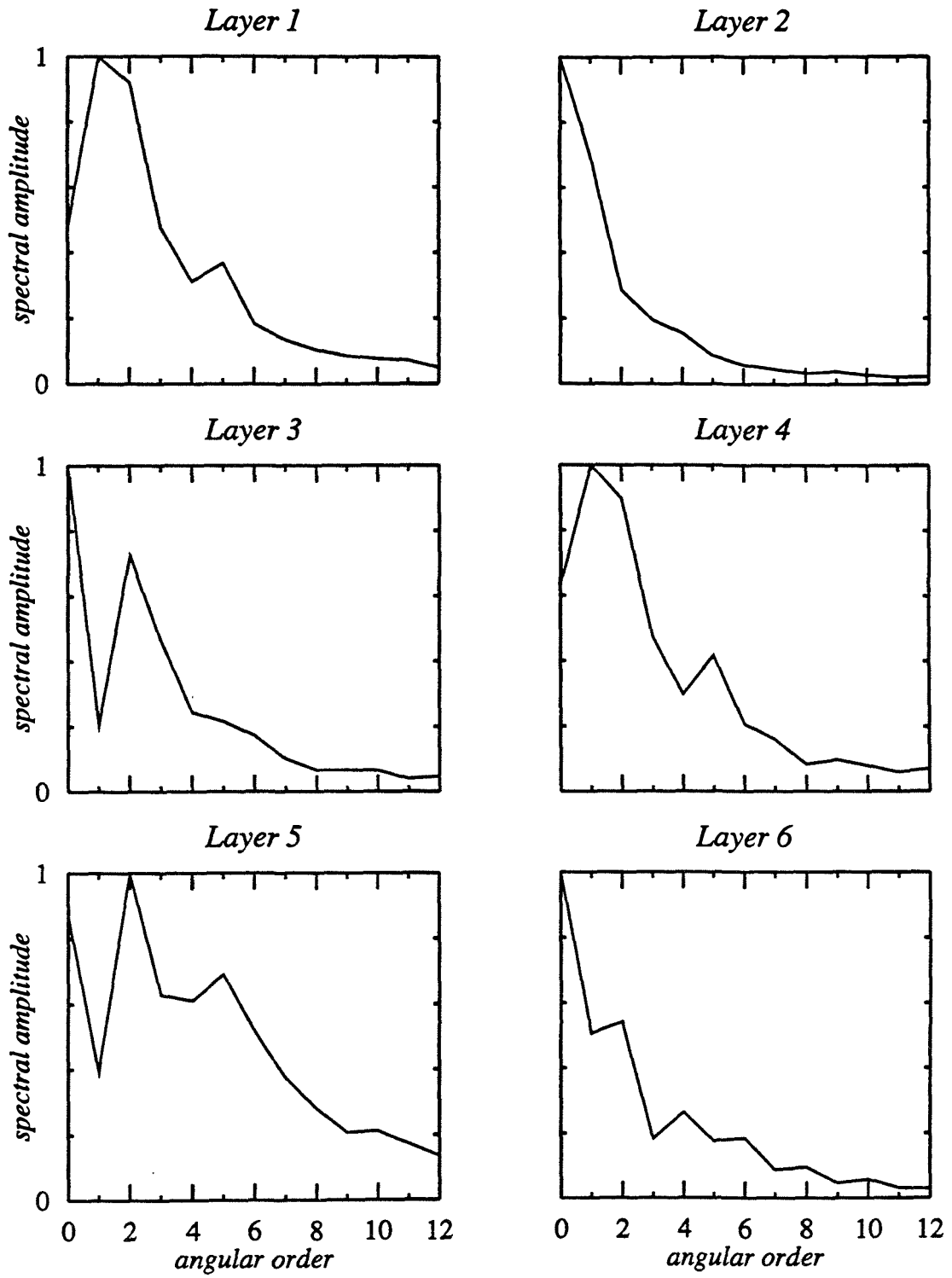


Fig. 5.10 Results of 12-layer inversion using the data weighting scheme defined by I^2 (model 11bSV_1P). Velocity (layers 1-11: S-wave, layer 12: P-wave) contours are given to the right of the corresponding layer. Solid lines represent positive velocity perturbations and dashed lines represents negative velocity perturbations. The first solid contour indicates the zero percent velocity anomaly.



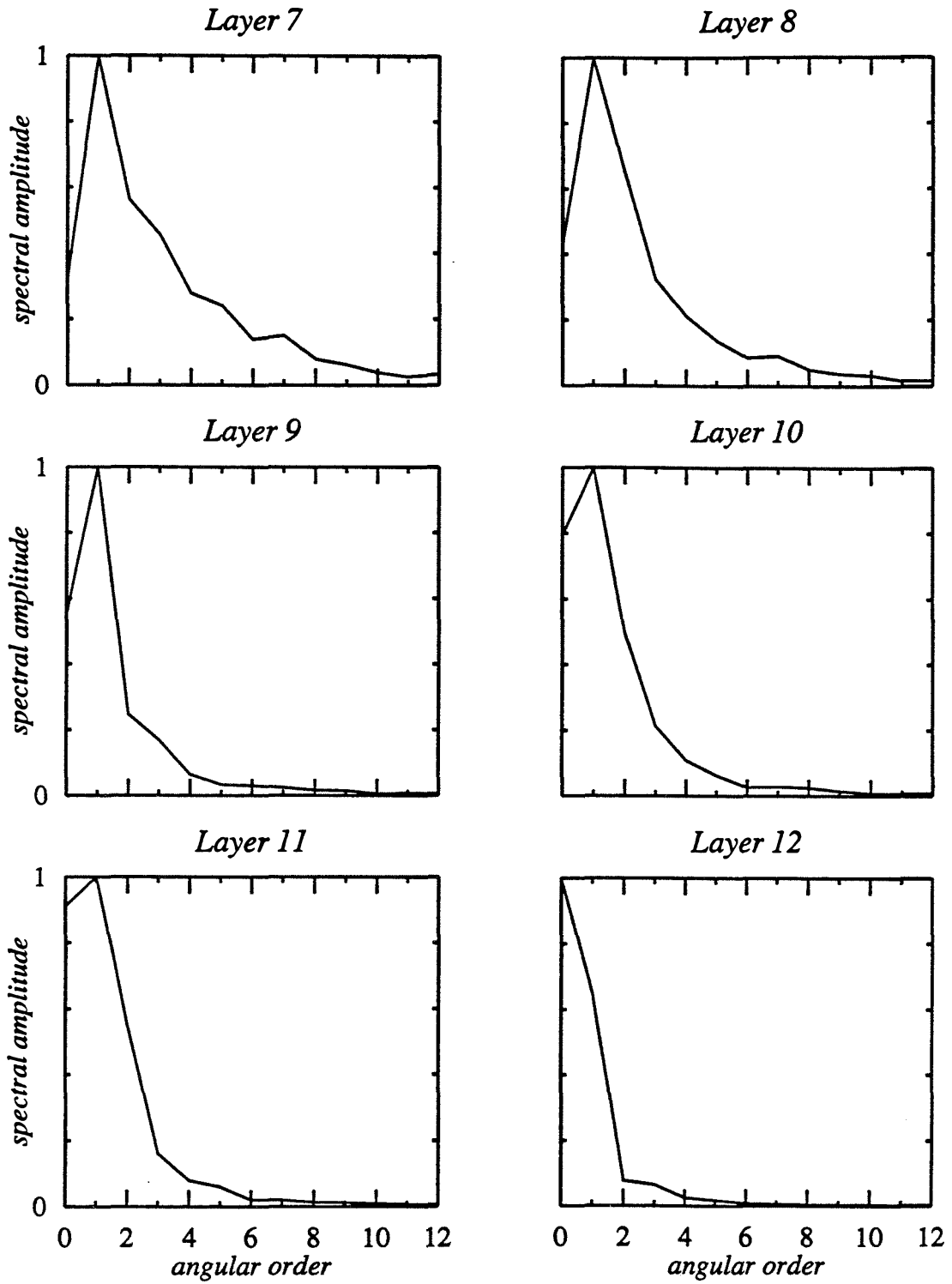


Fig. 5.11 Spectral amplitudes for model 11bSV_1P plotted as functions of ℓ for individual layers indicated at the top of each plot.

affected the top 4 layers in the same manner as for 11aSV_1P; there was no effect on structure for depths greater than 1022 km.

The mid mantle starts out quite heterogeneous, with lateral velocity anomalies ranging from -2.1% to 3.9% in the 1022-2088 km depth range, significantly larger than values given in model 11aSV_1P. Large-scale features begin to appear at 1555 km depth and extend down to the CMB. These changes are apparent in the spectral amplitudes shown in Fig. 5.10. Whereas layers 5 and 6 contain secondary amplitude peaks at $\ell = 2$, layers 7-12 do not contain these peaks and spectral amplitudes fall off rapidly for $\ell > 1$. These changes are observed in the spectral amplitudes shown in Fig. 5.11.

One pronounced feature that does not appear in either 11aSV_1P or 11aSV, and is difficult to explain, is the small, bullseye-like ring of high velocity under the west coast of South America. This anomaly does not show up as any obvious error in station locations for this region, or source parameter errors, such as source depth or centroid time. It also disappears when the inversion is performed with only half the seismograms, implying that one or more seismograms are contributing to this structural feature. However, a search of variance reductions for raypaths through this ring, and source characteristics for earthquakes in or near the ring yielded nothing unusual. The most likely source of such a ring is a source-time shift for which we do not solve. The inversions in this thesis assume that the CMT solutions give a source time with a no error. However, other tomography studies have included source-time shifts in their inversions [Su *et al.*, 1994] and have obtained relatively large source-time shifts (as much as 8 sec) [Su, personal communication] which can affect the three-dimensional modeling in unpredictable ways. This points to a shortcoming of some tomography studies. It is difficult to tell how much of the difference between data and synthetics is due to three-dimensional Earth structure and how much is due to variations in source parameters (in this case, relative to CMT). There is a tradeoff between variations in structure along the raypath and variations in source parameters and it is not straightforward to determine how much weight should be

given to these two phenomena since they affect the inversion results differently. A constant source-time error affects all seismograms from a single earthquake in the same way; only a sphere of anomaly around the source region will produce this. Ideally, results of several inversions should be presented which have the same input parameters and data set but which incorporate different weights to raypath and source effects (they may all satisfy the data equally well). For the models in this thesis, the source time was assumed from the CMT solutions and no attempt was made to correct for a shift. Thus, these models should be considered end-member examples of what results when the difference between data and synthetics is placed entirely in structure along the raypath.

Focusing on the lower mantle layers, Fig. 5.10 shows that the patterns are similar to those of model 11aSV_1P; lateral velocity perturbations vary between -0.8% and 1.4% in layer 11 and -1.2% and 1.3% in layer 10. Looking at a depth of 2088 km, a region of high velocity exists under Australia and up into Asia; this feature persists into the lowermost mantle and is strikingly similar in both models, suggesting a strong, real-Earth feature that survives the filtering of inversion techniques. A weaker low velocity region under Africa extends into the lowermost mantle and a low velocity anomaly under the Pacific persists into the outermost core, but is most prominent for depths 2630-2891 km. As Fig. 5.11 shows, structure in the lower mantle layers is relatively long-wavelength with spectral amplitudes falling off rapidly.

Crossing the CMB into the outermost core once again produces a change in velocity anomaly patterns, shown in Fig. 5.10. Layer 12 again exhibits relatively long-wavelength velocity structure with lateral velocity perturbations varying between -0.5% and 0.6% but the patterns are different from those in the lowermost mantle. The ring of high velocity anomaly has spread out to cover the entire Southern Hemisphere and a low velocity anomaly has extended into the Northern Hemisphere.

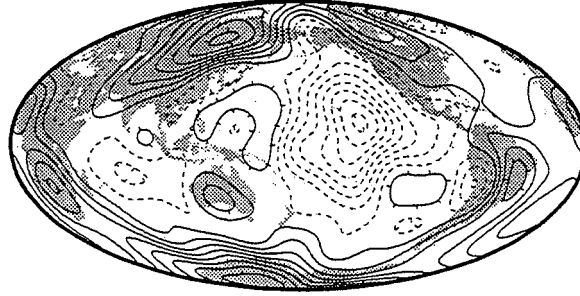
5.5.d 11-layered model with $1/M_0$ data weighting

For completeness, a short description of model 11bSV follows. 11bSV contains 11 mantle layers of S-wave velocity perturbations by inverting data using the weighting scheme defined by I^2 . Like 11aSV, 11bSV was obtained to compare the structural patterns and variance reductions with its 12-layered complement, 11bSV_1P, to assess the need for the 12th layer to describe lateral variations in velocity to explain the data. The input parameters are exactly the same as for 11bSV_1P, except for a reduction in the number of layers by one. The results of the 11-layer inversion are given in Fig. 5.12 with plotting details the same as those for Fig. 5.5. Fig. 5.13 shows spectral amplitudes for the model 11bSV; the amplitudes are plotted as functions of ℓ for individual layers.

As with model 11bSV_1P, the upper mantle layers are more heterogeneous than the rest of the mantle. As this plot shows, lateral velocity perturbations range from -8.3% to 8% in the top 220 km (layer 1) with a smaller range in layers 2-4. Model 11bSV looks almost exactly like model 11bSV_1P for layers 1-10. The amplitudes and patterns of anomalies in these layers are almost exactly the same, as the contour lines in Fig. 5.12 show. It follows that the spectral amplitudes are almost exactly the same, shown in Fig. 5.13.

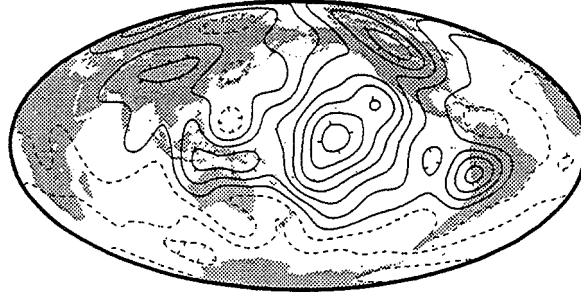
The lowermost mantle, illustrated in layer 11 of Fig. 5.12 is much more similar to layer 11 in model 11bSV_1P than the patterns seen in 11aSV_1P and 11aSV. As before, high velocity anomalies lie under continents (e.g., Asia and Australia) for depths 2630-2891 km. However, the patterns given by the contour lines are shifted a very small amount relative to 11bSV_1P; the range of velocity perturbations in the lowermost mantle of 11bSV is -0.8% to 1.4%. This figure shows that changing the parameterization from 11 layers to 12 layers changes the patterns in the lowermost mantle by a small amount. The results of the F test for models 11bSV_1P and 11bSV again indicate that velocity anomalies in the 12th layer are different from zero at the 99% confidence level.

Layer 1-depth range 0-220 km



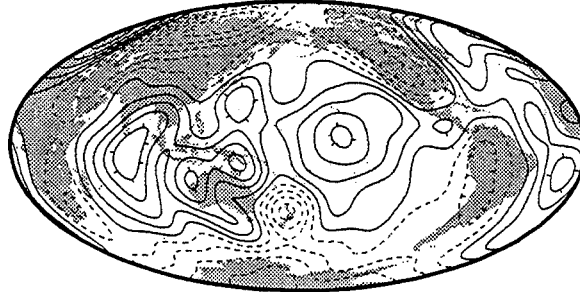
1.0%

Layer 2-depth range 220-400 km



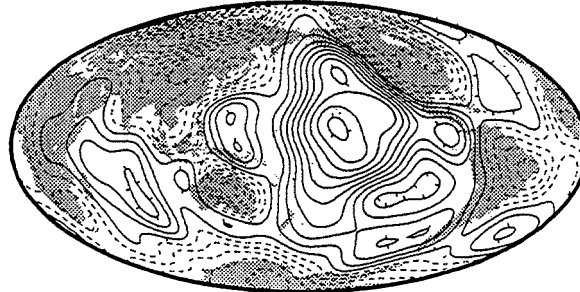
0.5%

Layer 3-depth range 400-670 km



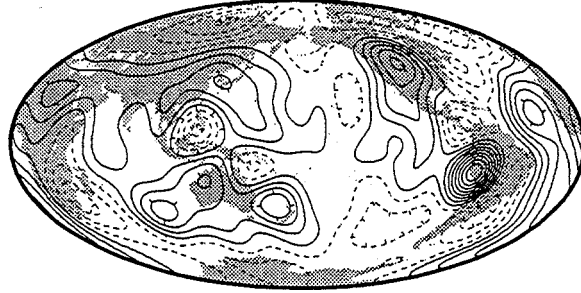
0.5%

Layer 4-depth range 670-1022 km



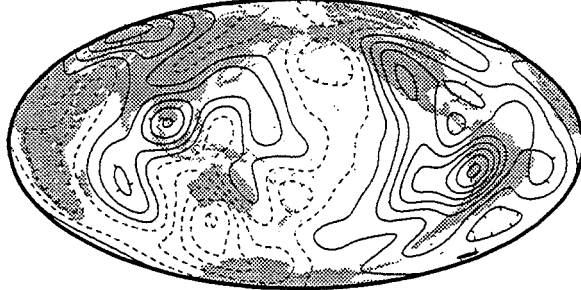
0.5%

Layer 5-depth range 1022-1284 km



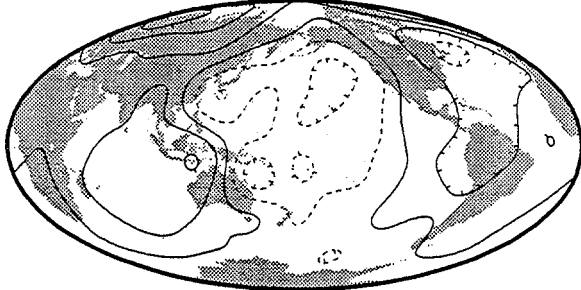
0.5%

Layer 6-depth range 1284-1555 km



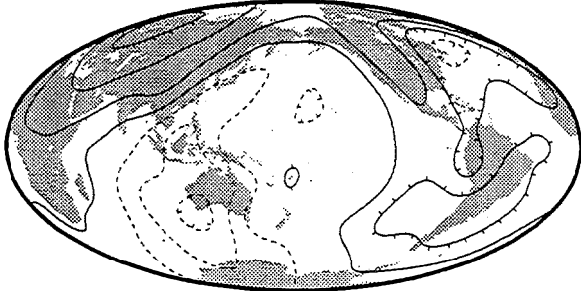
0.5%

Layer 7-depth range 1555-1816 km



0.5%

Layer 8-depth range 1816-2088 km



0.5%

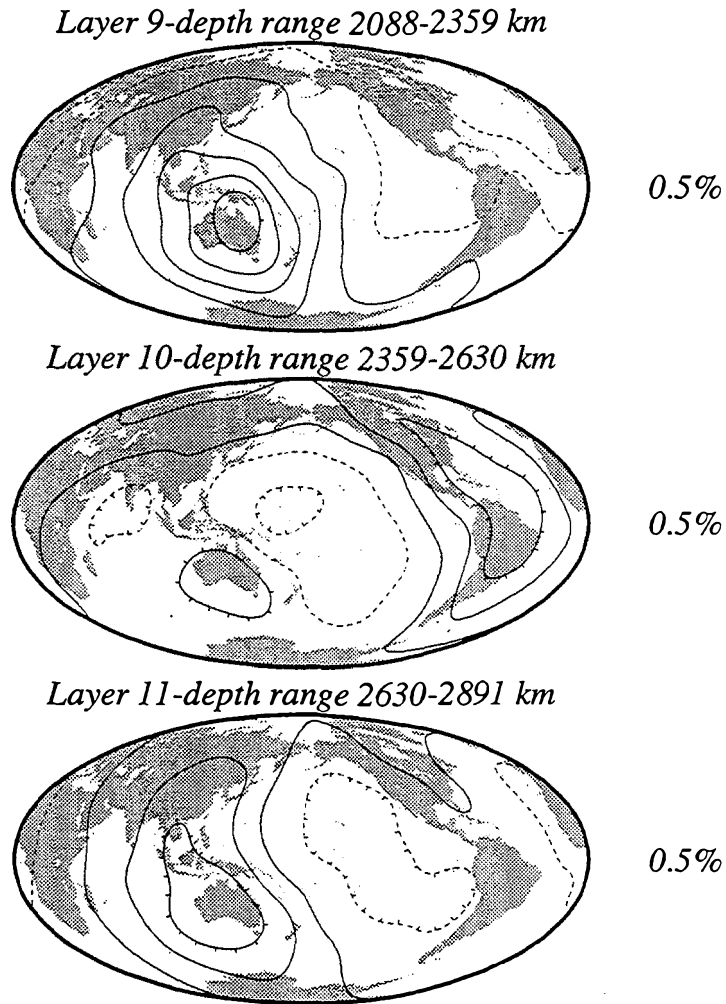
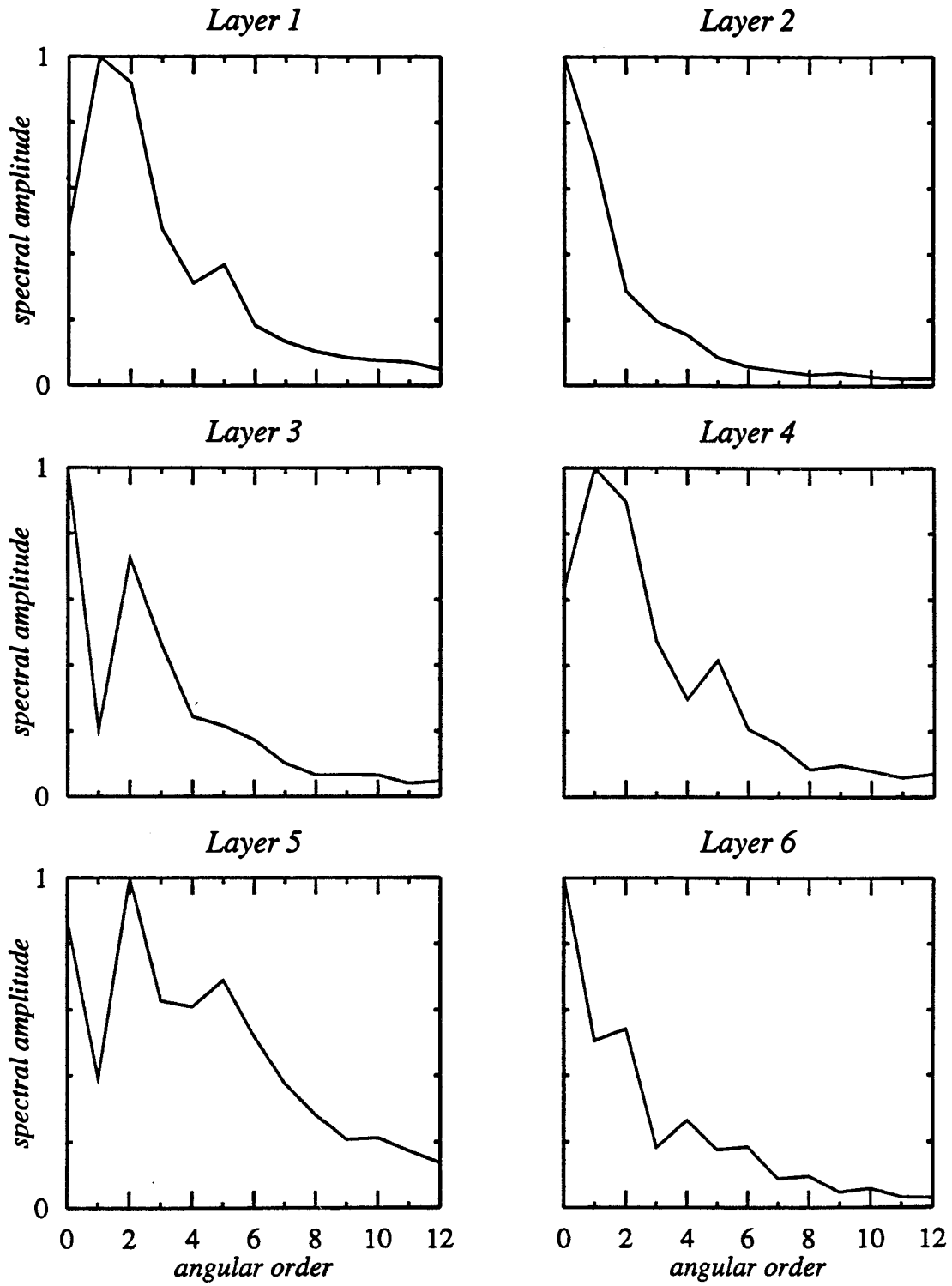


Fig. 5.12 Results of 11-layer inversion using the data weighting scheme defined by I^2 (model 11bSV). Velocity (layers 1-11: S-wave) contours are given to the right of the corresponding layer. Solid lines represent positive velocity perturbations and dashed lines represent negative velocity perturbations. The first solid contour indicates the zero percent velocity anomaly.



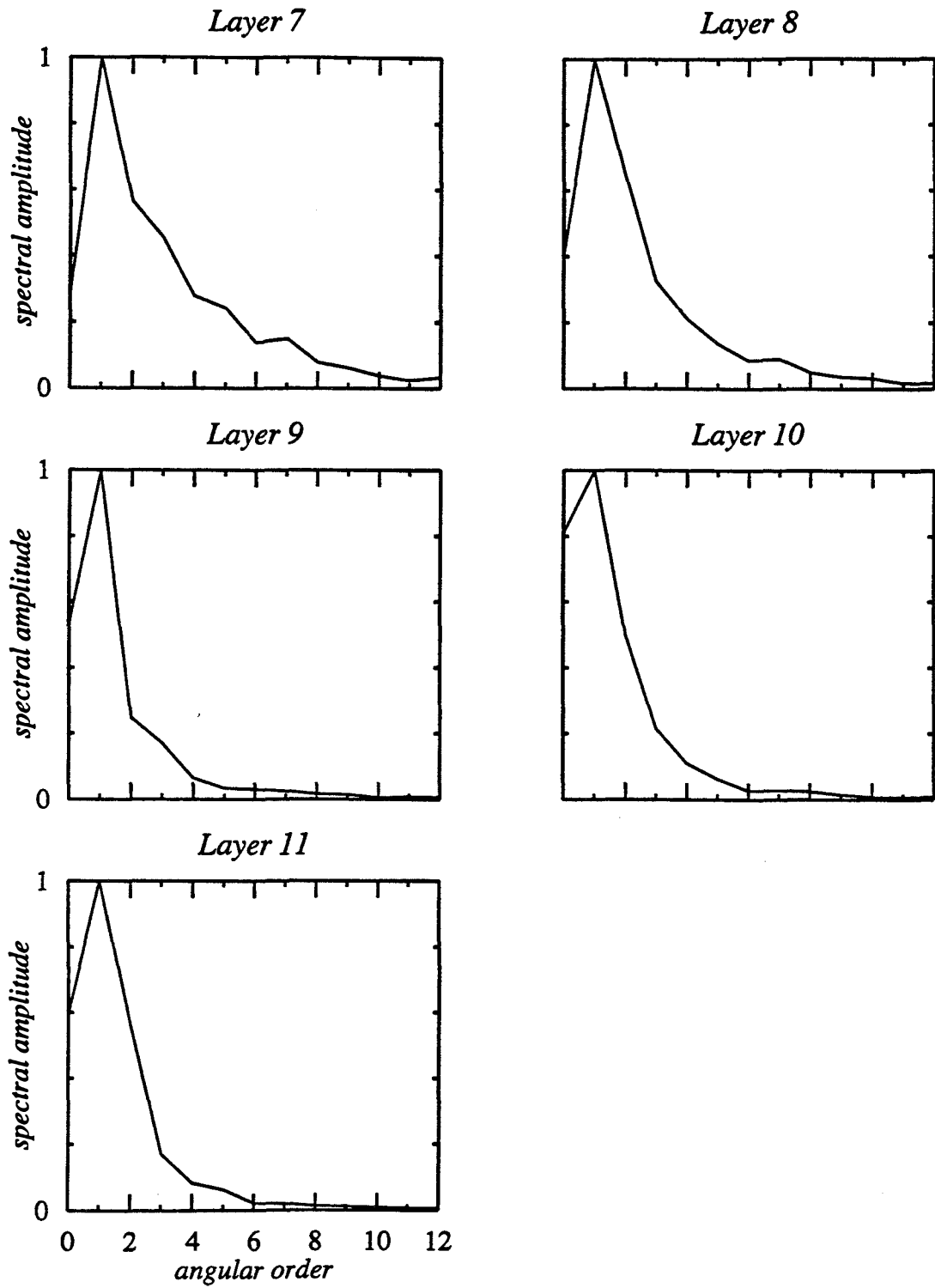


Fig. 5.13 Spectral amplitudes for model 11bSV plotted as functions of ℓ for individual layers indicated at the top of each plot.

5.6 Resolution

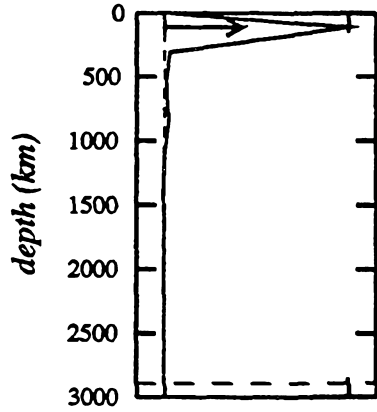
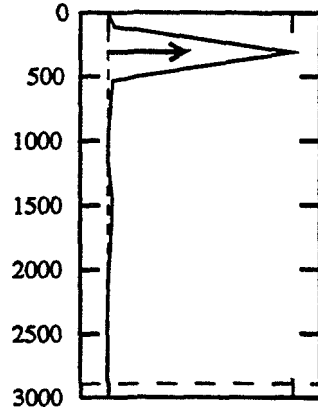
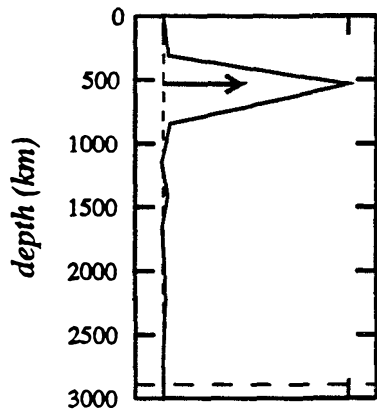
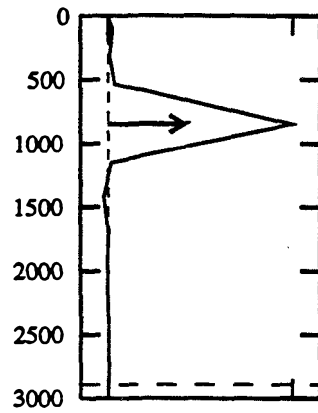
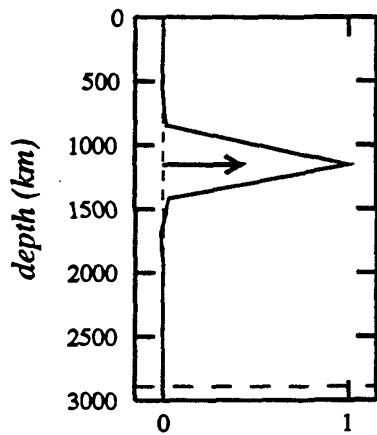
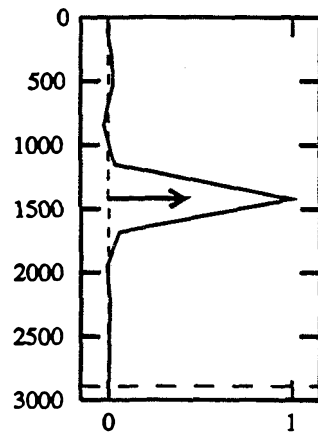
For the forward linear problem given by Eq. [5.9], the observed data values, \mathbf{b} , generally do not equal the computed values, \mathbf{Ax} , where \mathbf{x} is the computed, least-squares solution. This is because the "true" model, \mathbf{x}_{true} , is usually impossible to compute due to observational, parameterization, and computational errors. The resolution operator which defines the relationship between \mathbf{x} and \mathbf{x}_{true} ($\mathbf{x} = \mathbf{R}\mathbf{x}_{\text{true}}$) has matrix elements given by

$$\mathbf{R} = (\mathbf{A}^T \mathbf{W} \mathbf{A} + \lambda^2 \mathbf{L})^{-1} (\mathbf{A}^T \mathbf{W} \mathbf{A}). \quad [5.23]$$

If this is close to the identity matrix, then resolution is good. Depth resolution will not be better than the smallest parameterization element, i.e., the thickness of the layer.

Resolution plots are presented for inverse results using the definition in Eq. [5.23]. Values for specific coefficients and layers (given by the midpoint or "target depth") were obtained by examining the corresponding elements of \mathbf{R} . The narrower the half width of the resolution curve for a target depth, the better the resolution for that layer. The depth resolution for the target depth was estimated from the half width of the resolution curve. It is not surprising that the half widths increase with increasing target depth since the raypath coverage is more dense in the mid mantle than in the lower mantle and outermost core. These plots should not be confused with mode kernels.

Fig. 5.14 is a plot of resolution as a function of depth for the c_0^0 spherical harmonic expansion term for model 11aSV_1P. Any term could have been examined by choosing the associated elements of \mathbf{R} , producing different results; here c_0^0 was randomly selected. The resolution is plotted as a function of depth in km to a maximum depth of 3000 km, the depth of the midpoint of the deepest layer, and the CMB is given by the horizontal dashed line. The values of the resolution are normalized by the maximum value

Depth=110 km (S-wave)*Depth=310 km (S-wave)**Depth=535 km (S-wave)**Depth=846 km (S-wave)**Depth=1153 km (S-wave)**Depth=1420 km (S-wave)*

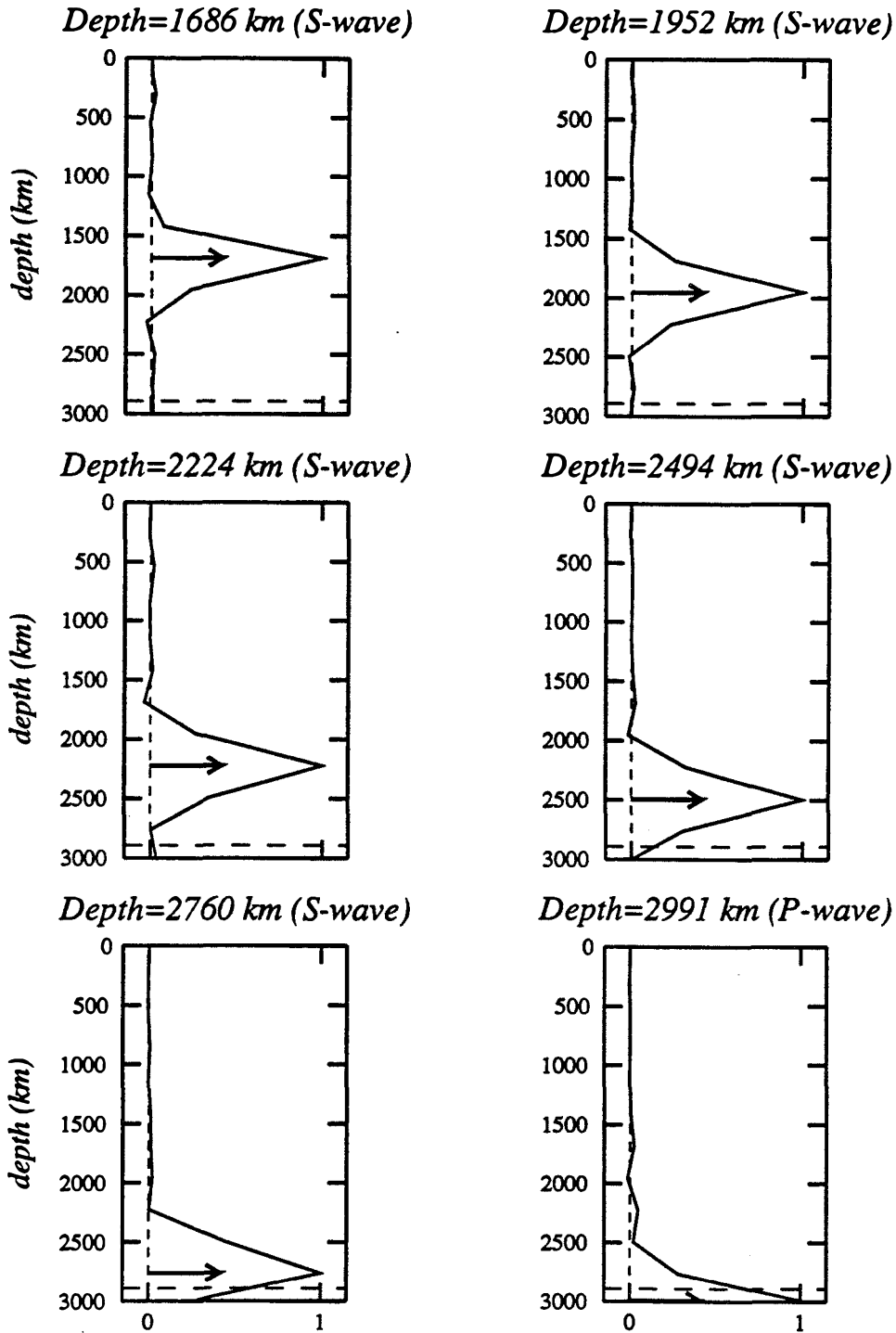
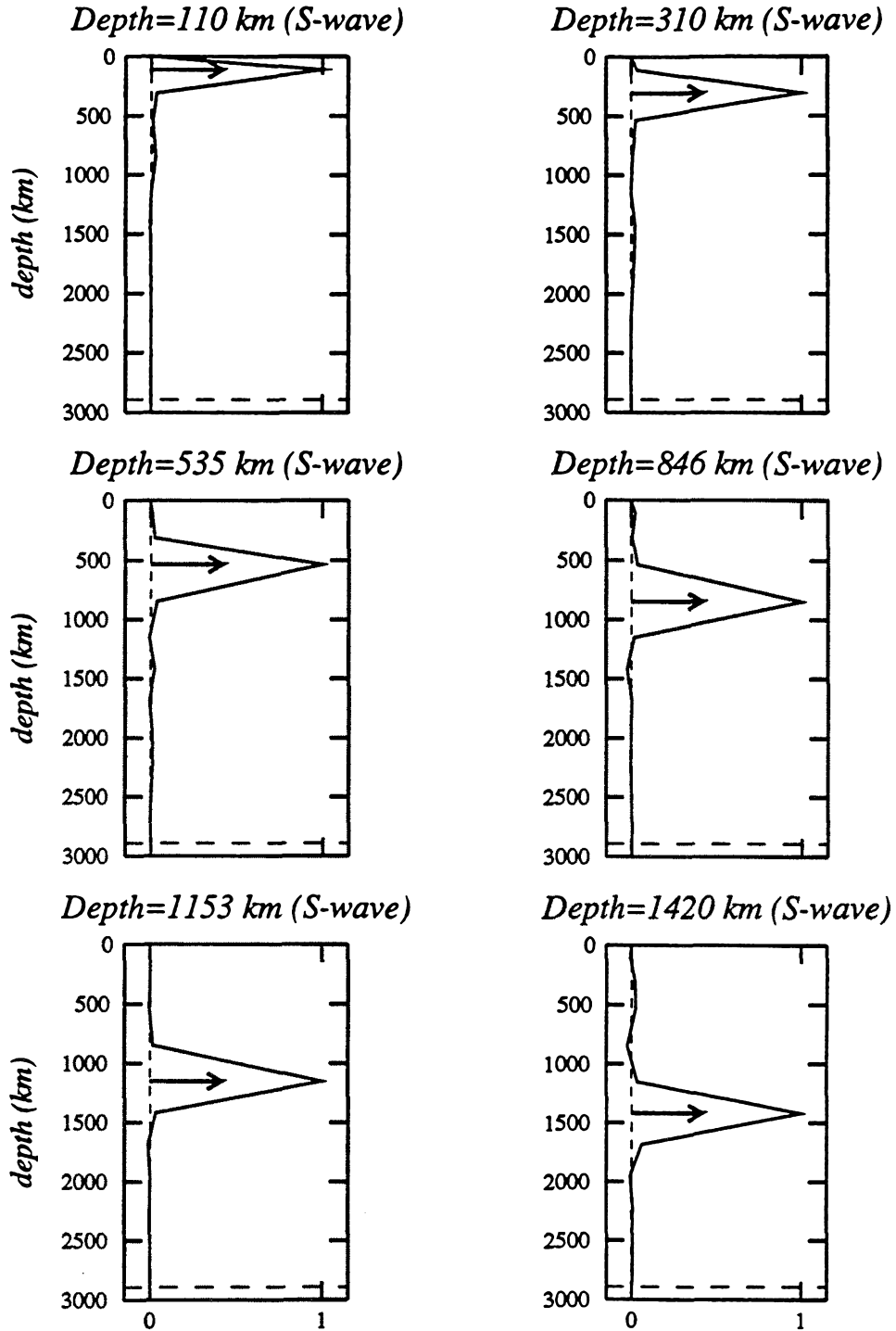


Fig. 5.14 Depth resolution for 12 target depths of model 11aSV_1P. The resolution is plotted as a function of depth and the target depths are indicated by the arrows drawn at the midpoint of each layer. The resolution curves have been normalized by the maximum value for each target depth. Note that the resolution is good for most layers, but that the half widths of the peaks, an indicator of resolution, grows with depth.

for each layer. The first 11 resolution plots correspond to S-wave velocity in the mantle and the 12th layer is for P-wave velocity in the outermost core layer. The target depth for a specific layer is given by the arrow pointing to the midpoint of that layer. If the resolution was perfect, the curve would peak only at the target depth and would be zero for all other depths, resulting in a sharp peak with no secondary peaks. As this plot shows, resolution is good for most depths, decreasing in quality with depth. The plot does not exhibit any large, undesired secondary peaks away from the target midpoint for any of the depths; some depths contain small secondary peaks, such as the slight peak in resolution around a depth of 1450 km for the target depth of 535 km and a slight peak around 250 km for the target depth of 1686. These peaks are small and do not constitute much spreading of the solution away from the target depths. The pattern retrieval resolution tests of Chapter 2 support this conclusion.

The half widths of the peaks in Fig. 5.14 are narrow for the first six target depths (depths < 1500 km) and their values indicate that resolution of 200-300 km for the upper mantle and 300-450 km for the lower mantle has been achieved. The widths increase with target depth and the plots for the lowermost mantle and outermost core indicate that depth resolutions of about 500 km have been attained. This is not as good as that achieved for the upper mantle, but it is not surprising given that lower mantle raypath coverage is less complete. As Fig. 5.15 shows, the resolution curves for the 11 target depths of model 11aSV are almost identical, indicating that differences in parameterization did not affect resolution.

Depth resolution was also examined for models 11bSV_1P and 11bSV. These curves are shown in Figs. 5.16 and 5.17. Like before, the resolution in the top six layers of these two models is good and there are no large secondary peaks. The half widths range from 200-300 km in the upper mantle and 500-600 km in the lower mantle. These resolution ranges are not as good as those resulting from 11aSV_1P and 11aSV in the mid and lower mantle, due to the different weighting of seismograms. There is no difference in



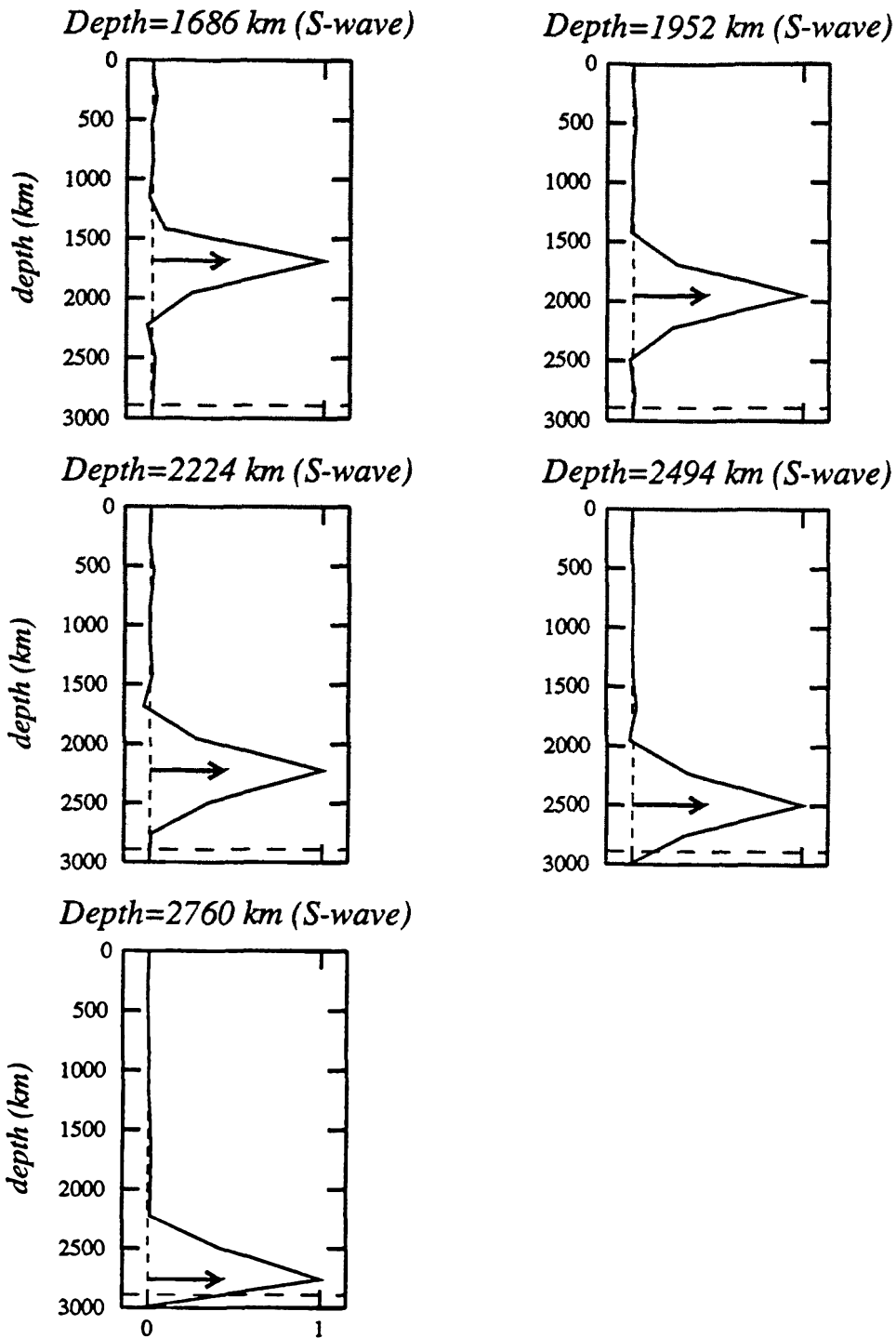
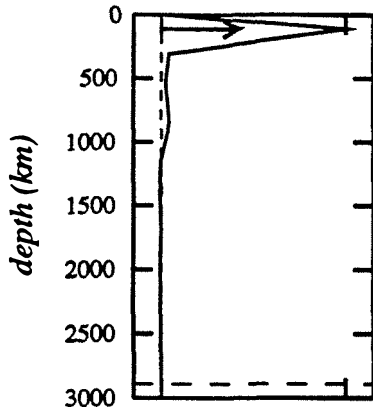
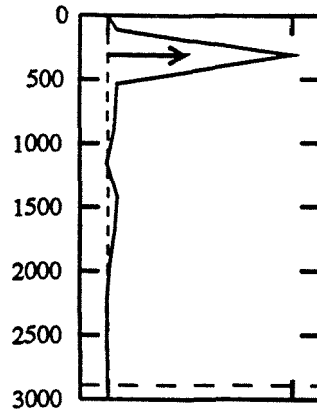
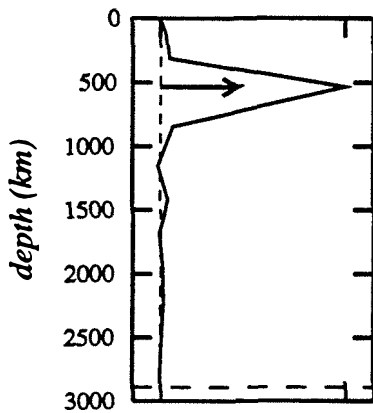
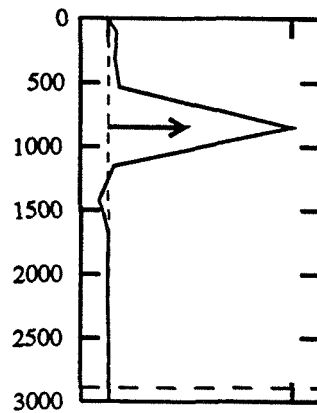
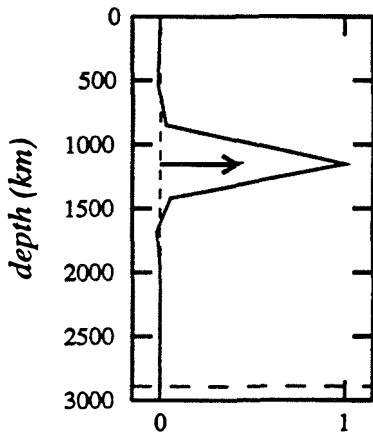
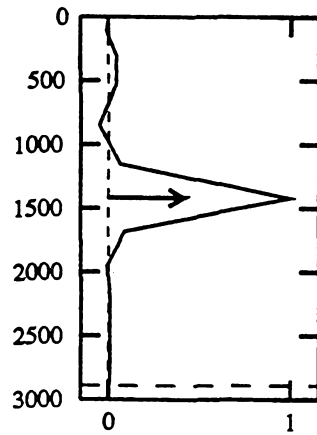


Fig. 5.15 Depth resolution for 11 target depths of model 11aSV. The resolution is plotted as a function of depth and the target depths are indicated by the arrows drawn at the midpoint of each layer. The resolution curves have been normalized by the maximum value for each target depth. Note that the resolution is good for most layers, but that the half widths of the peaks, an indicator of resolution, grows with depth.

Depth=110 km (S-wave)*Depth=310 km (S-wave)**Depth=535 km (S-wave)**Depth=846 km (S-wave)**Depth=1153 km (S-wave)**Depth=1420 km (S-wave)*

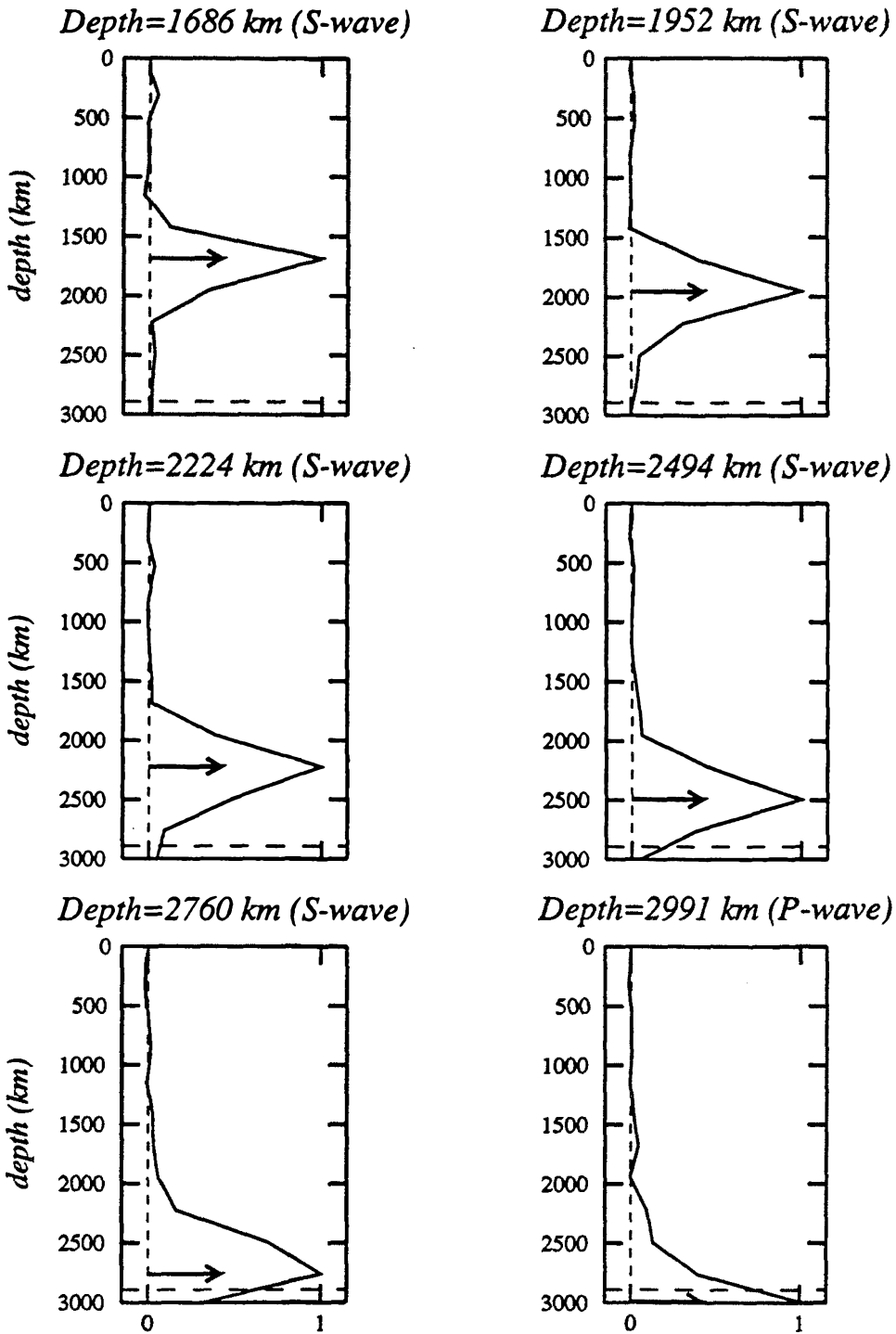
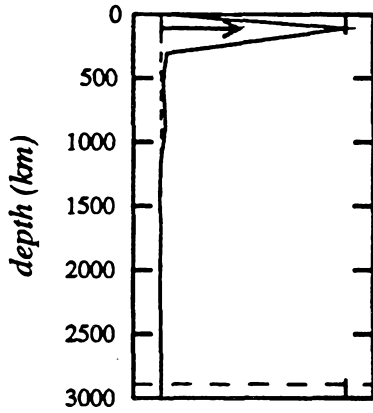
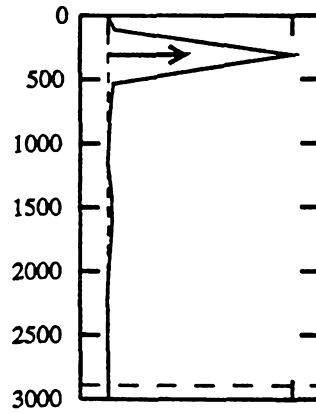
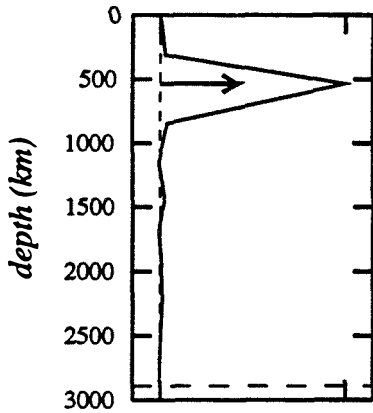
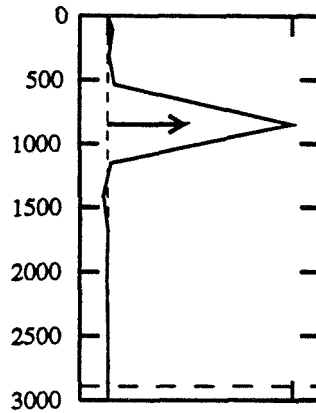
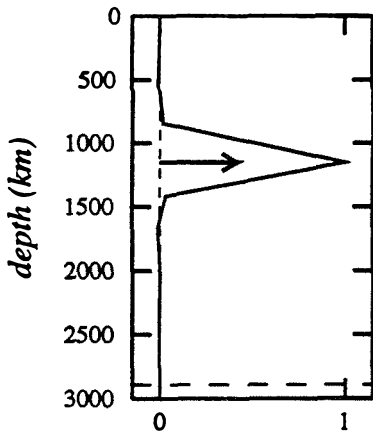
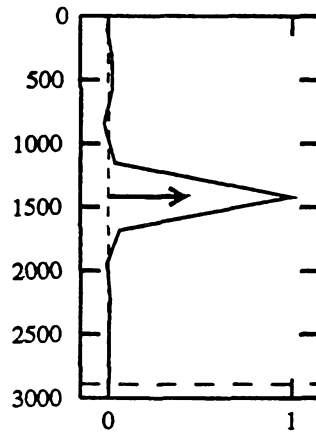


Fig. 5.16 Depth resolution for 12 target depths of model 11bSV_1P. The resolution is plotted as a function of depth and the target depths are indicated by the arrows drawn at the midpoint of each layer. The resolution curves have been normalized by the maximum value for each target depth. Note that the resolution is good for most layers, but that the half widths of the peaks, an indicator of resolution, grows with depth.

Depth=110 km (S-wave)*Depth=310 km (S-wave)**Depth=535 km (S-wave)**Depth=846 km (S-wave)**Depth=1153 km (S-wave)**Depth=1420 km (S-wave)*

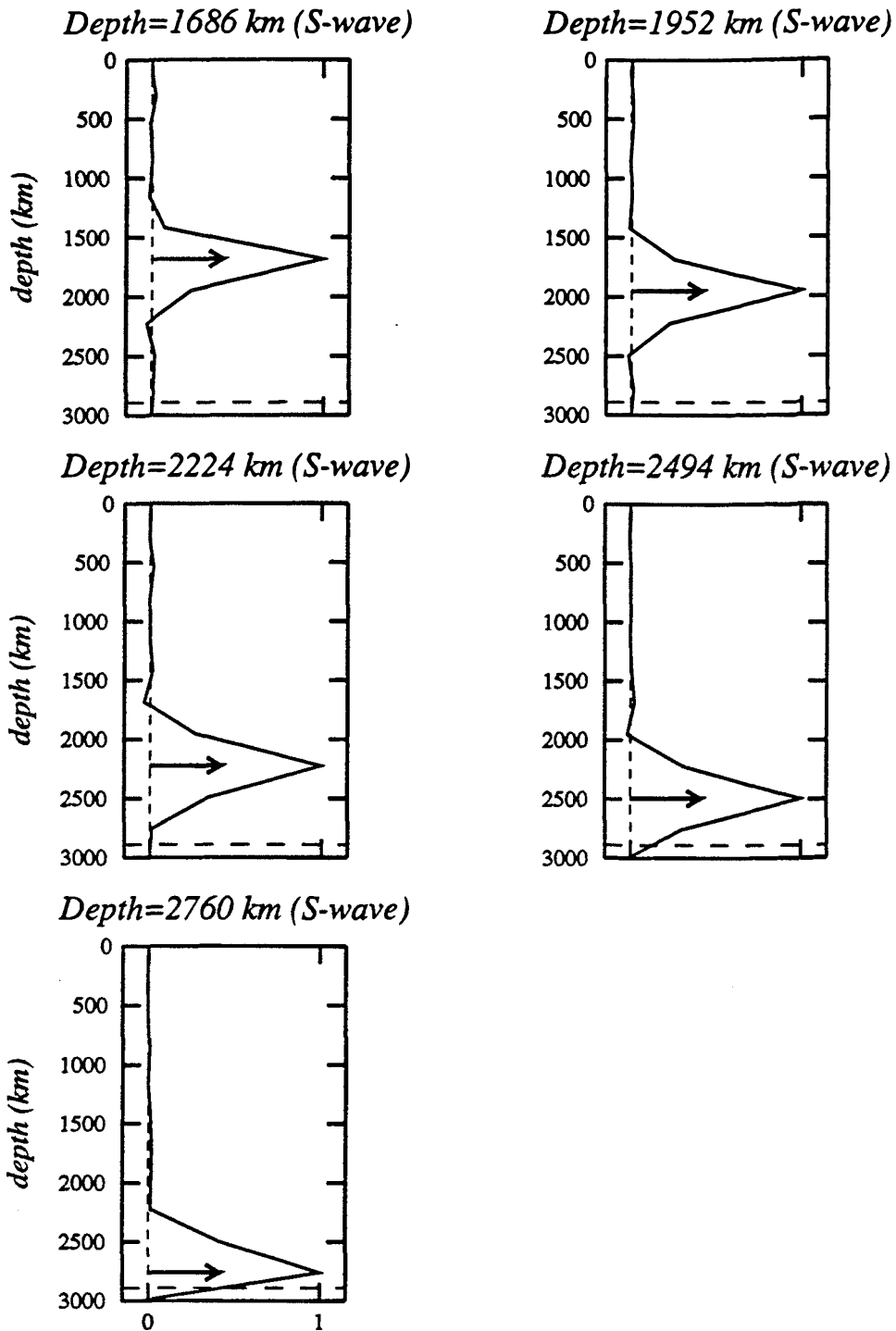


Fig. 5.17 Depth resolution for 11 target depths of model 11bSV. The resolution is plotted as a function of depth and the target depths are indicated by the arrows drawn at the midpoint of each layer. The resolution curves have been normalized by the maximum value for each target depth. Note that the resolution is good for most layers, but that the half widths of the peaks, an indicator of resolution, grows with depth.

resolution for 11bSV. The depth resolution remains almost the same for the lowermost mantle layer regardless of whether there is structure below it. The resolution results presented in this section all included contributions from the Rayleigh wave phase perturbations. Plots of depth resolution which did not include the contributions of phase perturbations showed that they had almost no effect on resolution in the upper mantle.

5.7 F test

As in many geophysical inverse problems, the optimal solution is that which has the smallest number of solution parameters to describe a model and still produces an acceptably small data-model misfit. In this case, it was not clear whether 11 mantle layers alone, or 11 layers with the 12th outermost core layer produced the optimum model of global Earth structure; this inverse problem uncertainty is partly the result of the more numerous mantle phases and their larger amplitudes in the data set. The statistical F ratio provides a test for the necessity of the 12th layer coefficients to describe global Earth structure.

The F ratio is a measure of confidence about whether coefficients describing a model are non-zero by comparing two statistics which follow the chi-square (χ^2) distributions [Draper and Smith, 1966]. The confidence is stated in terms of a probability between 0-100% after comparing the F ratio to a table of χ^2 distribution probabilities from random data sets. The particular F ratio used here is one which tests the significance of additional terms. Like the standard F ratio which is a ratio of two χ^2 distributions, this test is made by examining the ratio of the difference in the χ^2 distributions for the 11- and 12-layered models, to the value for the 12-layered model, each divided by the respective degrees of freedom [Draper and Smith, 1966]. By the definition of χ^2 , a ratio of the sum of squares of the deviations about the regressions (i.e., the sum of squares of the residuals,

or data variance), which represents the agreement between data and model fit, can be used as an F ratio measure. Specifically, the F ratio used here is given by

$$F = \frac{(SSR_1 - SSR_2)/(DOF_1 - DOF_2)}{SSR_2/DOF_2} \quad [5.24]$$

where SSR is the sum of squares of the residual, DOF is the number of degrees of freedom, and subscripts 1 and 2 stand for the 11- and 12-layered models, respectively. If F is large, it can be stated with a degree of confidence that the extra terms (layer 12 coefficients) are not zero and the fit with the additional terms is significantly improved

Table 5.1 Analysis of F test results of 11- and 12-layer inversions with $1/v_b$ and $1/M_0$ data weighting schemes.

Model	SSR	DOF	F ratio
11aSV (11 layers)	6.07×10^{13}	788,085	66.1
11aSV_1P (12 layers)	5.98×10^{13}	787,916	
11bSV (11 layers)	6.06×10^{13}	788,085	65.7
11bSV_1P (12 layers)	5.98×10^{13}	787,916	

over the fit with fewer terms. Table 5.1 summarizes the F test results of the 11- and 12-layer inversions with the two different data weighting schemes indicated.

As this table demonstrates, the F ratio suggests that at the 99% confidence level the null hypothesis can be discarded and the 12th layer is statistically significant in the three-dimensional models. It should be noted that the F ratio values are much larger than expected for the respective number of degrees of freedom. This is due to the inaccurate method of determining the number of degrees of freedom from the number of time points in each seismogram. For this inverse problem, each time point contributes to the inverse matrix but they are not all independent. There is no straightforward way of determining the correct DOF; therefore the numbers given above are probably too large. More generally, this test suggests that the requirement of more parameters than those provided by the 11-layered model is justified, however, it does not require that the 12th layer lie in the outermost core.

5.8 Conclusions

5.8.a Preferred model

Based on the evidence presented here, the preferred model is 11aSV_1P, the 12-layered model incorporating data weighted by the scheme defined by I¹. To summarize, this model produces velocity anomalies in the mantle and outermost core which are acceptable for first-order perturbation methods. In addition, the patterns of structure vary smoothly and do not exhibit inexplicable bulls-eye-shaped patches of intensely high or low velocity at depth with respect to PREM. The data variance reduction of entire body-wave portions as well as SnKS portions of seismograms are slightly better for the 12-layered model than for the 11-layered model, and the results of the statistical F ratio suggest that lateral velocity variations in the outermost core layer are not zero. This test does not

require, however, that the extra layer lie in the outermost core (as opposed to the lowermost mantle). Finally, the results of one-layer inversions (Chapter 4) also point to the possible existence of lateral variations in the outermost core, most likely between $\pm 0.5\%$ but not as large as $\pm 5\%$. If this is accurate, then outermost core P-wave velocity perturbations accompany S-wave velocity perturbations in the lowermost mantle to produce observed variations in SKS-S and SKKS-SKS travel times. The results of pattern retrieval resolution tests support the conclusion that structure of the outermost core has been obtained independently from the mantle. Multiplicative factors have been calculated from the resolution tests which can be used to place upper and lower bounds on the amount of power that actually resides in the lowermost mantle and outermost core layers from the three-dimensional inversions for real Earth structure.

One way in which lateral temperature variations in the lowermost mantle could affect the character of the outermost core and give the appearance of drastic lateral velocity variations, even if the outermost core is laterally homogeneous, is described as follows. Temperature variations in the lowermost mantle could dramatically affect the shape of CMB topography and any underlying stratified outermost core layers. Outermost core fluid lying beneath relatively cold mantle fluid would experience downwelling. Core fluid passing beneath a cold (high temperature gradient) patch of mantle will lose heat through conduction, immediately become denser, and fall away due to lower viscosity. A patch of fluid passing beneath a hot part of mantle will just stay hot and not necessarily rise. It is the cold downwellings, rotation of the Earth, and location of inner core tangent cylinders that control the locations of the upwellings. The shape of the affected outermost core layer may be highly correlated to the shape of CMB topography which is, in turn, correlated to lateral temperature variations in the lowermost mantle. Even if the thermal and compositional character of the affected stratified outermost core layer is laterally homogeneous, it may appear laterally heterogeneous in tomography inversions when the Earth is parameterized radially in shells of uniform thickness and radii. This would occur

if the amplitude and wavelength of variations were below the radial and lateral resolution of tomographic results, although they would still need to be quite large.

5.8.b Source of outermost core heterogeneity

A large number of studies strongly indicate thermal coupling between the mantle and core. Convection in the core is almost certainly due to rotation, cooling from above, and by growth of the inner core. Mantle convection on a global scale is driven, in part, by heat escaping from the core but regions of the outermost core are most likely influenced by lateral temperature variations in the lowermost mantle. For example, Ruff and Anderson [1980] proposed that the distribution of radioactivity in the lower mantle is a cause of motions in the core, i.e., differential cooling from above. Static features in the magnetic field suggest that flow in the core is coupled to the mantle where core fluid is upwelling beneath warmer mantle and downwelling beneath cooler mantle [Bloxham and Gubbins, 1987]. Gubbins [1988] maintains that the dynamo is driven by deep-seated fluid motions in the core, but also that these motions may be tied to temperature anomalies in the lower mantle because parts of the magnetic field appear to have a surface origin while others have deeper origins. Furthermore, Zhang and Gubbins [1992] propose that thermal interactions between the mantle and core is a plausible mechanism for strong lateral variations in heat flux across the CMB and model the fluid flow in the liquid core driven by lateral variations in temperature in the lowermost mantle.

Relatively warm lowermost mantle fluid (which appears as seismically slow regions) may be producing highs in CMB topography. This, in turn, may cause lateral movement of core fluid in a thin layer underneath the CMB or core fluid upwellings. Relatively cold mantle (appearing as seismically fast regions) will sink, causing depressions in CMB topography and downwellings in core fluid. In our model, if low velocities are associated with thermal lows, then relatively warm mantle fluid under Africa in D" is affecting outermost core velocities in the same region, and relatively cool mantle fluid

under Australia and part of Asia may be influencing outermost core velocities in the southern Pacific (shown by model 11aSV_1P). This model suggests that thermal coupling exists, but the correlation between mantle thermal anomalies and core thermal anomalies is not perfect. This implies that outermost core velocity structure is only partly influenced by temperature variations and that other sources heterogeneity are producing lateral variations in outermost core structure. Theoretical studies involving magnetic field secular variation data inversions suggest that outermost core fluid motions are influenced by lateral temperature variations in the mantle, but that the resulting temperature variations in the outermost core are only on the order of mK, which would not be resolvable by seismic methods [Bloxham and Jackson, 1990,1991].

Based on theoretical fluid dynamic arguments, if the outer core is well mixed, it will not support relative density heterogeneities, $\delta\rho/\rho$, larger than 10^{-4} [Stevenson, 1987]. Therefore, if the viscosity of core fluid is so much lower than mantle fluid, small deviations from adiabaticity will aid the initiation of convection and the rapid mixing of fluid with different compositional or thermal properties. The existence of lateral velocity variations indicates some deviation of outermost core fluid from the adiabat. Gubbins *et al.* [1982] present calculations for the thermal evolution of a stable, density-stratified layer growing downward from the CMB due to slow cooling of the whole Earth. They argue that a very slow cooling rate of the CMB will not maintain convection everywhere and that sub-adiabatic, density-stratified regions will develop. Usselman [1975] and Ruff and Anderson [1980] also consider a compositionally-stratified fluid outer core based on chemical and thermal arguments.

Lateral velocity variations are not solely a function of lateral temperature variations in a region. Stacey [1993] argued that if mantle seismic velocities were dependent on temperature alone, estimates for geoid deflections from density anomalies would be too small and estimates for heat flux would be too large. He concluded that unrealistically large temperature variations in the lower mantle would be required to

explain lower mantle velocity anomalies. He also concluded that, while temperature variations exist in the lower mantle, tomographic maps are dominated by compositional variations. This argument can be made for the outermost core as well. Tanaka and Hamaguchi [1993c] calculated maximum range lateral temperature variations in the outermost core based on their seismic velocity anomalies. Assuming that the outermost core was chemically inhomogeneous, a maximum temperature difference of 1.6 K was calculated from the difference of adiabatic gradients of temperature between regions of maximum and minimum velocity perturbations. When they assumed that the outermost core was homogeneous and that temperature differences were from non-adiabatic gradients, the temperature differences between the two regions were determined to be as large as 20 K. They concluded that the outermost core is chemically stably-stratified with small temperature variations.

The results presented in this thesis agree with the conclusions of Tanaka and Hamaguchi [1993c] that the outermost core is chemically heterogeneous and that lateral velocity anomalies are due to a combination of compositional and temperature differences. We examine what conditions are conducive to the formation of a stratified layer at the top of the outer core which is 200 km in thickness (the resolution of our inversions can only place a lower bound of 200 km on the thickness of the outermost core layer). A useful measure of stratification has been examined to place constraints on the departure of core fluid from adiabaticity and homogeneity. From the Adams-Williamson relation for a hydrostatic Earth exhibiting adiabaticity and chemical homogeneity,

$$\frac{d\rho}{dr} = -\frac{g\rho}{\phi} \quad [5.25]$$

where ϕ is the seismic parameter defined by

$$\phi = \alpha^2 - \frac{4}{3}\beta^2, \quad [5.26]$$

Bullen [1963] defined an index of inhomogeneity

$$\eta = -\frac{\phi}{\rho g} \frac{d\rho}{dr} \quad [5.27]$$

which is a useful measure of the stratification of the outermost core because it is sensitive to variations in chemical composition [Bullen, 1963]. In these equations, g is the acceleration of gravity, ρ is the density, and α and β are the P-wave and S-wave velocities, respectively. The index gives the ratio of actual density gradient to the gradient corresponding to a uniform composition and adiabatic compression. Thus, if $\eta \neq 1$, a region is radially heterogeneous, possibly containing phase changes. Considering the thermodynamic and hydrodynamic aspects of stratification, the index can be interpreted as follows: $\eta > 1$ corresponds to a stable region in which convection cannot occur, implying chemical inhomogeneity and/or a sub-adiabatic temperature gradient; $\eta \equiv 1$ corresponds to neutral stability where convection can occur; and $\eta < 1$ corresponds to instability, implying a high viscosity with strong superadiabatic temperature gradients [Melchior, 1986]. For this last case, the Brunt-Vaisälä frequency can be calculated for a fluid; a value of $8.6 \times 10^{-4} \text{ sec}^{-1}$ was calculated by Tanaka and Hamaguchi [1993c]. Bullen [1969] proposed that the outer 700 km of the outer core was mildly heterogeneous from a calculated index value of 1.4 at the CMB and diminishing to unity with depth. Masters [1979] used observed periods of free oscillations to calculate the inhomogeneity index for the outer core. His results indicated the possibility of a stratified, stable region near the surface of the core. Tanaka and Hamaguchi [1993c] calculated η from three velocity models and found a mean value of 1.5 immediately beneath the CMB. These estimates imply strongly stable stratification in the outermost core due to chemical inhomogeneity (including phase changes), a sub-adiabatic gradient of temperature, or both.

A low-velocity outermost core has been observed in previous studies [Hales and Roberts, 1971; Lay and Young, 1990], leading some authors to postulate a chemically-

stratified boundary layer. This is a plausible result of the upward migration of heterogeneities relatively low in density through the core to the CMB. Specifically, chemical stratification could result from the release and upward migration of light elements being released by inner core crystallization [Fearn and Loper, 1991] or outer core cooling (decreasing solubility). Model 11SV_1P lends support to some form of chemical stratification producing seismically lower velocities. Examination of the spherical harmonic expansion coefficient c_0^0 of P-wave velocity in the outermost core layer of 11aSV_1P indicates a global velocity decrease of 0.33% with respect to PREM (Fig. 5.5 was plotted with the c_0^0 terms removed). This coincides with a 0.3% velocity decrease in the outer 200 km of the core calculated from average SKS-SKKS and SKKS-SKKKS travel-time residuals of 0.6 sec by Tanaka and Hamaguchi [1993b].

The Earth's magnetic field can provide information about a thin outer core layer different in nature from the rest of the rotating, convecting fluid outer core. Secular variation calculations indicate that the core fluid does not rotate as a whole and that differential rotation takes place in the outermost layers with fluid moving slower near the equator than at the poles [Jault *et al.*, 1988]. A boundary layer on the order of 100 km thick would also support thermal wind motions in core fluid [Kohler and Stevenson, 1990] and geostrophic motions [Bloxham and Jackson, 1990]. A boundary layer much smaller or larger than this is not supported by the seismic evidence or fluid dynamic calculations. In particular, the chemically-stratified layer formed by light elements migrating from the inner core was estimated by Fearn and Loper [1981] to be about 70 km thick. Young and Lay [1990] estimate that the thickness of this layer is about 50-100 km, and Gubbins *et al.* [1982] propose that the outermost several hundred km is stratified. Bullen [1970] concluded that the outer several hundred km of the core was mildly heterogeneous, possibly associated with continuous phase changes, but that depths below that were probably uniform in chemical composition and phase. The thickness of the outermost core layer (200 km) of model 11aSV_1P falls into the proposed ranges. While this is the best

resolution obtainable with the nonuniform coverage of long-period data, more detailed regional studies of outermost core structure can be achieved with more dense, uniformly sampled SnKS waveform data sets.

It should be noted that CMB topography alone does not explain the residuals in SnKS travel times. A 5 km increase in CMB radius will produce SKS-SKKS residuals that are much smaller than the SKS-SKKS residuals of over ± 3 sec calculated with respect to PREM [Souriau and Poupinet, 1991], ± 5 sec calculated with respect to the Jeffreys-Bullen model [Schweitzer and Müller, 1986; Garnero *et al.*, 1988] and ± 5 sec with respect to PREM [Tanaka and Hamaguchi, 1993abc]. Although they do not explain the larger travel-time residuals, variations in topography may be partially responsible for fluid inhomogeneity. Models of CMB topography [Morelli and Dziewonski, 1987; Gudmundsson, 1989; Gwinn *et al.*, 1986] conclude that radial variations are on the order of 100-1000 m with respect to a constant radius. Even if this is not large enough to produce the up to ± 5 sec SKS-SKKS travel-time residuals, bumps or other features in topography may trap significant outermost core heterogeneities, creating pools of fluid which remain chemically distinct from the rest of the rigidly rotating outer core. Furthermore, CMB topographic features may aid in flow types which cannot occur in the rest of the outer core, such as thermal wind (of which eastward and westward drift, and geostrophic flow would be special cases), or turbulent in the extreme case, although this would tend to decrease the heterogeneity.

It has been suggested here that lateral velocity anomalies in the outermost core are due to compositional and temperature variations. The source and character of the variations have not been determined and it is not known yet whether material of different composition originates at the inner-outer core boundary or in the lowermost mantle, as Knittle and Jeanloz [1989] suggest. In order to place tighter constraints on the relative degrees of chemical and thermal effects on lateral velocity variations, more accurate estimates are needed of the dependence of seismic velocities on temperature and

compositional variations for a range of plausible fluid compositions for the outermost core.

Consider an outermost core consisting of a binary system of chemical ingredients. The melting point and shock velocity experiments indicate that the core is composed mainly of iron with a fraction (8-20% [Fearn and Loper, 1981]) of some lighter material. The light alloying element may be O, S, Si, N, H, He, or C. Sulphur and Oxygen are good candidates since they would reduce the melting temperatures of outer core liquid to estimated values at appropriate pressures [Anderson, 1989; Ahrens, 1979; Usselman, 1975] and satisfy seismic fits to equations of state [Butler and Anderson, 1978]. Theoretical outer core fluid compositions could be synthesized in terms of the atomic makeup of a variety of different percentages of constituent elements. These properties could then be used in thermodynamic calculations of equations of state for a range of outermost core chemical models. The acceptable models would be chosen according to how well they matched the observed lateral variations in velocity from three-dimensional inversions or lateral variations in travel-time residuals.

The effects of a slurry zone should also be considered in theoretical outermost core compositions. Loper [1991] suggests that the cooling of the core results in the freezing of the inner core, and that if the temperature of the core reaches the liquidus in the outer core above the inner-outer core boundary, a slurry of suspended crystals can exist in such a region. If regions in the top of the outer core are being cooled by the lowermost mantle, a slurry may also exist in pockets of fluid just beneath the CMB. The outer core may behave like a fluid even if temperatures are below the liquidus and if it contained 30% or more of suspended particles [Anderson, 1989].

The Bullen index of inhomogeneity, η , mentioned above, does not help distinguish between stratification due to chemical or temperature inhomogeneity. However a variation of the index will be more useful in clarifying the relative effects. Following Masters [1979], η can be rewritten

$$\eta = 1 - \frac{\alpha\phi\tau}{g} - \frac{\phi}{\rho g} \sum_{i=1}^n \left(\frac{\partial \rho}{\partial x_i} \right)_{p,s,x_j} \frac{dx_i}{dr} \quad [5.28]$$

where α is the coefficient of thermal expansion, ϕ is the seismic parameter, τ is the difference between the actual and adiabatic temperature gradients, g is the gravitational acceleration, ρ is density, and the summed terms represent a mixture of n components, each indicated by the subscript i . The partial derivative of density with respect to each component is carried out with constant pressure, p , entropy, s , and composition of other components, x_j . As Masters [1979] points out, this is a more straightforward way of showing the contributions of thermal and chemical inhomogeneities to η . To obtain the relative contribution departures from adiabaticity and chemical homogeneity, the effects of temperature and composition on bulk moduli and density would need to be calculated.

The thermal inhomogeneity contribution can be obtained by determining the effects of temperature on density, the bulk modulus, K_s , or seismic parameter also defined as

$$\phi = \frac{K_s}{\rho}. \quad [5.29]$$

This is accomplished by calculating the equations of state and Gruneisen parameters for a range of theoretical core compositions with elemental components considered above. Temperature variations can be represented as small perturbations to the reference bulk modulus [Anderson, 1989]. The effect of composition and phase on the seismic parameter is determined in terms of the atomic makeup of individual contributions to the theoretical core fluid chemical model. The composition contribution to seismic parameter, as a function of bulk modulus and density, can be calculated by considering the atomic properties such as weight, spacing and energy in terms of molar averages of constituent elements of the theoretical core fluid.

References

- Ahrens, T. J., Equations of state of iron sulfide and constraints on the sulfur content of the Earth, *J. Geophys. Res.*, **84**, 985-998, 1979.
- Aki, K. and P. G. Richards, *Quantitative Seismology*, Vols. 1 and 2, W. H. Freeman and Co., New York, 1980.
- Anderson, D. L., *Theory of the Earth*, Blackwell Scientific Publications, Boston, 1989.
- Anderson, D. L. and R. S. Hart, An Earth model based on free oscillations and body waves, *J. Geophys. Res.*, **81**, 1461-1475, 1976.
- Backus, G., Geographical interpretation of measurements of average phase velocities of surface waves over great circular and great semi-circular paths, *Bull. Seis. Soc. Am.*, **54**, 571-610, 1964.
- Backus, G. and F. Gilbert, Numerical applications of a formalism for geophysical inverse problems, *Geophys. J. R. astr. Soc.*, **13**, 247-276, 1967.
- Backus, G. and F. Gilbert, The resolving power of gross Earth data, *Geophys. J. R. astr. Soc.*, **16**, 169-205, 1968.
- Backus, G. and F. Gilbert, Uniqueness in the inversion of inaccurate gross Earth data, *Philos. Trans. R. Soc. London, Ser. A*, **266**, 123-192, 1970.
- Bloxham, J., Simple models of fluid flow at the core surface derived from geomagnetic field models, *Geophys. J. Int.*, **99**, 173-182, 1989a.
- Bloxham, J. On mapping the fluid flow at the core surface, *Eos Trans. AGU*, **70**, 1075, 1989b.
- Bloxham, J. and D. Gubbins, The secular variation of Earth's magnetic field, *Nature*, **317**, 777-781, 1985.
- Bloxham, J. and D. Gubbins, Thermal core-mantle interactions, *Nature*, **325**, 511-513, 1987.

- Bloxham, J. and A. Jackson, Lateral temperature variations at the core-mantle boundary deduced from the magnetic field, *Geophys. Res. Lett.*, **17**, 1997-2000, 1990.
- Bloxham, J. and A. Jackson, Fluid flow near the surface of Earth's outer core, *Rev. Geophys.*, **29**, 97-120, 1991.
- Boyle, J. and K. Dritz, An automated programming system to aid the development of quality mathematical software, *IFIP Proceedings*, North Holland, 542-546, 1974.
- Bullard, E. C., C. Freedman, H. Gellman, and J. Nixon, The westward drift of the Earth's magnetic field, *Phil. Trans. R. Soc.*, **A243**, 67-92, 1950.
- Bullen, K. E., An index of degree of chemical inhomogeneity in the Earth, *Geophys. J. R. astr. Soc.*, **7**, 584-592, 1963.
- Bullen, K. E., Compressibility-pressure gradient and the constitution of the Earth's outer core, *Geophys. J. R. astr. Soc.*, **18**, 73-79, 1969.
- Bullen, K. E., Comparison of sources of evidence on the variation of incompressibility in the Earth's deeper interior, *Phys. Earth and Plan. Int.*, **3**, 36-40, 1970.
- Butler, R. and D. L. Anderson, Equation of state fits to the lower mantle and outer core, *Phys. Earth and Plan. Int.*, **17**, 147-162, 1978.
- Cara, M., Observations d'ondes S_2 de type SH, *Pure Appl. Geophys.*, **114**, 141-157, 1976.
- Choy, G. L., Theoretical seismograms of core phases calculated by frequency-dependent full wave theory, and their interpretation, *Geophys. J. R. astr. Soc.*, **51**, 275-312, 1977.
- Clayton, R. W. and R. P. Comer, A tomographic analysis of mantle heterogeneities from body wave travel times, *Eos Trans. AGU*, **64**, 776, 1983.
- Dahlen, F. A., The normal modes of a rotating, elliptical Earth, *Geophys. J. R. astr. Soc.*, **16**, 329-367, 1968.
- Dahlen, F. A., The normal modes of a rotating, elliptical Earth- II Near-resonance multiplet coupling, *Geophys. J. R. astr. Soc.*, **18**, 397-436, 1969.
- Davies, J. H., *Some problems in mantle structure and dynamics*, Ph.D. Thesis, California Institute of Technology, 1990.
- Dongarra, J. J., J. R. Bunch, C. B. Moler, and G. W. Stewart, *LINPACK Users' Guide*, Society for Industrial and Applied Mathematics, Philadelphia, 1989.

- Draper, N. R. and H. Smith, *Applied Regression Analysis*, John Wiley and Sons, Inc., New York, 1966.
- Duffy, T. S. and T. J. Ahrens, Sound velocities at high pressure and temperature and their geophysical implications, *J. Geophys. Res.*, **97**, 4503-4520, 1992a.
- Duffy, T. S. and T. J. Ahrens, Lateral variations in lower mantle seismic velocity, in: *High-Pressure Research: Application to Earth and Planetary Sciences*, edited by Y. Syono and M. H. Manghnani, 197-205, 1992b.
- Dziewonski, A. M., Mapping the lower mantle: determination of lateral heterogeneity in P velocity up to degree and order 6, *J. Geophys. Res.*, **89**, 5929-5952, 1984.
- Dziewonski, A. M. and D. L. Anderson, Preliminary reference Earth model, *Phys. Earth and Plan. Int.*, **25**, 297-356, 1981.
- Dziewonski, A. M., Hager, B. H. and R. J. O'Connell, Large-scale heterogeneities in the lower mantle, *J. Geophys. Res.*, **82**, 239-255, 1977.
- Dziewonski, A. M. and J. H. Woodhouse, An experiment in systematic study of global seismicity: centroid-moment tensor solutions for 201 moderate and large earthquakes of 1981, *J. Geophys. Res.*, **88**, 3247-3271, 1983a.
- Dziewonski, A. M. and J. H. Woodhouse, Studies of the seismic source using normal-mode theory, in: *Earthquakes: Observation, Theory and Interpretation*, edited by E. Boschi and H. Kanamori, North-Holland Publishing Company, New York, 45-137, 1983b.
- Dziewonski, A. M. and J. H. Woodhouse, Global images of the Earth's interior, *Science*, **236**, 37-48, 1987.
- Fearn, D. R. and D. E. Loper, Compositional convection and stratification of Earth's core, *Nature*, **289**, 393-394, 1981.
- Flasar, F. M. and P. J. Gierasch, Turbulent convection within rapidly rotating superadiabatic fluids with horizontal temperature gradients, *Geophys. Astrophys. Fluid Dyn.*, **10**, 175-212, 1978.
- Garnero, E. J., D. Helmberger, and G. Engen, Lateral variations near the core-mantle boundary, *Geophys. Res. Lett.*, **15**, 609-612, 1988.
- Garnero, E. J. and D. V. Helmberger, Travel times of S and SKS: implications for three-dimensional lower mantle structure beneath the central Pacific, *J. Geophys. Res.*, **98**, 8225-8241, 1993.

- Giardini, D., Li, X.-D., and J. H. Woodhouse, Three-dimensional structure of the Earth from splitting in free-oscillation spectra, *Nature*, **325**, 405-411, 1987.
- Gilbert, F., The representation of seismic displacements in terms of travelling waves, *Geophys. J. R. astr. Soc.*, **44**, 275-280, 1976.
- Gilbert, F., Excitation of the normal modes of the Earth by earthquake sources, *Geophys. J. R. astr. Soc.*, **22**, 223-226, 1970.
- Gilbert, F. and A. M. Dziewonski, An application of normal mode theory to the retrieval of structural parameters and source mechanisms from seismic spectra, *Philos. Trans. R. Soc. London Ser. A*, **278**, 187-269, 1975.
- Gubbins, D., Thermal core-mantle interactions and time-averaged paleomagnetic field, *J. Geophys. Res.*, **93**, 3413-3420, 1988.
- Gubbins, D. and J. Bloxham, Geomagnetic field analysis - III. Magnetic fields on the core-mantle boundary, *Geophys. J. R. astr. Soc.*, **80**, 695-713, 1985.
- Gubbins, D. and M. Richards, Coupling of the core dynamo and mantle: thermal or topographic? *Geophys. Res. Lett.*, **13**, 1521-1524, 1986.
- Gubbins, D., C. J. Thomson, and K. A. Whaler, Stable regions in the Earth's liquid core, *Geophys. J. R. astr. Soc.*, **68**, 241-251, 1982.
- Gudmundsson, O., *Some problems in global tomography: modeling the core-mantle boundary and statistical analysis of travel time data*, Ph.D. Thesis, California Institute of Technology, 1989.
- Gudmundsson, O. and R. W. Clayton, A 2-D synthetic study of global traveltimes tomography, *Geophys. J. Int.*, **106**, 53-65, 1991.
- Gudmundsson, O., J. H. Davies, and R. W. Clayton, Stochastic analysis of global traveltimes data: mantle heterogeneity and random errors in the ISC data, *Geophys. J. Int.*, **102**, 25-43, 1990.
- Gutenberg, B., On focal points of SKS, *Bull. Seis. Soc. Am.*, **28**, 197-200, 1938.
- Gutenberg, B., PKKP, P'P', and the Earth's core, *Trans. AGU*, **32**, 373-390, 1951.
- Gutenberg, B. and C. F. Richter, On seismic waves, *Gerlands Beitr. z. Geophysik*, **54**, 94-136, 1939.

- Gwinn, C. R., T. A. Herring, and I. I. Shapiro, Geodesy by radio-interferometry: studies of the forced nutations of the Earth 2: Interpretation, *J. Geophys. Res.*, **91**, 4755-4765, 1986.
- Hager, B. H. and R. W. Clayton, Constraints on the structure of mantle convection using seismic observations, flow models, and the geoid, in: *Mantle Convection*, edited by W. R. Peltier, Gordon and Breach Science Publishers, New York, 657-763, 1989.
- Hales, A. L. and J. L. Roberts, The travel times of S and SKS, *Bull. Seis. Soc. Am.*, **60**, 461-489, 1970a.
- Hales, A. L. and J. L. Roberts, The velocities in the outer core, *Bull. Seis. Soc. Am.*, **61**, 1051-1059, 1971.
- Herrin, E., W. Tucker, J. Taggart, D. W. Gordon, and J. L. Lobdell, Estimation of surface focus P travel times, *Bull. Seis. Soc. Am.*, **58**, 1273-1291, 1968.
- Hide, R., Interaction between the Earth's liquid core and solid mantle, *Nature*, **222**, 1055-1056, 1969.
- Inoue, H., Y. Fukao, K. Tanabe, and Y. Ogata, Whole mantle P-wave travel time tomography, *Phys. Earth and Plan. Int.*, **59**, 294-328, 1990.
- Jault, D., C. Gire and J.-L. Le Mouél, Westward drift, core motions and exchanges of angular momentum between core and mantle, *Nature*, **333**, 353-356, 1988.
- Jault, D. and J.-L. Le Mouél, The topographic torque associated with a tangentially geostrophic motion at the core surface and inferences on the flow inside the core, *Geophys. Astrophys. Fluid Dyn.*, **48**, 273-296, 1989.
- Jeffreys, H., The times of the core waves, *Mon. Not. Roy. Astr. Soc., Geophys. Suppl.*, **4**, 594-615, 1939.
- Jeffreys, H. and K. E. Bullen, *Seismological Tables*, British Association for the Advancement of Science, London, 1958.
- Jeffreys, H. and B. S. Jeffreys, *Methods of Mathematical Physics*, 3rd ed., Cambridge University Press, 1956.
- Jones, G. M., Thermal interaction of the core and the mantle and long-term behavior of the geomagnetic field, *J. Geophys. Res.*, **82**, 1703-1709, 1977.
- Jordan, T. H., A procedure for estimating lateral variations from low-frequency eigenspectra data, *Geophys. J. R. astr. Soc.*, **52**, 441-455, 1978.

- Jordan, T. H. and D. L. Anderson, Earth structure from free oscillations and travel times, *Geophys. J. R. astr. Soc.*, **36**, 411-459, 1974.
- Kennett, B. L. N. and E. R. Engdahl, Traveltimes for global earthquake location and phase identification, *Geophys. J. Int.*, **105**, 429-465, 1991.
- Kind, R. and G. Müller, Computations of SV waves in realistic Earth models, *J. Geophys.*, **41**, 149-172, 1975.
- Kind, R. and G. Müller, The structure of the outer core from SKS amplitudes and travel times, *Bull. Seis. Soc. Am.*, **67**, 1541-1554, 1977.
- Knittle, E. and R. Jeanloz, High-pressure metallization of FeO and implications for the Earth's core, *Geophys. Res. Lett.*, **13**, 1541-1544, 1986.
- Knittle, E. and R. Jeanloz, Simulating the core-mantle boundary: an experimental study of high-pressure reactions between silicates and liquid iron, *Geophys. Res. Lett.*, **16**, 609-612, 1989.
- Kohler, M. D. and D. J. Stevenson, Modeling core fluid motions and the drift of magnetic field patterns at the CMB by use of topography obtained by seismic inversion, *Geophys. Res. Lett.*, **17**, 1473-1476, 1990.
- Kohler, M. D. and T. Tanimoto, One-layer global inversion for outermost core velocity, *Phys. Earth and Plan. Int.*, **72**, 173-184, 1992.
- Lawson, C., R. Hanson, D. Kincaid, and F. Krogh, Basic linear algebra subprograms for Fortran usage, *ACM Trans. Math. Software*, **5**, 308-371, 1979.
- Lay, T., Structure of the core-mantle transition zone, *Eos Trans. AGU*, **70**, 49, 54-55, 58-59, 1989.
- Lay, T. and C. J. Young, The stably-stratified outermost core revisited, *Geophys. Res. Lett.*, **17**, 2001-2004, 1990.
- Lerner-Lam, A. L. and T. H. Jordan, Earth structure from fundamental and higher-mode waveform analysis, *Geophys. J. R. astr. Soc.*, **75**, 759-797, 1983.
- Li, X.-D., D. Giardini, and J. H. Woodhouse, Large-scale three-dimensional even-degree structure of the Earth from splitting of long-period normal modes, *J. Geophys. Res.*, **96**, 551-577, 1991a.
- Li, X.-D., D. Giardini, and J. H. Woodhouse, The relative amplitudes of mantle heterogeneity in P-velocity, S-velocity, and density from free-oscillation data, *Geophys. J. R. astr. Soc.*, **105**, 649-657, 1991b.

- Li, X.-D. and T. Tanimoto, Waveform inversion of long-period seismic data for global structure, in: *Seismic Tomography: Theory and Practice*, edited by H. M. Iyer and K. Hirahara, Chapman and Hall, London, 64-91, 1993.
- Lognonné, P. and B. Romanowicz, Modelling of coupled normal modes of the Earth: the spectral method, *Geophys. J. Int.*, **102**, 365-395, 1990.
- Loper, D. E., The nature and consequences of thermal interactions twixt core and mantle, *J. Geomag. Geoelectr.*, **43**, 79-91, 1991.
- Masters, G., Observational constraints on the chemical and thermal structure of the Earth's deep interior, *Geophys. J. R. astr. Soc.*, **57**, 507-534, 1979.
- Masters, G., H. Bolton, and P. Shearer, Large-scale 3-dimensional structure of the mantle, *Eos Trans. AGU*, **73**, 201, 1992.
- Masters, G., T. H. Jordan, P. G. Silver and F. Gilbert, Aspherical Earth structure from fundamental spheroidal-mode data, *Nature*, **298**, 609-613, 1982.
- Melchior, P., *The physics of the Earth's core*, Pergamon Press, New York, 1986.
- Merrill, R. T. and M. W. McElhinny, *The Earth's magnetic field*, Academic Press, New York, 1983.
- Monin, A. S. and A. M. Yaglom, *Statistical fluid mechanics*, Vol. 1, MIT Press, Cambridge, MA, 1971.
- Montagner, J.-P., Regional three-dimensional structures using long-period surface waves, *Ann. Geophys.*, **4**, 283-294, 1986.
- Morelli, A. and A. M. Dziewonski, Topography of the core-mantle boundary and lateral homogeneity of the liquid core, *Nature*, **325**, 678-683, 1987.
- Nakanishi, I. and D L. Anderson, Measurements of mantle wave velocities and inversion for lateral heterogeneity and anisotropy 1. Analysis of great circle phase velocities, *J. Geophys. Res.*, **88**, 10,267-10,283, 1983.
- Nakanishi, I. and D L. Anderson, Measurements of mantle wave velocities and inversion for lateral heterogeneity and anisotropy- II. Analysis by the single-station method, *Geophys. J. R. astr. Soc.*, **78**, 573-617, 1984.
- Nataf, H.-C., Nakanishi, I. and D. L. Anderson, Anisotropy and shear-velocity heterogeneities in the upper mantle, *Geophys. Res. Lett.*, **11**, 109-112, 1984.

- Nataf, H.-C., Nakanishi, I. and D. L. Anderson, Measurement of mantle wave velocities and inversion for lateral heterogeneity and anisotropy 3. Inversion, *J. Geophys. Res.*, **91**, 129-169, 1986.
- Nelson, R. L., A study of the seismic waves SKS and SKKS, *Bull. Seis. Soc. Am.*, **44**, 39-55, 1954.
- Nolet, G., Higher Rayleigh modes in Western Europe, *Geophys. Res. Lett.*, **2**, 60-62, 1975.
- Olson, P., Toroidal flow in the outer core and the thermal regime below the core-mantle boundary, *Geophys. Res. Lett.*, **16**, 613-616, 1989.
- Pedlosky, J., *Geophysical fluid dynamics*, Springer-Verlag, New York, 1979.
- Phinney, R. A. and R. Burridge, Representation of the elastic-gravitational excitation of a spherical Earth model by generalized spherical harmonics, *Geophys. J. R. astr. Soc.*, **34**, 451-487, 1973.
- Pulver, S. and T. G. Masters, PcP-P travel times and the ratio of P to S velocity variations in the lower mantle, *Eos Trans. AGU*, **71**, 1464, 1990.
- Randall, M. J., SKS and seismic velocities in the outer core, *Geophys. J. R. astr. Soc.*, **21**, 441-445, 1970.
- Romanowicz, B., Multiplet-multiplet coupling due to lateral heterogeneity: asymptotic effects on the amplitude and frequency of the Earth's normal modes, *Geophys. J. R. astr. Soc.*, **90**, 75-100, 1987.
- Romanowicz, B. and G. Roullet, First-order asymptotics for the eigenfrequencies of the Earth and application to the retrieval of large-scale lateral variations of structure, *Geophys. J. R. astr. Soc.*, **87**, 209-239, 1986.
- Romanowicz, B. and R. Snieder, A new formalism for the effect of lateral heterogeneity on normal modes and surface waves- II. General anisotropic perturbation, *Geophys. J. R. astr. Soc.*, **93**, 91-99, 1988.
- Ruff, L. and D. L. Anderson, Core formation, evolution, and convection: a geophysical model, *Phys. Earth and Plan. Int.*, **21**, 181-201, 1980.
- Schweitzer, J. and G. Müller, Anomalous difference traveltimes and amplitude ratios of SKS and SKKS from Tonga-Fiji events, *Geophys. Res. Lett.*, **13**, 1529-1532, 1986.

- Simmons, G. and H. Wang, *Single Crystal Elastic Constants and Calculated Aggregate Properties: a Handbook*, MIT Press, Cambridge, 1971.
- Souriau, A. and G. Poupinet, A latitudinal pattern in the structure of the outermost liquid core, revealed by the travel times of SKKS-SKS seismic phases, *Geophys. Res. Lett.*, **17**, 2005-2007, 1990.
- Souriau, A. and G. Poupinet, A study of the outermost liquid core using differential travel times of the SKS, SKKS SKKS and S3KS phases, *Phys. Earth and Plan. Int.*, **68**, 183-199, 1991.
- Stacey, F., Does lower mantle tomography indicate temperature variations that affect the core, *J. Geomag. Geoelectr.*, **45**, 1229-1234, 1993.
- Stevenson, D. J., Turbulent thermal convection in the presence of rotation and a magnetic field, *Geophys. Astrophys. Fluid Dyn.*, **12**, 139-169, 1979.
- Stevenson, D. J., Limits on lateral density and velocity variations in the Earth's outer core, *Geophys. J. R. astr. Soc.*, **88**, 311-319, 1987.
- Su, W-J. and A. M. Dziewonski, Predominance of long-wavelength heterogeneity in the mantle, *Nature*, **352**, 121-126, 1991.
- Su, W-J. and A. M. Dziewonski, On the scale of mantle heterogeneity, *Phys. Earth and Plan. Int.*, **74**, 29-54, 1992.
- Su, W-J., R. L. Woodward, and A. M. Dziewonski, Deep origin of mid-ocean-ridge seismic velocity anomalies, *Nature*, **360**, 149-152, 1992.
- Su, W-J., R. L. Woodward, and A. M. Dziewonski, Degree 12 model of shear velocity heterogeneity in the mantle, *J. Geophys. Res.*, **99**, 6945-6980, 1994.
- Sumino, Y. and O. L. Anderson, Elastic constants of minerals, in: *Handbook of Physical Properties of Rocks*, Vol. III, edited by R. S. Carmichael, CRC Press, Boca Raton, FL, 39-137, 1984.
- Takeuchi, H. and M. Saito, Seismic surface waves, in: *Computational Physics*, Academic Press, New York, **11**, 217-295, 1972.
- Tanaka, S. and H. Hamaguchi, Degree one heterogeneity at the top of the Earth's core, revealed by SmKS travel times, in: *Dynamics of Earth's Deep Interior and Earth Rotation*, *Geophys. Mon. 72, IUGG*, **12**, 127-134, 1993a.

- Tanaka, S. and H. Hamaguchi, Travel times and velocities in the outer core based on the global observations of SmKS seismic phases, *Tohoku Geophys. J. (Sci. Rep. Tohoku Univ. Ser. 5)*, **34**, 55-87, 1993b.
- Tanaka, S. and H. Hamaguchi, Velocities and chemical stratification in the outermost core, *J. Geomag. Geoelectr.*, **45**, 1287-1301, 1993c.
- Tanimoto, T., Waveform inversion of mantle Love waves: the Born seismogram approach, *Geophys. J. R. astr. Soc.*, **78**, 641-660, 1984.
- Tanimoto, T., The three-dimensional shear wave structure in the mantle by overtone waveform inversion- I. Radial seismogram inversion, *Geophys. J. R. astr. Soc.*, **89**, 713-740, 1987.
- Tanimoto, T., The 3-D shear wave structure in the mantle by overtone waveform inversion- II. Inversion of X-waves, R-waves and G-waves, *Geophys. J. R. astr. Soc.*, **93**, 321-334, 1988.
- Tanimoto, T., Long-wavelength S-wave velocity structure throughout the mantle, *Geophys. J. Int.*, **100**, 327-336, 1990a.
- Tanimoto, T., Predominance of large-scale heterogeneity and the shift of velocity anomalies between the upper and lower mantle, *J. Phys. Earth*, **38**, 493-509, 1990b.
- Toksöz, M. N. and D. L. Anderson, Phase velocities of long-period surface waves and structure of the upper mantle 1. Great-circle Love and Rayleigh wave data, *J. Geophys. Res.*, **71**, 1649-1658, 1966.
- Usselman, T. M., Experimental approach to the state of the core: Part II. composition and thermal regime, *Am. J. Sci.*, **275**, 291-303, 1975.
- Widmer, R., G. Masters, and F. Gilbert, Observably split multiplets-data analysis and interpretation in terms of large-scale aspherical structure, *Geophys. J. Int.*, **111**, 559-576, 1992.
- Woodhouse, J. H., The coupling and attenuation of nearly resonant multiplets in the Earth's free oscillation spectrum, *Geophys. J. R. astr. Soc.*, **61**, 261-283, 1980.
- Woodhouse, J. H. and F. A. Dahlen, The effect of a general aspherical perturbation on the free oscillations of the Earth, *Geophys. J. R. astr. Soc.*, **53**, 335-354, 1978.
- Woodhouse, J. H. and A. M. Dziewonski, Mapping the upper mantle: three-dimensional modeling of Earth structure by inversion of seismic waveforms, *J. Geophys. Res.*, **89**, 5953-5986, 1984.

- Woodward, R. L. and G. Masters, Global upper mantle structure from long-period differential travel times, *J. Geophys. Res.*, **96**, 6351-6377, 1991a.
- Woodward, R. L. and G. Masters, Lower-mantle structure from ScS-S differential travel times, *Nature*, **352**, 231-233, 1991b.
- Woodward, R. L. and G. Masters, Upper mantle structure from long-period differential traveltimes and free oscillation data, *Geophys. J. Int.*, **109**, 275-293, 1991c.
- Zhang, Y-S., *Three-dimensional modeling of upper mantle structure and its significance to tectonics*, Ph.D. Thesis, California Institute of Technology, 1992.
- Zhang, K. and F. H. Busse, Generation of magnetic fields by convection in a rotating spherical fluid shell of infinite Prandtl number, *Phys. Earth and Plan. Int.*, **58**, 208-222, 1990.
- Zhang, K. and D. Gubbins, On convection in the Earth's core driven by lateral temperature variations in the lower mantle, *Geophys. J. Int.*, **108**, 247-255, 1992.
- Zhang, Y-S. and T. Tanimoto, Three-dimensional modelling of upper mantle structure under the Pacific ocean and surrounding area, *Geophys. J. Int.*, **98**, 255-269, 1989.

Appendix A1: A Theoretical, Magnetohydrodynamic Discussion

The thermal wind equations, in which the Coriolis force is balanced by pressure gradients and horizontal density gradients rather than by Lorentz forces, are used to describe patterns of magnetic field drift associated with core fluid motions near the core-mantle boundary (CMB). The advection of magnetic field may be due in part to the flow driven by such horizontal temperature gradients, just as east-west air flow is driven by north-south temperature gradients in the Earth's atmosphere. It is argued that this flow may be concentrated in a shell near the CMB, and the horizontal temperature gradients are expected to be directly proportional to horizontal gradients in CMB topography, the lowest harmonics of which are approximately constrained in seismology. Part of the zonal drift is then associated with the $\ell = 2$, $m = 0$ harmonic of CMB topography, and anticyclones are attached to topographic highs (thermal highs). Comparison of our derived flow pattern with those determined purely by magnetic field observations provides tentative support for this model.

A simple model is developed here for that part of core fluid motion due to core-mantle boundary topography. The basic idea is as follows: relatively cold mantle just above the CMB is more dense and will sink causing a depression in the CMB, whereas relatively hot mantle is less dense and will rise, resulting in positive CMB topographic relief or "bumps". The relationship between the deformation of an interface and the pattern of convective thermal anomalies is not necessarily so simple [cf. Hager and Clayton, 1989] especially if the lowermost mantle (D") is a compositional layer [Lay, 1989] but the most commonly assumed correlation was chosen. Cold, topographic lows

cool the core from above and promote more vigorous vertical convection in the locally cold core fluid. Warm, topographic highs are associated with lower vertical heat flow and warmer core fluid. This is illustrated in Fig. A1.1. Simple mixing length recipes for turbulent convection suggest temperature deviations away from an adiabat of order 10^{-3} K but with a large uncertainty [Stevenson, 1987]. These will also be the horizontal temperature variations on an equipotential. Horizontal as well as vertical heat flows can be expected [Flasar and Gierasch, 1978] and the relationship between the magnitude of the mantle temperature fluctuations and those in the core may well be non-linear, but the sense of the correlation is clear: topographic highs of the CMB are associated with thermal highs in the outermost core.

In consideration of the dynamics, the standard approach is adopted in which fluid acceleration relative to the rotating frame is ignored and viscous effects are ignored. The Lorentz force is also neglected in the outermost core because the toroidal component of the field should decrease to a low value in the outermost few hundred kilometers of the core due to the low conductivity of the mantle [Merrill and McElhinny, 1983]. The Lorentz force is dominated by a term that is proportional to the cross product of this toroidal field with the poloidal current. Here, the artificiality of current sheets that arise in some dynamo models is excluded. The Boussinesq approximation in which the only dynamically significant density variations are those caused by thermal expansion is also adopted. This leads to the standard thermal wind equation, well known to atmospheric dynamicists [e.g., Pedlosky, 1979] and occasionally discussed for the core [e.g., Olson, 1989]:

$$2\Omega \times \mathbf{v} = -\frac{\nabla P'}{\rho_0} - \mathbf{g} \alpha T \quad [\text{A1.1}]$$

where Ω is the mean Earth angular velocity, \mathbf{v} is the fluid velocity relative to this frame, P' is the non-hydrostatic component of the fluid pressure, ρ_0 is the mean fluid density, α is the coefficient of thermal expansion, T is the deviation of the temperature away from

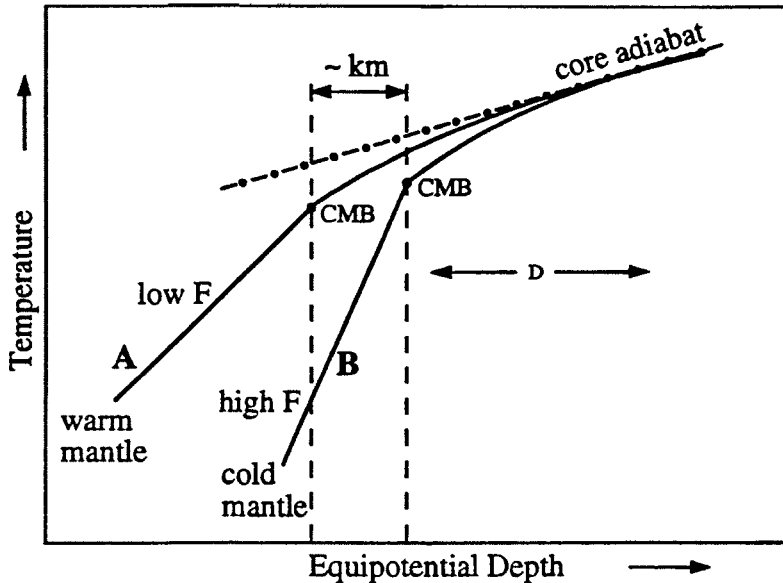


Fig. A1.1 Schematic representation of temperature profiles near the CMB. Temperature and depth scales are shown grossly distorted to clarify the important features. Profile A corresponds to a low heat flow region and topographic high. Profile B is a high heat flow region and topographic low. Notice that at a given depth within the core, the temperature on profile A is high relative to profile B. This correlation of topographic and thermal highs is central to the model described in the text. Note also that the absolute temperature at the CMB is lower for the high heat flow case (A) than for the low heat flow case (B), because the CMB on profile A is at a lower pressure. This effect is actually much bigger than the temperature difference at a fixed equipotential depth, but dynamically irrelevant.

some mean core adiabat, and \mathbf{g} is gravitational acceleration. The solution to the equation of motion can be found by taking the curl of both sides; however, by doing so, information concerning any flow that is purely geostrophic (i.e., Coriolis force balanced by a pressure gradient) is lost. This results in

$$(2\boldsymbol{\Omega} \cdot \nabla)\mathbf{v} = \nabla \times (\mathbf{g}\alpha T). \quad [\text{A1.2}]$$

The further assumption is made that the thermal wind is primarily confined to a layer that is thin compared to the core radius. This is not a boundary layer (which is much thinner yet) but a layer in which the horizontal temperature gradients and the associated wind are dynamically dominant. This layer could be of order one hundred kilometers thick (but with a large uncertainty) and arise in two ways. First, it could be the region within which the boundary-generated buoyancy driving thermal convection is confined. This is in the spirit of local prescriptions for turbulent convection [Monin and Yaglom, 1971], if one assumes that the mixing length is equal to the distance from the CMB. According to this view, the temperature anomaly T decays in amplitude over some characteristic distance $D \ll R_c$, the core radius, as illustrated in Fig. A1.1. The second reason for this thin layer approximation is that it may correspond to the region in which the Lorentz force is small. At deeper levels, there is a large enough toroidal field for which flows of the type considered here are effectively damped. In either case, solutions to Eq. [A1.2] are sought in which the velocity decays over a characteristic distance D as one goes downward into the core. These solutions have the property that the shear is parallel to the flow, i.e.,

$$\frac{\partial}{\partial r} \rightarrow \frac{1}{D}.$$

Since $D \ll R_c$, it follows that spherical coordinate θ and ϕ derivatives of the velocity (but not the temperature) can be neglected relative to radial derivatives. (This is exactly analogous to the meteorological approach to thermal winds.) Then

$$v_{\theta} = \frac{g\alpha\varepsilon}{2\Omega \sin \theta \cos \theta} \frac{\partial T}{\partial \varphi} \quad [\text{A1.3}]$$

and

$$v_{\varphi} = \frac{g\alpha\varepsilon}{2\Omega \cos \theta} \frac{\partial T}{\partial \theta} \quad [\text{A1.4}]$$

for the values of these velocity components at the CMB, where $\varepsilon = \frac{D}{R}$. As usual, θ is the colatitude, φ is longitude, and $g=|g|$.

Continuity dictates that v_r is smaller than v_{θ} or v_{φ} by a factor of $\varepsilon \ll 1$. Notice, however, that the predicted flow is not purely toroidal in general, although toroidal components tend to dominate. In the limit of fairly rapid θ -variation of T not near the equator (i.e., $\frac{T}{\varepsilon} \gg \left| \frac{\partial T}{\partial \theta} \right| \gg T$; $\theta \neq \frac{\pi}{2}$) it is clear that the vorticity of the flow is radial and proportional to $\nabla^2 T$ with a positive (negative) constant of proportionality in the Northern (Southern) hemisphere. This means that anticyclones are associated with temperature highs, the same as meteorological experience.

Quantitatively, the fundamental assumption of this model is the expression that core temperature variations are proportional to CMB topography variations, or

$$T(\theta, \varphi) = \beta f(\theta, \varphi) \quad [\text{A1.5}]$$

where β is the constant of proportionality, and T and f are assumed to have zero means. If CMB topography is given in terms of a spherical harmonic expansion, the temperature is expressed in terms of the same expansion coefficients multiplied by β :

$$T(\theta, \varphi) = \beta \sum_{\ell=0}^L \sum_{m=0}^{\ell} \left(g_{\ell}^m \cos m\varphi + h_{\ell}^m \sin m\varphi \right) P_{\ell}^m(\cos \theta) \quad [\text{A1.6}]$$

and

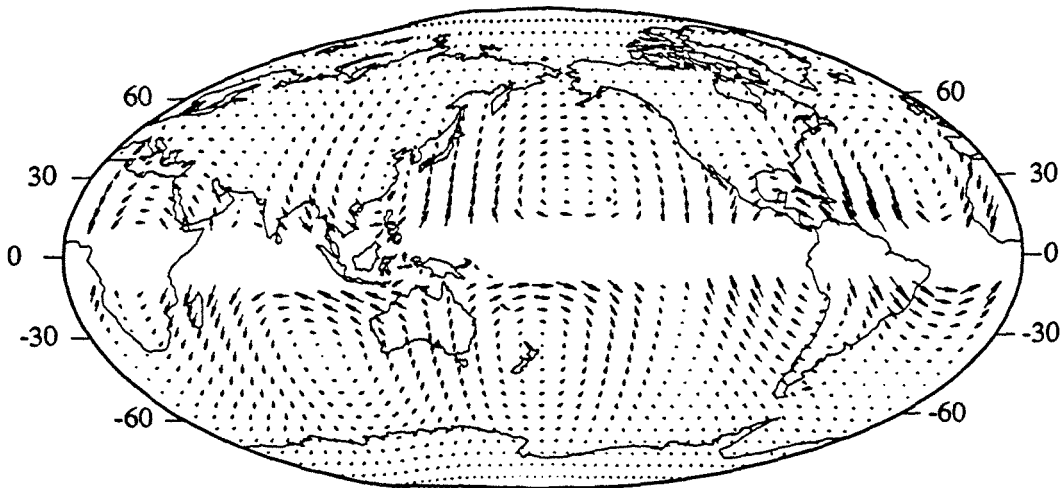
$$f(\theta, \varphi) = \sum_{\ell=0}^L \sum_{m=0}^{\ell} \left(g_{\ell}^m \cos m\varphi + h_{\ell}^m \sin m\varphi \right) P_{\ell}^m(\cos \theta). \quad [\text{A1.7}]$$

This choice cannot be rigorously justified. However, the numerical values are plausible. For $\beta = 10^{-3}$ K/km, and topographic relief \sim km, temperature fluctuations are not enormously different from values suggested by turbulent convection models [Stevenson, 1979, 1987], resulting in $|\mathbf{v}| \sim 10^{-2}$ cm/sec comparable to westward drift. Clearly this model is most suited to estimating the pattern of core fluid and not the magnitude of that flow. For the same reason, uncertainties in the magnitude of CMB topography even by factors of ten are less important to assessing the model than the pattern of CMB topography.

Maps of the velocity field are given in Figs. A1.2 and A1.3 with corresponding CMB topography maps. Fig. A1.2 shows the velocity flow field using the CMB results of Morelli & Dziewonski [1987] and Fig. A1.3 shows the velocity flow field using the results of Gudmundsson [1989]. Both maps illustrate that closed loops of fluid flow are closely related to topography highs and lows, as expected. Although topography maps vary widely from worker to worker, there are features common to the maps studied here. For example, all maps show an anticyclone (due to the CMB topography high) underneath the Indian Ocean. Note that this flow is mostly but not purely toroidal. The continents have been drawn only for establishing the frame of reference.

Comparisons with magnetic field data results of Bloxham [1989a] given in Fig. A1.4 indicate that thermal winds may indeed be largely responsible for core fluid motions. The fluid flow map in Fig. A1.4 is a result of the inversion of magnetic field data recorded during the time interval 1935-1940 but it displays similar general characteristics to maps of flow during other time intervals. For example, as in the velocity map given by thermal winds, fluid flow in Fig. A1.4 is anticyclonic underneath the Indian Ocean and over south-central Asia. Our model is probably only relevant to field components that are steady although it is possible for dynamos to have steady velocity fields yet unsteady magnetic fields.

(a)



(b)

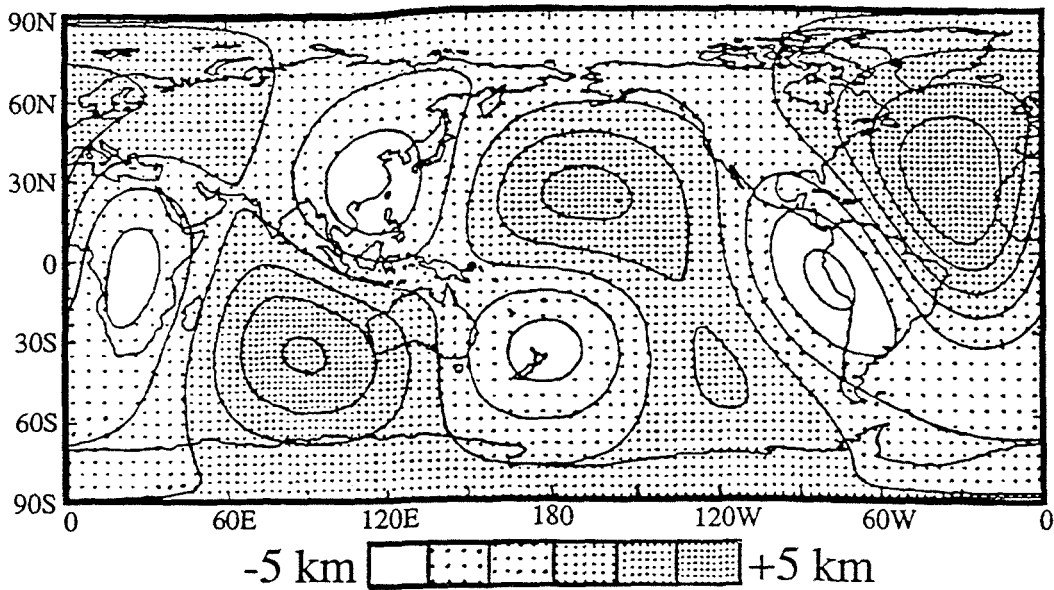
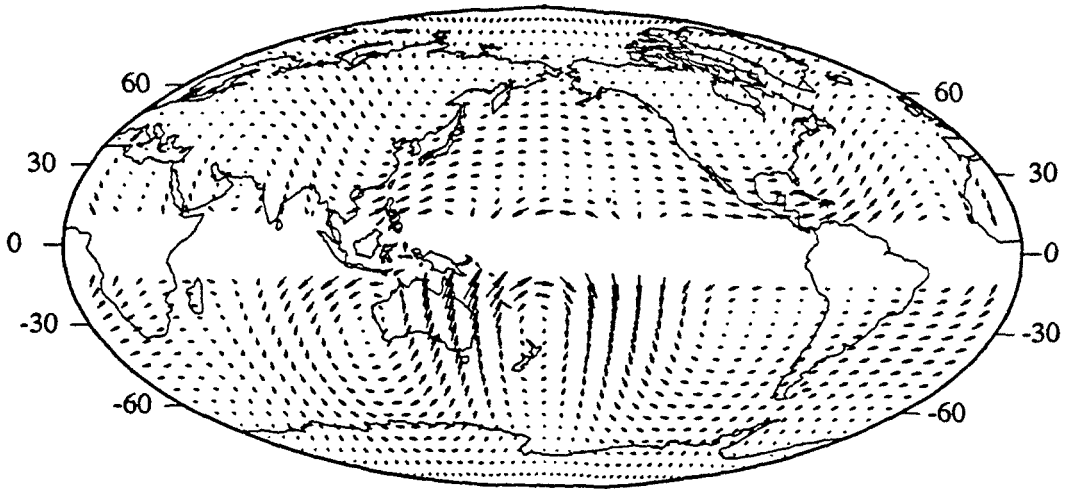


Fig. A1.2 (a) Core fluid patterns based on the thermal wind model described in the text using results from (b). (b) Map of CMB topography obtained by Morelli and Dziewonski [1987] (results are from inversion of compressional core-phase data with spherical harmonic expansion up to degree and order 4).

(a)



(b)

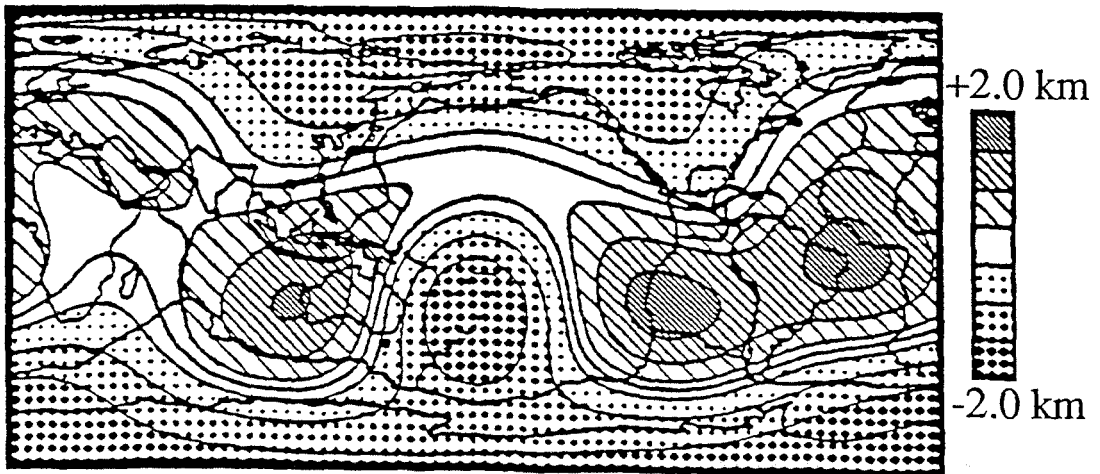
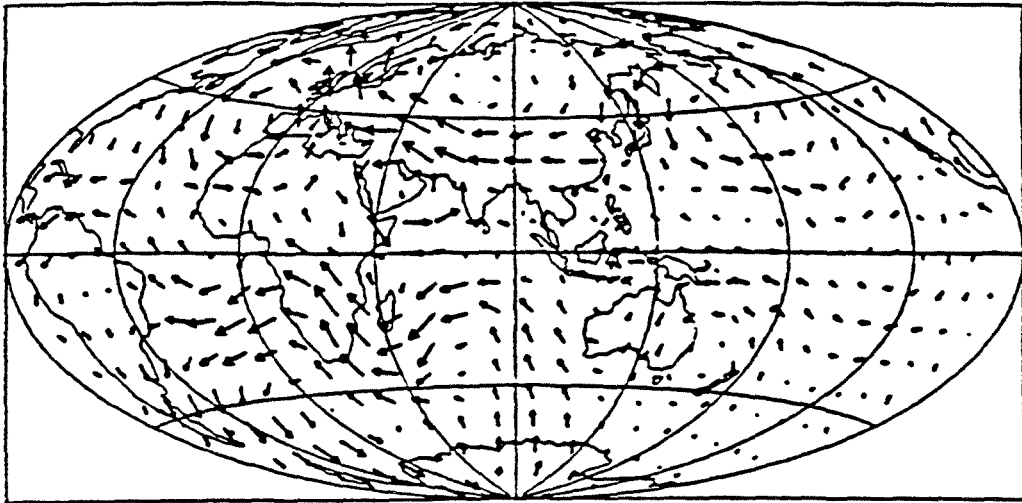


Fig. A1.3 (a) Core fluid patterns based on the thermal wind model described in the text using results from (b). (b) Map of CMB topography map obtained by Gudmundsson [1989] (results are from inversion of compressional core phases with spherical harmonic expansion up to degree and order 5).



→ 20 km/yr

Fig. A1.4 Core fluid velocity map of Bloxham [1989a] obtained from the inversion of magnetic field data for time interval 1935-1940.

The expressions for velocity containing the $\ell = 2$, $m = 0$ component of CMB topography expansion is given by

$$v_{\theta} = 0 \quad [\text{A1.8}]$$

and

$$v_{\varphi} = -\frac{3}{2} \frac{g\alpha\varepsilon}{\Omega} \sin\theta g_2^0. \quad [\text{A1.9}]$$

This expression describes the pattern of westward drift if the $\ell = 2$, $m=0$ topography expansion coefficient is positive; fluid velocity is eastward if the coefficient is negative. It is the only term which globally describes this pattern. Fig. A1.2a shows strong westward drift in regions south of New Zealand and in the Indian Ocean. Fig. A1.3a shows less westward drift and regions of strong eastward drift, possibly due to the large negative $\ell = 2$, $m = 0$ CMB topography coefficient. This model does not work near the equator since certain velocity terms diverge. This arises through our failure to retain θ and φ derivatives in the derivation of v_{θ} and v_{φ} (Eqs. [A1.3] and [A1.4]). More fundamentally, the Coriolis force cannot be expected to dominate near the equator and other effects, neglected here, will be important. However, the model behaves very well to within ten degrees of the equator and it can be used to predict patterns in core fluid velocity. In several respects, it is surprising that this model shows tentative evidence of validity. There are surely other sources of near-CMB flow and only one component has been determined here. Moreover, the validity of the thin layer approximation ($\varepsilon \ll 1$) is debatable. Models that do not use this approximation [e.g., Bloxham, 1989b] show less correlation between flow and topography. As seismic and other models improve, it may become possible to decide whether a relatively thin layer thermal wind component contributes to core flow; more about the core can thereby be learned.

If outer core horizontal fluid flow is driven by horizontal temperature gradients due to CMB topography, then the thermal wind equations, expressed as a function of

CMB topography, describe the advection of magnetic field resulting from core fluid motions. This model describes zonal drift by the velocity expression containing the $\ell = 2$, $m = 0$ topography coefficient and predicts that westward drift should not be a dominant feature in core fluid motions if CMB topography harmonic terms other than $\ell = 2$, $m = 0$ contribute much power. The thin layer version of this model predicts that anticyclones are associated with thermal and topographic highs, and a comparison of magnetically derived flow maps with our maps provides tentative support for this version.

Appendix A2: An Adjustment to the Correction for Epicentral Distance due to Ellipticity

The corrections to epicentral distance and eigenfrequency for a specific normal mode due to ellipticity are calculated as

$$\delta\theta^e = \frac{-a\alpha\omega}{\left(\ell + \frac{1}{2}\right)U} 3\sin\Delta \cos 2\phi_{\text{mp}} \sin^2\Theta \quad [\text{A2.1}]$$

and

$$\delta\omega^e = \omega\alpha(1 - 3\cos^2\Theta) \quad [\text{A2.2}]$$

following the development in Woodhouse and Dziewonski [1984; see their Appendix]. In these expressions, 'a' represents Earth radius, α is the ellipticity splitting coefficient for a specific mode, ω is the mode eigenfrequency, ℓ is the angular order, U is group velocity, Δ is the epicentral distance, ϕ_{mp} is the azimuth (clockwise from north) of the midpoint of the minor arc from the great circle pole, and Θ represents the colatitude of the pole of the great circle path. These corrections are different for each mode but the approximations are good only for large ℓ (or $\ell \gg m$) as will be shown in the following. As a result, they can only be applied to a subset of normal modes used in the construction of synthetic seismograms.

Woodhouse and Dziewonski [1984] derived the corrections due to ellipticity from the derivation of phase perturbations due to lateral heterogeneity; these, in turn, were expressed as functions of wave number and phase velocity perturbations for major and minor arc great circle surface wave paths. However, wave number 'k' is an asymptotic

approximation from the asymptotic form of the Legendre function. Specifically, for large ℓ ,

$$P_{\ell}^m(\cos\theta) \cong \ell^m \left(\frac{2}{\ell\pi \sin\theta} \right)^{\frac{1}{2}} \cos \left\{ \left(\ell + \frac{1}{2} \right) \theta - \frac{1}{2} m\pi - \frac{1}{4} \pi \right\} \quad [\text{A2.3}]$$

[Jeffreys and Jeffreys, 1956]. From this, the wavelength, L , along the surface meridian is calculated as

$$L = \frac{2\pi a}{\left(\ell + \frac{1}{2} \right)}$$

and wave number, k , is given as

$$k = \frac{\left(\ell + \frac{1}{2} \right)}{a}.$$

It follows from the approximation used in this derivation that the distance correction, $\delta\theta^e$, can only be made for modes with large ℓ . A similar argument can be made for modes with group velocities which are not too small.

Observations confirm the theoretical conclusions. The distance correction is expected to be small for all modes, but plots of distance correction (calculated using Eq. [A2.1]) vs. angular order show that this is true only for a subset of the modes. Fig. A2.1 shows this correction breaking down for modes with small ℓ . Fig. A2.1a is a plot of distance correction vs. ℓ (for all fundamental modes and overtones used in the inversions presented in this thesis) for the distance correction between an earthquake which occurred on April 23, 1985 in the Philippine Islands and which was recorded at station TAU. The majority of distance corrections due to ellipticity shown in this plot are small ($< 10\%$), but the corrections become unrealistically large for $\ell < 5$. Fig. A2.1b is a plot of distance correction vs. group velocity for the same seismogram, from which it is clear that corrections should not be made for modes whose corresponding group velocities are less than ~ 2 km/sec. Fig. A2.2 shows similar plots for an earthquake which occurred on November 22, 1984 in the South Atlantic Ridge and which was recorded at station CHTO. This figure also shows unrealistically large distance corrections for modes with

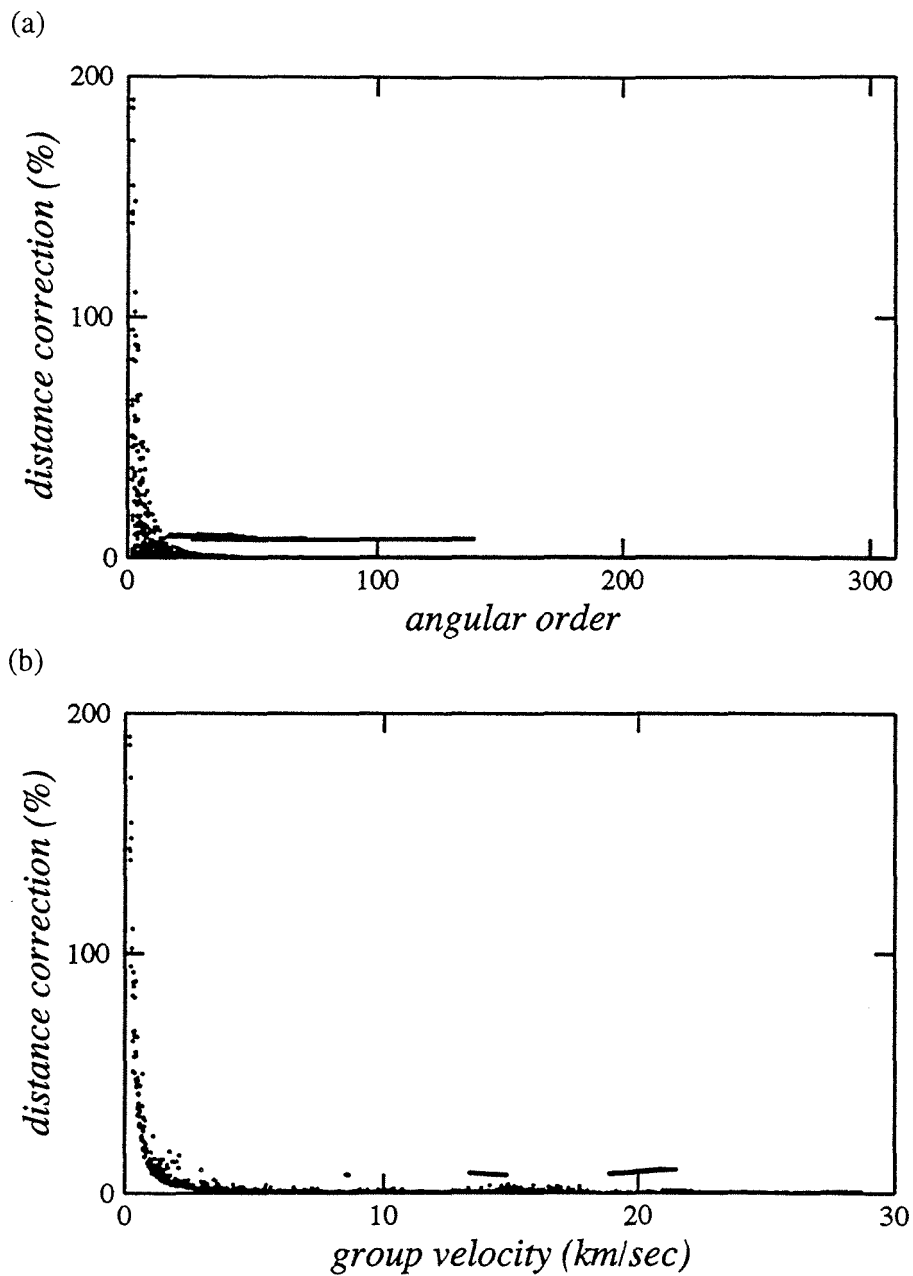


Fig. A2.1 Ellipticity distance correction given by Eq. [A2.1] as a function of (a) angular order and (b) group velocity for seismogram recorded at station TAU on April 4, 1985 for an earthquake which occurred in the Philippine Islands.

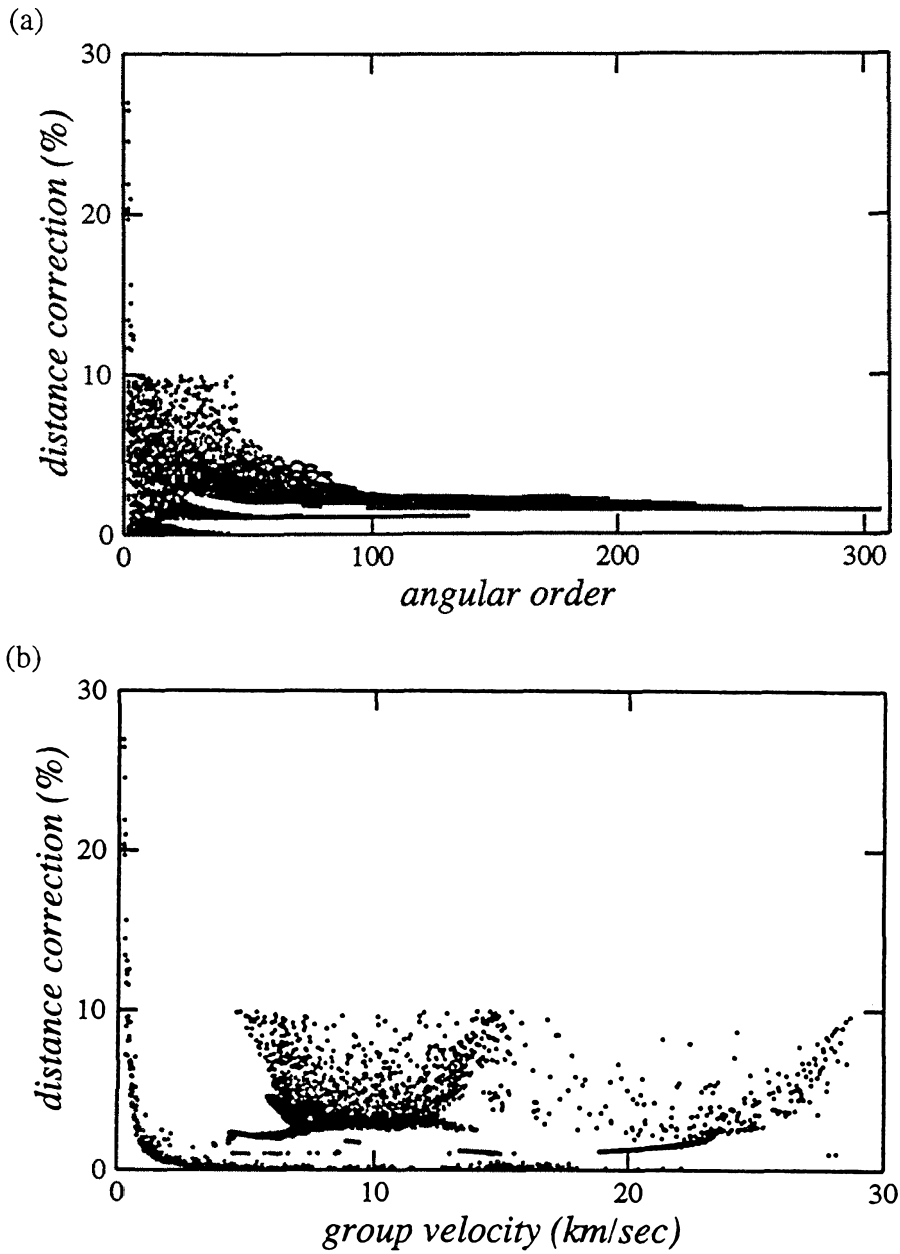


Fig. A2.2 Ellipticity distance correction given by Eq. [A2.1] as a function of (a) angular order and (b) group velocity for seismogram recorded at station CHTO on November 22, 1984 for an earthquake which occurred in the South Atlantic Ridge.

corresponding $\ell < 5$ and group velocity less than ~ 2 km/sec. Based on these observations, the distance correction due to ellipticity was applied to modes with $\ell > 5$ in the inversions presented in Chapter 5.